Multi-Modal Separations for the Biosciences

Daniel Aaron Nelson
Falcon, Colorado

B.S., Colorado State University, 2010

A Dissertation presented to the Graduate Faculty
of the University of Virginia in Candidacy for the Degree of
Doctor of Philosophy

Department of Chemistry

University of Virginia
May 2016

_____

_____

_____

_____

_____

Abstract

The separation, detection, and quantification of cells and DNA in biological samples is crucial to the fields of biomedical science, forensic science, and clinical diagnostics. Applications of such analyses are numerous and include, but are not limited to, health prognosis, human identification, and cancer diagnostics. The use of microfluidic devices offers many advantages such as low sample and reagent volume, fast analysis time, potential for integration, low-cost materials, and point-of-collection capabilities.

The chapters that follow describe the development and use of three different modes of separation, on the microfluidic scale, for DNA quantification, cell counting, human identification, and tumor cell isolation. **Chapter 1** provides the necessary background on the three modes of separation, electrophoresis, magnetophoresis, and acoustophoresis, as well as provides many examples of the use of each separation mode in clinical and forensic applications. The work in **Chapter 2** describes the development of a dual-force system for multiplexing a bead-based DNA assay that can quantify DNA at the sub-single cell level. This method is also shown to be useful for the counting of white blood cells in patient whole blood samples. A further adaptation of the multiplexed bead-based assay is presented in **Chapter 3**. Here, the system is optimized for separating DNA from cellular components in dried blood and cheek swab samples. In addition to purifying DNA, this method eliminates the need for quantification of DNA prior to amplification. In **Chapter 4**, progress towards an inexpensive, fully-automated, rotationally-driven microdevice system for the separation and detection of STR fragments for forensic applications is presented. Finally, in **Chapter 5**, a microfluidic device was designed and optimized for the separation and isolation of circulating tumor cells from whole blood samples.

Table of Contents

List of Figures

List of Tables

Abbreviations:

AD – Alzheimer's Disease

APD – Avalanche Photodiode

AS-PCR – Allele Specific Polymerase Chain Reaction

AuNP – Gold Nanoparticle

bp – base pair

CAC – COC-PSA-COC

CBC – Complete Blood Count

CDH – Coronary Heart Disease

CE – Capillary Electrophoresis

COC – Cyclic Olefin Copolymer

CODIS – Combined DNA Index System

COP – Cyclic Olefin Polymer

CTA – Cellulose Triacetate

CTC – Circulating Tumor Cell

CTC – COC-PeT-COC

DA – Dark Area

DFA – Dual Force Aggregation

DNA – Deoxyribonucleic Acid

Dt – Dilution Threshold

FAM – Fluorescein

FFA – Free Flow Acoustophoresis

FFF – Free-Flow Fractionation

FS – Forward Scatter

GuHCl – Guanidine Hydrochloride

HDL – High Density Lipoprotein

HF – Hydrofluoric Acid

hgDNA – Human Genomic DNA

IPA – Isopropanol

IV – Irrotational Vorticity

JOE – 6-carboxy-4’,5’-dichloro-2’7’dimethoxyfluroescein, succinimidyl ester

LDL – Low Density Lipoprotein

LIF – Laser-induced Fluorescence

LOD – Limit of Detection

LP – Long Pass

MES – Methanesulfonic Acid

MMP – Magnetic Microparticle

PBS – Phosphate Buffered Saline

PC – Polycarbonate

PC3 – Prostate Adenocarcinoma Cell Line

PCL – Print-Cut-Laminate

PCR – Polymerase Chain Reaction

PDMS – Poly(dimethylsiloxane)

PEO – Poly(ethylene oxide)

PeT – Polyester Toner

PMMA – Poly(methyl methacrylate)

PMT – Photomultiplier Tube

PSA – Pressure Sensitive Adhesive

PSA – Prostate Specific Antigen

PZT – Piezoelectric Transducer

RBC – Red Blood Cell

RDM – Rotationally-Driven Microdevice

RFU – Relative Fluorescence Units

RMF – Rotating Magnetic Field

ROX – 5-carboxy-X-rhodamine, succinimidyl ester

S/N – Signal-to-Noise

SP – Short Pass

SPE – Solid Phase Extraction

SS – Side Scatter

STR – Short Tandem Repeat

T/P – Trough-to-Peak

taSSAW – Tilted Angle Standing Surface Acoustic Wave

TBE – Tris-Borate-EDTA

TE – Tris-EDTA

WBC – White Blood Cell

μCE – Microchip Capillary Electrophoresis

μPMT – Micro photomultiplier

μTAS – Micro Total Analysis System

Acknowledgments

First, I would like to thank Dr. James Landers for the opportunity to perform research in his laboratory for the last six years. While in the Landers research group, I gained exposure and experience to numerous aspects of academic, government, and industrial environments, and I am very grateful for all of the opportunities I have been presented with. I would like to thank Dr. Doris Haverstick, without whom the work in this thesis most definitely would not be possible. Thank you for the never ending supply of blood samples that kept my projects alive, and continue to keep our laboratory running. I would also like to thank Dr. Gordon Laurie and the Biotechnology Training Program for both funding and valuable experience in industrial environments and interdisciplinary collaboration. I would like to thank all of the scientists that I have had the privilege to work with over the last six years, particularly the past and present members of the Landers group. These individuals include, in no particular order, Dr. Jerome Ferrance, Dr. Francisco Lara, Dr. Daniel Leslie, Dr. Brian Root, Dr. Jenny Lounsbury, Dr. Briony Strachan, Dr. Brian Poe, Dr. Jingyi Li, Dr. Kerui Xu, Dr. Yiwen Ouyang, Dr. Orion Scott, Dr. Qian Liu, Brandon Thompson, Jacquelyn Duvall, Kimberly Jackson, Hillary Sloane, Charlie Clark, An-Chi Tsuei, and Daniel Mills. In addition, I would like to thank Prof. Chuck Henry, who provided the support and guidance early in my undergraduate career that set me on this path. I would also like to thank the members of my committee, Dr. Jill Venton, Dr. Timothy MacDonald, Dr. David Cafiso, Dr. Andreas Gahlmann, and once again, Dr. Doris Haverstick.

To all of the friends that I have made during my time in Charlottesville that helped keep me sane under the stress and pressure that is graduate school. Thank you for providing the kind of support and outlet that is necessary for success. Stacy, Mike, and Mike, thank you

for always being there when I needed it, especially early in my graduate career. Your support and advice have been crucial over the last six years. Thank you to Chris and Ashley and their boys for providing constant moral support from 1600 miles away in Colorado.

To Shannon, I can't thank you enough for deciding to come to UVA. You are the best thing that happened to me during grad school. Thank you for your unwavering support and love. You continue to push me to be a better scientist, but more importantly a better person. I love you.

Finally, I want to thank my family, Mom, Dad, Kay, Pam, Brad, Connor, and Carolyn. There is no way I get to this point without all of you. You guys are my motivation and make me want to strive to do my best every single day. Mom and Dad, you have provided the ultimate foundation and have been the best support system someone could ask for. I dedicate this dissertation to you guys. I love you all so much.

The X-Phoresis Toolkit for Separations of Cells and Biomolecules

1.1 Overview

Since first being described by Manz et al. in 1990, microfluidic analysis in the form of micro-total analysis systems (μTAS), or lab-on-a-chip, has grown immensely (**Fig. 1**).[1] Microfluidics offers many advantages over conventional instrumentation and analysis, such as reduced volume, fast analysis, and the ability to integrate multiple processes. Adding to the attractiveness, ease of fabrication, reduced materials cost, and potential for portable, point-of-care analysis have made microfluidics and μTAS all the more popular.

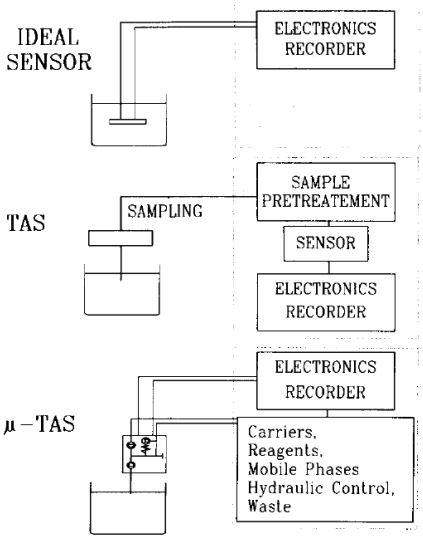

Figure 1: Schematic diagram of an ideal chemical sensor, a 'total chemical analysis system' (TAS) and a miniaturized TAS (μ-TAS). Adapted from [1].

Over the last 26 years, numerous different analytical and bioanalytical processes have been translated to the microfluidic format, and one of the most popular application areas has been separations. Microchip capillary electrophoresis (μCE) separations were the foundation of microfluidics when the concept of μTAS was initially described by Manz et al, and continues to be a prominent application. The field has expanded greatly, and several new and promising separation techniques have evolved as suitable for, and perhaps only possible at, the microfluidic scale. In addition to μCE, this chapter describes magnetophoresis and acoustophoresis, as examples of those novel analytical processes. Basic theory and numerous

examples are presented to demonstrate how each of these separation techniques continue to expand and push the boundaries of separations science.

1.2 Electrophoresis

Electrophoresis is a comprehensive term that refers to the migration of charged solutes or particles of any size in a liquid medium under the influence of an electrical field. The first electrophoresis method was used to study proteins and was referred to as the free-solution or moving boundary method, devised by Tiselius in 1937.[2] This technique was used to study protein-protein interaction and measure electrophoretic mobility, which describes the velocity of migration per applied electric field. The electrophoretic mobility of a particle can be described in Equation 1:

$$\mu = \frac{v}{E} = \frac{Q}{6\pi r\eta}$$

where *v* is the velocity of the particle, *E* is the field strength, Q is the charge on the particle, r is the radius of the particle, and η is the viscosity of the liquid medium. As shown in the equation, electrophoretic mobility is directly proportional to the net charge and inversely proportional to the size of the molecule and the viscosity of the medium.

Although electrophoretic separation of biologically relevant macromolecules in gels (or paper) has been the workhorse of modern biomedical research[3], the advent of capillary electrophoresis has revolutionized separations. Electrophoretic separation in capillaries with inner diameters ranging from 20 to 75 μm has resulted in exceptional resolving power, separation speed, and small sample analysis capabilities. An even greater impact of CE, however, is the ability to apply these separation principles to a variety of analytes that include

not only proteins and polynucleic acids, but also peptides, small drug-like molecules, and even ions.

For over two decades, substantial effort and development has gone into translating CE to the microfluidic scale, and developing more complex microchip designs, advanced detection systems, and new applications. μCE shares many of the same advantages as traditional CE, however, the method also benefits from high speed – normally fourfold to tenfold faster than conventional CE – simplicity, capability for integration of multiple functions, and the potential for automation. Microchips can be constructed from substrates such as glass (borofloat or soda lime), silicon (as per microelectronic chips), a variety of polymeric materials (plastic), or cast from silicone-like materials (polydimethylsiloxane).

The translation of CE to μCE has also benefited from the ability to use many of the same detection modalities. In both methods, separated analytes are detected and measured as they pass a point in the capillary or microchannel that is interrogated. Optical modes of detection for both CE and μCE include, fluorescence, refractive index, chemiluminescence, and Raman spectroscopy. The most popular form of detection is laser-induced fluorescence (LIF) due to its high sensitivity. LIF is effective for naturally fluorescent analytes, as well as analytes that are easily labeled with fluorophores. An exemplary electropherogram from a μCE separation of amino acids and neurotransmitters with fluorescence detection is shown in **Figure 2**.[4]

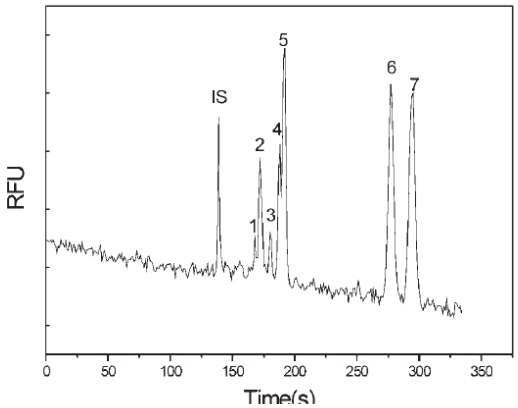

Figure 2. Electropherograms of a standard solution of amino acids and catecholamines. Peak identification: internal standard; (1) norepinephrine; (2) dopamine; (3) Alanine; (4) Taurine; (5) Glycine; (6) Glutamic acid; (7) Aspartic acid; Adapted from [4].

In addition to optical detection, mass spectrometry and electrochemical detectors have also been interfaced with CE and μCE.

The range of applications for μCE continues to expand, and the method has been shown to provide effective analysis for numerous applications with the clinical and forensic sectors. In particular, clinical applications of μCE have expanded immensely in the last 25 years, and the reader is directed to reviews by Guihen et al.[5], Verpoorte et al.[6], Li et al.[7], and Woolley et al.[8], for extensive and in-depth perspectives at how μCE has been utilized in clinical chemistry. For the purpose of this chapter, select applications of μCE are covered, specifically for measuring and monitoring biomarkers, such as lipids, peptides, carbohydrates, and hormones, are presented.

The use of μCE for the study of blood sugar levels was explored by Yatsushiro et al.[9] Glucose was labeled in human blood and μCE performed on a plastic microdevice in order to measure blood sugar levels without the need for calibration, enzymes, or other complicated procedures. Glucose was shown to be accurately detected, and the peak intensity was determined to correlate linearly with the concentration of glucose from 1.0 mM to 300 mM. When compared to the conventional enzymatic method used in clinical tests, the μCE method showed strong correlation, confirming the potential for this method to be used while providing a simplified procedure and reduced sample consumption.

As mentioned above, mass spectrometry detection can be coupled to μCE devices to increase the separation power and provide increased amounts of information. Mass spectrometry was coupled to a μCE device for the detection and analysis of carnitines in urine by Deng et al.[10] Carnitines are compounds that play a significant role in the metabolism of

fatty acids. When a patient is deficient of carnitine, cardiac failure is a possibility, making detection of carnitine compounds important. The authors reported the μCE separation of carnitine and three acylcarnitines from urine in less than 48 seconds on a glass microdevice coupled to a mass spectrometer (**Fig. 3**).

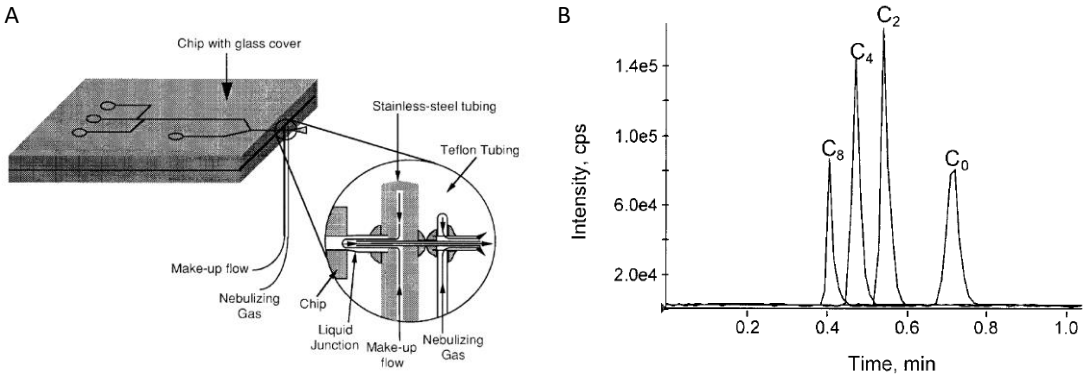

Figure 3: A) Schematic drawing of the glass chip-based CE/MS apparatus and the expanded view of the coupled microsprayer. B) Quadrupole SIM CE/MS analysis of a synthetic mixture containing three acyl carnitines and carnitine (70-248 fmol loaded onto the chip) with alkyl chain lengths including 8, 4, 2, and 0 carbon atoms, respectively. Adapted from [10].

Cortisol is another biomarker of interest, as it considered a reliable indicator of stress. Koutny et al. developed a multiplexed, electrophoretic immunoassay to measure cortisol in blood serum.[11] A rabbit polyclonal anti-cortisol antiserum and a fluoresceinated cortisol derivative were incubated before being separated on the microdevice. The free labeled antigen was separated from bound antigen in just 30 seconds, and the cortisol concentration was determined based on the intensity of the free labeled antigen. The device was able to determine cortisol within the range of clinical interest (1 – 60 μg/dL).

The monitoring of lipoproteins, particularly high-density lipoproteins (HDL), is important for the diagnosis of coronary heart disease (CDH). HDL can be separated into two major subclasses, HDL_2 and HDL_3, and it is believed that inhibition of oxidative modification of low-density lipoprotein (LDL) by HDL_2 plays a central role in CDH. Therefore, separation

and detection of HDL_2 levels is important for predicting CDH. Qian et al. developed a poly(dimethylsiloxane) (PDMS)/glass microchip for fast electrophoretic separation of the two subclasses of HDL.[12] The authors demonstrated baseline resolution of the two subclasses, and saw both peaks in healthy patients, while the HDL_2 peak disappeared in CDH patients. A method such as this could provide rapid screening for the diagnosis of CDH at the point of care.

Another important use of μCE for diagnostics was demonstrated by Mohamadi et al. for Alzheimer's disease (AD).[13] While the cause of AD is not well known, there is evidence that the accumulation of β-amyloid (Aβ) peptides in amyloid plaques is one of the key indicators or progression of the disease. Five different Aβ peptides (Aβ1-37, Aβ1-38, Aβ1-39, Aβ1-40, and Aβ1-42) are regularly present in cerebrospinal fluid (CSF) at concentrations ranging from 1-10 ng/mL. While the ratio of concentrations between the five peptides remains relatively constant in healthy individuals, Aβ1-42 has been shown to be reduced in AD patients, and therefore, makes the determination of Aβ1-42 levels of importance. The authors were able to demonstrate reproducible separation of the varying peptides and quantified the amount of Aβ1-42, however, they readily admit at that the sensitivity needs to improve in order to detect Aβ1-42 levels without the need for preconcentration.

While the use of μCE for biomarker analysis continues to grow, one of the first, and most popular applications of μCE, was the analysis of DNA. μCE has demonstrated promise as a high-speed, high-throughput method for screening of DNA for genetic mutations, polymorphisms, genotyping, and DNA sequencing. Unlike most charged biomolecules, the mass-to-charge ratio for DNA is independent of size, and therefore, a sieving matrix or polymer network is required to separate different lengths of DNA. As the charged DNA

molecules migrate through the polymer network, they become hindered to a degree that is based on the size of the molecule (i.e. larger molecules are hindered more than smaller ones). High-resolution DNA separations over a large range of DNA lengths are achieved on traditional CE instruments through the use of well-established polymers, are carried out across a 37 cm capillary, and separation times are on the time scale of tens of minutes. One of the main challenges μCE has faced is the ability to approach the same level of resolution as capillaries in microchannels that are significantly shorter, typically no longer than ~10cm.

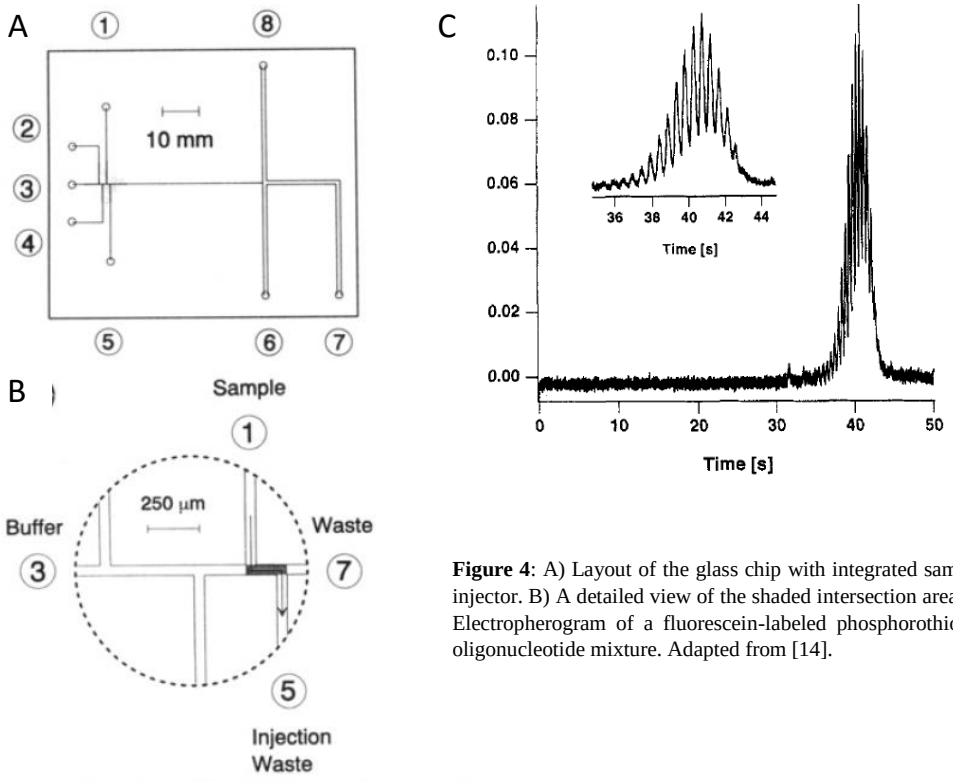

Figure 4: A) Layout of the glass chip with integrated sample injector. B) A detailed view of the shaded intersection area C) Electropherogram of a fluorescein-labeled phosphorothioate oligonucleotide mixture. Adapted from [14].

One of the first DNA separations performed on a μCE device was by Effenhauser et al.[14] The authors reported the separation of a synthetic mixture of fluorescent phosphorothioate oligonucleotides ranging from 10 to 25 bases in length on a glass microdevice. The channel architecture was designed to specifically provide a known volume of sample for an unbiased electrokinetic injection (**Fig. 4A**). When coupled with high electric

fields (2300 V/cm), size-based separation of the oligonucleotides was achieved in 45 seconds over 3. 8 cm (**Fig. 4B**). Woolley et al. fabricated a μCE array in glass, and demonstrated high resolution separations of fluorescently-labeled ΦX174 *Hae* III DNA restriction fragments.[15] The fragments ranged from 70-1000 base pairs and the separations were completed in 120 sec.

Shortly after the success of DNA separation on glass devices, the use of polymeric substrates such as poly(methyl methacrylate) (PMMA), poly(dimethylsiloxane) (PDMS), and acrylic copolymer resin was demonstrated. These materials were attractive due to their low cost, variety of properties, and simple fabrication, particularly amenable to mass-production. McCormick et al. showed successful separations of the same ΦX174 *Hae* III DNA restriction fragments as Woolley et al., on injection molded acrylic copolymer.[16] These separations were completed in less than 3 minutes and had relative standard deviations in migration time less than 1% for all peaks in six consecutive runs on seven different chips. The authors also presented Ohm's law plots that demonstrated that the cross-sectional area of the acrylic channels was similar to that of a fused-silica capillary, and as a result, the heat dissipation was comparable, suggesting limited Joule heating effects. Wabuyele et al. reported single molecule detection of double-stranded DNA in both PMMA and polycarbonate (PC) devices and studied the effect of pH on the migration time for both substrates.[17] The authors observed that the pH did not influence the migration time and saw a 4-fold increase in the number of detected events when using narrow channels. Single molecule sizing of λ-DNA, M13 (7.2 kbp) and pUC19 (2.7 kbp) was achieved.

Mutation detection using μCE has been described by Tian et al.[18] Mutations found on the BRCA1, BRCA2, and PTEN genes were amplified by allele-specific PCR (AS-PCR) and

analyzed on a μCE device. Methods optimized for separation of the mutations on traditional CE following AS-PCR, were translated to a μCE device. Separation times were less than 170 seconds on a 55 mm separation device, compared to ~24 min for traditional CE. Further, deletion and insertion mutations showed the same resolution as the CE method, while specific point mutations show slightly lower resolution.

In addition to mutations and polymorphisms, μCE has been extensively used for genotyping and DNA sequencing, particularly for human identification in the field of forensics. Short tandem repeats (STRs) are 2-7 bp repeating units in non-coding regions of DNA (loci), and are used as the gold standard for human identification in the forensic science. The length of each of these repeats (alleles) at a given location (locus) can vary greatly between individuals, providing an effective mode for human identification. The greater the number of loci interrogated, the less likely two individuals will share the same profile. The national DNA database utilizes 13 different core loci that lower the probably of a random match to lower than 1×10^{-13}, however, the use of 18- or 24-loci is common for further discrimination. The separation of the 13 core loci requires single-base resolution since there are common alleles that differ by only a single base pair. Significant progress continues to be made in achieving such resolution on microchips. Schmalzing et al. first described the separation of single- and four-locus STR samples in less than two minutes on a silicon-based microdevice.[19] This represented a 10- to 100-fold decrease in time compared to traditional CE or slab gel methods. Separation of up to nine loci was demonstrated by Shi et al. and showed baseline resolution of alleles that differed by only 2 bp. These separations were completed on 10 cm microchips in 30 minutes. Full STR analysis on a glass microdevice was also shown by Karlinsey et al.[20] In this case, the authors focus on the development of a single

detection system for four and five-color STR analysis using an acousto-optic tunable filter (AOTF). The resulting system showed full STR profiles for a five-color, 16-loci STR kit on a glass microdevice.

Outside of separating STRs for human identification, microfluidics provides the opportunity to integrate all important procedures for STR analysis onto one device. Typical workflow for STR analysis includes DNA extraction, multiplexed STR PCR amplification, and STR DNA separation. Several different examples of integrated STR analysis have been reported. As a first step towards integrated STR analysis, Easley et al. reported a sample-in-answer-out microfluidic genetic analysis system capable of accepting whole blood and outputting a genetic profile.[21] All three phases of genetic analysis were present and a genetic profile confirming the presence of Bacillus anthracis (anthrax) in whole blood was obtained in less than 30 minutes.

Le Roux et al. presented the early stages of an integrated STR analysis system by combining the multiplexed STR PCR and μCE onto a single device.[22] The authors demonstrated the integration of PCR and μCE on a cyclic olefin polymer (COP) plastic device with results that were comparable to conventional instrumentation. In addition, single-base resolution was achieved, along with the necessary precision to accurately identify each allele, all in a 7 cm channel. A version of a portable STR analysis system was also demonstrated by Liu et al.[23] A glass-wafer device that consisted of STR PCR and μCE was used at a mock crime scene (**Fig. 5A**). Blood sample collection, DNA extraction, and STR analysis on the μCE device were all completed in the field. A 9-loci STR profile was generated for each sample and provided a 'mock' CODIS hit in less than 6 hours (**Fig. 5B**). Both of these works showed the potential for the development of a portable genetic analysis system, however,

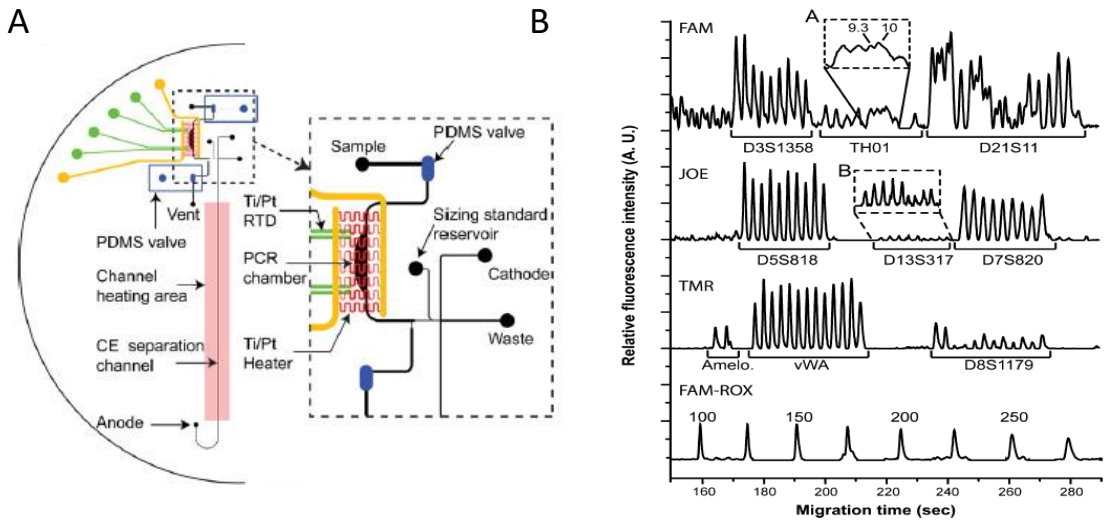

Figure 5: A) Design of the PCR-CE microchip for forensic DNA analysis. The integrated device consists of 7-cm-long electrophoretic separation channels (black), 160-nL PCR chambers (black), RTDs (green), PCR heaters (red), and PDMS microvalves (blue). B) Expanded view of the heater, RTD, PCR chamber and CE co-injector. C) The 9-plex STR allelic ladder separation obtained on the portable PCRCE microsystem. Adapted from [23].

several improvements were necessary to realize a truly integrated system. Namely, the work presented in both studies relied on DNA extraction and purification taking place off-chip, prior to PCR/μCE analysis.

Le Roux et al. followed up their primary work by addressing the issue of off-chip extraction and showed a fully integrated device that incorporated all three phases of STR analysis (**Fig. 6A**).[24] A unique enzymatic liquid-phase extraction method was added to liberate DNA from cells collected from a buccal swab or FTA card. The target DNA is then aliquoted and mixed with PCR reagents before infrared-mediated PCR amplification. The PCR product is mixed with a sizing ladder and are once again separated in 7 cm. This system provided full 18-loci profiles in under 2 hours that matched conventional instrumentation (**Fig. 6B**). Just prior to this work published by Le Roux et al, Liu et al. also developed a fully integrated glass microdevice, similar to the one presented above, that incorporated DNA

A

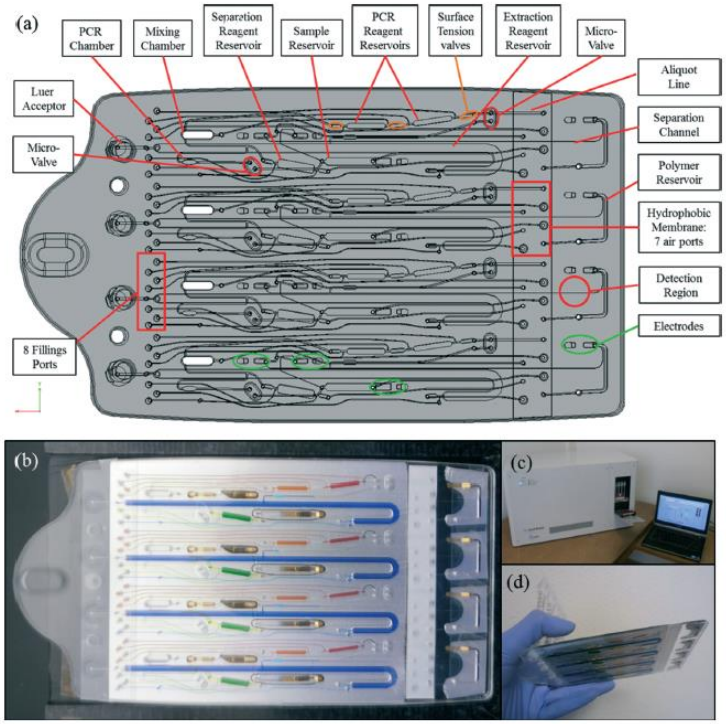

B

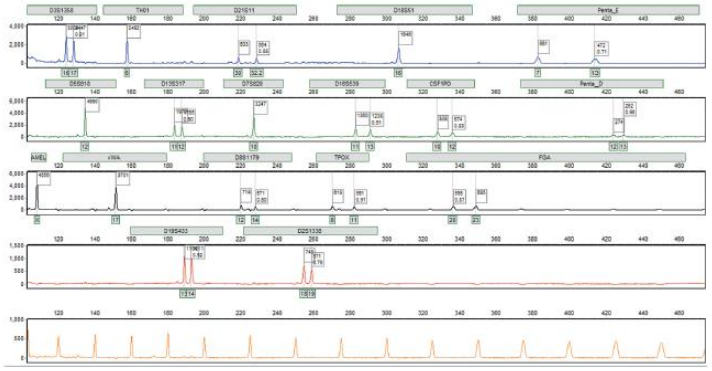

Figure 6: Microfluidic chip for "sample-in-answer-out" integrated DNA processing. (a) Schematic representation of the microchip with major microfluidic features. (b) Bottom view of the cartridge containing the fluidic layout with blue reagents in the extraction reagent reservoir, red and orange reagents in the PCR reagent reservoirs, green reagents in the separation reagent reservoir and polymer in the polymer reservoir. (c) Microchip inside the instrument enabling its functionality with swabs attached and computer for software control. (d) View of the microchip with swabs attached to it with a hand scale. B) Electropherogram of integrated LE–PCR–ME. Allele calls are 100% concordant with conventional profiles. Adapted from [24]

purification on-chip prior to STR analysis.[25] Target DNA was bound to beads and purified before being transferred to a PCR chamber for STR amplification. The fluorescently labeled PCR product was introduced into a separation chamber where the fragments were separated and detected. Compared to the Le Roux et al. device and method, this device was fabricated in glass, the procedure took 3 hours to complete, and the method produced full 9-plex STR profiles.

1.3 Magnetophoresis

Methods such as CE and μCE are suitable for small biomolecules or ions, as described above, however, for biomolecules that are of large molecular weight, these methods are no longer applicable. An alternative method called magnetophoresis is a promising technique that can provide the necessary separation of large biomolecules and cells. Magnetophoresis the migration of particles in a liquid via magnetic field-induced force. The force that a biomolecule or cell experiences in a magnetic field, B, can be described by Equation 1:

$$F = \frac{(\chi_p - \chi_m)}{\mu_0} V(\boldsymbol{B} \cdot \nabla) \cdot \boldsymbol{B}$$

where χ_p is the volume magnetic susceptibility, χ_m is the volume magnetic susceptibility of the medium, μ_0 is the vacuum magnetic permeability, V is the volume of the particle, and B is the magnetic flux density. By accounting for the drag force in a liquid, $F_D = -6\pi\eta r v$, the velocity of a particle under magnetophoresis can be described by Equation 2:

$$v = \frac{2}{9}\frac{(\chi_p - \chi_m)}{\mu_0 \eta} r^2 (\boldsymbol{B} \cdot \nabla) \cdot \boldsymbol{B}$$

By this definition, the magnetophoretic velocity of a particle is directly proportional to the difference in volume magnetic susceptibility between the particle and the medium ($\chi_p - \chi_m$), the square radius of the particle r^2, and the gradient of the magnetic field $(\boldsymbol{B} \cdot \nabla) \cdot \boldsymbol{B}$.

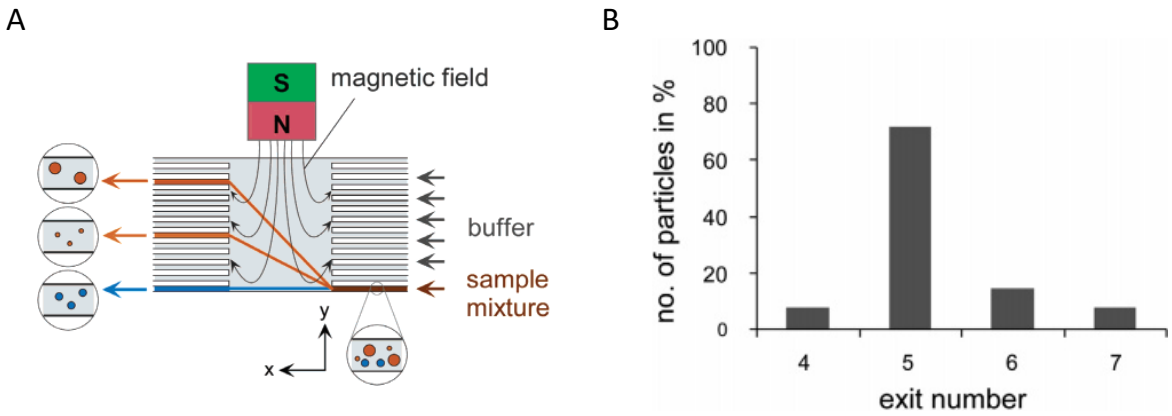

Figure 7: A) Concept of free-flow magnetophoresis. Magnetic particles are pumped into a laminar flow chamber; a magnetic field is applied perpendicular to the direction of flow. Particles deviate from the direction of laminar flow according to their size and magnetic susceptibility and are thus separated from each other and from nonmagnetic material. B) Distribution of particle deflection as obtained in an experiment with the 4.5-ím Dynabeads at a flow rate of 200 μL/hr. Adapted from [27].

Magnetophoresis has typically been used as a form of free-flow fractionation (FFF). First described by Giddings et al.[26], FFF is the use of external forces for the fractionation of microparticles in a flowing liquid. Several different types of external forces have been applied to the idea of FFF and in addition to magnetophoresis, include dielectrophoresis, thermophoresis, electrophoresis, and acoustophoresis (described below). Pamme et al. demonstrated the effectiveness of magnetophoresis as an FFF method by separating 2.0 and 4.5 µm magnetic particles from one another, and from nonmagnetic 6.0 µm particles (**Fig. 7**)[27]. As predicted, the 4.5 µm particles migrated further than the 2.0 µm particles, and the 6.0 µm nonmagnetic particles did not migrate at all. The applied flow rate, along with the strength and gradient of the magnetic field were the factors that had the greatest influence on the degree of deflection for the different particles. Kawano et al. introduced a two-dimensional magnetophoresis device that used two triangular shaped magnets placed on either side of a

capillary cell to create a magnetic field gradient for the separation of 1, 3, and 6 μm polystyrene particles in a paramagnetic medium.[28] The particles migrated along the edge of the magnet gradient until reaching a point where the magnetic force was equal to the drag force, at which time the particle passes between the two magnets. The migration distance at which the particle passes through the magnets can be used to determine the magnetic susceptibility of the particle. The authors used this method to experimentally determine the magnetic susceptibility values for oxygenated and de-oxygenated blood cells, with great success.

While some blood cells inherently have paramagnetic properties that allow them to be isolated from other non-magnetic particles, many biomolecules and cells do not possess such properties. Therefore, separation via magnetophoresis must be facilitated by the binding of cells and biomolecules to magnetic particles that can then be manipulated in the presence of a magnetic field. Two common applications of this method include DNA capture and cell isolation. Hale et al. developed a continuous flow microfluidic device for the separation of DNA from blood using magnetophoresis.[29] A blood sample was lysed and mixed with magnetic particles before being introduced into the microfluidic device. The microdevice was

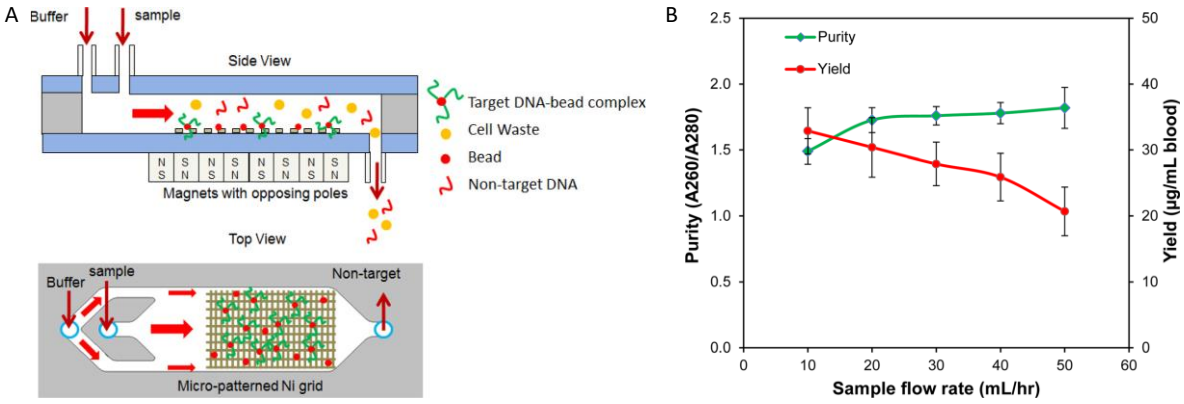

Figure 8: A) Schematic of a microfluidic chip for DNA isolation. The overall dimensions of the device are 75mm x 25mm x 0.7mm and the channel height is 100 μm. The schematic is not to scale. B) Purity and yield of DNA isolation at various sample flow rates. Adapted from [29].

fabricated to that the bottom of the channel was patterned with nickel to produce short-range magnetic fields, while external permanent magnets provided the long-range fields (**Fig. 8A**). The long-range fields were used to pull the magnetic particles to the bottom of the channel, while the purpose of the short-range fields was to trap and immobilize the magnetic particles once they reached the bottom. This method showed a DNA yield from blood samples around 20 μg/mL when running at a flow rate of 50 mL/hr (**Fig. 8B**).

Another continuous flow DNA isolation method was described by Karle et al.[30] Similar to Hale et al., a cell lysate sample (E. coli) was incubated with a magnetic bead suspension before being subjected to a magnetic field. Comparatively, rather than subjecting the sample to a bed of magnets under a microfluidic channel, the beads were carried through a series of microfluidic channels containing washing and elution buffer by a rotating magnet. This provided a method of DNA extraction, as opposed to just DNA capture. DNA recovery was reported to be 147% compared to bead-based extraction typically performed in tube.

Shim et al. presented a magnetophoretic method that can collect up to 95% of DNA-bound magnetic particles from solution to concentrate a DNA sample.[31] The uniqueness of this method lies in the use of a 4-base uracil region on the complimentary DNA strand attached to the magnetic particles. This complimentary strand binds the target DNA and after isolating the particles with a magnet and washing, the DNA can be detached through an enzymatic reaction using uracil-specific excision reagent. A processing time of one hour and DNA concentration of over 1000-fold was reported.

Multiple methods describing the detection and quantification of DNA using magnetophoresis have been reported. A method utilizing magnetic microparticles (MMPs)

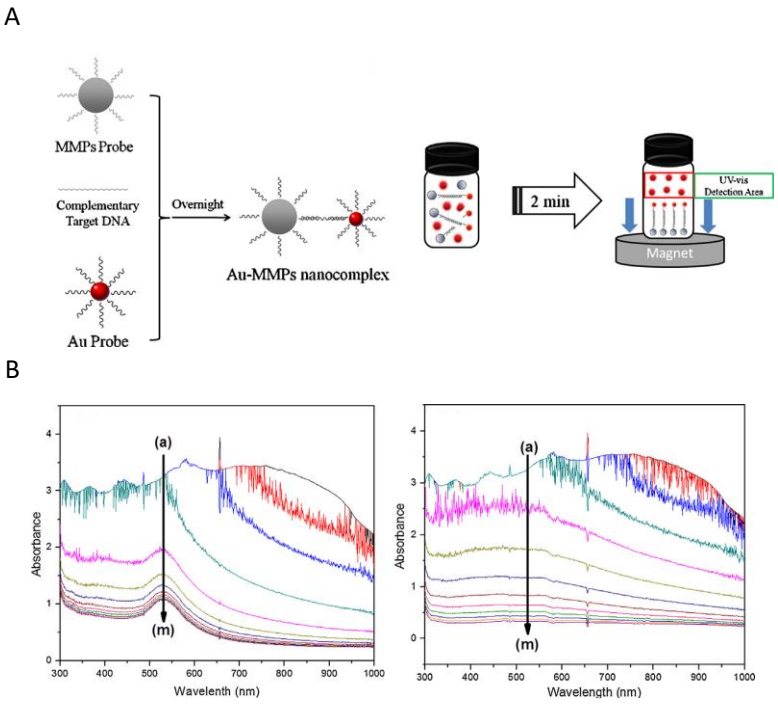

Figure 9: A) Illustration of optical signal of Au NPs, as used for DNA detection. B) Time-based UV–Vis spectra of qualitative detection solution on a magnet (0–2 min → (a–m)): (A) non-target DNA, (B) target DNA. Adapted from [32].

and gold nanoparticles (Au NPs) was described by Zhou et al.[32] Au-MMP nano-complexes were formed in the presence of DNA and generated a color signal. When the solution of bound complexes and unbound particles was exposed to a magnetic field for 2 minutes, the complexes were drawn to the bottom of the solution (**Fig. 9A**). The remaining unbound Au NPs remained in solution and provided a color response that could be directly quantified via UV/Vis spectroscopy. The change of color after exposure to the magnetic field could then be correlated to the amount of DNA present in the solution (**Fig. 9B**). The authors report a limit of quantitation of 0.1 nM. Leslie et al.[33] and Strachan et al.[34] described a similar target-specific hybridization method for qualitative determination of DNA. A DNA target was amplified via PCR and the product was added to a microwell containing magnetic beads bound with oligonucleotides that were complimentary to the target sequence. In the presence of a rotating magnetic field, the target sequence would hybridize to multiple oligo-coated beads bringing the beads together into aggregates. This aggregation was used to determine the presence of the target DNA. In the absence of the target DNA, the beads would remain disperse in the magnetic field. This method has been

applied to the detection of salmonella[35], viruses[36], and the detection of single-point mutations in the KRAS gene[37].

In addition to DNA, magnetophoresis can be used for the separation of various cell types through the use of antibody-antigen interactions. Such methods have been applied to several types of cells and examples are described below. Hematopoietic progenitor cells are immune cells that can differentiate into both red and white blood cells, and have shown promise as a substitute for bone marrow transplantation. Jing et al. presented two variations on the use of magnetophoresis for the separation of hematopoietic progenitor cells from peripheral blood leukocytes as an alternative to low throughput flow cytometry.[38, 39] In the first method, magnetic particles that were labeled with anti-CD34+ antibody were incubated with a sample of CD34+ progenitor cells. After binding, the sample was processed in a flow channel with a quadrupole magnet. Migrated in the magnetic field and were collected and counted. Fresh blood samples had an average purity of 2.2% before processing and 90% after processing, with and average recovery of 39%. Samples that were cryogenically stored, the initial purity was 2.6% and was 77% after processing, with a recovery of 30%. The variation on this method presented by Jing et al., focused on the negative selection of progenitor cells via labeling of the leukocytes rather than the progenitor cells. The authors stated an initial purity between 0.37% and 9% before enrichment, and 30% to 85% after processing, with a recovery of 49 to 84%. The throughput of this method was 6.7×10^4 cells/s and resulted in a 3.5 $\log_{10}$ depletion of T-lymphocytes, an important factor for effective transplantation.

Another example of immunomagnetic-capture magnetophoresis is presented by Glynn et al. for the isolation of CD4+ cells.[40] Similar to Jing et al., a blood sample was incubated with anti-CD4+ magnetic particles before being added to a microfluidic device. The sample

was driven through the device using finger pressure, and the beads and bound cells were deflected towards a permanent magnet that was placed perpendicular to the channel, and into a capture chamber (**Fig. 10A**). The cells and beads packed into the chamber, and the cell concentration was estimated by measuring the level of packing via a bright-field microscope (**Fig. 10B**). The sample can be processed in just 15 seconds and showed a high capture efficiency of 93%. This device showed a linear response across clinically relevant values for CD4+ values when estimating CD4+ count and is ideal for point-of-care environments due to its lack of instrumentation.

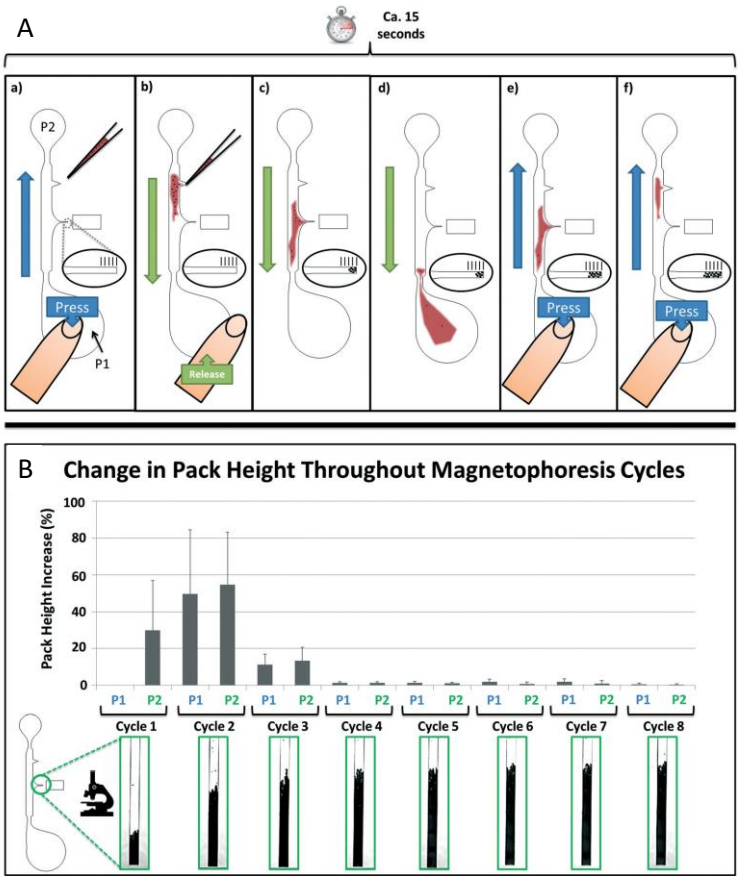

Figure 10: A) Operation of one cycle to isolate CD4+ cells (shown as black circles) from whole blood. Direction of flow pressure is shown with blue (towards P2) and green (towards P1) arrows. Elliptical insert represents a zoomed view of the capture chamber. B) Analysis of the heights of the cell/bead pack in the capture chamber from 1–8 cycles. "P1" (blue) and "P2" (Green) indicate the direction of the fluidic force. Images bordered in green represent zoomed micrographs of the capture chamber at the completion of a cycle. Adapted from [40].

Finally, magnetophoresis has shown great promise in the area of rare cell isolation, such as circulating tumor cells (CTCs). CTCs are rare cells shed from primary tumors into the blood stream, and provide an opportunity to detect, study, and characterize those tumors. Once again utilizing antibody-antigen interactions, immunomagnetic beads coated in epithelial cell adhesion molecule (EpCAM) antibodies were used to bind to epithelial tumor cells spiked in a

blood sample. A microfluidic device was developed by Kim et al. for cell separation via lateral magnetophoresis.[41] In this device, a ferromagnetic wire array was inlaid on the bottom of the microchannel to generate the gradient magnetic field. Two individual streams of buffer and a blood sample with spiked cancer cells were introduced on one end of the device. As the sample flows through the device, the bead-bound CTCs are influenced by the magnetic field and are deflected to a collection reservoir, while the non-magnetic blood cells remain uninfluenced by the field, and flow into a separate reservoir. The authors report a flow rate of 5 mL/hr, with 90% capture efficiency and a purity of 97%. Jeong Won Park et al. also describe a microfluidic magnetophoretic device for CTC separation using ferromagnetic wire.[42] Contrary to Kim et al., this device infuses sample via two individual streams with a separate buffer stream in the middle hydrodynamically focusing the sample to the walls of the channel (**Fig. 11A**). In addition, the magnetic field in this device deflects and focuses the bound CTCs towards the center of the microdevice into the buffer stream, while non-bound blood cells remain along the channel walls and are collected. The authors report a processing flow rate of 40 µL/min, allowing for analysis of 400 µL of blood in 10 minutes (2.5 mL/hr).

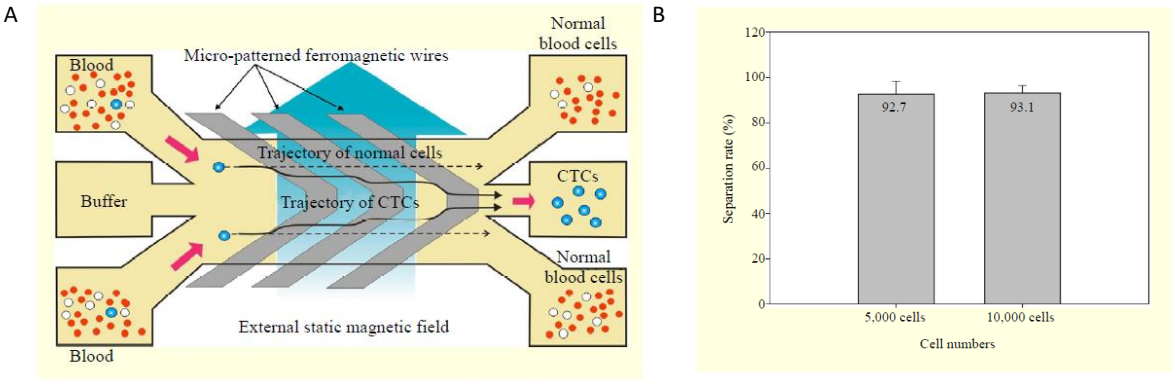

Figure 11: A) Schematic diagram showing the working principles of a microdevice for separation of CTCs using lateral magnetophoresis and immunomagnetic nanobeads. B) CTC recovery efficiency of the microdevice using lateral magnetophoresis at an external magnetic field. Adapted from [42].

This is compared to the analysis of 5 mL/hr by Kim et al. Similar to Kim et al., the authors describe a capture efficiency of 93% and purity that remains above 90% (**Fig. 11B**).

1.4 Acoustophoresis

Use of an acoustic standing wave for manipulation of particles has been demonstrated for nearly five decades, and has become an area of high interest in the field of microfluidics over the last three. A standing wave in a microfluidic device is typically generated via the high frequency vibration of a piezoelectric transducer (PZT), where the microfluidic channel acts as an acoustic resonator, reflecting the wave, and creating a pressure node within the channel. Particles exposed to the acoustic standing wave experience a primary radiation force, F_r, that can be described by **Equation 3**.

$$F_r = -\left(\frac{\pi p_0^2 V_p \beta_m}{2\lambda}\right) \cdot \Phi(\beta, \rho) \cdot \sin\left(\frac{4\pi \cdot x}{\lambda}\right) \tag{3}$$

V_p is the volume of the particle, p_0 is the applied pressure amplitude, β_m is the compressibility of the medium, λ is the wavelength of the acoustic standing wave, x is the distance from a pressure node, and Φ is the acoustic contrast factor, represented by:

$$\Phi = \frac{5\rho_p - 2\rho_m}{2\rho_p + \rho_m} - \frac{\beta_p}{\beta_m} \tag{4}$$

where ρ_p and ρ_m are the density of the particle and medium respectively, and β_p and β_m correspond to their compressibilities. This acoustic contrast factor determines whether a given particle will move towards the pressure node or the pressure antinode based on the density and compressibility of the particle.

As described in Equation 1, the force that a particle experiences scales with the volume of the particle, making this an attractive method for size-based separation of cells and other particles. This method is described as free-flow acoustophoresis (FFA), and the basic principle lies in the use of an acoustic standing wave, orthogonal to the flow of particles, that forces the particles towards a pressure node while they are moving with the flow. Two particles of different size that are subjected to the same acoustic field will move towards the pressure node at different rates, with the larger particle moving faster due to experiencing a greater force in the field according to Equation 3. Use of FFA was reported as early as 1995 by Johnson and Feke using an orthogonal standing wave with a node in the center of a channel and two separate inlet flows.[43] As the particles were influenced by the standing wave in the channel, the larger particles were moved toward the node at a rate greater than that of the smaller particles. By fabricating a barrier at the outlet that split the channel, fractions consisting of the two separated populations of particles could be collected. This idea can be expanded to several different particle populations by designing microfluidic architecture that provides multiple outlets for particles that migrate at different rates based on their intrinsic properties. Petersson et al. demonstrated the FFA separation of polystyrene beads that were 2, 5, 8, and 10 μm in diameter.[44] Each population migrated differently based on

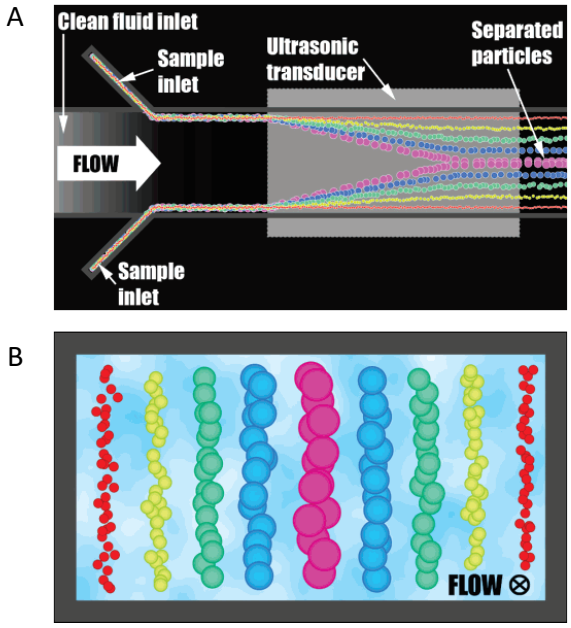

Figure 12: A) Schematic diagram showing the working principles of a microdevice for separation of CTCs using lateral magnetophoresis and immunomagnetic nanobeads. B) CTC recovery efficiency of the microdevice using lateral magnetophoresis at an external magnetic field. Adapted from [44].

size, and specific microfluidic architecture facilitated the collection of each population fraction individually (**Fig. 12**).

Outside of basic particle manipulation and size separation, acoustophoresis has found great success in separating cellular populations for various applications. One of the most popular applications of FFA for the separation of cells, is the isolation of circulating tumor cells (CTCs). As described above, CTCs are rare cells shed from primary tumors into the blood stream, and provide an opportunity to detect, study, and characterize those tumors. Using the same FFA principle, with an orthogonal wave and microfluidic splitting, Augustsson et al.[45] and Magnusson et al.[46] were the first to demonstrate the separation of a sample of prostate cancer cell line from a population of white blood cells. This method was shown to be effective and provided proof of principle, however, the red blood cells were lysed, the WBCs were diluted 1:10 prior to analysis, and separation efficiency decreased with increasing flow rate, limiting sample throughput. While not explicitly stated, lysis, dilution, and low flow rate were likely required to decrease the complexity of the sample in order maintain efficient separation.

Augustsson et al. improved upon this principal work by introducing a second transducer to the separation system at a different frequency than the separation transducer.[47] The second transducer was used to 'pre-focus' the entire sample into two nodes prior to entering the separation channel, and brought all of the cells to the same velocity (**Fig. 13**). This eliminated any negative effects that would arise from parabolic flow in the channel that would cause cells to migrate at different velocities and decrease separation efficiency. Antfolk et al. expanded further on this type of design by either adding additional fluidic architecture that allowed for the concentration of WBCs in addition to the cancer cells, or used a single

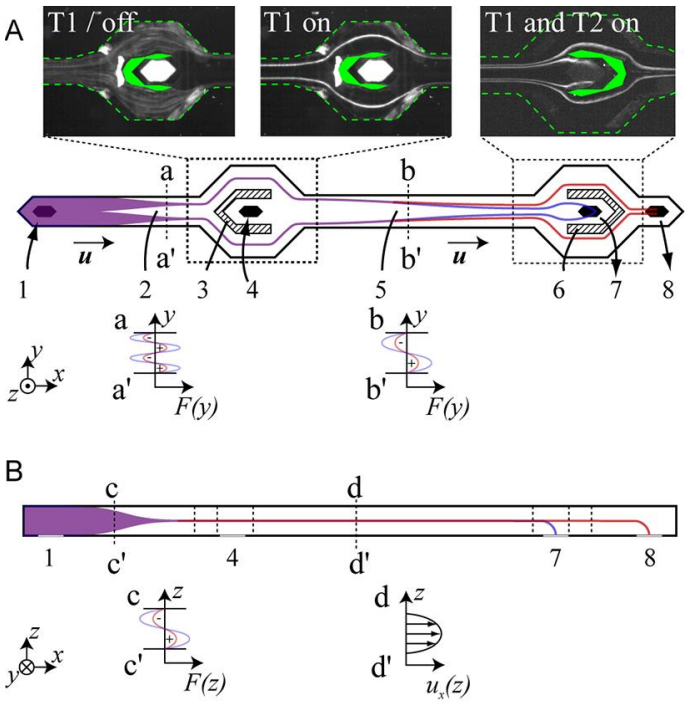

Figure 13: Top view schematic of 'pre-focus' microdevice. Insets show prealigned (T1 on) and nonprealigned (T1 off) microbeads at the end of the prealignment channel, and 5 and 7 μm beads separated at the central outlet (T1 andT2 on). (B) Side view schematic. Cells/particles are prealigned in the vertical direction by means of an acoustic force (c-c′) to minimize the influence of the parabolic flow profile (d-d′) in the channel, which may otherwise affect the trajectories of the cells. Adapted from [47].

inlet and eliminated the use of a laminar sheath flow.[48, 49] Finally, isolation of tumor cells from actual patient samples was recently reported by Li et al. on a device that utilized tilted-angle standing surface acoustic waves (taSSAWs).[50] After optimization with cancer cell lines, samples from three breast cancer patients were analyzed. While CTCs were successfully isolated from these patient samples, the results were not compared to the conventional method to determine the efficiency of this method.

Other early uses of acoustic manipulation of particles came in the form of particle and cell concentration. Typically, to concentrate cells or particles, an acoustic wave is used to focus particles into a node and collecting the fraction without the surrounding medium. Yasuda et al. described the concentration of red blood cells in a quartz chamber[51], while Goddard and Kaduchak used cylindrical capillaries for particle concentration.[52] Nordin et al. describe a two-hundredfold volume concentration of dilute cell and particle suspensions using acoustophoresis.[53] Through the integration of two-dimensional focusing (i.e. vertical and horizontal standing waves), they report concentration factor approaching 200 with cell or particle recovery as high as 98%. Jakobsson et al. surpassed this success by demonstrating

thousand-fold volumetric concentration of live cells by recirculating the sample within the microfluidic device.[54]

Alternatively, the same method can be used to remove particles or cells in order to collect cell- or particle-free solution. An example of this was presented by Lenshof et al. for collection of blood cell-free plasma.[55] Using a standing wave, all cellular material was focused to the center of a channel where it was removed through several outlets in the bottom

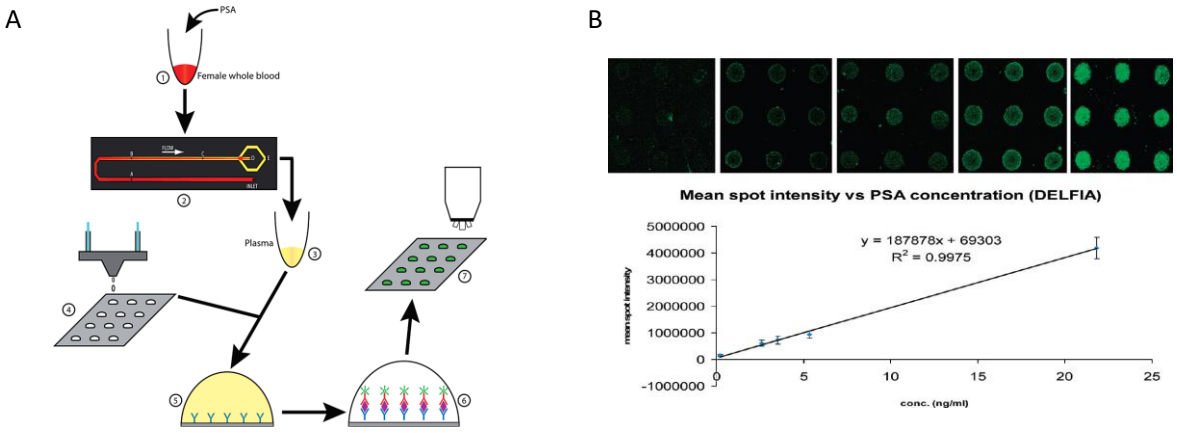

Figure 14: A) Schematic of the all chip based whole blood plasmapheresis and PSA diagnostics: (1) spiking of PSA in female whole blood,(2) ultrasonic standing wave driven microchip plasmapheresis, (3)plasma collected via injector sample loops, (4) microarraying of PSA antibody, (5) microchip incubation in obtained plasma, (6) sandwich assay, and (7) fluorescence readout. B) Microarray results of the titration series of blood plasma derived from PSA spiked female whole blood. Adapted from [55].

of the channel, while the plasma is collected at the end of the device (**Fig. 14A**). The plasma was shown to contain less than 6.0 x 10^9 erythrocytes/L, a standard requirement recommended by the Council of Europe. In addition, the authors coupled the plasmapheresis device to a previously developed prostate specific antigen (PSA) sandwich antibody microarray and showed detection of clinically relevant levels of PSA in the purified plasma (**Fig. 14B**). Similarly, Dykes et al. removed platelets form peripheral blood progenitor cell products by concentrating the larger leukocytes to the pressure node while the smaller platelets, moving slower than the leukocytes, were removed before being focused.[56]

While many applications of FFA harness acoustic pressure to focus and concentrate particles or cells to a node, the opposite effect can be utilized for particles with different acoustic contrast factors, where particles are moved away from the pressure node. Petersson et al. demonstrated the separation of lipids from erythrocytes for blood purification prior to retransfusion of blood collected during surgery.[57] The sign of the acoustic contrast factor for the lipid particles is opposite the sign of the acoustic contrast factor for the erythrocytes, which results in the lipid particles moving towards the anti-nodes at the channel walls, while the erythrocytes move towards the pressure node at the center of the channel (**Fig. 15**). The authors demonstrated a 70% enrichment of erythrocytes and an 80% removal of lipid particles.

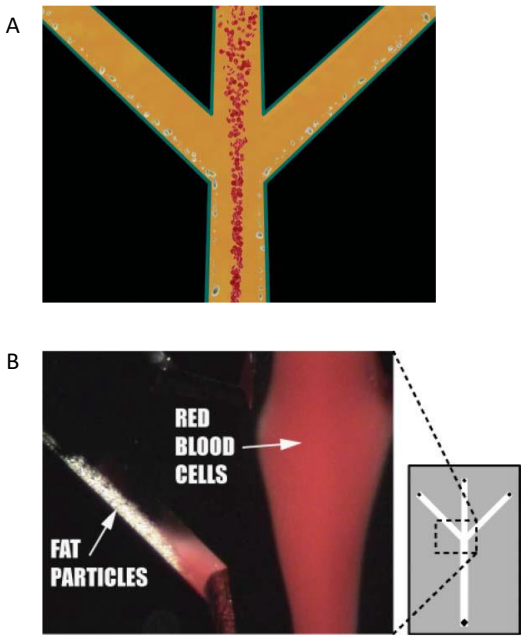

Figure 15: A) A schematic showing the main channel split into three outlet channels allowing the laminar flow properties to collect erythrocytes and lipid particles separately. B) Human lipid particles separated from human erythrocytes at the trifurcation of 350 mm separation chip with ultrasound turned on. Adapted from [57].

A series of other cell separation applications using FFA have been described. Yang et al. presented an acoustophoretic method for sorting viable mammalian cells by utilizing the size difference between viable cells and those that have undergone apoptosis.[58] Sub-populations of white blood cells have been separated with very high purity and high recovery using the pre-focus FFA method described above. A method described as affinity-bead-mediated acoustophoresis can be used to further discriminate between populations of cells that show similar inherent acoustic properties. By labeling cells with anti-body-coated magnetic beads, the acoustic properties of the targeted cells can be altered by creating bead-

cell complexes. The change in size, density, and compressibility due to the addition of beads allows for targeted cells to be isolated from nontargeted cells via acoustophoresis. This method was used by Lenshof et al.[59] to isolate CD4+ cells from other peripheral blood cells (**Fig. 16A**). When compared to standard magnetic cell sorting, the acoustophoretic method provided an improvement in separation efficiency (65 ± 22% vs. 56 ± 15%) and similar levels of purity (87 ± 12% vs. 93 ± 3%) (ref) (**Fig. 16B**).

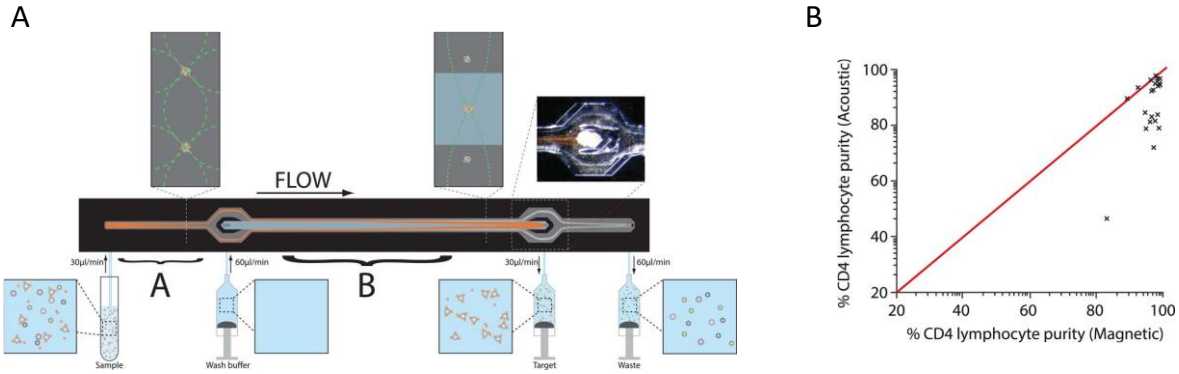

Figure 16: A) (A) Prefocusing zone. (B) Separation region. The pre-focusing step will ensure that the transfer of all particles across the separation channel starts from identical positions, thereby eliminating loss in separation efficiency due to the laminar flow profile. B) Purity of acoustic and magnetic sorted CD41 T lymphocytes. Comparison of CD41 lymphocyte purities obtained with parallel magnetic and acoustic separations (n 5 22). Results from the magnetic enrichments are plotted against results obtained from the corresponding acoustic enrichments. The red line indicates the diagonal iso effective line. Adapted from [59].

In addition to isolating populations with similar acoustic properties, bead-assisted focusing can be used for particles that fall below the threshold for acoustic focusing. Typically, in FFA, when the size of a particle is below 1 μm, the primary radiation force acting on the particle is too weak to overcome other fluidic forces in the system. To overcome this problem, the small particles can be bound to larger particles to alter their acoustic properties, similar to cells described above. Persson et al. used this technique to bind bacteriophages using antigens and then acoustically collect the beads.[60] The application demonstrated by the authors was for phage display, whereby a library of bacteriophages that genetically encode for a variety of affinity binders was exposed to antigen-coated microbeads. The beads bind bacteriophages of interest and the beads are collected and washed. As this process is repeated

with traditional methods, such as centrifugation or magnetic capture, to increase selectivity of bacteriophages, loss of beads and increased contamination are common problems. The use of acoustophoresis provided a continuous-flow, closed system that did not require sample handling, and was shown to yield comparable results to conventional methods. Antfolk et al. showed an alternative method for focusing sub-micrometer particles and bacteria by using two-dimensional acoustophoresis.[61] In addition to the traditional horizontal wave used in one-dimensional FFA, the authors also employ a vertical wave to alter the acoustic streaming velocity field and allow the focusing of E. coli and particles as small as 0.5 μm.

Conclusions

This chapter described vastly increasing area of microfluidic separations and the numerous techniques that allow for effective separation of particles, cells, or biomolecules of interest. The number of applications for microfluidics in the fields of clinical and forensic chemistry extend far beyond the scope of this chapter, however, the examples addressed here demonstrate the diversity of the technique and promise of this field in the future. Many of the examples presented here show continued improvement in throughput, automation, sensitivity, integration, and cost-effectiveness that is allowing microfluidics to become more widely accepted in the fields of clinical and forensic science.

References

1. Manz, A.; Graber, N.; Widmer, H. M., Miniaturized Total Chemical-Analysis Systems - A novel concept for chemical sensing. *Sensors and Actuators B-Chemical* **1990**, 1, 244-248.

2. Tiselius, A.; Svensson, H., The influence of electrolyte concentration on the electrophoretic mobility of egg albumin. *Trans Faraday Soc* **1940**, 36, 16-22.

3. Destrobisol, G.; Santini, S. A., Electrophoresis on cellulose-acetate and cellogel - current status and perspectives. *Journal of Chromatography A* **1995**, 698, 33-40.

4. Shi, B. X.; Huang, W. H.; Cheng, J. K., Determination of neurotransmitters in PC 12 cells by microchip electrophoresis with fluorescence detection. *Electrophoresis* **2007**, 28, 1595-1600.

5. Guihen, E., Recent advances in miniaturization-The role of microchip electrophoresis in clinical analysis. *Electrophoresis* **2014**, 35, 138-146.

6. Verpoorte, E., Microfluidic chips for clinical and forensic analysis. *Electrophoresis* **2002**, 23, 677-712.

7. Li, S. F. Y.; Kricka, L. J., Clinical analysis by microchip capillary electrophoresis. *Clinical Chemistry* **2006**, 52, 37-45.

8. Pagaduan, J. V.; Sahore, V.; Woolley, A. T., Applications of microfluidics and microchip electrophoresis for potential clinical biomarker analysis. *Analytical and Bioanalytical Chemistry* **2015**, 407, 6911-6922.

9. Yatsushiro, S.; Kataoka, M., Application of microchip electrophoresis for clinical tests. *Electrical Engineering in Japan* **2011**, 177, 19-25.

10. Deng, Y. Z.; Henion, J.; Li, J. J.; Thibault, P.; Wang, C.; Harrison, D. J., Chip-based capillary electrophoresis/mass spectrometry determination of carnitines in human urine. *Analytical Chemistry* **2001**, 73, 639-646.

11. Koutny, L. B.; Schmalzing, D.; Taylor, T. A.; Fuchs, M., Microchip electrophoretic immunoassay for serum cortisol. *Analytical Chemistry* **1996**, 68, 18-22.

12. Qian, J. J.; Ji, H. Y.; Cong, H.; Wang, H. M.; Jin, Q. H., Application of Polydimethylsiloxane/Glass microchips for fast electrophoretic separation of serum high-density lipoprotein subclasses. *Chinese Journal of Analytical Chemistry* **2012**, 40, 230-235.

13. Mohamadi, M. R.; Svobodova, Z.; Verpillot, R.; Esselmann, H.; Wiltfang, J.; Otto, M.; Taverna, M.; Bilkova, Z.; Viovy, J. L., Microchip electrophoresis profiling of A beta peptides in the cerebrospinal fluid of patients with Alzheimer's disease. *Analytical Chemistry* **2010**, 82, 7611-7617.

14. Effenhauser, C. S.; Paulus, A.; Manz, A.; Widmer, H. M., High-speed separation of antisense oligonucleotides on a micromachined capillary electrophoresis device. *Analytical Chemistry* **1994**, 66, 2949-2953.

15. Woolley, A. T.; Mathies, R. A., Ultra-high-speed DNA fragment separations using microfabricated capillary array electrophoresis chips. *Proceedings of the National Academy of Sciences of the United States of America* **1994**, 91, 11348-11352.

16. McCormick, R. M.; Nelson, R. J.; AlonsoAmigo, M. G.; Benvegnu, J.; Hooper, H. H., Microchannel electrophoretic separations of DNA in injection-molded plastic substrates. *Analytical Chemistry* **1997**, 69, 2626-2630.

17. Wabuyele, M. B.; Ford, S. M.; Stryjewski, W.; Barrow, J.; Soper, S. A., Single molecule detection of double-stranded DNA in poly(methylmethacrylate) and polycarbonate microfluidic devices. *Electrophoresis* **2001**, 22, 3939-3948.

18. Tian, H.; Brody, L. C.; Fan, S.; Huang, Z.; Landers, J. P., Capillary and microchip electrophoresis for rapid detection of known mutations by combining allele-specific

DNA amplification with heteroduplex analysis. *Clinical Chemistry* **2000**, 47, 173-185.

19. Schmalzing, D.; Koutny, L.; Adourian, A.; Belgrader, P.; Matsudaira, P.; Ehrlich, D., DNA typing in thirty seconds with a microfabricated device. *Proceedings of the National Academy of Sciences of the United States of America* **1997**, 94, 10273-10278.

20. Karlinsey, J. M.; Landers, J. P., AOTF-based multicolor fluorescence detection for short tandem repeat (STR) analysis in an electrophoretic microdevice. *Lab on a Chip* **2008**, 8, 1285-1291.

21. Easley, C. J.; Karlinsey, J. M.; Bienvenue, J. M.; Legendre, L. A.; Roper, M. G.; Feldman, S. H.; Hughes, M. A.; Hewlett, E. L.; Merkel, T. J.; Ferrance, J. P.; Landers, J. P., A fully integrated microfluidic genetic analysis system with sample-in-answer-out capability. *Proceedings of the National Academy of Sciences of the United States of America* **2006**, 103, 19272-19277.

22. Le Roux, D.; Root, B. E.; Reedy, C. R.; Hickey, J. A.; Scott, O. N.; Bienvenue, J. M.; Landers, J. P.; Chassagne, L.; de Mazancourt, P., DNA analysis using an integrated microchip for multiplex PCR amplification and electrophoresis for reference samples. *Analytical Chemistry* **2014**, 86, 8192-8199.

23. Liu, P.; Yeung, S. H. I.; Crenshaw, K. A.; Crouse, C. A.; Scherer, J. R.; Mathies, R. A., Real-time forensic DNA analysis at a crime scene using a portable microchip analyzer. *Forensic Science International-Genetics* **2008**, 2, 301-309.

24. Le Roux, D.; Root, B. E.; Hickey, J. A.; Scott, O. N.; Tsuei, A.; Li, J. Y.; Saul, D. J.; Chassagne, L.; Landers, J. P.; de Mazancourt, P., An integrated sample-in-answer-

out microfluidic chip for rapid human identification by STR analysis. *Lab on a Chip* **2014**, 14, 4415-4425.

25. Liu, P.; Li, X.; Greenspoon, S. A.; Scherer, J. R.; Mathies, R. A., Integrated DNA purification, PCR, sample cleanup, and capillary electrophoresis microchip for forensic human identification. *Lab on a Chip* **2011**, 11, 1041-1048.

26. Giddings, J. C.; Brantley, S. L., Shear field-flow fractionation - Theoretical basis of a new highly selective technique. *Separation Science and Technology* **1984**, 19, 631-651.

27. Pamme, N.; Manz, A., On-chip free-flow magnetophoresis: Continuous flow separation of magnetic particles and agglomerates. *Analytical Chemistry* **2004**, 76, 7250-7256.

28. Kawano, M.; Watarai, H., Two-dimensional flow magnetophoresis of microparticles. *Analytical and Bioanalytical Chemistry* **2012**, 403, 2645-2653.

29. Hale, C.; Darabi, J., Magnetophoretic-based microfluidic device for DNA isolation. *Biomicrofluidics* **2014**, 8, 11.

30. Karle, M.; Miwa, J.; Czilwik, G.; Auwarter, V.; Roth, G.; Zengerle, R.; von Stetten, F., Continuous microfluidic DNA extraction using phase-transfer magnetophoresis. *Lab on a Chip* **2010**, 10, 3284-3290.

31. Shim, S.; Shim, J.; Taylor, W. R.; Kosari, F.; Vasmatzis, G.; Ahlquist, D. A.; Bashir, R., Magnetophoretic-based microfluidic device for DNA Concentration. *Biomedical microdevices* **2016**, 18, 28.

32. Zhou, H.; Kim, J.; Zou, F.; Koh, K.; Park, J. Y.; Lee, J., Rapid detection of DNA by magnetophoretic assay. *Sensors and Actuators B-Chemical* **2014**, 198, 77-81.

33. Leslie, D. C.; Li, J.; Strachan, B. C.; Begley, M. R.; Finkler, D.; Bazydlo, L. A. L.; Barker, N. S.; Haverstick, D. M.; Utz, M.; Landers, J. P., New detection modality for label-free quantification of DNA in biological samples via superparamagnetic bead aggregation. *Journal of the American Chemical Society* **2012**, 134, 5689-5696.

34. Strachan, B. C.; Sloane, H. S.; Lee, J. C.; Leslie, D. C.; Landers, J. P., Investigation of the DNA target design parameters for effective hybridization-induced aggregation of particles for the sequence-specific detection of DNA. *Analyst* **2015**, 140, 2008-2015.

35. Strachan, B. C.; Sloane, H. S.; Houpt, E.; Lee, J. C.; Miranian, D. C.; Li, J. Y.; Nelson, D. A.; Landers, J. P., A simple integrated microfluidic device for the multiplexed fluorescence-free detection of Salmonella enterica. *Analyst* **2016**, 141, 947-955.

36. DuVall, J. A.; Borba, J. C.; Shafagati, N.; Luzader, D.; Shukla, N.; Li, J. Y.; Kehn-Hall, K.; Kendall, M. M.; Feldman, S. H.; Landers, J. P., Optical imaging of paramagnetic bead-DNA aggregation inhibition allows for low copy number detection of infectious pathogens. *Plos One* **2015**, 10, 16.

37. Sloane, H. S.; Kelly, K. A.; Landers, J. P., Rapid KRAS mutation detection via Hybridization-induced aggregation of microbeads. *Analytical Chemistry* **2015**, 87, 10275-10282.

38. Jing, Y.; Moore, L. R.; Williams, P. S.; Chalmers, J. J.; Farag, S. S.; Bolwell, B.; Zborowski, M., Blood progenitor cell separation from clinical leukapheresis product by magnetic nanoparticle binding and magnetophoresis. *Biotechnology and Bioengineering* **2007**, 96, 1139-1154.

39. Jing, Y.; Moore, L. R.; Schneider, T.; Williams, P. S.; Chalmers, J. J.; Farag, S. S.; Bolwell, B.; Zborowski, M., Negative selection of hematopoietic progenitor cells by continuous magnetophoresis. *Experimental Hematology* **2007**, 35, 662-672.

40. Glynn, M. T.; Kinahan, D. J.; Ducree, J., Rapid, low-cost and instrument-free CD4+cell counting for HIV diagnostics in resource-poor settings. *Lab on a Chip* **2014**, 14, 2844-2851.

41. Kim, S.; Han, S. I.; Park, M. J.; Jeon, C. W.; Joo, Y. D.; Choi, I. H.; Han, K. H., Circulating tumor cell microseparator based on lateral magnetophoresis and immunomagnetic nanobeads. *Analytical Chemistry* **2013**, 85, 2779-2786.

42. Park, J. W.; Lee, N. R.; Cho, S. M.; Jung, M. Y.; Ihm, C.; Lee, D. S., Microdevice for separation of circulating tumor cells using embedded magnetophoresis with V-shaped Ni-Co nanowires and immuno-nanomagnetic beads. *Etri Journal* **2015**, 37, 233-240.

43. Johnson, D. A.; Feke, D. L., Methodology for fractionating suspended particles using ultrasonic standing wave and divided flow fields. *Separations Technology* **1995**, 5, 251-258.

44. Petersson, F.; Aberg, L.; Sward-Nilsson, A. M.; Laurell, T., Free flow acoustophoresis: Microfluidic-based mode of particle and cell separation. *Analytical Chemistry* **2007**, 79, 5117-5123.

45. Augustsson, P.; Magnusson, C.; Grenvall, C.; Lilja, H.; Laurell, T., In *14th International Conference on Miniatruized Systems for Chemsitry and LIfe Sciences*; Groningen, The Netherlands, 2010, pp 1592-1594.

46. Magnusson, C.; Augustsson, P.; Haflidadottir, B.; Lenshof, A.; Ceder, Y.; Laurell, T.; Lilja, H., Label free prostate cancer cell isolation from blood by acoustic standing wave technology - acoustophoresis. *Cancer Research* **2014**, 74, 1.

47. Augustsson, P.; Magnusson, C.; Nordin, M.; Lilja, H.; Laurell, T., Microfluidic, label-free enrichment of prostate cancer cells in blood based on acoustophoresis. *Analytical Chemistry* **2012**, 84, 7954-7962.

48. Antfolk, M.; Antfolk, C.; Lilja, H.; Laurella, T.; Augustsson, P., A single inlet two-stage acoustophoresis chip enabling tumor cell enrichment from white blood cells. *Lab on a Chip* **2015**, 15, 2102-2109.

49. Antfolk, M.; Magnusson, C.; Augustsson, P.; Lija, H.; Laurell, T., Acoustofluidic, label-free separation and simultaneous concentration of rare tumor cells from white blood cells. *Analytical Chemistry* **2015**, 87, 9322-9328.

50. Li, P.; Mao, Z. M.; Peng, Z. L.; Zhou, L. L.; Chen, Y. C.; Huang, P. H.; Truica, C. I.; Drabick, J. J.; El-Deiry, W. S.; Dao, M.; Suresh, S.; Huang, T. J., Acoustic separation of circulating tumor cells. *Proceedings of the National Academy of Sciences of the United States of America* **2015**, 112, 4970-4975.

51. Yasuda, K.; Umemura, S.; Takeda, K., Concentration and fractionation of small particles in liquid by ultrasound. *Japanese Journal of Applied Physics Part 1-Regular Papers Short Notes & Review Papers* **1995**, 34, 2715-2720.

52. Goddard, G.; Kaduchak, G., Ultrasonic particle concentration in a line-driven cylindrical tube. *Journal of the Acoustical Society of America* **2005**, 117, 3440-3447.

53. Nordin, M.; Laurell, T., Two-hundredfold volume concentration of dilute cell and particle suspensions using chip integrated multistage acoustophoresis. *Lab on a Chip* **2012**, 12, 4610-4616.

54. Jakobsson, O.; Oh, S. S.; Antfolk, M.; Eisenstein, M.; Laurell, T.; Soh, H. T., Thousand-fold volumetric concentration of live cells with a recirculating acoustofluidic device. *Analytical Chemistry* **2015**, 87, 8497-8502.

55. Lenshof, A.; Ahmad-Tajudin, A.; Jaras, K.; Sward-Nilsson, A. M.; Aberg, L.; Marko-Varga, G.; Malm, J.; Lilja, H.; Laurell, T., Acoustic whole blood plasmapheresis chip for prostate specific antigen microarray diagnostics. *Analytical Chemistry* **2009**, 81, 6030-6037.

56. Dykes, J.; Lenshof, A.; Astrand-Grundstrom, I. B.; Laurell, T.; Scheding, S., Efficient removal of platelets from peripheral blood progenitor cell products using a novel micro-chip based acoustophoretic platform. *Plos One* **2011**, 6, 10.

57. Petersson, F.; Nilsson, A.; Holm, C.; Jonsson, H.; Laurell, T., Separation of lipids from blood utilizing ultrasonic standing waves in microfluidic channels. *Analyst* **2004**, 129, 938-943.

58. Yang, A. H. J.; Soh, H. T., Acoustophoretic sorting of viable mammalian cells in a microfluidic device. *Analytical Chemistry* **2012**, 84, 10756-10762.

59. Lenshof, A.; Jamal, A.; Dykes, J.; Urbansky, A.; Astrand-Grundstrom, I.; Laurell, T.; Scheding, S., Efficient purification of CD4+ lymphocytes from peripheral blood progenitor cell products using affinity bead acoustophoresis. *Cytometry Part A* **2014**, 85A, 933-941.

60. Persson, J.; Augustsson, P.; Laurell, T.; Ohlin, M., Acoustic microfluidic chip technology to facilitate automation of phage display selection. *Febs Journal* **2008**, 275, 5657-5666.

61. Antfolk, M.; Muller, P. B.; Augustsson, P.; Bruus, H.; Laurell, T., Focusing of sub-micrometer particles and bacteria enabled by two-dimensional acoustophoresis. *Lab on a Chip* **2014**, 14, 2791-2799.

Dual-Force Aggregation for the Multiplexed Quantitation of DNA and Enumeration of White Blood Cells from Whole Blood Samples

2.1 Introduction

The detection and quantification of DNA in biological samples is a keystone for the molecular sciences, impacting sequencing and genetic fingerprinting in many aspects of biomedical science, forensic science and clinical diagnostics.[1-3] For example, the mass of sample DNA is often quantified[4] in order to ensure that the correct mass of template DNA is available for the efficient amplification by the polymerase chain reaction (PCR), for a core component of many nucleic acid (NA) based assays. This is normally achieved through fluorospectrometry[5] or spectrophotometry[6], both of which require costly instrumentation and assay protocols that can be time-consuming.

Silica particles have played a significant role in the development of analytical methods for interrogating the genome, primarily in the solid phase extraction (SPE) of DNA from crude samples[7-9]. The binding of polynucleic acids (NA) to the silica, driven by a chaotrope-induced phenomenon, represents the dominant commercialized technology for NA purification today, and has for several decades.[8, 10, 11] More recently, silica particles have been magnetized to enable robotic platforms for NA purification[12, 13], and used for SPE in microdevices.[14,15] Magnetic particles have been further exploited in microscale (nL-μL) systems in a number of ways, including fluid migration through ferrofluidic pumps[16], reagent mixing[17] and analyte detection and quantification.[18]

The binding of DNA to magnetic silica beads is pertinent to a completely different application in ways that will be clarified later. That application, blood cell counting, is an extremely important method for the evaluation of patient health status. In particular, white blood cell (WBC) counts are used to screen for a wide range of diseases and conditions,

diagnose infections, allergies, or leukemia, and can be used to monitor a patient's response to various treatments. The most common methods for determining WBC counts rely on instruments such as a Coulter counter, a flow cytometer, or a CBC instrument. While these methods are effective, these benchtop instruments are large, expensive, and can be complex in operation. There have been several attempts to reduce the size, cost, and time of analysis for instruments used in cell counting with goals towards simplicity and point-of-care analysis. Holmes et al. reported the use of single cell impedance cytometry on a microfluidic scale for blood counting by measuring the impedance of single cells at two frequencies.[19] Huh et al. and Yang et al. have developed microfluidic flow cytometry methods for counting and sorting cells of interest.[20, 21] Cheng et al. describe a method for counting cells using changes in conductivity due to ions released from surface-immobilized cells in a microfluidic device.[22] While all of these methods show promise, many remain complex in method and expensive in reagents and instrumentation, requiring high-cost fluors and detection systems.

Recently, we described an aggregation-based assay utilizing 8 μm silica-coated paramagnetic particles to visually quantitate the DNA, and we purported that this represented a new label-free detection modality for DNA in biological samples.[23] The DNA-sensitive magnetic bead aggregation provides an inexpensive method for DNA quantification that can be performed by unskilled personnel, using inexpensive polymeric microdevices and readily available laboratory equipment. Briefly, a chaotropic salt binds much of the water in a DNA sample, dehydrating the DNA and enhancing its binding to the silica particle surface.[24] Application of a rotating magnetic field (RMF) enhances the kinetics of this process where the rapid (minutes) binding of DNA strands to multiple paramagnetic particles causes them to aggregate to the extent where they are visible to the naked eye. In the absence of DNA

(negative control), the RMF maintains a homogenous particle dispersion, a critical aspect of quantitation. The degree of particle aggregation (or dispersion) is determined through digital image analysis and calculated using an in-house algorithm written in Mathematica®. These results are referred to as Dark Area (DA) and, when normalized to a negative control, become % Dark Area (%DA), where 100% Dark Area refers to complete bead dispersion in the absence of DNA.

In the originally published work, it was reported that the dynamic range for DNA quantification using this single-plex assay as 4-80 pg/μL[23], and this sensitivity was comparable to commercial fluorescence-based quantitation assays.[25] Although this phenomenon is associated with attractive economics, accuracy, and ease-of-use, analysis of a single microwell at a time provided inadequate throughput for multiple samples, and needed to be improved dramatically to enable real-world functionality in the laboratory.

As mentioned briefly, this bead aggregation technology is also applicable as a cell counting method for various biological samples.[26] The aggregation caused by DNA released from lysed cells was found to correlate well with the original starting cell count after back calculation (assuming 6.25 pg DNA/cell). While this initial method was shown to be robust, it required multiple dilutions of a blood sample, adding manual, time-consuming steps and lacked the ability to multiplex samples. A recent report by Ouyang et al. described an integrated device for WBC counting via bead aggregation that allowed for the multiplexing of up to four samples.[27] This method, however, required that each sample be analyzed at six individual dilutions to more accurately determine WBC counts. While the integrated nature of the device improves analysis time slightly, this method remains time consuming when applied to the traditional well-based assay.

Here, the goal of the work in this chapter is to explore coupling agitation with the RMF to allow for effective multiplexed sample analysis for DNA quantification, decreases the analysis time by ~35-fold, and increases the sensitivity of DNA detection to a limit of detection (LOD) of 250 fg/μL. Further goals include using the multiplexing system for improved, multiplexed cell counting via bead aggregation. The ability to accurately determine WBC counts while developing a more rapid method for use in screening of samples for WBC count is described. Taking advantage of the increased dynamic range provided by this newly developed system, a rapid, multiplexed method, requiring only a single dilution of a whole blood sample, is achieved and demonstrated.

2.2 Materials and Methods

2.2.1 Reagents

MagneSil superparamagnetic particles, pre-purified hgDNA (female) were purchased from Promega™ (Carlsbad, CA). Lambda phage genomic DNA (48.5 kb long) from *E. coli* infected with CI8S7Sam7 in storage buffer [10 mM Tris-HCl (pH 7.5, 10 mM NaCl, 1 mM EDTA] was purchased from USB (Cleveland, OH). Guanidine hydrochloride (GuHCl), 2-(4-morpholino) methanesulfonic acid (MES, enzyme grade), hydrochloric acid, sodium hydroxide, acetone and ethanol were purchased from Fisher (Fair Lawn, NJ). 2-Amino-2-(hydroxymethyl)- 1,3-propanediol (Trizma base, 99.9%) was purchased from Sigma (St. Louis, MO). All solutions were prepared in Nanopure™ water (Barnstead/Thermolyne, Dubuque, IA). Quant-iT™ PicoGreen® dsDNA assay kit was purchased from Invitrogen, part of Life Technologies™ (Grand Island, NY)

2.2.2 Microwell Fabrication

A VersaLASER system 3.50 from Universal Laser Systems (Scottsdale, AZ) was used to fabricate microwells, cutting through 1.0 mm-thick poly(methyl methacrylate) (PMMA) purchased from Astra Products (Baldwin, NY). Each microwell device was prepared as a 12-well circular array of 5-mm-diameter circular wells on a 4-cm square device, designed in AutoCAD. These were then thermally bonded using established methods[28] to a second 4-cm square 1.5-mm-thick PMMA, purchased from McMaster-Carr (Santa Fe Springs, CA). Microwells were sterilized in 2M hydrochloric acid for 30 min, then rinsed with Nanopure™ water prior to use.

2.2.3 Device Design

Adapting from a device design previously used to perform the pinwheel assay[23], a device consisting of 12 microwells, 5 mm in diameter and 1 mm deep, was fabricated from PMMA. Wells were initially organized in a 96-well plate-like layout, and were eventually organized so the center of each well was equidistant from the center of the device.

2.2.4 Reagent and Sample Preparation

Superparamagnetic particles (30 µL) were washed three times in 6M GuHCl pH 6.1 and resuspended in 1 mL of 6M GuHCl pH 6.1. Lambda phage genomic and human genomic DNA were initially prepared at concentrations of 1 ng/µL by diluting concentrated stock solutions with 1X TE buffer. Samples were further serially diluted from 1 ng/µL to 0.250 pg/µL. Fluorospectrometer samples were prepared according the Thermo Scientific PicoGreen® protocol. Blood samples were de-identified and supplied by the UVA Medical Laboratory. All samples were analyzed within 24 hours of collection. Samples were initially

prepared by lysing 10 µL of whole blood in 990 µL of 6M GuHCl and allowed to incubate for 5 minutes at room temperature. After incubation, samples were serially diluted between 6 and 13 times as necessary for specific experiments.

2.2.5 Assay Instrumentation

Images of the microwells were collected by using a T1i DSLR camera with MP-E 65 mm f/2.8 1−5× macro lens purchased from Canon U.S.A., Inc. (Lake Success, NY). A Thermix Stirrer model 120S magnetic stir plate was purchased from Fisher Scientific (Fair Lawn, NJ). Three, 5-mm x 5-mm cylinder neodymium magnets were purchased from Emovendo (Petersburg, WV). A MS3 basic vortexer was purchased from IKA (Wilmington, NC). A Ledu compact desk magnifier lamp was purchased from Guy Brown Products (Brentwood, TN) and used without optics to provide lighting around the entire sample. Magnetic and vortexer rotation speeds were determined using a digital photo laser non-contact tachometer, purchased from Amazon.com (Seattle, WA). Mathematica, license obtained through the University of Virginia, was used for image analysis via the algorithm described previously[23]. Fluorospectrometer studies were completed on a NanoDrop 3300 from Thermo Scientific (Wilmington, DE).

2.2.6 Assay Protocol

A 12-plex microdevice was placed securely inside a foam frame on top of the vortexer. GuHCl (16 µL), paramagnetic particles (3 µL), and sample (1 µL) were added to each well. The vortexer was placed under the RMF (2400 rpm) and the speed of the vortexer set to 650 rpm. After 60 seconds under the RMF, the speed of the vortexer was reduced to 475 rpm. After another 60 seconds, the speed was reduced to 315 rpm for 5 seconds. After this time

the vortexer was removed from the RMF and allowed to run for 15 more seconds. Once the assay was complete, each well was individually photographed, and the photographs analyzed using a Kapur algorithm in the program Mathematica®. The program produced the Dark Area values that were translated to % Dark Area values and plotted versus the concentrations prepared or WBC count. Fluorospectrometer assays were performed according to the Thermo Scientific protocol (www.nanodrop.com).

2.3 Results and Discussion

2.3.1 The DFA System

In previous work, a 20 μL bead-based assay was carried out in a single 5 mm microwell positioned directly at the center of the RMF, and allowed for the homogenous distribution of 8 μm paramagnetic particles in the absence of DNA. However, in proximal wells that were not positioned directly at the RMF center, the particles did not remain homogenously distributed, but rather followed a larger circular path in the RMF that resulted in the particles being dragged to the edge of the wells (see **Fig. 1**). This was problematic because in order to maximize the dynamic range of the system, the beads needed to remain in a homogenously dispersed state in the absence of DNA for effective image processing (algorithm described above) to define the zero aggregation state (100% Dark Area). In the absence of this effect, processed images from the proximal wells did not allow for significant discrimination between a negative response (no aggregation in the absence of DNA) and a DNA-induced aggregation (at high [DNA]) (**Fig. 1**). As a result, image capture and analysis could only be carried out in the single well at the center of the RMF.

In an effort to optimize particle dispersion and minimize the accumulation of the particles at the microwell wall, we employed irrotational vorticity (IV) (a vortexing motion)

as an additional force. This force was used to counter the RMF-induced movement of particles to the wall by driving the particles towards the center of the microwell. We refer to this effect as 'dual-force aggregation' or DFA. The optimization of the DFA system for DNA quantitation with acceptable accuracy across different DNA samples is described in the following sections.

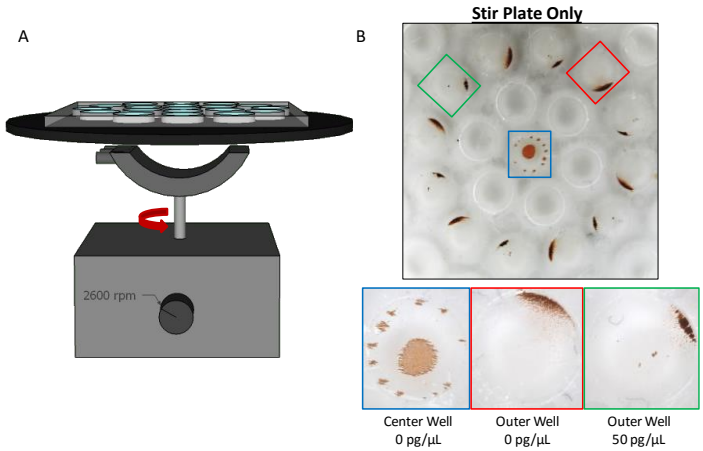

Figure 1: Multiplexing with RMF Below Device. **A**. A schematic of the previously-used RMF system while multiplexing where the MF rotates below the device. **B**. Attempts to quantify DNA samples in wells away from the center of the device proved unsuccessful due to accumulation of beads along the sides of the wells. The data indicated minimal dynamic range between negative controls and DNA-induced aggregation.

2.3.2 Optimization of DFA Assay for DNA Quantitation

Due to its uniform length, accessibility and cost-effectiveness, we chose to use λ-phage genomic DNA (48.5 kb) as a standard to optimize quantification in the DFA assay. A number of system parameters needed to be simultaneously, yet individually evaluated, including: 1) the size of the magnetic field i.e., type, size and number of magnets, 2) the magnetic field strength, i.e., the height of the RMF above the microdevice, 3) the rotation speed of the magnet, and 4) the IV speed.

2.3.2.1 Magnet Height

Several different types and combinations of magnets were explored to identify a magnet that would provide the size and strength of magnetic field necessary to obtain consistent aggregation across all wells. Tested magnets (described below) included the original magnet previously described with the pinwheel phenomenon, a large homemade magnet made up of a series of cylindrical neodymium rare earth magnets, and a combination

of both types of magnets. In an attempt to increase the magnitude of the magnetic field to accommodate multiplexing, a permanent magnet was augmented with cylindrical neodymium (NdFeB) rare earth magnets (the number varied based on the strength of the original magnet), and is defined as Mag-1 (**Fig. 2A**). Furthermore, the distance between the rotating magnet and the top surface of the chip, *h*, was varied, as this controlled the magnetic field strength. The magnetic field strength was measured as the rotating magnet was raised in 1 mm increments. Not surprisingly, the RMF strength varied dramatically with change in *h*, from 8 Gauss (*h* = 1.9 cm) to 30 Gauss (*h* = 1.1 cm). Using effective bead dispersion in the absence of DNA as the metric, compared to a positive control of 50 pg/μL λ-phage DNA, the optimal magnetic field strength (in conjunction with IV force, discussed below) was found to be 25 Gauss when *h* = 1.3 cm. When *h* < 1.3 cm, the RMF dominated, reducing the effective bead dispersion in the absence of DNA. Field strengths at *h* > 1.3 cm did not provide the necessary aggregation to maximize the dynamic range of the system. **Figure 2B** illustrates the effect of *h* on the degree of aggregation. As the magnet is moved away from the device, the degree of aggregation is reduced while the dispersion of beads in the absence of DNA remains the same. It is noted that at high concentrations, a reduction in aggregation due to the change in *h* was

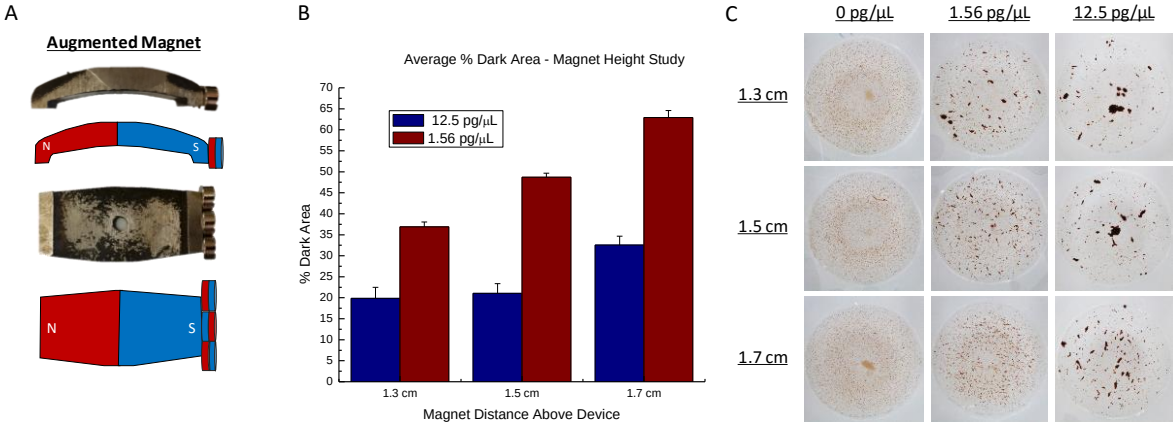

Figure 2: Study of magnet height above device. **A**. A picture of the stir-bar magnet that has been augmented with three cylindrical rare earth magnets, defined as Mag-2. **B**. A histogram illustrating the differences in % Dark Area as the magnet is moved away from the device. **C**. Images of wells illustrating the difference in dark area for both concentrations at different magnet heights.

less prominent, however, at lower concentrations the degree of aggregation was much more sensitive to *h*. As a result, the dynamic range of the system was reduced when *h* = 1.3 cm.

Studies of an in-house fabricated magnet, Mag-2, are presented in **Figure 3** and showed trends that were similar to Mag-1 described above, however aggregation was less reproducible at varying heights and velocities, and the magnet was required to be significantly closer to the device. When the magnet was 0.9 cm above the device, the largest amount of aggregation (lowest %DA) was observed with the magnet rotating at 3000 rpm. As the velocity of the magnet was reduced the beads did not aggregate as well and the %DA increased almost 2-fold when the speed of the magnet was 1000 rpm. Mag-2 was then raised to *h* = 1.2 cm and the overall trend showed a significant reduction in the amount of aggregation at all RMF velocities.

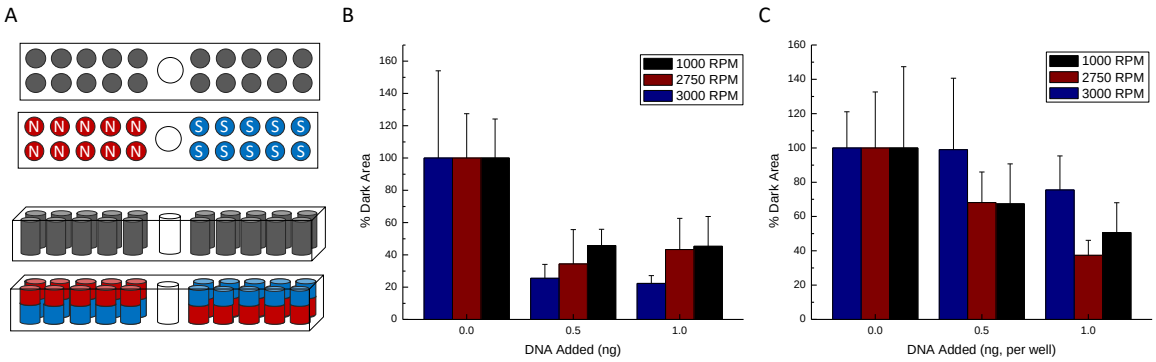

Figure 3: Exploratory Studies of In-House Magnet. A. A schematic of the in-house fabricated magnet that is made up of a series of cylindrical rare earth magnets, defined as Mag-2. B. A histogram representing a study of RMF speed, DNA concentration, and % Dark Area at 0.9 cm above the device. B. The same studies performed at a height of 1.2 cm.

2.3.2.2 Irrotational Vorticity

Equally as important as the value of '*h*', is the magnet rotation speed and the IV. As previously described, the RMF below the device drastically reduced the difference in aggregation between a well with 50 pg/μL of DNA and one with no DNA (**Fig. 4A**), and the RMF from above the device improved but did not eliminate this effect (**Fig. 4B**). In addition, the IV force alone provided no distinguishable difference between wells with DNA and those

without (**Fig. 4C**). Therefore, it became clear that the balance between the RMF and IV forces would be critical in providing optically-distinguishable aggregations that were DNA-dependent, and ultimately provide reproducible quantification of DNA. Using the augmented bar magnet, which had a magnetic strength of 25 Gauss, there was a fine tipping point with the IV rotation speed – above 650 rpm, the IV effect overpowered the RMF-induced movement of beads to the wall and, thus, the beads began to concentrate in the center of each well, similar to **Figure 4C**. If the IV speed was reduced below 315 rpm, the force was ineffective, the RMF effect dominated, and the beads mobilized to the wall; under these conditions, the negative controls began to resemble those in **Figure 4B** and caused a reduction in sensitivity and dynamic range of the system.

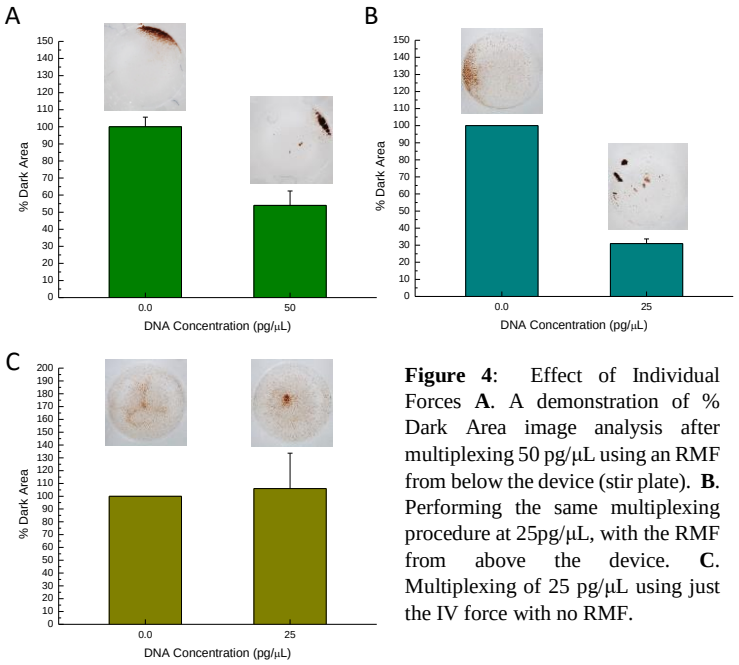

Figure 4: Effect of Individual Forces **A**. A demonstration of % Dark Area image analysis after multiplexing 50 pg/μL using an RMF from below the device (stir plate). **B**. Performing the same multiplexing procedure at 25pg/μL, with the RMF from above the device. **C**. Multiplexing of 25 pg/μL using just the IV force with no RMF.

2.3.2.3 Magnet Rotation Speed

Using the effective aggregation of beads at a given DNA concentration across the 12 wells as the metric, the rotation speed of the magnet was varied from 1000-3000 rpm at IV speeds varying from 300-800 rpm (100 rpm increments). In addition to using the IV to counter the RMF, a step-wise control in IV speed was also studied to explore further improving the overall aggregation by taking advantage of the effect of different IV speeds. This involved exploring a 'mixing step' (high speed IV, 'vortexing' each well), an 'aggregation step'

(intermediate speed IV, RMF and IV forces balanced), and a ‘mobilization step’ (low speed IV, no RMF, centering aggregates). These studies were completed systematically by varying the IV rpm (300-800 rpm) during the assay (all other parameters constant) until a combination of IV speeds resulted in the most favorable aggregation of the particles compared to a single rpm for the length of the assay (data not shown). It was determined that the three speeds that provided optimal, reproducible, aggregation were 650, 475, and 315 rpm.

2.3.2.4 DFA Optimized Parameters

The metric for optimization all of the aforementioned parameters, field size, magnetic strength, RMF speed, and IV speed, was achieving comparable aggregation in each of the 25 wells containing equivalent DNA concentrations with a % Dark Area that varied by less than 10% (i.e., the relative standard deviation <10%). The system was considered optimized with

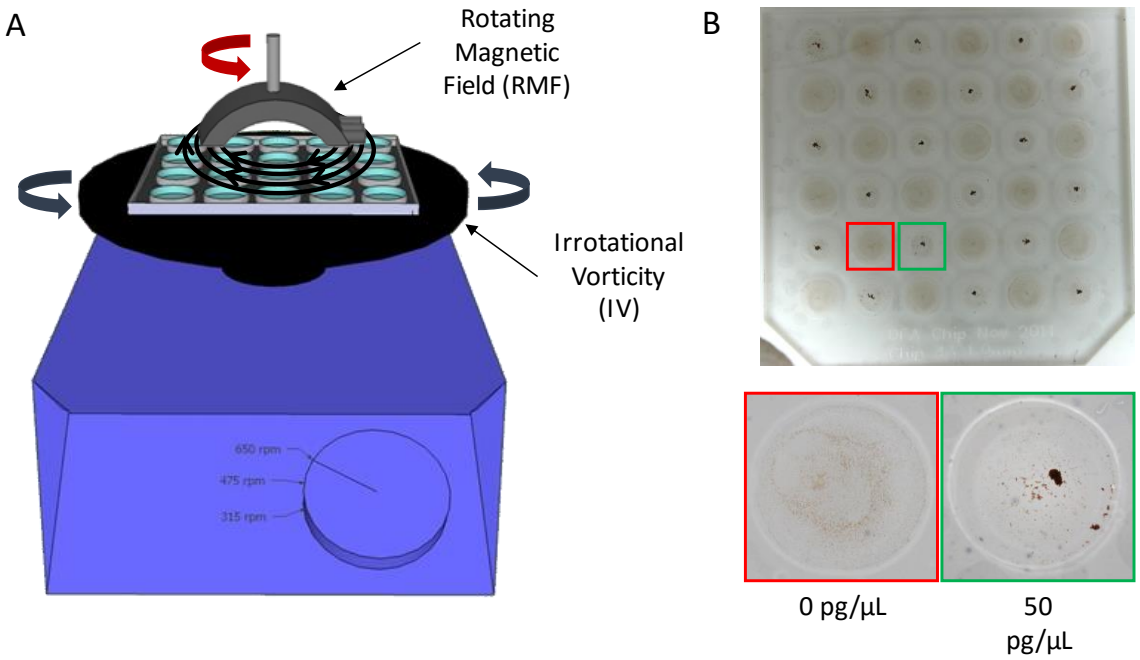

Figure 5: Schematic Representation of Dual Force Aggregation Set-Up. A. The microdevice is placed in a foam frame atop an agitator while the MF rotates from above the device. B. A photograph of a 36-well microdevice with alternating concentrations of 0 pg/µL (red) and 12.5 pg/µL (green).

the following parameters: RMF of 25 Gauss at a velocity of 2400 rpm, at a distance of 1.3 cm between the top surface of the device and the magnet, and IV decreasing step-wise from 650 rpm (60 sec) to 475 rpm (60 sec) and finally to 315 rpm (20 sec). The final 15 sec of IV at 315 rpm takes place in the absence of an RMF in order to mobilize the aggregates to the center of the wells, while beads in the negative control wells remain dispersed. This reduces variability in aggregation induced by the same concentration of DNA in different wells. These parameters provided the ideal system; tight DNA-bead aggregates centered in the wells with positive samples, and dispersed beads with negative samples or blanks. **Figure 5A** shows a schematic representation of the DFA system while **Figure 5B** demonstrates the difference between negative controls and positive samples across 12 wells under the optimal conditions described above.

2.3.2.5 Microwell Layout

During optimization and validation, a major source of variability was discovered in the orientation and layout of the wells on the multi-well device. Initial designs of the well plate mimicked that of a 96-well, grid-like plate, with vision towards automated pipetting and maximum multiplexing potential. While performing optimization studies, it was noted that the corner wells on the plate were aggregating less than the wells in the center. When a single

Table 1: Select exemplary data illustrating the difference in aggregation across the inner 16 wells of the device. Higher reproducibility observed when wells grouped by distance from center. Average aggregation across all wells without grouping shows much greater variability.

	A	B	B	C		A	B	B	C		A	B	B	C
	62333	50137	59485	48069		46517	36056	37491	29993		60689	57387	55653	48847
	61330	51697	57527	51954		41343	37505	40686	29308		67438	54521	55595	42613
	63478	56474	57652	58790		53244	37847	40895	32510		63921	57302	46904	44052
	69841	58395	56036	57181		51273	41452	42948	36285		61419	57318	48983	43205
Average	**64245.50**	**54175.75**		**53998.50**	**Average**	**48094.25**	**38215.00**		**32024.00**	**Average**	**63366.75**	**56632.00**		**44679.25**
STD	3832.17	3896.14		4913.44	**STD**	5313.24	2293.39		3156.68	**STD**	3046.66	1407.82		2840.56
%CV	5.96	7.19		9.10	**%CV**	11.05	6.00		9.86	**%CV**	4.81	2.49		6.36

All Wells	
Average	57523.69
STD	5436.74
%CV	9.45

All Wells	
Average	39709.56
STD	6705.97
%CV	16.89

All Wells	
Average	54115.44
STD	7592.74
%CV	14.03

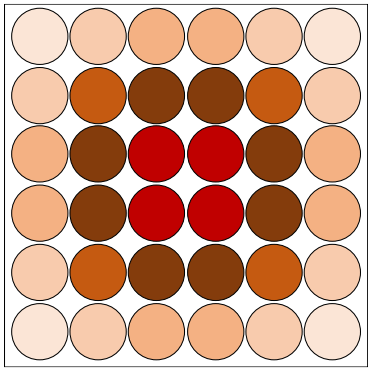

Figure 6: A schematic representation of the position of each well with respect to the center of the device. The center four wells (red) experience the strongest magnetic field while the four corner wells (light brown) experience the weakest magnetic field.

concentration of hgDNA was placed in 16 wells, aggregated, and then analyzed, there was high variability in the %DA on the order of 15-20% CV (**Table 1**). After further exploration, it was hypothesized that, due to the parabolic nature of the rotating magnetic field, the strength of the field was not uniform across all wells in the grid-like layout. This would lead to the center wells experiencing the strongest magnetic field, while the wells furthest away from the center would experience the weakest field. Ultimately, this would explain the large differences in aggregation.

To better understand the impact of the parabolic RMF, the wells were grouped together based on the distance of each well from the very center of the plate. The resulting groups are represented in **Figure 6**. To simplify the studies, subsequent experiments focused only on the 16 inner wells of the plate. Once again, a single concentration of hgDNA was added to all 16 wells, followed by aggregation and analysis. When only looking at the aggregation from a given group of wells, the variability was reduced to between 4-9% CV in most experiments (**Table 1**). These studies validated the hypothesis of a variable RMF, while also confirming the reproducibility of

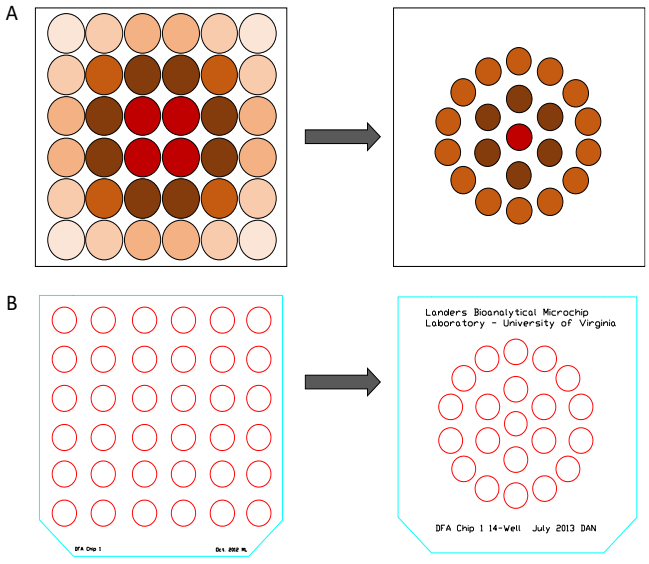

Figure 7: A. Schematic illustrating circular design change, maximizing number of wells at a given distance from the center of the device. B. CAD drawings of final working design.

wells that were the same distance from the center of the plate.

The results from these experiments, and a better understanding of the RMF, led to a fundamental change layout of the wells on the multi-well plate. While the grouped wells showed reasonable reproducibility within each group (<10% CV), the number of wells in each group is limited, which in turn limits the multiplexing capabilities for a given sample. In addition, the complexity of the method and analysis increases as more wells are added to the plate. Therefore, unlike the grid layout described above, a new design that placed the wells in a circular layout was created. The wells were all placed at the same distance from the center, and created a single group of 12–14 wells, each 5 mm in diameter (**Fig. 7**). **Figure 8** shows the difference between negative controls and positive samples across 12 wells under the optimal conditions described above.

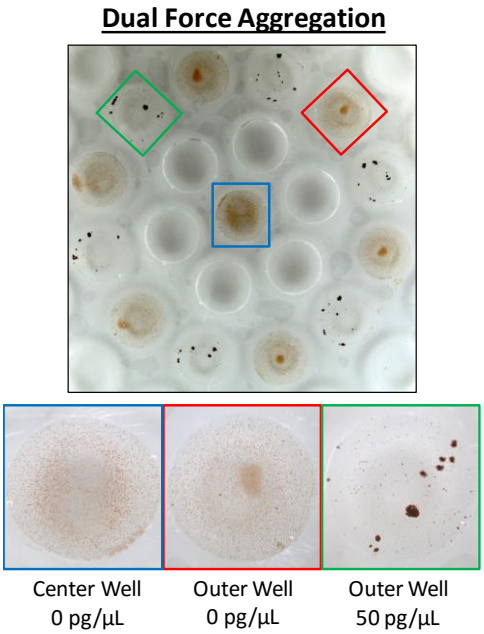

Figure 8. A photograph of the improved 12-well microdevice with alternating concentrations of 0 pg/µL (red) and 12.5 pg/µL (green).

2.3.3 λ-Phage DNA Samples

With operational parameters and device layout determined, standard curves relating the % Dark Area of aggregated beads to λ-phage DNA concentrations ranging from 0-25 pg/µL were generated. The standard curves that resulted were similar to those reported previously[23] (**Fig. 9A**) with an exponential decay in %DA as DNA concentration increased; a plot of the natural log of both the DNA concentration and the % DA is shown in **Figure 9A (inset)**. The LOD for the DFA system for λ-phage genomic DNA is ~1.5 pg/µL, representing

more than a 2-fold decrease in LOD compared to the 4 pg/µL achievable with the previously reported system[23]. The increased sensitivity likely emanates from the ability of the IV to enhance DNA-particle interaction, allowing for the formation of tighter aggregates at lower DNA concentrations, but while still maintaining the dispersion of particles not bound to DNA. While the sensitivity has improved with the DFA system, the dynamic range of the system has not. Instead, improved interaction between the particles and the DNA saturates the aggregation of the beads at a lower concentration, plateauing at a DA of 20%.

To test the accuracy of DNA quantification, a second set of DNA samples ranging in concentration from 2 pg/µL to 16 pg/µL was interrogated on the same chip at the same time as a standard curve. **Figure 9B** shows the relationship between prepared concentrations and the measured values from the standard curve, where the dotted line denotes a 1:1 correlation. A fit of the data shows and R^2 value of 0.9990 and a slope of 0.975, demonstrating the ability for the system to accurately determine random DNA concentrations from a standard curve

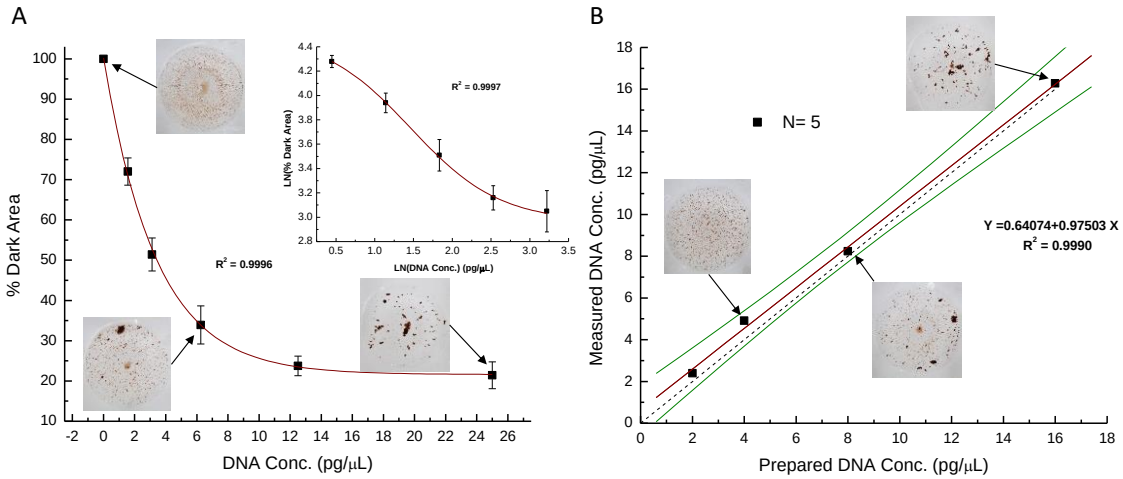

Figure 9: λ-Phage DNA Standard Curves. A. A standard curve was generated for serially diluted λ-phage DNA from 25 pg/µL. Inset pictures illustrate the degree of aggregation visualized for various concentrations on the curve. B. To illustrate the capability for quantification, the correlation between prepared concentrations and measured values of a second set of DNA samples is shown. The dotted line represents a 1:1 correlation, while the red line is a line of best fit surrounded on either side by green lines representing 95% confidence bands.

generated on the same device. It is clear that the quantitative results from the DFA assay compare favorably with the known values for the prepared samples.

2.3.4 Human Genomic DNA Samples

Analogous experiments were performed using pre-purified human genomic DNA (hgDNA). Standard curves were generated under the same conditions used for the λ-phage DNA experiments, this time with DNA concentrations ranging from 0 pg/μL to 12.5 pg/μL. The curve trends mirror those with λ-phage DNA, as does the maximum % Dark Area which plateaued around 20% (**Fig. 10A**). The LOD for hgDNA is 0.250 pg/μL, a dramatic improvement over 10 pg/μL when reported with the previous system[23]. As previously stated, an increase in sensitivity with this system is due to an enhanced interaction of the DNA sample with the particles. In addition, the increase in sensitivity is likely related to DNA length. It has been previously shown that the extent of aggregation at a given DNA concentration is dependent on DNA length[23]. That report showed in samples that differed in length by 43 Kbp, there was an order of magnitude difference in DNA concentration required for the same degree

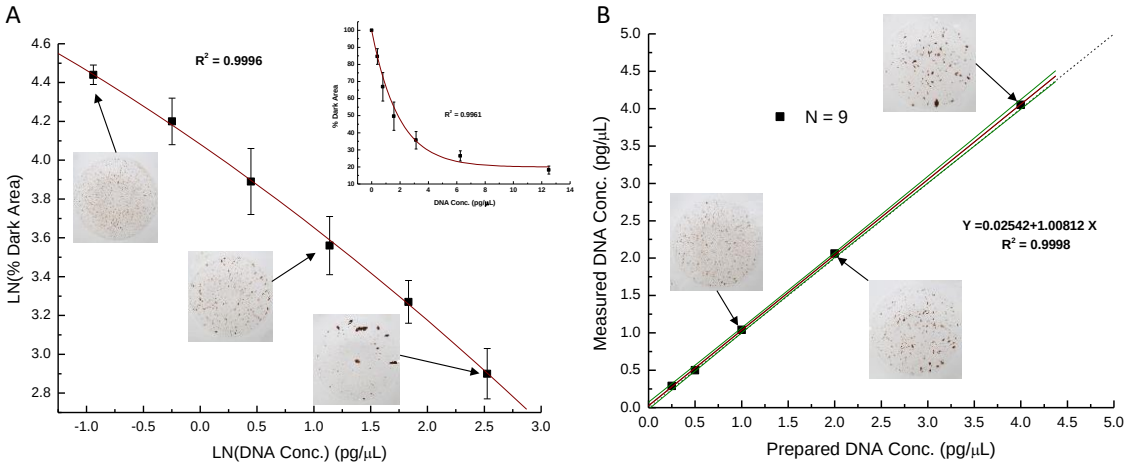

Figure 10: Human Genomic DNA Standard Curves. A. A standard curve was generated from serially diluted human genomic DNA, beginning at 12.5 pg/μL. Inset pictures illustrate the degree of aggregation visualized for various concentrations on the curve. B. To illustrate the capability for quantification, the correlation between prepared concentrations and measured values of a second set of DNA samples is shown. The dotted line represents a 1:1 correlation while the red line is a line of best fit surrounded on either side by green lines representing 95% confidence bands.

of aggregation. The manufacturer of the standard hgDNA (Promega™) simply states that 90% of the DNA is greater than 50 Kbp in length, and that the source of DNA is from multiple volunteers (manufacturer product information). In contrast, the λ-phage genome remains largely intact at 48.5 Kbp. Therefore, due to the increase in average length for hgDNA relative to λ-phage, an increase in sensitivity is expected.

Similar to the λ-phage studies, a second set of hgDNA concentrations ranging from 0.25 pg/μL to 4 pg/μL were interrogated simultaneously with a hgDNA standard curve to determine the accuracy of DNA quantitation. **Figure 10B** shows the relationship between prepared concentrations and the measured values from the standard curve, where the dotted line denotes a 1:1 correlation. A fit of the data (each point n=9) yields an R^2 value of 0.9999 and a slope of 1.008, demonstrating a strong correlation to expected values and the ability for the system to accurately determine random DNA concentrations from a standard curve generated on the same device.

2.3.5 Comparing DFA to Spectrophotometric Methods

After successfully achieving a 12-plex pinwheel assay with improved sensitivity, the same standard DNA samples (λ-phage, hgDNA) utilized in the earlier experiments were quantified with a commercial fluorospectrometer (NanoDrop™ 3300) to provide a direct comparison with a validated system. Samples were quantitated via the PicoGreen® assay protocol provided by Thermo Scientific. **Figure 11** shows a correlation plot demonstrating the accuracy of the fluorospectrometer to quantify samples from a standard curve. In addition, the data from the λ-phage and hgDNA samples were added to the plots for a direct comparison. DFA is shown to comparably quantify DNA with accuracy at a lower LOD compared to the fluorescence method. A table illustrating the differences and advantages of DFA is shown in

Table 2. The fluorospectrometer limit of detection is 1 pg/µL for double-stranded (ds) DNA while the limits of detection for the DFA method are ~1.5 pg/µL and 0.250 fg/µL for λ-phage DNA and pre-purified human DNA, respectively. Another advantage to the DFA system over the fluorescent method involves assay time and instrumentation. DFA requires no fluor labeling, incubation times, individual sample measurements which allows a decrease in overall assay time from approximately 2-10 seconds per analysis plus five minutes for fluor incubation, to 140 seconds to simultaneously analyze 12 samples. Furthermore, DFA has the

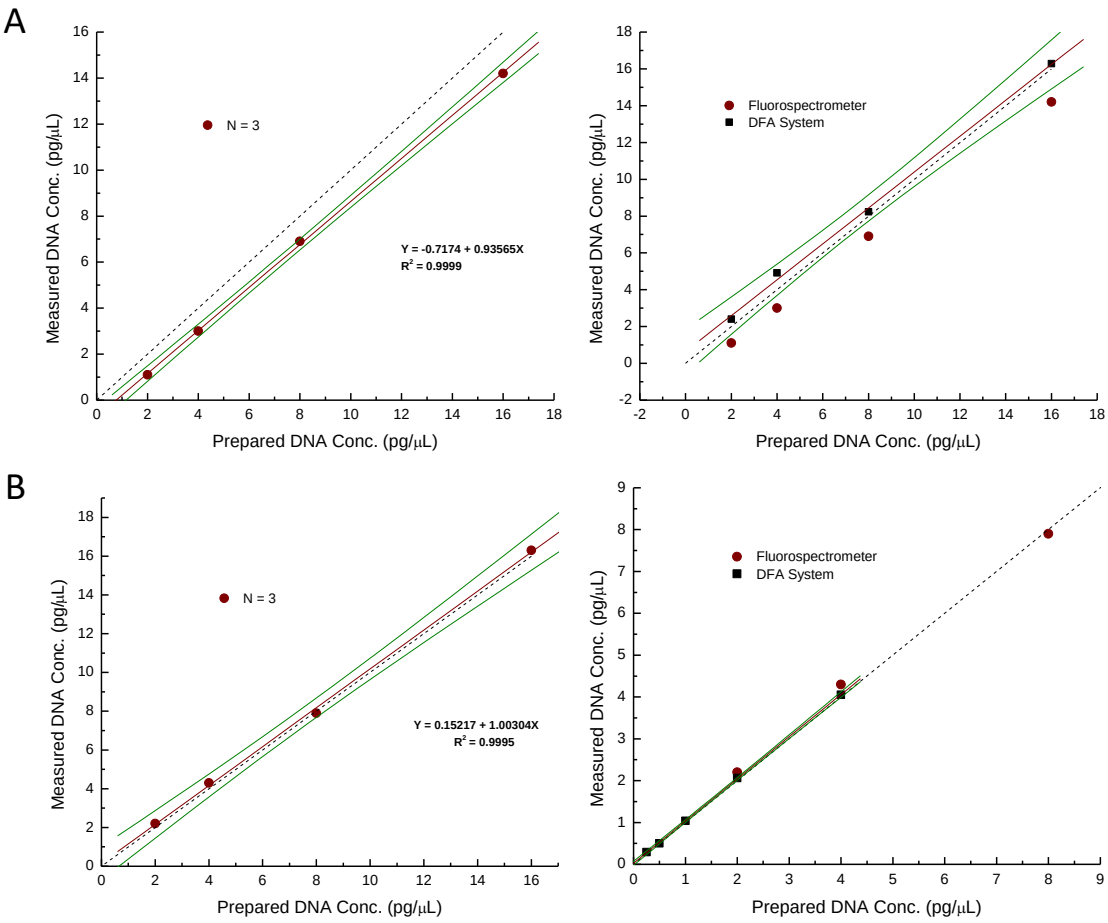

Figure 11: Comparison of DFA to Fluorospectrometer. A. Plots demonstrating the correlation of prepared concentrations and measured values of both λ-phage DNA when using a fluorospectrometer and the DFA system. The dotted line represents a 1:1 correlation, while the red line is a line of best fit surrounded on either side by green lines representing 95% confidence bands. B. Correlation plots of measured and prepared concentrations of hgDNA when quantitating with both a fluorospectrometer and the DFA system.

Table 2: Brief comparison of DNA quantitation methods. DFA provides cost effective, sensitive quantitation without the need for fluors. In addition, start-up instrument costs are also reduced in comparison to fluorospectrometric methods.

Method	Cost Per Analysis	Time per Analysis	Instrument Cost	Fluors Needed?	Need to calibrate each time?	Automatable?	Limit of Detection
Fluoro-spectrometry	~$2.00	~10 sec	$12,000	Yes	Yes	No	1 pg/μL
DFA	<$0.25	140 sec per device (12 wells)	$1300	No	No	Yes	0.250 pg/μL

benefit of a reduction in cost. A fluorospectrometer such as the NanoDrop™ 3300 retails for ~$12,000 plus fluorescent reagents, while the camera, agitator, and magnet, of the DFA system costs a total of ~$1300 with no cost for fluorescent reagents. Finally, while the fluorosprectrometer provides a significantly larger dynamic range (1 pg/μL – 1000 pg/μL for dsDNA), the DFA system still provides a dynamic range that spans over two orders of magnitude. Overall, the DFA system provides a comparable, rapid alternative DNA quantification method to a fluorospectrometer.

2.3.6 White Blood Cell Counting

With accurate and sensitive DNA quantification demonstrated, white blood cell counting was applied to the system. While the previous aggregation methods in our lab that were used for cell counting were shown to be effective and accurate[26], there was a need for higher throughput, with a decrease in complexity, if these methods were to be fully realized as a rapid, point-of-care options for white blood cell counting. To increase throughput, multiple samples must be processed simultaneously in a reduced amount of time and, in an effort to limit complexity, the number of manual steps in sample preparation prior to analysis should be reduced. Each of these problems are addressed below using multiplexed aggregation and single-dilution sample preparation.

2.3.6.1 Original Pinwheel Blood Cell Counting Methods

The use of bead aggregation for both WBC and bacteria cell counting was previously reported by Li et al.[26], and was explored further on an integrated microfluidic device by Ouyang et al.[27] (results described above). The DFA system described above was applied to white blood cell counting directly from a crude whole blood sample and an example of a typical result is seen in **Figure 12.** DNA from samples that varied in WBC count from 2.38 – 20.16 x 10^3 WBCs/μL results in aggregation of the magnetic beads, while in the absence of DNA, the beads remain entirely dispersed. To demonstrate the capability of DFA to provide accurate WBC counts, as described by Li et al. and Ouyang et al., their methods were adapted and applied to the DFA system. A whole blood sample was lysed in guanidine hydrochloride, allowed to incubate for 5 minutes at room temperature, and was serially diluted. Samples were diluted over the range of 100-180000X, and were interrogated on the DFA system and the resultant aggregation images analyzed. This process was completed for six whole blood samples that ranged in WBC counts from 2.2 to 14.5 x 10^3 cells/μL. The %DA values were plotted against the dilution factor, and resulted in six different standard curves, each with the form of:

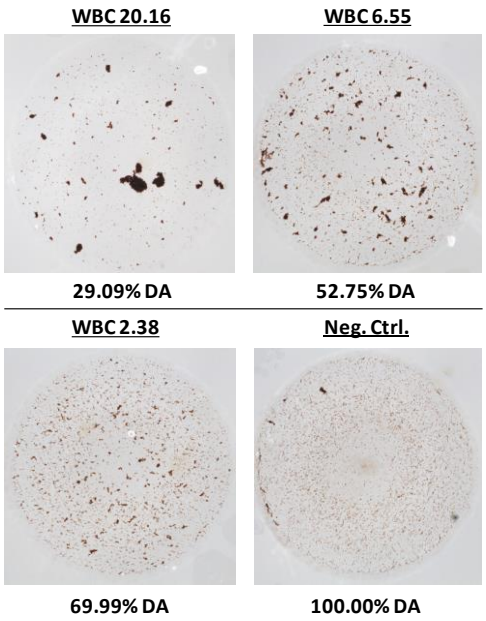

Figure 12: Exemplary wells illustrating the degree of aggregation associated with varying WBC counts. Higher WBC counts = More DNA = Greater aggregation.

$$y = 0.9*exp(-x/\theta) + 0.1$$

as illustrated in **Figure 13A**. Similar to the Ouyang method[27], a 'dilution threshold' (Dt) was determined for each curve by solving for θ, and the known WBC counts were plotted against the Dt values to generate a standard curve. Blinded blood samples were then analyzed using the same method and calculated Dt values were compared to the standard curve to calculate the starting WBC count. As shown in **Figure 13B**, the blinded WBC counts determined using the Ouyang method[27] on the DFA system correlated very well with the Coulter counter values obtained from conventional analysis in the UVA Medical laboratory.

2.3.6.2 Simplifying the WBC Counting Method

Originally, Li et al.[26] demonstrated the bead-based WBC counting assay using a single well, single dilution protocol. This method, while simple, was time-consuming as a result of each sample requiring independent exposure to the RMF for five minutes in order to obtain reproducible results. Furthermore, while this method claimed use of a single dilution to analyze known samples, the single-dilution factor used, varied for different ranges of white blood cell count. A dilution factor of 8000X was used for WBC counts above 4000 cells/μL,

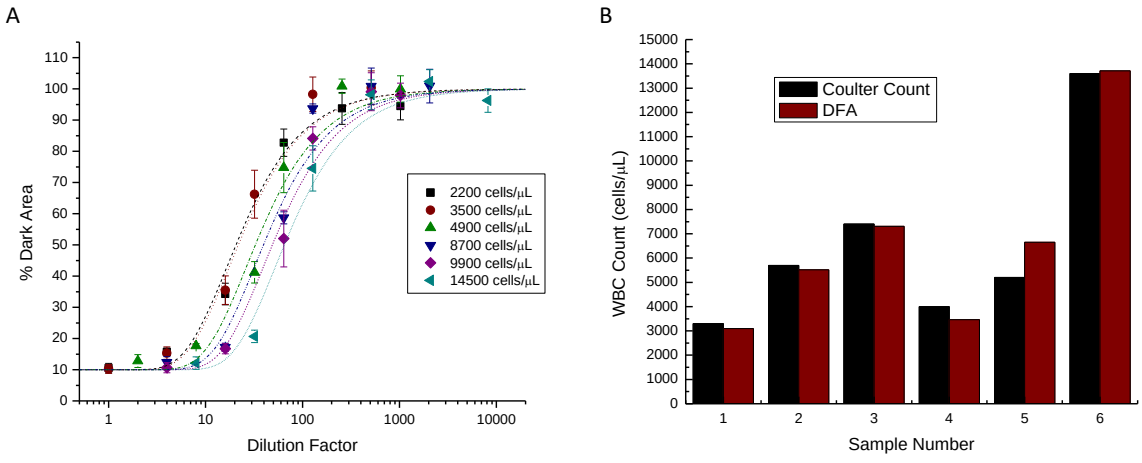

Figure 13: A) DFA analysis of 6 blood samples of varying WBC counts. Each sample was diluted 6 times and the % Dark Area plotted vs. Dilution Factor B) Six blinded blood samples analyzed and compared to the standard curves (A). DFA results show strong correlation to given clinical values.

and a dilution factor of 4000X was used for WBC counts below 4000 cells/µL. Therefore, to ensure that the aggregation (%DA) fell within the dynamic range for a given unknown sample, it was actually necessary to analyze each sample, at minimum, over two dilutions. This results in a minimum of a 2X increase in analysis time for each unknown sample.

The Ouyang method[27] also yielded accurate WBC counts based on bead aggregation, however, it remains time-consuming and laborious for screening multiple samples. In order to decrease the assay time and take full advantage of the multiplexing capabilities of the DFA system, the bead-based method for determination of the WBC count needed to be simplified. During the course of analyzing a series of eight blood samples on the DFA system using the Ouyang method, it was observed that as many as four individual dilution factors might provide the necessary dynamic range for analysis of all samples on the DFA system. This is illustrated in **Figure 14,** which shows the *%DA vs. Dilution Factor* plots for eight different blood samples. In this combination of standard curves, multiple dilutions in the linear range of the curves show the greatest potential for large %DA dynamic ranges across a wide range of WBC counts. This suggested that the DFA system may only require a single dilution for any given WBC count, a protocol modification that would dramatically simplify the process and expedite the WBC count screening method.

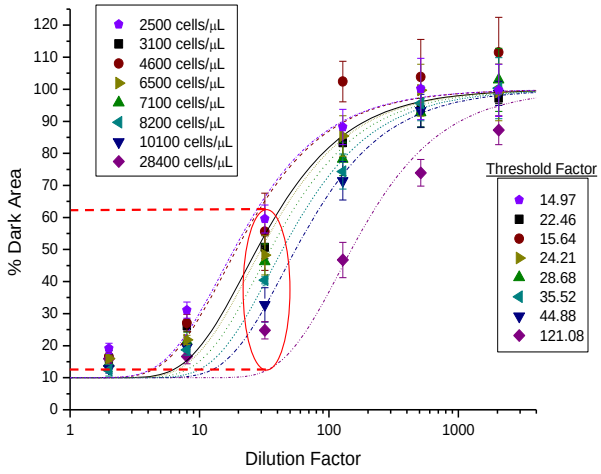

Figure 14: Analysis of blood samples using the six-dilution method show the potential for use of a single dilution for all samples. Red highlighted region shows wide distribution of % Dark Area values for 7 samples spanning a large range of WBC counts.

2.3.6.3 Determining the Optimal Dilution Factor

Based on the standard curves discussed in the previous section, it appeared that a dilution factor between 1600X and 12800X would be adequate for covering the range of WBC counts that would be encountered in patient samples. Fifteen fresh blood samples obtained from the UVA Medical Laboratory were analyzed using the DFA system at dilution factors of 1600X, 3200X, 6400X, and 12800X. The resultant %DA for each sample at each dilution was used to plot *%DA vs. WBC count* (**Fig. 15**). Higher WBC count samples, regardless of dilution, are expected to result in lower %DA (i.e., higher aggregation) due to larger mass of DNA. **Figure 15** illustrates that this trend remained true across all four of the tested dilutions, however, certain dilutions showed smaller dynamic ranges and larger variability (discussed in detail below).

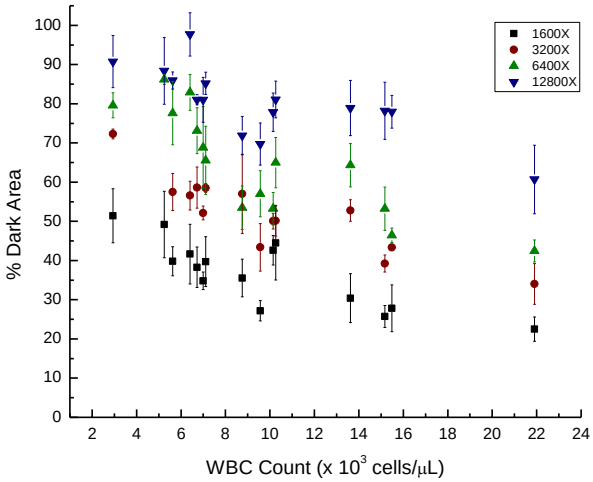

Figure 15: Fifteen fresh samples analyzed at dilution factors of 1600X, 3200X, 6400X and 12800X to observe trends in % Dark Area when plotted vs. WBC count. Each dilution factor demonstrated the expected trend of higher WBC count = lower % Dark Area and showed varying dynamic ranges.

To more accurately determine which of the four dilution factors were adequate to cover the range of WBC counts in patients, each dilution was analyzed individually (**Fig. 16**). The 1600X dilution factor resulted in %DA values below 50% DA for almost all WBC counts, with a WBC count of 21.9 x 10^3 cells/μL showing the greatest aggregation with approximately 20% DA (**Fig. 16A**). This dilution factor showed a small dynamic range and high variation in % DA across the samples, as indicated by the correlation value (R^2 = 0.653) on an

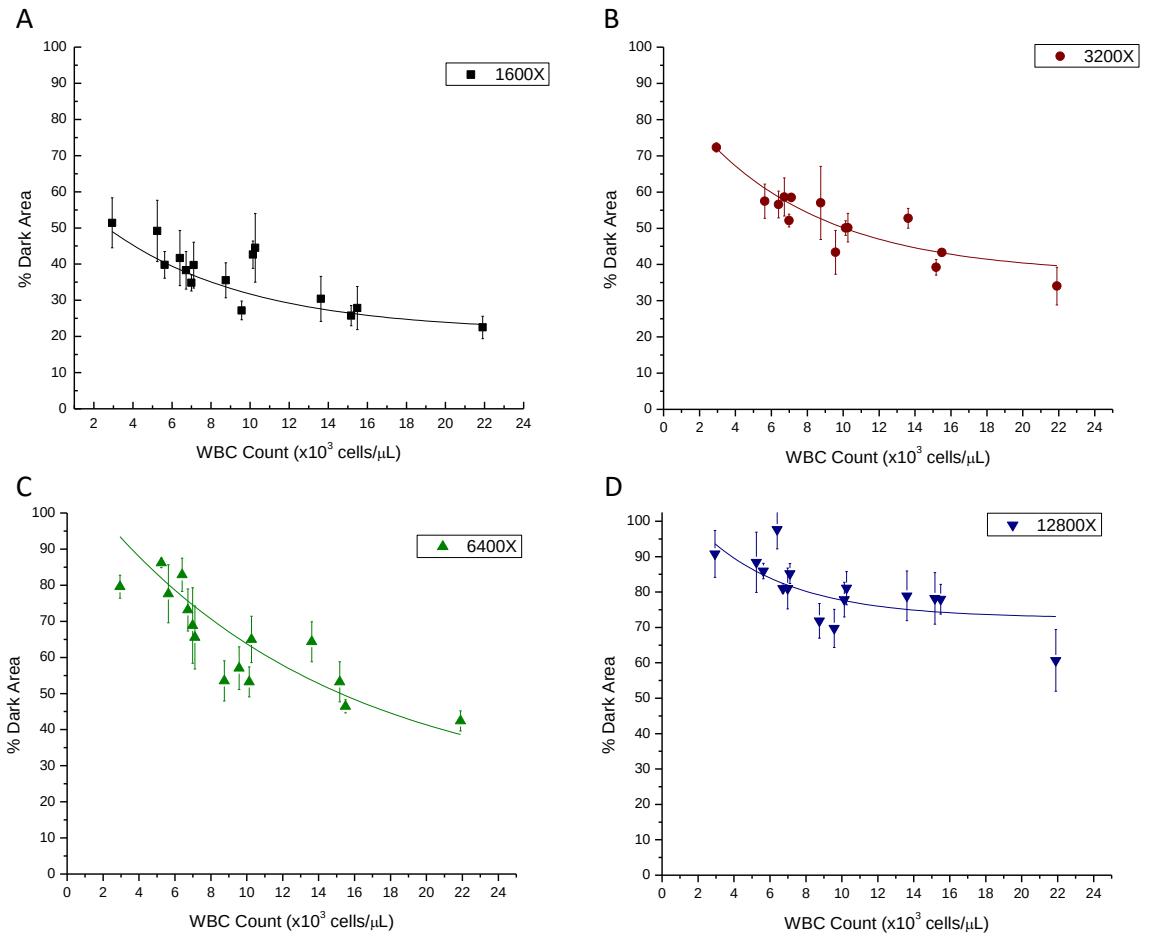

Figure 16: The same fifteen fresh samples analyzed at dilution factors of 1600X, 3200X, 6400X, and 12800X to observe trends in % Dark Area when plotted vs. WBC count. Each dilution factor broken down and analyzed individually. With $R^2 = 0.955$, 3200X dilution was determined to be optimal for further studies.

exponential decay fit. At the other end of the dilution factor dynamic range, the 12800X dilution factor showed a majority of %DA values above ~70% DA, with only WBC 21.9 x 10^3 cells/μL falling below ~60% DA (**Fig. 16D**). Furthermore, below a WBC count of 7.0 x 10^3 cells/μL, a majority of the healthy range, the % DA values were >80% DA for all samples, approaching the same level of aggregation as the negative control. Finally, when fit to the same exponential curve, the correlation value (R^2) was only 0.427.

The remaining dilution factors, 3200X and 6400X, showed the most promise with good correlation, low variability, and a large dynamic range. The 6400X dilution factor ranged from 42% DA for the blood sample with the highest WBC count (21.9 x 10^3 cells/μL)

to 79% DA for the lowest (2.94 x 10^3 cells/μL), however, some WBC counts in between those values exceeded 80% DA, indicating high variability of aggregation (**Fig. 16C**). Despite this increase in dynamic range (relative to 1600X and 12800X), there was still unacceptable variability between the samples and the measured % DA (R^2 = 0.882). The 3200X dilution factor showed the largest dynamic range (72% to 34% DA) across the same WBC count range (**Fig. 16B**). In addition, this dilution factor showed the lowest amount of variability between samples, in terms of correlation value (R^2 = 0.955). Ultimately, the 3200X dilution factor was determined to be the optimal single-dilution factor for covering all necessary WBC counts.

2.3.6.4 Optimized WBC Counting Method

With the optimal dilution factor defined, a series of fresh whole blood samples were obtained and analyzed via the new method, and a single *%DA vs. WBC count* standard curve was generated. Each sample was diluted and lysed in 6M GuHCl for 5 minutes prior to further dilution with GuHCl to a final factor of 3200X. Six samples were analyzed simultaneously on the DFA system via a 14-well custom microplate, allowing for duplicate analysis per microplate, and two microplates were processed per blood sample. This process was replicated three times for each sample resulting in n = 12 analyses per blood sample. Once plotted, the data were fit to an exponential decay with a correlation value (R^2) of 0.995 (**Fig. 17A**). With the ability to multiplex on the DFA system, a single sample lysed in triplicate, could be analyzed (aggregation + image detection) in less than 5 minutes (<10 minutes including lysing time), compared to greater than 11 minutes (>41 minutes with lysis) using the Ouyang method[27] (**Table 3**).

With a standard curve established, 18 fresh, blinded samples were analyzed via the same lysing and analysis as described above. Each sample was once again lysed in triplicate and four wells were analyzed per replicate, for a total of 12 analyses per sample. The %DA values were converted to WBC counts, and those WBC counts were compared to the original values obtained from UVA Medical Laboratory. As seen in **Figure 17B**, 18 out of 18 (100%) of the analyzed samples were within 1.75 WBC count units of the given clinical value, 15 out of 18 (83%) were within 1.0 WBC count units, and 9 out of 18 (50%) were within 0.5 WBC count units. **Figure 17C** illustrates the strong correlation between the clinical values and the DFA values for WBC count (slope = 1.08; R^2 = 0.974). This data demonstrates that the use of

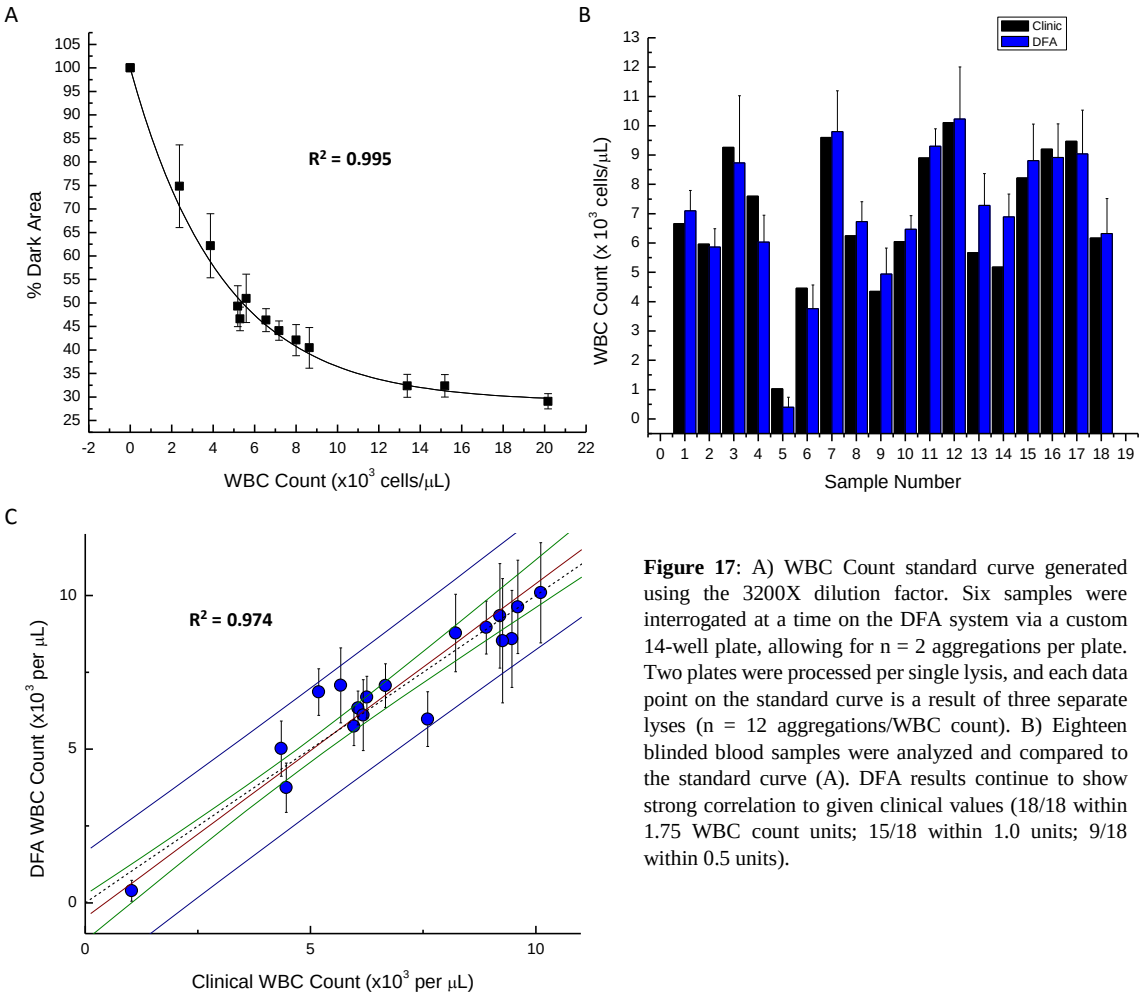

Figure 17: A) WBC Count standard curve generated using the 3200X dilution factor. Six samples were interrogated at a time on the DFA system via a custom 14-well plate, allowing for n = 2 aggregations per plate. Two plates were processed per single lysis, and each data point on the standard curve is a result of three separate lyses (n = 12 aggregations/WBC count). B) Eighteen blinded blood samples were analyzed and compared to the standard curve (A). DFA results continue to show strong correlation to given clinical values (18/18 within 1.75 WBC count units; 15/18 within 1.0 units; 9/18 within 0.5 units).

a single dilution factor for the lysis and analysis of whole blood samples has not compromised the accuracy of the bead aggregation method for determining WBC counts.

Table 3: A comparison of WBC counting methods using the original Li et al method, the integrated Ouyang et al. method, and the new Nelson et al. method on the DFA system. The Nelson et al. method provides a 60-fold decrease in total assay time compared to the Li et al. method, and a 13-fold decrease compared to the Ouyang et al. method, all while decreasing the complexity of the assay.

Method/System	Number of Samples Analyzed per Assay	Incubation Time	Number of Dilutions per Sample	Dilution Time	Aggregation Time	Average Total Assay Time
Li et al. /Single Well	1	30 min	2-3	4 min/sample	10-15 min per sample (5 min per dilution)	44-49 min per sample
Ouyang et al. /Integrated	4	30 min	5	2 min for 4 samples (0.5 min per sample)	6 min for 4 samples (1.5 min per sample)	39 min for 4 samples (9.5 min per sample)
Nelson et al./DFA	13	5 min	1	2 min for 13 samples (0.15 min per sample)	2.5 min for 13 samples (0.19 min per sample)	9.5 min for 13 samples (0.73 min per sample)

As an illustration of the potential for this method as a rapid screening technique for WBC count, the original standard curve was separated into three regions defining high WBC count (>10.0 x 10^3 cells/μL; leukocytosis), normal WBC count (3.0 – 10.0 x 10^3 cells/μL), and low WBC count (<3.0 x 10^3 cells/μL; leukopenia) (**Fig. 18A**). Similar regions were illustrated on the clinical value comparison chart (**Fig. 18B**). A % DA value of less than 36.5% indicates a high WBC count above 10.0 x 10^3 cells/μL, while a % DA between 36.5% and 65.2% yields a WBC count between 3.0 – 10.0 x 10^3 cells/μL, and a % DA value above 65.2% results in a WBC count less than 3.0 x 10^3 cells/μL. As shown in both plots, 18 out of 18 (100%) samples were correctly called as either high, normal, or low WBC counts. Ultimately, this demonstrates the possibility for the single-dilution method on the DFA system to be used as both a semi-quantitative, rapid WBC count screening method, as well as an accurate, quantitative method for the determination of WBC counts from whole blood samples.

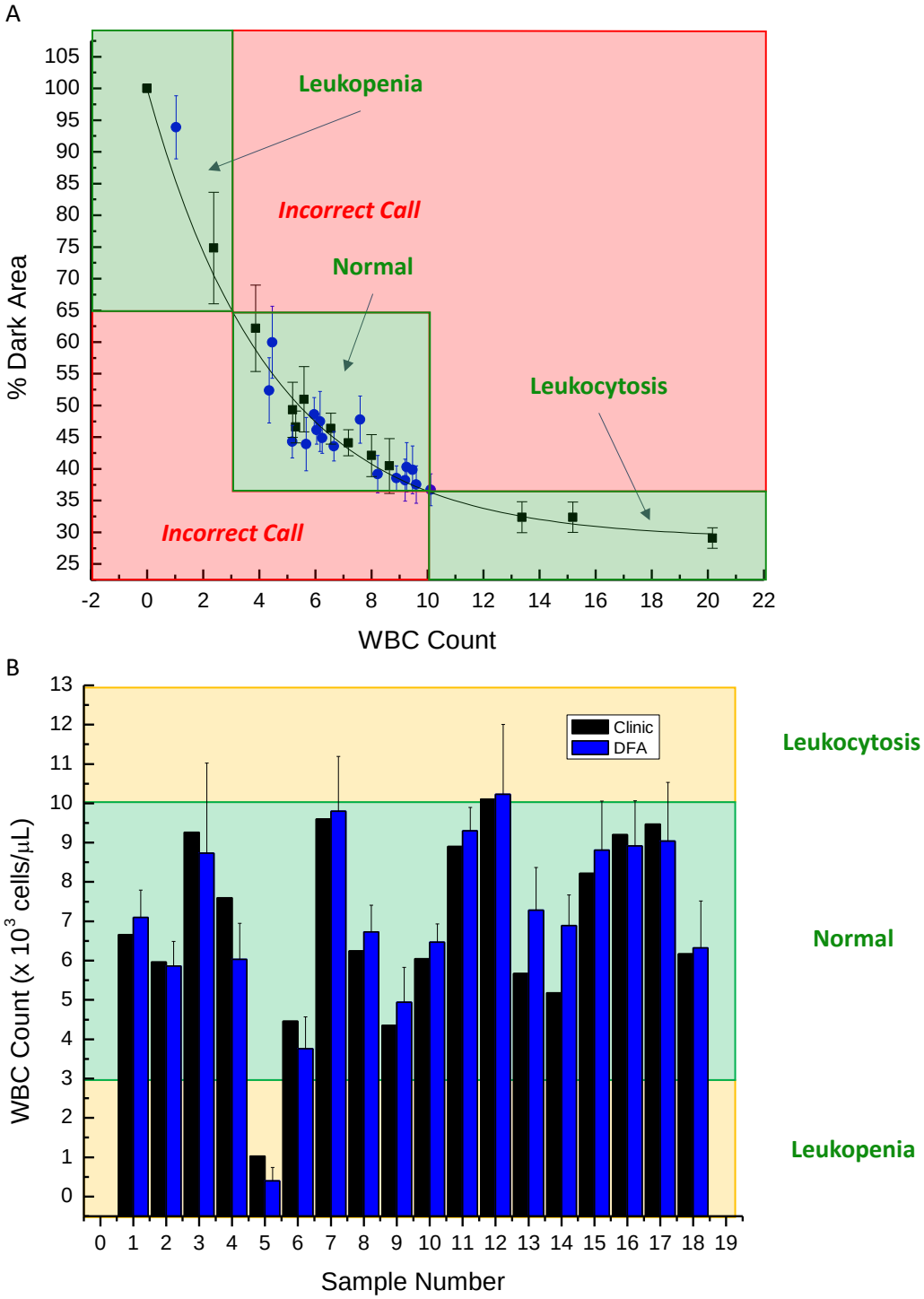

Figure 18: A) The original standard curve was broken down into three separate regions defining high WBC count (>10.0 x 10^3 cells/µL; leukocytosis), normal WBC count (3.0 – 10.0 x 10^3 cells/µL), and low WBC count (<3.0 x 10^3 cells/µL; leukopenia). All 18 samples are called correctly. B) Normal vs. abnormal regions added to clinical value comparison. As represented in the standard curve plot (A), all samples are correctly screened and called as 'normal' or abnormal.

2.4 Conclusions

This work describes the comprehensive and methodical optimization of the DNA quantitation method based on the 'pinwheel effect' described in an earlier report,[23] in an effort to achieve the goal of multiplexed DNA analysis. Numerous key technological advances described here validate this label-free method to provide a bead-based aggregation assay for DNA quantitation, with simplicity and advantages that we believe will allow it to compete with existing commercial quantitation techniques. The DFA approach allows for a 140 second, 12-plex assay in a simple circular microwell array, providing a ~4-fold reduction in assay time compared to a conventional fluorospectrometer, while reducing cost by almost 10-fold. Further, for double stranded hgDNA, the DFA system offers ~4-fold increase in sensitivity with an LOD of 0.250 pg/μL over the 1 pg/μL of the fluorospectrometer. To put this in perspective, this mass of DNA represents less than $1/10^{th}$ of the DNA resulting from lysing a single cell in 1 μL of solution. When detected in the microdevice well, the final concentration would be ~320 fg/ μL, greater than the LOD for this method. Overall, we have demonstrated that DFA provides a label-free method for DNA quantitation that should be competitive with the more conventional quantification methods. Moreover, when considering the offshoot applications described in the original report (white cell enumeration, cultured cell and bacterial cell counting), the sensitivity and robustness of DFA presents an interesting path for future analytical methods.

In addition, addressing the goal of cell counting, the capabilities of the DFA system for both rapid WBC count screening, and accurate, multiplexed WBC counts have been presented. We verified previously established bead-based WBC counting methods using the system and showed that accuracy was maintained. After validation, we set out to improve the

simplicity of the method while also reducing the amount of time needed to process each sample. The increased sensitivity and dynamic range provided by the DFA system allowed us to establish a single dilution factor that could be applied to all whole blood samples analyzed, regardless of WBC count. After establishing the optimal dilution factor, 100% of samples (18 out of 18) were correctly screened and identified as high, normal, or low, and were within 1.75 WBC count units from the expected clinical values. The ability for the DFA system to analyze 13 samples in 2 minutes and 20 seconds with a total analysis time of 9.5 minutes (including incubation and dilution), represents a 60-fold decrease in total assay time per sample compared to the previously described Li et al. method, and a 13-fold decrease compared to the Ouyang method, all while decreasing the complexity of the assay. In the future, this method shows potential in other cell counting applications such as cultured and bacterial cell counting. Furthermore, this assay and instrumentation are amenable to portable analysis. The integration of image capture with the DFA system, along with the development of system automation, would allow for a single, portable unit to be transported to clinical labs for testing in a clinical lab environment.

2.5 References:

1. Budowle, B.; Baechtel, F. S.; Comey, C. T.; Giusti, A. M.; Klevan, L.,DNA protocols for typing forensic biological evidence - Chemiluminescent detection for human DNA quantation and restriction-fragment-length-polymorphism (RFLP) analyses and manual typing of polymerase chain-reaction (PCR) amplified polymorphisms. *Electrophoresis* **1995**, 16, 1559-1567.

2. Piatak, M.; Luk, K. C.; Lifson, J. D., Quantitative competitive polymerase chain-reaction for accurate quantitation of HIV DNA and RNA species. *Biotechniques* **1993**, 14, 70-&.

3. Singh, N. P.; McCoy, M. T.; Tice, R. R.; Schneider, E. L., A simple technique for quantitation of low-levels of DNA damage in individual cells. *Experimental Cell Research* **1988**, 175, 184-191.

4. Ballantyne, K. N.; van Oorschot, R. A. H.; Mitchell, R. J., Comparison of two whole genome amplification methods for STR genotyping of LCN and degraded DNA samples. *Forensic Science International* **2007**, 166, 35-41.

5. Wittwer, C. T.; Herrmann, M. G.; Moss, A. A.; Rasmussen, R. P., Continuous fluorescence monitoring of rapid cycle DNA amplification. *Biotechniques* **1997**, 22, 130-139.

6. Shim, S. M.; Kim, J. H.; Jung, S. E.; Kim, D. J.; Oh, J. H.; Han, B. G.; Jeon, J. P., Multilaboratory assessment of variations in spectrophotometry-based DNA quantity and purity indexes. *Biopreservation and Biobanking* **2010**, 8, 187-192.

7. Lee, H. Y.; Park, M. J.; Kim, N. Y.; Sim, J. E.; Yang, W. I.; Shin, K.-J., Simple and highly effective DNA extraction methods from old skeletal remains using silica columns. *Forensic Science International: Genetics* **2010**, 4, 275-280.

8. Sturk-Andreaggi, K.; Diegoli, T. M.; Just, R.; Irwin, J., Evaluation of automatable silica-based extraction methods for low quantity samples. *Forensic Science International: Genetics Supplement Series* **2011**, 3, e504-e505.

9. Demeke, T.; Jenkins, G. R., Influence of DNA extraction methods, PCR inhibitors and quantification methods on real-time PCR assay of biotechnology-derived traits. *Analytical and Bioanalytical Chemistry* **2010**, 396, 1977-1990.

10. Amory, S.; Huel, R.; Bilić, A.; Loreille, O.; Parsons, T. J., Automatable full demineralization DNA extraction procedure from degraded skeletal remains. *Forensic Science International: Genetics* **2012**, 6, 398-406.

11. Witt, S.; Neumann, J.; Zierdt, H.; Gébel, G.; Röscheisen, C., Establishing a novel automated magnetic bead-based method for the extraction of DNA from a variety of forensic samples. *Forensic Science International: Genetics* **2012**, 6, 539-547.

12. White, D., Butler, B., Creswell, D., Smith, C., Magnesil™ paramagnetic particles: novel magnetics for DNA purification. *Promega Notes* **1998**, 12.

13. Frégeau, C. J.; Lett, C. M.; Fourney, R. M., Validation of a DNA IQ™-based extraction method for TECAN robotic liquid handling workstations for processing casework. *Forensic Science International: Genetics* **2010**, 4, 292-304.

14. Reedy, C. R.; Bienvenue, J. M.; Coletta, L.; Strachan, B. C.; Bhatri, N.; Greenspoon, S.; Landers, J. P., Volume reduction solid phase extraction of DNA from dilute, large-volume biological samples. *Forensic Science International-Genetics* **2010**, 4, 206-212.

15. Bienvenue, J. M.; Legendre, L. A.; Ferrance, J. P.; Landers, J. P., An integrated microfluidic device for DNA purification and PCR amplification of STR fragments. *Forensic Science International-Genetics* **2010**, 4, 178-186.

16. Pamme, N., Magnetism and microfluidics. *Lab on a Chip* **2006**, 6, 24-38.

17. Lee, S. H.; van Noort, D.; Lee, J. Y.; Zhang, B.-T.; Park, T. H., Effective mixing in a microfluidic chip using magnetic particles. *Lab on a Chip* **2009**, 9, 479-482.

18. Moser, Y.; Lehnert, T.; Gijs, M. A., On-chip immuno-agglutination assay with analyte capture by dynamic manipulation of superparamagnetic beads. *Lab Chip* **2009**, 9, 3261-7.

19. Holmes, D.; Pettigrew, D.; Reccius, C. H.; Gwyer, J. D.; van Berkel, C.; Holloway, J.; Davies, D. E.; Morgan, H., Leukocyte analysis and differentiation using high speed microfluidic single cell impedance cytometry. *Lab on a Chip* **2009**, 9, 2881-2889.

20. Huh, D.; Gu, W.; Kamotani, Y.; Grotberg, J. B.; Takayama, S., Microfluidics for flow cytometric analysis of cells and particles. *Physiological Measurement* **2005**, 26, R73-R98.

21. Yang, S.-Y.; Hsiung, S.-K.; Hung, Y.-C.; Chang, C.-M.; Liao, T.-L.; Lee, G.-B., A cell counting/sorting system incorporated with a microfabricated flow cytometer chip. *Measurement Science & Technology* **2006**, 17, 2001-2009.

22. Cheng, X.; Liu, Y.-s.; Irimia, D.; Demirci, U.; Yang, L.; Zamir, L.; Rodriguez, W. R.; Toner, M.; Bashir, R., Cell detection and counting through cell lysate impedance spectroscopy in microfluidic devices. *Lab on a Chip* **2007**, 7, 746-755.

23. Leslie, D. C.; Li, J.; Strachan, B. C.; Begley, M. R.; Finkler, D.; Bazydlo, L. A. L.; Barker, N. S.; Haverstick, D. M.; Utz, M.; Landers, J. P., New detection modality for label-free quantification of DNA in biological samples via superparamagnetic bead aggregation. *Journal of the American Chemical Society* **2012**, 134, 5689-5696.

24. Melzak, K. A.; Sherwood, C. S.; Turner, R. F. B.; Haynes, C. A., Driving forces for DNA adsorption to silica in perchlorate solutions. *Journal of Colloid and Interface Science* **1996**, 181, 635-644.

25. Sassolas, A.; Leca-Bouvier, B. D.; Blum, L. J., DNA biosensors and microarrays. *Chemical Reviews* **2008**, 108, 109-139.

26. Li, J. Y.; Liu, Q.; Xiao, L.; Haverstick, D. M.; Dewald, A.; Columbus, L.; Kelly, K.; Landers, J. P., Label-free method for cell counting in crude biological samples via paramagnetic bead aggregation. *Analytical Chemistry* **2013**, 85, 11233-11239.

27. Ouyang, Y.; Li, J.; Haverstick, D. M.; Landers, J. P., Print-cut-laminate fabrication of a rotation-driven microfluidic disc for white blood cell enumeration based on magnetic bead aggregation. *Analytical Chemistry* **2016**, [Submitted].

28. Sun, Y.; Kwok, Y. C.; Nguyen, N. T., Low-pressure, high-temperature thermal bonding of polymeric microfluidic devices and their applications for electrophoretic separation. *Journal of Micromechanics and Microengineering* **2006**, 16, 1681-1688.

Quantitation-Free Method for STR Analysis of Dried Blood Samples using PCR-Ready DNA via Dual-Force Aggregation

3.1 Introduction

Human identification in the field of forensic science is most commonly performed using DNA analysis in the form of short tandem repeats (STRs). STRs are short sequences of DNA, typically 2-6 base pairs in length, that are repeated many times in a row throughout the genome. The number and length of each of these repeats (alleles) can vary greatly between individuals, providing an effective mode for human identification. The probability of two unrelated individuals having the same alleles across 13 locations of repeats (loci) used in the Combined DNA Index System (CODIS) is 1×10^{-13}.[1]

The first step in the process of generating copies of STR sequences is the extraction of DNA from various forensic biological samples. This step is crucial to the analysis process as the amount and purity of DNA determine the success of STR amplification via the polymerase chain reaction (PCR). The efficiency of extraction is important to limit the loss of DNA in rare samples, as well as ensure enough DNA is available for PCR reactions to enable the generation of a full genetic profile. As with any DNA amplification, PCR of STR sequences (henceforth, STR PCR) can be sensitive to inhibitors such as proteins, nucleases, and other cellular materials, and therefore, requires high efficiency purification.[2] Several different types of extraction methods that have been validated by individual forensic laboratories, and these typically can be described as either solid phase or liquid phase methods. Solid-phase extraction methods offer enhanced purification through the binding of DNA to beads, which allows potential inhibitors such as proteins to be washed away prior to eluting the DNA.[3-5] These methods, however, typically require multiple handling and washing steps, increasing

complexity. Liquid-based extraction methods eliminate the need for a solid phase and can simplify the overall process by requiring only one or two steps, however, do not provide the purification afforded by a solid-phase method.[6]

In addition to the extraction and purification of sample DNA, the mass or number of copies of DNA used as template in STR PCR reactions is important for generation of a full genetic profile. Too little DNA will result in the failure of different loci to amplify, while too much DNA will cause problems in detection and interpretation of electropherograms. As a result, quantification of DNA is vital to the success of STR PCR. There are a number of quantification methods that are used to quantify DNA[7], with the most popular including UV/Vis and fluorescence spectroscopy due high sensitivity. UV/Vis spectroscopy allows for the quantification of DNA in the range of 1 – 250 pg/μL by measuring the absorbance at the wavelength of 260 nm.[8] While simple, this method suffers from poor sensitivity and can be prone to non-specific detection from contaminating proteins.

Fluorescence spectroscopy methods overcome the issue of sensitivity and specificity, however, they add complexity to the method. DNA intercalation methods use fluorescent dyes to bind to DNA and fluorescent signal is proportional to DNA concentration, with a dynamic range of 1 pg/μL – 1 ng/μL.[9] While the limit of detection is much improved over UV absorption, the method is time-consuming due to the constant need for calibration, and detection hardware is costly. The 'gold standard' method for DNA quantification is the fluorescence-based method real-time quantitative PCR (qPCR), which measures the change in fluorescence over time as PCR product is generated.[10] The number of cycles, when correlated to fluorescent signal, can be used to determine the starting concentration of DNA. In addition to being sensitive, this method also provides an indication of the amount of

'amplifiable' DNA. The presence of inhibitors, highly degraded DNA, or a limited starting quantity of DNA may cause the qPCR reaction to fail, and would provide valuable information about the starting DNA template before use in STR PCR. Despite these advantages, the method remains time consuming (> 2 hrs.), is relatively complicated, and requires expensive instrumentation for thermal cycling and fluorescence detection.

Ideally, a method could be developed that could simplify the extraction process, provide purified DNA, and eliminate the need for quantitation of a DNA samples prior to STR PCR. The DFA assay described in **Chapter 2** may provide this alternative sample preparation method by utilizing the simplicity of a liquid-based extraction, while providing the purification of a solid-phase method. In addition, if the amount of DNA capable of binding to the beads in the purification step could be controlled, the need for quantification prior to STR PCR could be eliminated.

The goal of the work in this chapter is to develop such an assay for analysis of forensically-relevant samples, including buccal (cheek) cell swabs and dried blood on various substrates (e.g. cotton, denim). Briefly, samples would be extracted via a simple liquid-based extraction method and are processed on the DFA system. The DNA causes aggregation of beads, as previously described, and the amount of DNA collected is limited by the concentration of beads present. The DNA is then eluted from the beads, similar to solid-phase extraction, and ready for STR PCR. The amount of DNA collected from the assay after elution is studied using qPCR, and successful STR PCR is demonstrated from the eluent. The aggregation and elution of DNA from various sample types is characterized, and in particular, issues in the aggregation of DNA from dried buccal swab samples is studied in depth.

3.2 Materials and Methods

3.2.1 Reagents

MagneSil superparamagnetic particles, pre-purified hgDNA (female), and PowerPlex18® (PP18) STR PCR kits were purchased from Promega™ (Carlsbad, CA). Guanidine hydrochloride (GuHCl), 2-(4-morpholino) methanesulfonic acid (MES, enzyme grade), hydrochloric acid, sodium hydroxide, acetone and ethanol were purchased from Fisher (Fair Lawn, NJ). 2-Amino-2-(hydroxymethyl)- 1,3-propanediol (Trizma base, 99.9%) was purchased from Sigma (St. Louis, MO). All solutions were prepared in Nanopure™ water (Barnstead/Thermolyne, Dubuque, IA). SYBR Green® qPCR kit was purchased from Affymetrix (Santa Clara, CA). Foam swabs were obtained from Texwipe (Kernersville, NC). ZyGEM extraction kits were purchased from VWR (Radnor, PA).

3.2.2 Sample Preparation

Human genomic DNA samples and bead solutions were prepared as described in **Chapter 2**. Buccal cell samples were collected from random donors by swabbing either the left or right cheek vigorously. After collection, swabs were allowed to dry for a minimum of 24 hours before elution. Elution and extraction steps were completed according to manufacturing protocols. Dried blood stains were prepared by spiking 10 μL of fresh whole blood (<24 hours after collection) onto small fragments of cotton and denim fabric, as well as a petri dish. Spiked samples were allowed to dry for a minimum of 24 hours at room temperature. DNA was extracted from the dried samples by placing the fragment of fabric or swab in to 50 μL of 6M GuHCl with 10 μL of Proteinase K. Samples were then heated at 56 °C for 10-35 minutes. STR PCR amplifications of the collected DNA were prepared according to manufacturer's protocols.

3.2.3 Assay Protocol

The procedure for aggregating of magnetic particles in the presence of DNA is described in Chapter 2. Elution of DNA from the aggregated beads was completed by removing the GuHCl from each well, adding and removing an 80%/20% isopropanol (IPA):water solution, and adding 1X TE buffer. The plate of wells was then placed back into the DFA system and exposed to both the RMF (2000 rpm) and the IV for 1 minute at 830 rpm, followed by 2 minutes at 475 rpm. Pictures were taken of the wells after both the aggregation and the elution. The eluent was collected from each well and immediately mixed with primers and master mix from either a SYBR Green qPCR kit or a PP18 STR PCR kit. Thermal cycling conditions were as follows for qPCR: 50 °C for 2 minutes, 95 °C for 10 minutes, [95 °C for 15 seconds and 60 °C for 30 seconds] x 30. For STR amplification, conditions were: 96 °C for 2 minutes, [94 °C for 10 seconds and 60 °C for 1 minute] x 30, and 60 °C for 5 minutes. Samples were separated and detected on an ABI PRISM 310 genetic analyzer (Applied Biosystems) with a peak detection threshold set at 50 RFU.

3.3 Results and Discussion

3.3.1 Quantitation-Free STR DNA Preparation Method

One of the most time-consuming, yet important, steps in the preparation of sample for STR analysis is DNA quantification. The amount of DNA used in STR PCR is crucial for obtaining full, balanced human identification profiles. Guidelines for analyzing the quality of profiles used in human identification have been described by Hedman et al. and Oorschot et al.[11, 12] Briefly, this includes a minimum peak height threshold (~50 RFU) for identifying peaks from background noise, and that all peaks have similar peak heights, indicating equal amplification of each allele during PCR. Typical quantitation methods can be time consuming

and require expensive fluorophores and detectors. Here, an alternative method for STR sample preparation that does not require a quantification step prior to STR PCR, is proposed. In a broad overview of the proposed process, a dried sample undergoes a simple liquid-based extraction using either ZyGEM enzyme, or guanidine and proteinase K. The extracted sample would be processed on the DFA system via the method described in **Chapter 2**. After the DNA binds to the beads and forms aggregates, the guanidine would be removed and replaced by 1X tris-EDTA buffer. As with standard solid phase DNA extraction, the TE buffer is used as an elution buffer and the DFA system is used to facilitate the elution of the DNA from the beads. This elution, containing the collected DNA, would be immediately ready for STR PCR without any further processing. The goal of using this method is to control the amount of beads in the assay, such that the amount of DNA that can be collected from a sample is limited and constant, regardless of the starting concentration of a sample. Utilizing the binding capacity of a known concentration of beads to normalize the amount of DNA obtained in a sample would eliminate the need for quantification.

3.3.1.1 Effectiveness of TE Elution

The first step in validating this proposed method was to determine the effectiveness of a TE elution step using DFA. To test this, 1 µL of 2 ng/µL hgDNA was added to a series of wells containing beads, and the normal DFA protocol completed. After aggregation, the GuHCl was removed from each well and was replaced by 1X TE buffer. The wells were placed back in the DFA system and again exposed to both the RMF and the IV force. The level of aggregation (%DA) was determined after both the aggregation step and the elution step, and the difference in %DA was calculated (**Fig. 1**). Following the same pattern that correlated the level of aggregation to an amount of DNA present in **Chapter 2**, it was

hypothesized that the amount of dispersion of beads (the difference in %DA between aggregation and elution) was likely correlated to the amount of DNA that was eluted from the beads. As shown in **Figure 1**, the use of 1X TE alone was relatively effective in eluting the DNA, however, a number of wells continued to show signs of aggregation after the elution step. This effect results in a lower %DA after elution and would correlate to less DNA eluted off of the beads. It was hypothesized that the efficiency of GuHCl removal was playing a role in the effectiveness of the elution. Residual GuHCl may be providing enough of a chaotropic environment to maintain DNA binding to the beads.

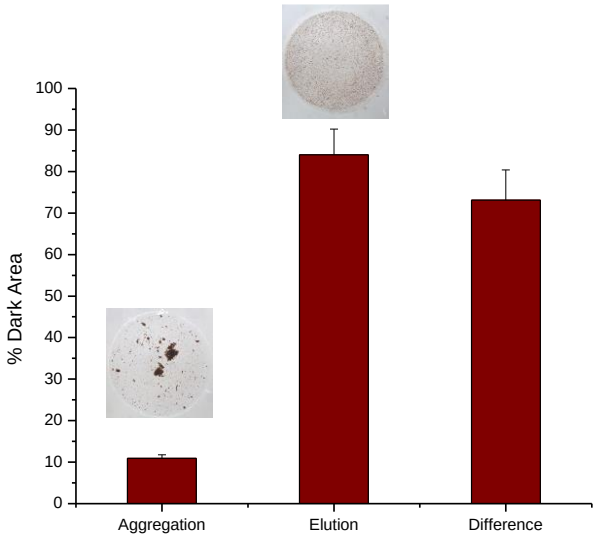

Figure 1: TE Elution Effectiveness. A histogram describing the %DA after aggregation and after elution, as well as the difference between the two %DA.

3.3.1.2 Impact of IPA Wash

To eliminate any residual GuHCl, an 80%/20% (v/v) solution of isopropanol-to-water was added to the well after the removal of GuHCl, as described previously in solid-phase extraction methods. To test the effectiveness of the IPA wash, hgDNA was aggregated in a series of wells, as previously described, and prior to elution, half of the wells were washed with IPA solution while the other half of the wells were not (**Fig. 2A**). Elution buffer was then added to all wells and the samples collected. The amount of DNA recovered from the samples was determined through qPCR, and the results are shown in **Figure 2B**. Overall, the IPA resulted in a larger difference in %DA between aggregation and elution steps, and the

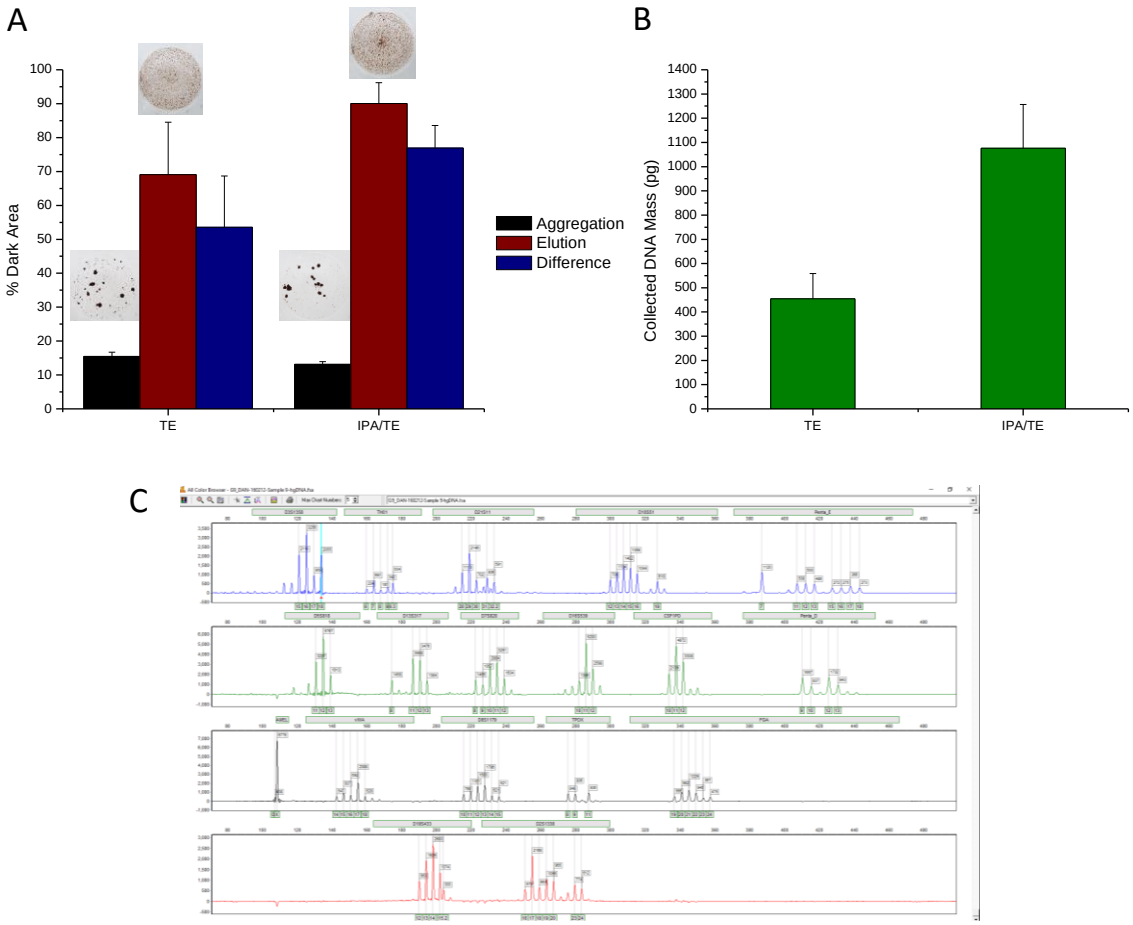

Figure 2: Addition of IPA Wash. A) A histogram describing the %DA values for after both aggregation and elution of hgDNA for TE elution alone, as well as an IPA wash, followed by TE elution (n=6). B) A representation of the amount of DNA recovered from the beads after the both TE and IPA/TE elution steps (n=6). C) A PowerPlex18 STR profile generated from STR PCR using the DNA eluent from the bead assay. Multiple peaks are observed for each locus due to the heterogeneity of the pre-purified DNA.

correlated to more than a 2X improvement in amount of DNA recovered per well. In addition to validating the effectiveness of the IPA step in the procedure, the qPCR showed that an average mass of 1 ng of DNA was being recovered from each well. To confirm that this amount of DNA would be sufficient for STR PCR, hgDNA was collected post-assay, and was amplified using the PowerPlex18 STR PCR kit, and then separated on a traditional capillary instrument. The resulting profile showed several peaks at each locus due to the heterogeneity of the hgDNA sample (multiple donors) and all peaks showed peak heights >200 RFU (**Fig.**

2C). In the forensic community, a minimum peak height threshold of ~50 RFU is commonly used to ensure peak identification from background noise.[12]

3.3.2 Buccal Swab Analysis

3.3.2.1 ZyGEM Extraction

Following the confirmation of elution from the developed procedure, and confirming that the amount of DNA recovered from the assay was sufficient for STR PCR, attempts were made to analyze forensically relevant samples, including dried buccal (cheek) swabs, and dried blood on cotton, denim, and cotton swabs, using this method. One of the most popular sources of DNA in forensic samples comes from buccal, or cheek, swabs. A series of dried buccal swabs were extracted via ZyGEM and the concentration of DNA was determined via fluorescence spectroscopy. The concentration of the extracted DNA was determined to be between 1.1-2.6 ng/µL. As described in **Chapter 2**, hgDNA at concentrations greater than 250 pg/µL, yielded maximum aggregation using the DFA assay. A similar result was expected for buccal swabs, however, each of the samples from four donors showed minimal aggregation (high %DA) (**Fig. 3**). In addition, all samples showed very similar aggregation despite as much as a 2X difference in starting DNA concentration.

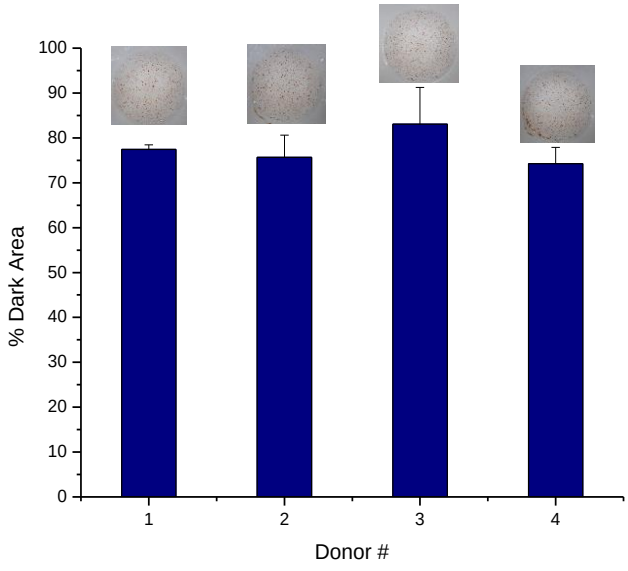

Figure 3: A histogram and images of the aggregation associated with buccal swabs collected from four individuals. DNA concentration ranged from 1.1-2.6 ng/µL, based on fluorescence spectroscopy (n=3).

3.3.2.2 Qiagen Extraction

To determine if the lack of aggregation was due to the ZyGEM extraction method alone, an alternative extraction technique was used to remove DNA from buccal cells. A commercial Qiagen extraction kit was used for extraction of two individual donors and the DNA quantified via fluorescence. DNA concentration was determined to be 1.2 ng/µL and 7.3 ng/µL for each sample, respectively. Each sample was then aggregated on the DFA system and the images analyzed. As shown in **Figure 4**, the highly concentrated sample showed greater aggregation than the ZyGEM samples, however, the sample with roughly the same amount of DNA as the ZyGEM extractions showed roughly the same high %DA. This was an indication that the ZyGEM extraction technique was not the sole cause of poor aggregation.

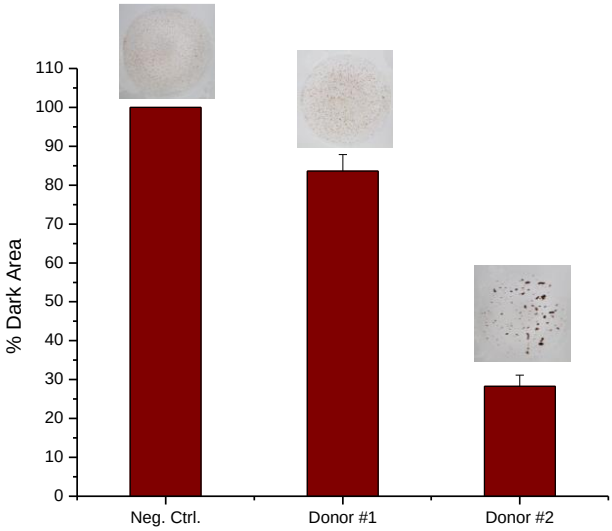

Figure 4: Images and %DA values for buccal samples extracted using a Qiagen extraction kit. DNA concentrations: Donor #1 – 1.2 ng/µL; Donor #2 – 7.3 ng/µL (n=3).

To further explore the cause of poor aggregation, each reagent in the Qiagen extraction kit was tested by spiking the reagent into a well with 1 ng of hgDNA and the chaotropic salt, guanidine hydrochloride (GuHCl), and then perfoming the assay. Ultimately, no individual reagent had a negative impact on aggregation, and bead aggregation was maximized in the presence hgDNA (data not shown). It was important to determine whether there was any DNA shearing during extraction in a Qiagen spin column. DNA length plays an important role in the binding and aggregation of the 8 µm particles, so any shortening of the DNA due to the filter may have been the cause of poor aggregation. A 1 ng/µL sample was split into

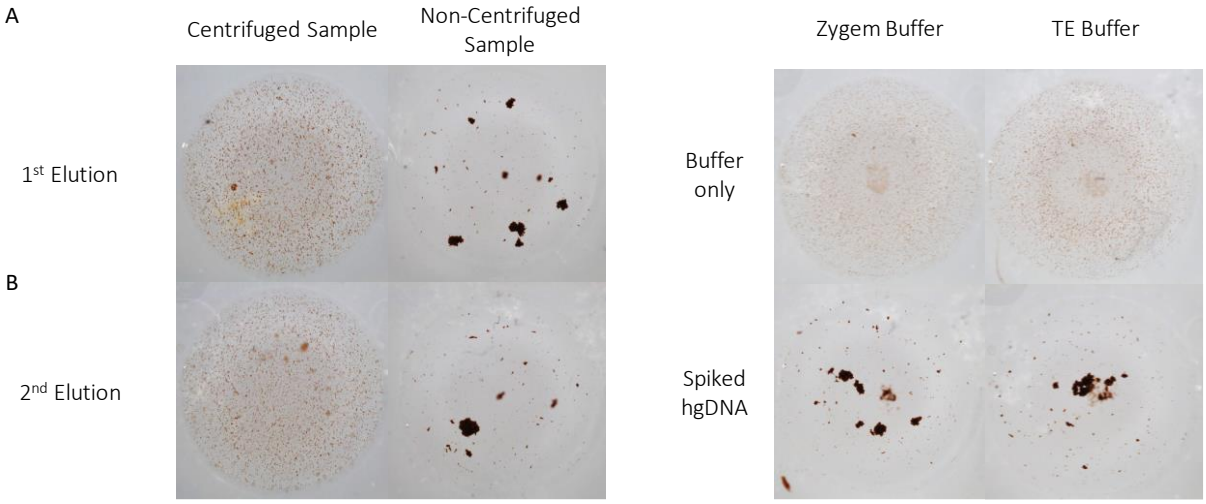

Figure 5: A) Images of aggregation from 1 ng/µL DNA passed through a Qiagen column compared to the same concentration of DNA without passing through the column. B) Aggregation after a second elution step performed on the column, compared to hgDNA without the column. C) Images of aggregation in the presence of just buffers D) Images of aggregation after spiking 1 µL of 1 ng/µL hgDNA.

two aliquots and one was centrifuged through the Qiagen column followed by analysis using DFA, while the other sample was simply analyzed on the DFA system. The DNA sample that was centrifuged through the column showed no aggregation compared to the non-centrifuged sample (**Fig. 5A**). In the event that the DNA had bound to the filter, a second elution step was performed and still, no aggregation was observed **Fig. 5B**). These results suggested that when using the Qiagen extractions, the lack of aggregation may have been due to the DNA becoming sheared by the filter to lengths that limit the effectiveness of DNA binding beads together at lower concentrations.

3.3.2.3 Modified ZyGEM Protocol

To simplify the extraction procedure and avoid the use of filters, studies resumed with ZyGEM extraction. Both the ZyGEM extraction buffer and the DNA dilution buffer were individually tested to determine potential inhibitory properties. Aggregation in the presence of both buffers alone was studied, followed by the spiking of 1 µL of 1 ng/µL hgDNA. Neither buffer showed negative effects on aggregation (**Fig. 5 C&D**). The next set of experiments

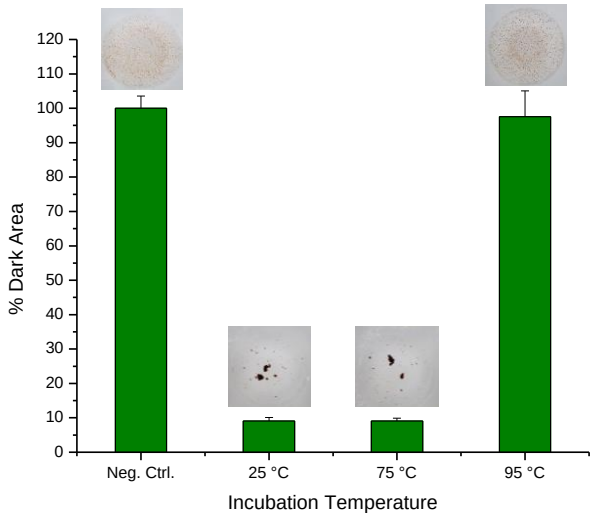

Figure 6: Images of aggregation and % DA values for hgDNA incubated at three separate temperatures. Negative impacts on aggregation were only when DNA was heated to 95 °C (n=3).

explored each step of the heating protocol in ZyGEM extraction. In the ZyGEM protocol, a majority of the incubation takes place at 75 °C, and after incubation, the sample is brought to 95 °C to deactivate the enzyme prior to further downstream analysis. DNA is known to denature at 95 °C and it was hypothesized that this may be having a negative impact on the aggregation. A sample of 1 ng/µL hgDNA was split into three aliquots. One aliquot was heated to 95 °C, the second to only 75 °C, and the third left at room temperature (25 °C). All three samples were then analyzed on the DFA system. Both the 25 °C and the 75 °C samples showed no negative effects on aggregation, while the 95 °C sample did not aggregate, and the beads remained dispersed like the negative control (**Fig. 6**). This indicated that the 95 °C was likely one factor in the failure of the early ZyGEM-extracted samples, and because this step is used only to reversibly denatured the enzyme, it can be eliminated. The only problem that may follow from that is active enzyme can inhibit PCR, however, most PCR methods begin with a 95 °C denaturing step that may allow for enzyme denaturing. After eliminating the 95 °C step, an attempt was made to

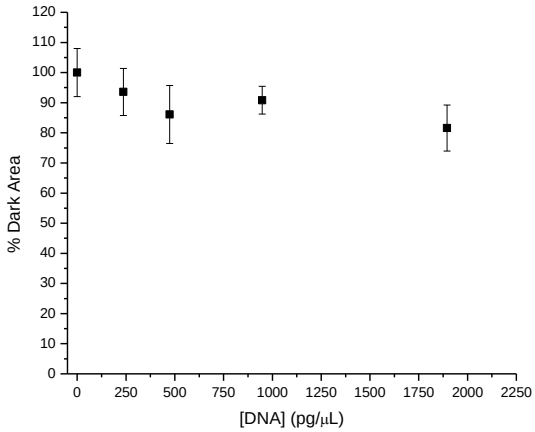

Figure 7: An aggregation standard curve generated from the serial dilution of DNA from a buccal swab. The sample was initially quantified at 1.895 ng/µL and was serially diluted three times before being analyzed on DFA (n=3).

analyze a new buccal swab sample and create an aggregation standard curve for quantification of unknown samples. A donor sample was collected, dried, and extracted using the ZyGEM w/o 95 °C procedure. The sample was quantified at 1.9 ng/µL and was serially diluted three times before being analyzed on DFA. Despite the removal of the 95 °C step, each sample across the series of dilutions continued to show minimal aggregation (**Fig. 7**).

3.3.2.4 ZyGEM Variable Tests

In addition to the heating and buffer tests, a series of other ZyGEM variables were tested to determine if any single component or condition in ZyGEM might be accounting for the lack of aggregation when analyzing DNA from dried buccal swabs. Each variable was analyzed by attempting to aggregate 1 µL of 1 ng/µL hgDNA, in the presence of a given

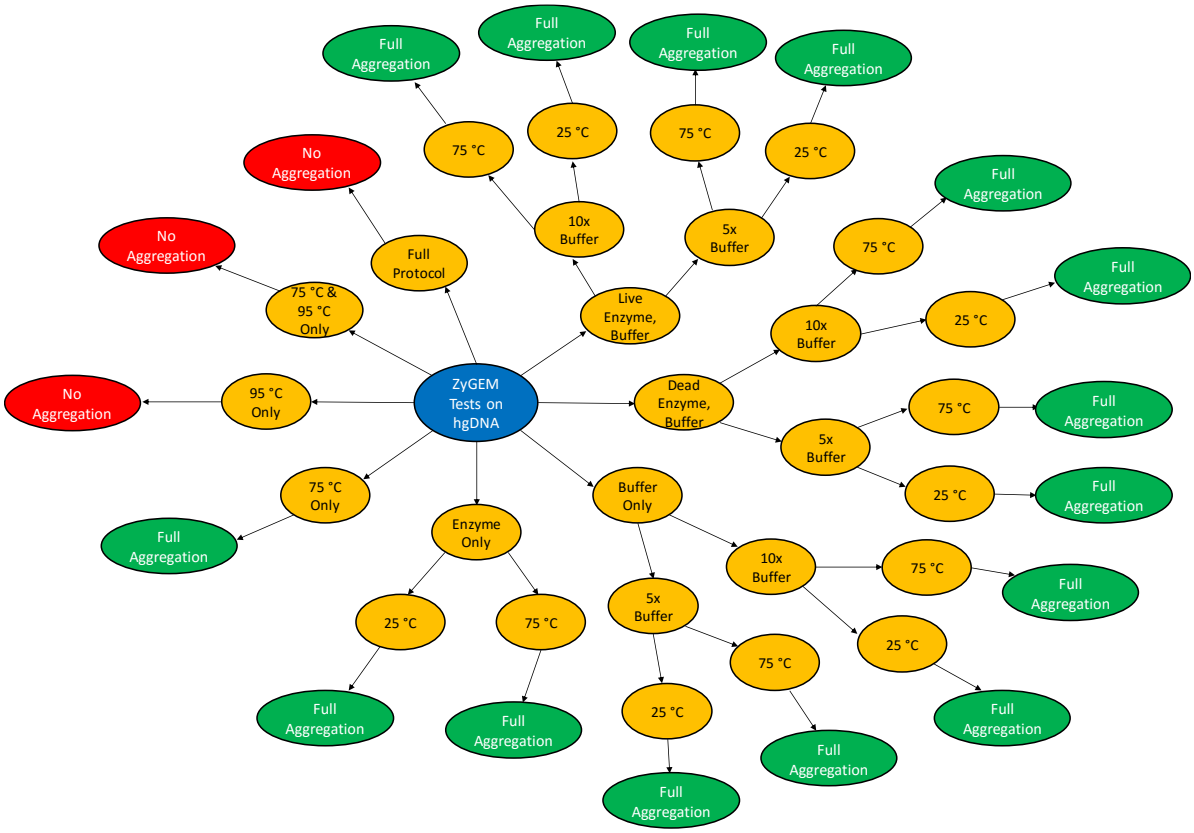

Figure 8: A flow chart describing a series of variable and conditions associated with ZyGEM extraction. Each variable was analyzed by attempting to aggregate 1 µL of 1 ng/µL hgDNA in the presence of a given reagent or under a specific set of conditions. All conditions showed full aggregation except those involving the 95 °C step.

reagent or under a specific set of conditions related to ZyGEM extraction. A schematic network describing the various combinations of variables tested is shown in **Figure 8**. After testing all variations, the only parameter in the ZyGEM protocol that appeared to have a negative effect on aggregation was the 95 °C heating step.

3.3.2.5 Swab Inhibition Studies

Retaining all of the manufacturer's suggested conditions for the ZyGEM reagents, the protocol was altered by excising the 95 °C step. This showed little-to-no impact on aggregation of hgDNA, it was determined that ZyGEM was likely not the cause of poor aggregation of dried buccal swab DNA. Focus was shifted to the composition of the swab and potential inhibitors that could be preventing aggregation. It was hypothesized that if inhibitors were present on a swab, they may have been coming off the swab during the initial elution procedure. To counter this potential effect, a pre-washing of the swab with either water or TE buffer might remove the inhibitors and restore aggregation upon analysis. To test

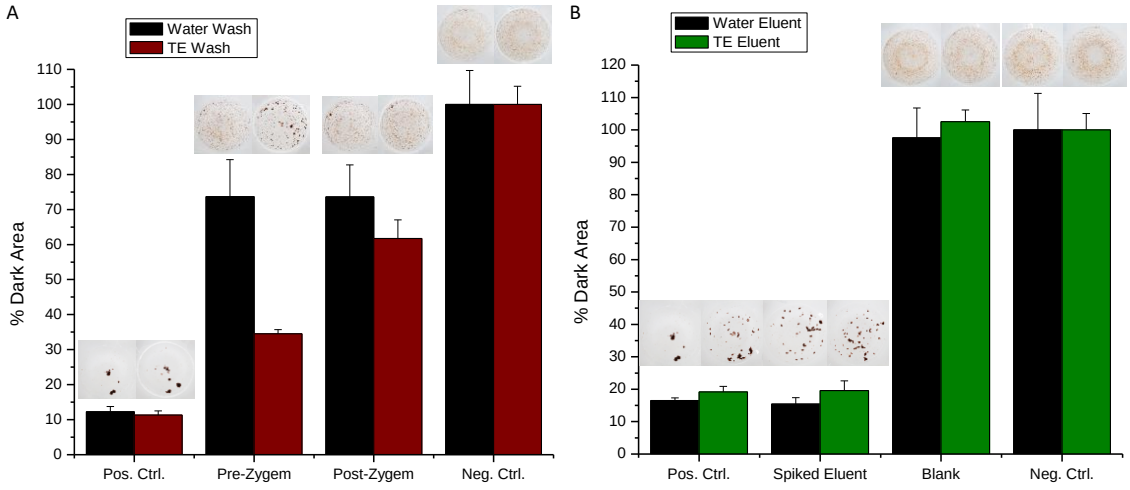

Figure 9: A) A histogram describing the %DA associated with samples from swabs that were pre-washed with water or TE buffer. DNA was quantified at 1.49 and 1.37 ng/µL for water and TE washed swabs, respectively. TE buffer was showed slight improvement, however, no samples mimicked the positive control (n=3). B) A histogram describing the %DA associated with samples were DNA was spiked into the water and TE pre-wash eluents. Eluents were spiked with 1 µL of 250 pg/µL hgDNA. No negative results were observed due to potential inhibitors washed from the swabs (n=3).

this, swabs were rinsed with distilled water or TE buffer and allowed to dry. Once dry, 10 µl of a 25 ng/µL solution of hgDNA was spiked onto each swab and allowed to dry overnight. The swabs were then eluted according to the ZyGEM protocol, quantified (200 µL, 1.49 and 1.37 ng/µL after elution) and split into two aliquots. The first aliquot was immediately tested for aggregation on the DFA system while the other aliquot was processed under normal ZyGEM extraction conditions and quantified prior to DFA analysis. As shown in **Figure 9A**, the swabs that were washed with water continued to show poor aggregation compared to the positive control (1 µL of 0.25 ng/µL). The TE-washed swabs demonstrated a slight improvement in aggregation compared to water, however, the aggregation was still significantly lower than the positive control aggregation, despite being at a higher concentration (**Fig. 9A**). A decrease in aggregation was observed in the post-ZyGEM, TE-washed sample, but was expected due to a 5-fold dilution of the sample by ZyGEM reagents. These results did not immediately indicate that inhibitors were present, or that if there were inhibitors they could be removed from the swab prior to use.

To further confirm the lack of inhibitors coming off the swab, the initial swab-wash eluents were spiked with 1 µL of 0.25 ng/µL hgDNA and analyzed for aggregation. The DNA analyzed in both the water and TE wash eluents showed aggregation equal to that of the positive control (**Fig. 9B**). This

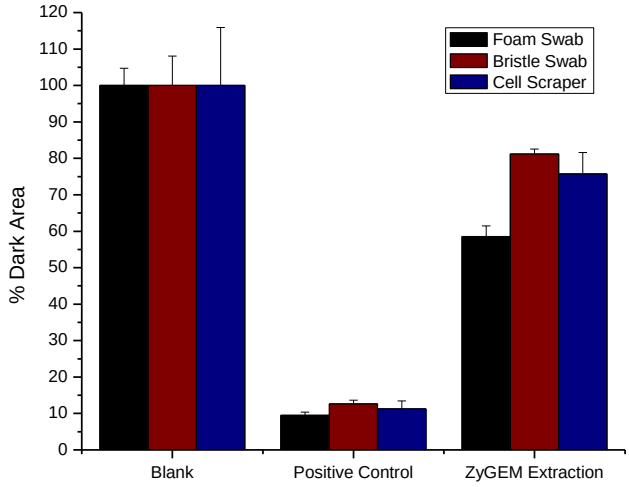

Figure 10: Multiple different swab types were tested under normal ZyGEM conditions. No particular material or swab demonstrated significant improvement over another. Samples from all three swab types continued to show poor aggregation compared to the positive controls (n=3).

provided further indications that inhibitors from the swab limiting aggregation was unlikely. Alternatively, given that freshly prepared DNA aggregated as expected, even in the presence of swab eluent, the focus was shifted towards something in the drying process having the largest impact on aggregation. Further, when multiple different swab types were tested under normal ZyGEM conditions, no particular material or swab demonstrated significant improvement over another (**Fig. 10**). Samples from all three swab types continued to show poor aggregation compared to the positive controls.

3.3.2.6 Multiple Cell Types

As an alternative to cheek cells, several other cell types, were studied to determine if the lack of aggregation was specific to epithelial cheek cells. Lung cells (H522 cell line) were obtained from cell culture and 10 μL were dried on buccal swabs. At a concentration of 516 cells/μL, with a DNA concentration of 6.25 pg/cell, a total of 32,250 pg, or 32.25 ng of DNA was added to each swab. Despite this high concentration, the sample showed very little aggregation (74% DA) after ZyGEM extraction compared to the negative control (**Fig. 11A**). Following analysis, 1 ng of hgDNA was added to the well consisting of the lung cell DNA, and full aggregation of the beads was observed. A similar experiment was performed on a swab that contained dried vaginal epithelial cells. Upon analysis, the vaginal swab sample showed almost the exact same level of aggregation as the lung cell sample (73% DA) (**Fig. 11B**).

One final attempt to understand the impact of the cell type included the study of a prostate adenocarcinoma cell line (PC3). Similar to the other experiments, PC3 cells (10 μL) were spiked onto a swab and allowed to dry before elution and extraction via ZyGEM. The

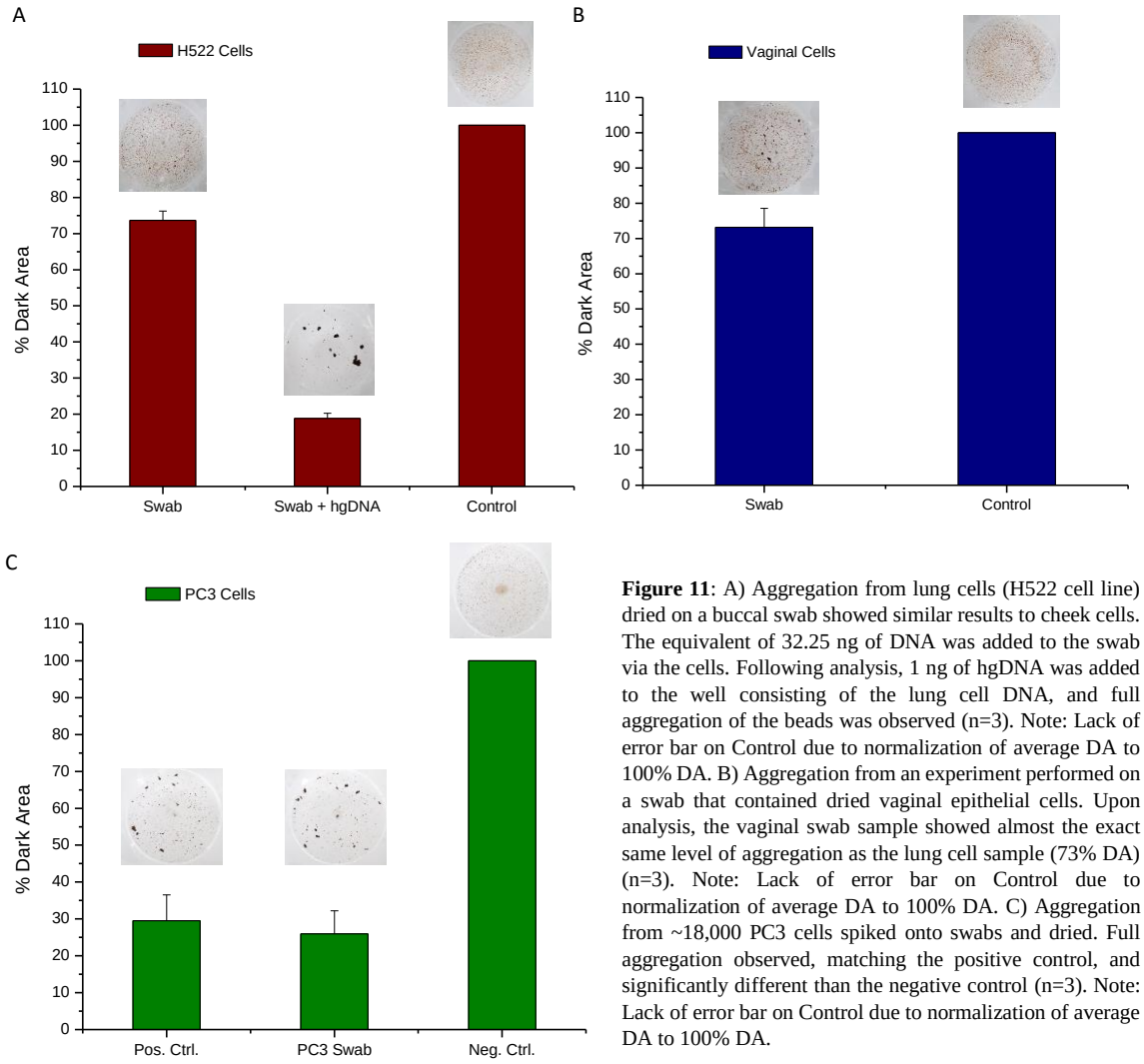

Figure 11: A) Aggregation from lung cells (H522 cell line) dried on a buccal swab showed similar results to cheek cells. The equivalent of 32.25 ng of DNA was added to the swab via the cells. Following analysis, 1 ng of hgDNA was added to the well consisting of the lung cell DNA, and full aggregation of the beads was observed (n=3). Note: Lack of error bar on Control due to normalization of average DA to 100% DA. B) Aggregation from an experiment performed on a swab that contained dried vaginal epithelial cells. Upon analysis, the vaginal swab sample showed almost the exact same level of aggregation as the lung cell sample (73% DA) (n=3). Note: Lack of error bar on Control due to normalization of average DA to 100% DA. C) Aggregation from ~18,000 PC3 cells spiked onto swabs and dried. Full aggregation observed, matching the positive control, and significantly different than the negative control (n=3). Note: Lack of error bar on Control due to normalization of average DA to 100% DA.

concentration of cells was 1.8 x 10^3 cells/µL, and therefore, ~18,000 cells were dried on the swab. At 6.25 pg/cell, the amount of DNA calculated to be on the swab was 1.125 x 10^5 pg, or 112.5 ng. Samples were eluted in 400 µL, resulting in a final concentration of 45 cells/µL. Upon analysis, the beads fully aggregated and were shown to have the same saturated %DA as the 1 ng/µL positive control (**Fig. 11C**). It is possible that the aggregation was caused by the overwhelming amount of DNA present compared to the other cell types. The concentration of cells from a cheek eluate sample, however, was determined to be 300 cells/µL after elution in 400 µL of H_2O, greater than 6.5-fold the number of cells, and amount of DNA,

obtained from the PC3 cells. Consequently, it seems unlikely that the successful aggregation of PC3 cell DNA was strictly due to the amount of DNA in the assay.

3.3.2.7 Impact of Saliva on Aggregation

The next component in the assay that was studied was the impact of saliva. Attempts were made to isolate the cheek epithelial cells from eluted saliva swabs through centrifugation and resuspension. Cells were counted before and after washing to account for cell loss and provide an accurate starting concentration. Analysis of post-washed samples showed no improvement in aggregation, and the difference in %DA remained >50% (**Fig. 12**). Doubling the amount of sample added to the extraction also did not improve the amount of aggregation observed. To further assess the impact of saliva on aggregation, three separate samples were prepared that incorporated PC3 cells on a swab with no cheeks cells or saliva, a swab with cheek cells and saliva, and a PC3 cell-spiked water sample. For each of the swabs, the same number of cells (18,000) were spiked onto either a clean swab or a swab containing cheek cells and saliva. The same number of cells were also spiked into 400 µL of water without a swab. The goal of the experiment was to try to determine the amount of DNA coming off the swab (PC3 cells without saliva vs. PC3 cells in water) and determine if saliva was inhibitory to the aggregation

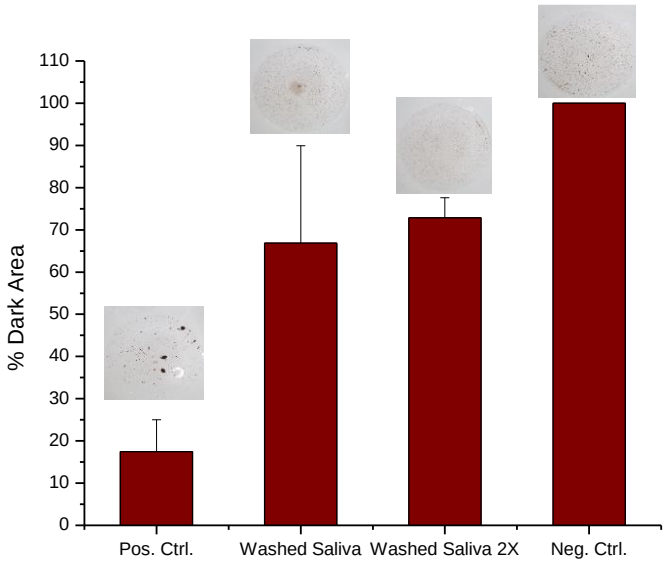

Figure 12: Analysis of post-washed samples show no improvement in aggregation (n=3). Doubling the amount of sample added to the extraction also did not improve the amount of aggregation observed. Note: Lack of error bar on Control due to normalization of average DA to 100% DA.

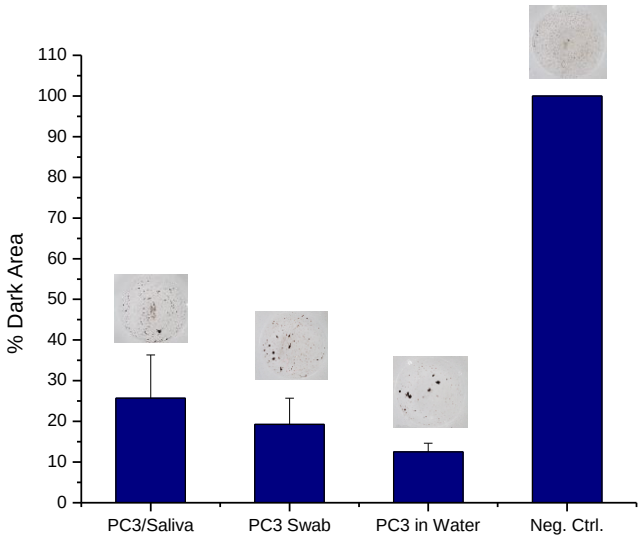

Figure 13: Three samples spiked with PC3 cells aggregated very well after extraction, matching the %DA values that were observed with previous PC3 samples. PC3 cells spiked into saliva did not show significantly reduced amount of aggregation (n=3). Note: Lack of error bar on Control due to normalization of average DA to 100% DA.

of PC3 cells (PC3 cells without saliva vs. PC3 cells with saliva). As shown in **Figure 13**, all three samples aggregated very well after extraction, matching the %DA values that were observed with previous PC3 samples. The saliva did not appear to have any negative impact on the aggregation, and actually showed better aggregation than PC3 cells without saliva and cheek cells.

Several more tests comparing different combinations of variables were completed using two different extraction techniques and two separate donors. First, a comparison between the effectiveness of a simple GuHCl incubation versus full ZyGEM extraction was

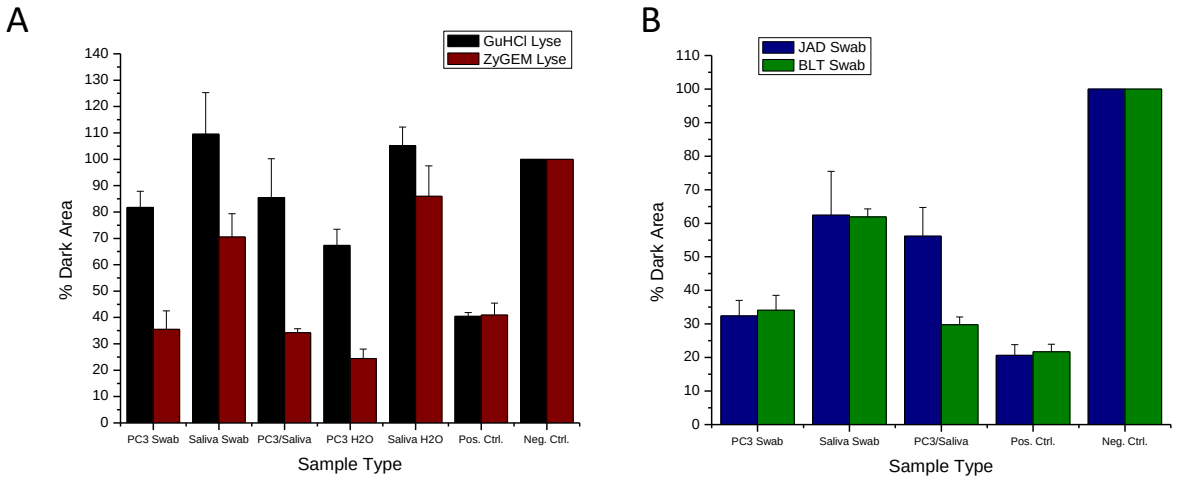

Figure 14: A) A comparison between the effectiveness of a simple GuHCl incubation versus full ZyGEM extraction. The ZyGEM extraction performed significantly better than using only GuHCl (n=3). B) Two individual donor samples were compared across three variables and despite a three-fold difference in DNA concentration (1.81 ng/µL vs 0.61 ng/µL), each showed the exact same aggregation on two of the three tests. Note: Lack of error bar on Control due to normalization of average DA to 100% DA (n=3).

completed. Across all variables, the ZyGEM extraction performed significantly better than using only GuHCl, however, normal cheek swab samples continued to underperform compared PC3-spiked samples (**Fig. 14A**). In addition, two individual donor samples were compared across the same three variables and despite a three-fold difference in DNA concentration, showed the exact same aggregation on two of the three tests (**Fig. 14B**). The samples containing PC3 cells and saliva showed a 30% DA difference, however, the more aggregated sample was actually the sample with the lower starting concentration of extracted saliva DNA.

3.3.2.8 Effect of Swab Drying Time

Finally, the last variable tested in an attempt to understand the lack of aggregation from dried buccal swabs, was time. The variable of time had not been changed throughout the entirety of the buccal swab studies. All cheek swab samples were collected from donors and allowed to dry for a minimum of 24 hours. This was to mimic the forensic environment where it is well known that a large backlog exists in collected samples waiting to be processed, and all swabs would likely be dry by the time of processing. Rather than let the swabs dry for a minimum of 24 hours, a series of collected swabs were only allowed to rest for 10 minutes before

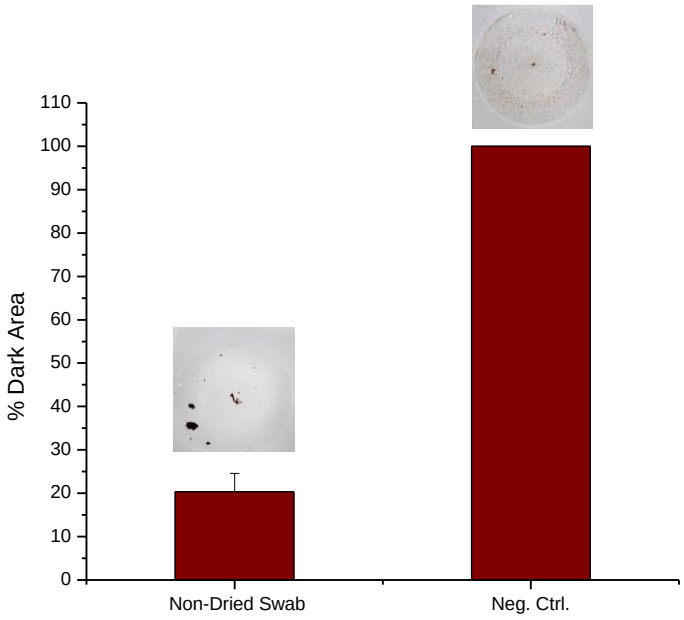

Figure 15: Aggregation success when the swabs were only allowed to dry for 10 minutes before processing, compared to a minimum of 24 hours (n=12). Note: Lack of error bar on Control due to normalization of average DA to 100% DA.

performing ZyGEM extraction and DFA analysis. As shown in **Figure 15**, DNA from twelve separate swabs showed full aggregation and %DA values averaged 20%. This was a drastic improvement over samples that were allowed to dry for a minimum of 24 hours.

3.3.2.9 Freezing Swab Eluent for Storage

At this time, studies were not completed to show the maximum amount of time a swab could be allowed to dry before observing a significant loss in aggregation. Alternatively, a new method for storing samples long term was explored. Knowing that a backlog exists and that it is not feasible for swab samples to be analyzed within 10 minutes of collection, a method for storing swab eluent at <-20 °C was explored. Swab samples were collected, eluted after 10 minutes, and the eluent aliquoted 4 times. Three of the four aliquots were placed at -20 °C, and one aliquot was placed at -196 °C. The samples were then analyzed over the course of six days, comparing the aggregation to that of the day the swab was collected and eluted. Each sample showed full aggregation (~20% DA) on each of the five days that samples were analyzed (**Fig. 16A**). In addition to direct analysis, the extracted eluent was serially diluted five times and the aggregation analyzed (**Fig. 16B**). While showing some variation in %DA

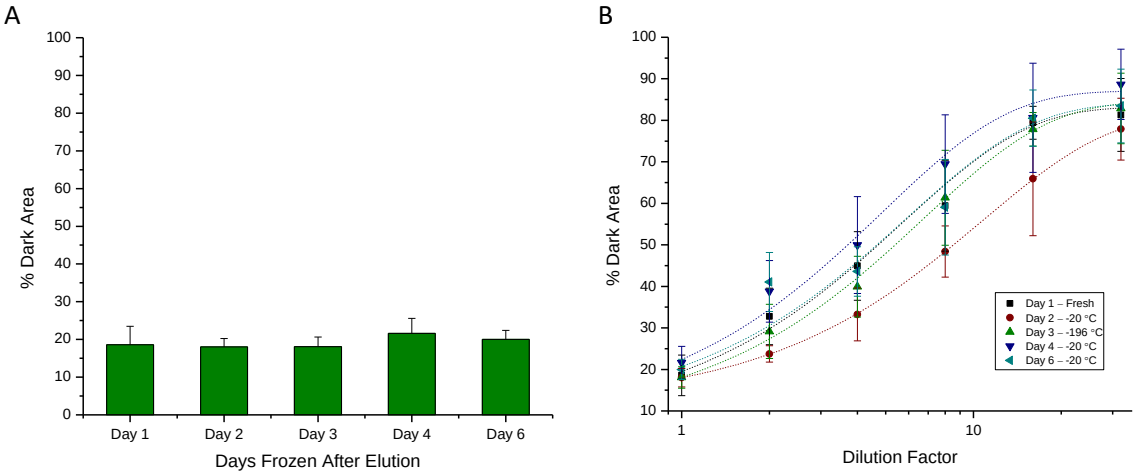

Figure 16: A) The impact of freezing swab eluent for delayed testing was studied. Samples showed full aggregation six days after elution when kept at < -20 °C (n=3). B) A serial dilution of samples from each day showed slight variability in %DA (n=3).

at each dilution, there was not a clear trend in the %DA from each day to suggest that aggregation was impacted by the temperature or time.

Ultimately, it remains unclear the impact that drying is having on the samples that causes poor aggregation of the extracted DNA. More studies are needed such as analysis of DNA length before and after drying, with the thought that in the drying process, the DNA may be breaking down to lengths that are insufficient for binding together multiple 8 μm beads. In addition, further studies are needed to test samples that remain frozen for longer than six days, and the maximum time allowed before a swab must be eluted and frozen to avoid losses in aggregation associated with drying.

3.3.3 Dried Blood Analysis

3.3.3.1 Dried Blood Analysis Proof-of-Principle

Another common source of DNA in forensics comes from dried blood stains. A series of blood samples with varying amounts of DNA were spiked onto three different substrates (cotton fabric, denim, foam swab) and allowed to dry for 24 hours. After drying, DNA was extracted from the samples by placing the substrate in GuHCl with proteinase K and incubated

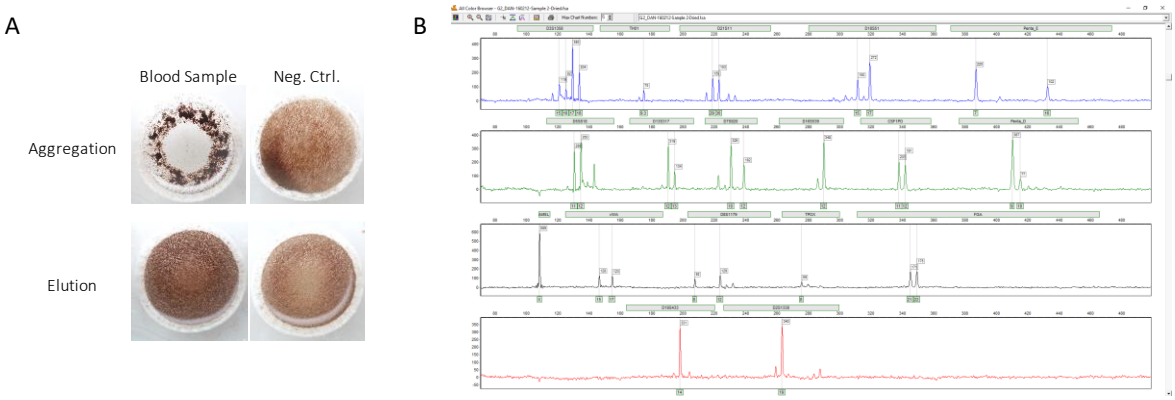

Figure 17: A) Dried blood samples showed full aggregation compared to buccal swabs. Beads became dispersed after the elution process. B) An STR profile generated from the DNA released from the aggregated beads. Signal saw ~10-fold reduction compared to hgDNA elution profile.

at 56 °C. The samples were then aggregated as described above. Unlike the buccal swab samples, the dried blood samples on cotton aggregated fully (**Fig. 17A**). Following aggregation, the DNA was washed with IPA, and eluted from the beads using 1X TE buffer (**Fig. 17A**). STR PCR was performed on the collected samples and the product separated on a conventional capillary system (**Fig. 17B**). Despite the high DNA yield and successful amplification of STR loci from hgDNA samples that were eluted from the beads, preliminary results from blood samples dried on pieces of cotton material showed full profiles with ~10-fold reduction in peak height compared to profiles generated from hgDNA.

3.3.3.2 Maximizing DNA Yield

A series of optimization studies were completed in an attempt to increase the amount of DNA collected from the assay and, as a result, improve the overall signal of the peaks in the STR profile. To try and concentrate the DNA in the eluent, the volume of 1X TE used for elution was compared at 15 μL and 10 μL. Simultaneously, the concentration of beads in each well was increased by 2X, 3X, and 4X in order to increase the binding capacity of the assay and collect more DNA. STR profiles were generated from multiple samples under each condition, and the average peak height across each colored fluorophore was compared (**Fig. 18A**). The conditions that provided the highest peak heights across all colors were 4X concentration of beads and an elution volume of 15 μL. An exemplary profile generated from a dried blood sample on cotton fabric, using the optimized parameters, is shown in **Figure 18B**.

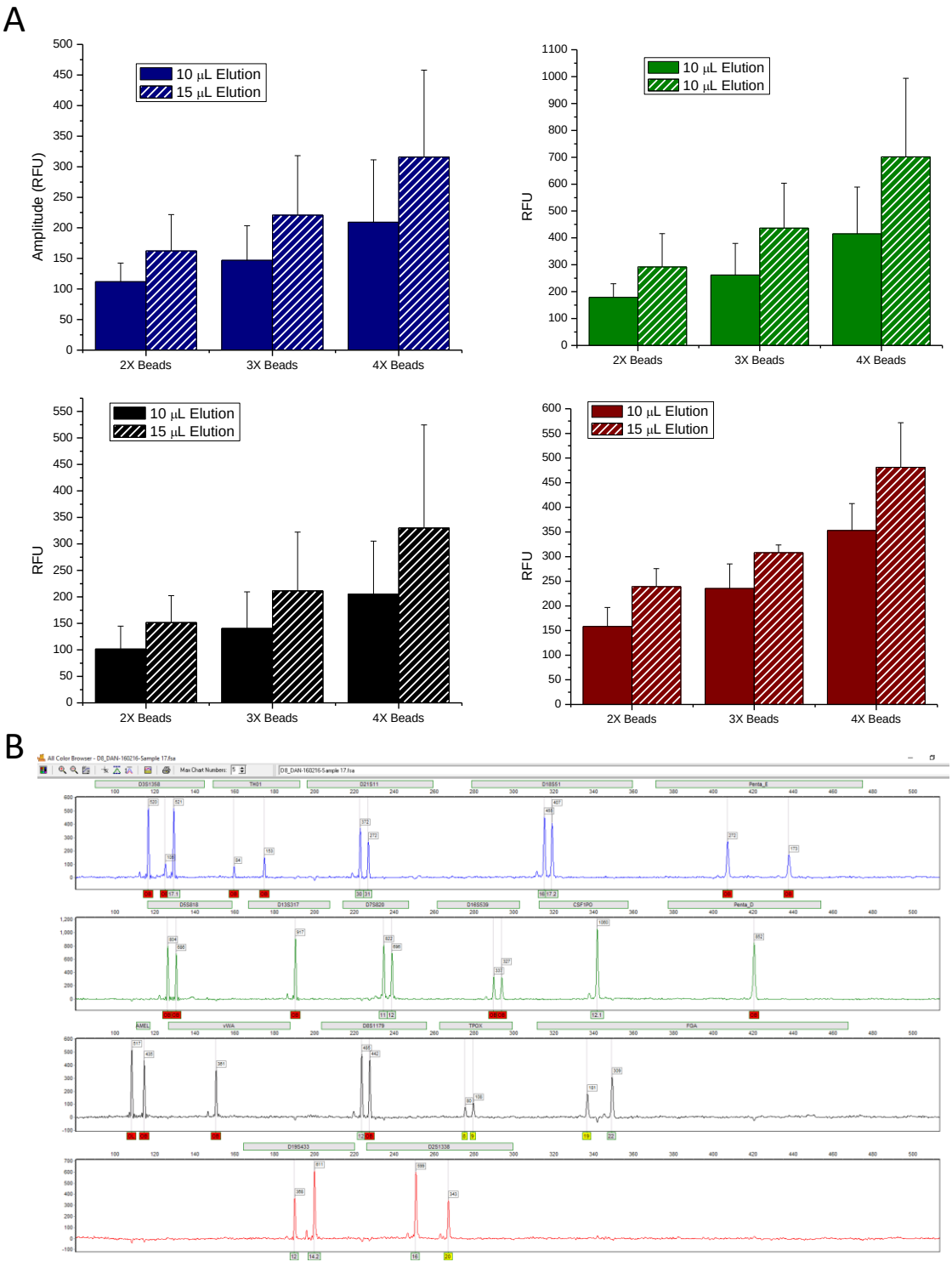

Figure 18: A) A comparison of the average peak height across each colored fluorophore in STR profiles generated under differing bead and elution conditions. The conditions that provided the highest peak heights across all colors were 4X concentration of beads with an elution volume of 15 µL. B) An exemplary profile generated from a dried blood sample on cotton fabric, using the optimized parameters.

3.3.3.3 Normalizing DNA Yield

There is a distinct and obvious advantage to a DNA analysis protocol for STR profiling that doesn't require DNA quantitation, specifically, the amount time from extraction to STR analysis could be reduced by >2 hours, and there would be a significant reduction in cost by removing the need for expensive fluorophores, thermocyling equipment, and fluorescent detectors. With the goal of eliminating the need for quantitation, samples with distinctly different starting concentrations must all provide full STR profiles after analysis. Theoretically, this method facilitates this need by providing the same amount of PCR-ready DNA regardless of starting sample concentration. Due to the binding capacity of the beads in each well, the amount of DNA that can be collected from each sample is limited. By introducing sample in excess, the binding of the beads is saturated and the excess DNA, unable to bind to the beads, is removed with the GuHCl prior to elution. This, in effect, normalizes the concentration of DNA across all samples.

3.3.3.4 Analysis of Dried Blood on Cotton Substrate

This theory was tested by analyzing dried blood samples from 6 separate donors, all with varying white blood cell (WBC) counts, and therefore starting DNA concentrations. Samples (10 μL) were dried on small pieces of cotton fabric and allowed to dry for a minimum of 24 hours. DNA was extracted from the dried samples via incubation in GuHCl at 56 °C with the addition of Proteinase K. Following extraction, samples were analyzed under the optimized conditions described above, and STR profiles were obtained for each sample. A comparison of average peak heights for each color of a given sample is shown in **Figure 19A**. All six samples gave profiles with average peak heights no lower than 100 RFU. Four of the

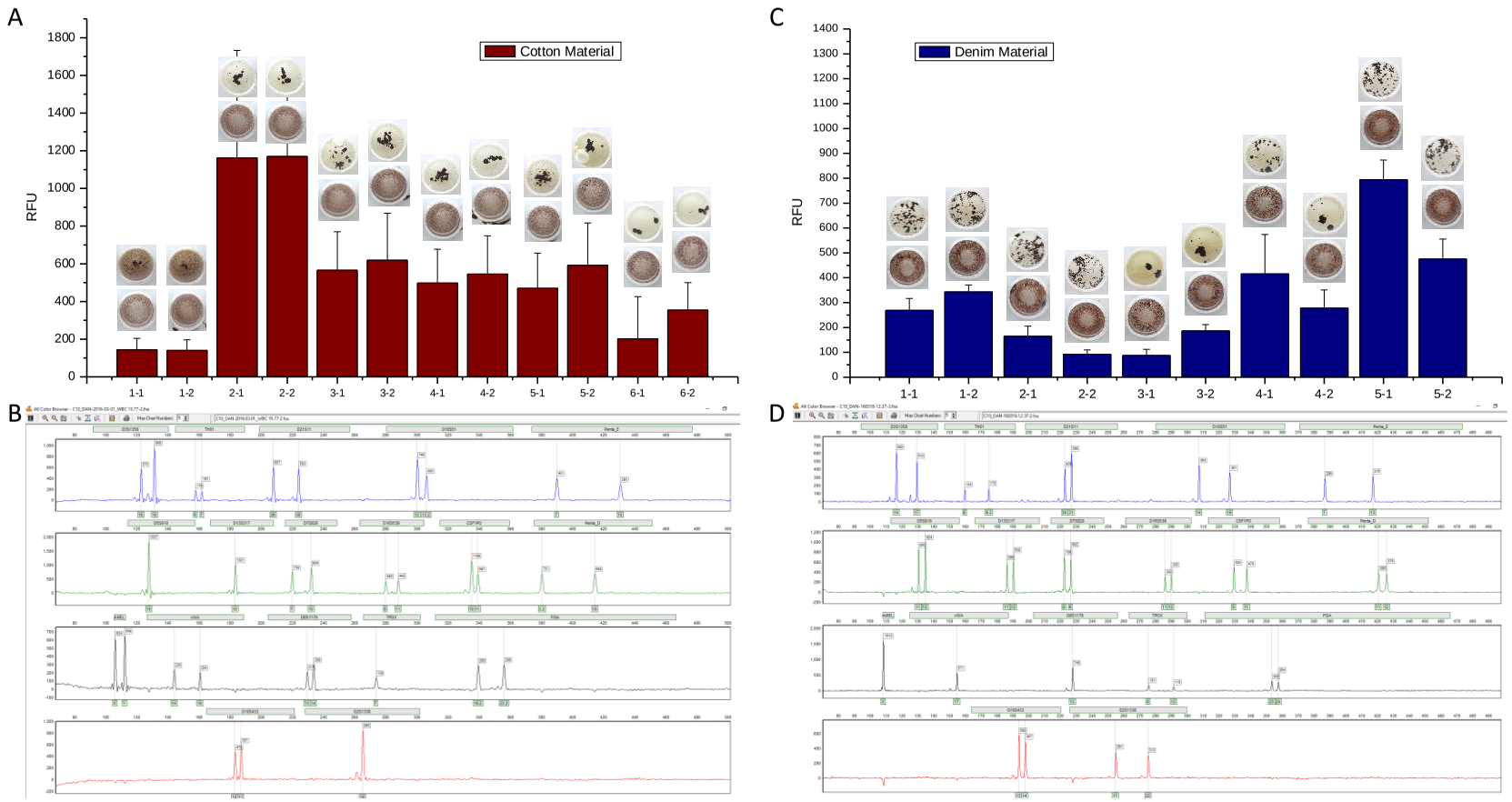

Figure 19: Analysis of samples that were dried on small pieces of cotton fabric. A) A comparison of average peak heights for each color of a given sample. All twelve samples gave profiles with average peak heights no lower than 100 RFU. Images of beads after both aggregation and elution are shown above each bar. B) An exemplary STR profile from a blood sample dried on cotton fabric. C) Analysis of samples that were dried on small pieces of Denim fabric. A comparison of average peak heights for each color of a given sample. Images of beads after both aggregation and elution are shown above each bar. D) An exemplary STR profile from a blood sample dried on denim fabric

six samples showed very similar peak heights despite the large difference in starting concentration of DNA for each sample. The lowest signal came from the sample with the lowest starting concentration, while the highest signal came from the second lowest starting concentration. The low signal for the WBC 4.91 sample was predictable due to the poor level of aggregation seen in the assay (**Fig. 19A**), indicating a low amount of bound DNA. The aggregation for the WBC 6.77 sample, however, was similar to the aggregation of the higher concentrations, yet yielded more DNA. It is unclear at this time what might have caused the increased amount of sample collected. An example of an STR profile from blood dried on denim samples is shown in **Figure 19B**.

3.3.3.5 Analysis of Dried Blood on Denim Substrate

A similar experiment was completed with six different samples that were dried on small pieces of denim fabric. There was significantly more variability in the average peak heights across the samples, however, 5 of 6 samples showed average peak heights above 100 RFU across all colors. One potential cause for the variability may have come from the differences in effectiveness of elution of each of the samples. As the images show in **Figure 19C**, several samples aggregated differently from others, and upon elution, many samples showed signs of incomplete elution (small aggregates observable). One hypothesis is that the tighter the aggregate, the more difficult it is to break that aggregate apart and release the DNA upon elution. More studies need to be completed to assess the differences in elution between samples, correlate the aggregation %DA to the effectiveness of elution, and understand the impact that has on the amount of DNA collected. An example of an STR profile from blood dried on denim samples is shown in **Figure 19D**.

3.3.3.6 Analysis of Dried Blood on Foam Substrate

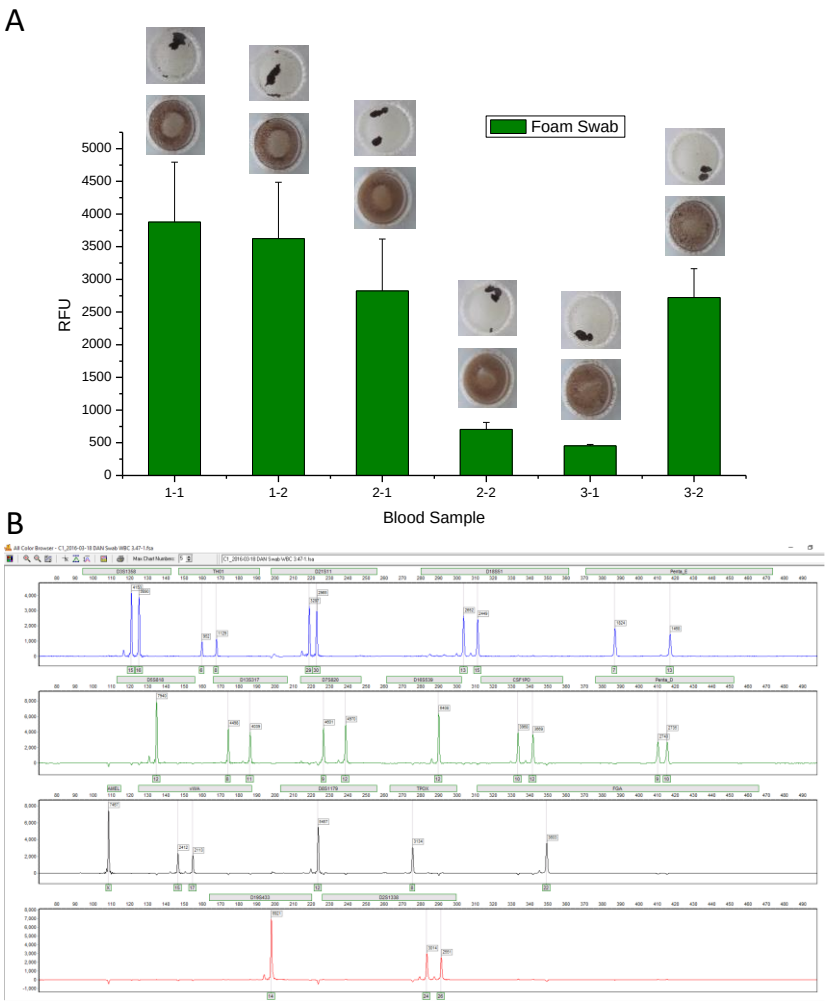

Figure 20: Analysis of samples that were dried on a plastic surface and sampled by a foam swab. A) A comparison of average peak heights for each color of a given sample. Images of beads after both aggregation and elution are shown above each bar. B) An exemplary STR profile from a dried blood spot sampled by a foam swab.

The final sample type tested was a foam swab used to collect blood that had been dried on a plastic surface. The swab was wetted and scraped across the dried sample in one fluid motion. The aggregation and elution of each sample is represented in **Figure 20A**, as well as the average peak height across all colors in an ABI profile. For most of the samples, the average signal in each color was significantly higher compared to other dried blood samples, however, multiple samples showed low STR peak heights. Low STR peak heights were observed despite seeing strong aggregation and high dispersion of the beads after the aggregation and elution steps, respectively (**Fig. 20A**). Despite the variation in average peak heights from sample to sample, all six samples gave full profiles with RFUs greater than 450. An example STR profile is shown in **Figure 20B**.

3.4 Conclusions

The goal of the work in this chapter was to develop an assay that would simplify sample preparation prior to STR PCR. This assay would eliminate the need for quantitation of DNA in a forensically-relevant sample, while providing a simplified combination of both solid- and liquid-phase extraction. The data presented shows that the assay was successful, as the amount of DNA retrieved from the aggregation of hgDNA was quantified via qPCR as ~1.0 ng/μL. This value was inside the typical DNA concentration range for STR PCR, and successful STR PCR was demonstrated from a collected sample.

In addition, the aggregation and elution was characterized for each sample type. The dried buccal swabs were unable to provide significant enough aggregation for further STR analysis and numerous variables were examined to determine the cause of poor aggregation. Ultimately, when swabs were analyzed immediately after collection, full aggregation was observed. Attempts were made to freeze the eluent in order to provide a mode of long-term storage, and preliminary results were promising, with full aggregation observed 6 days after initial elution.

Finally, attempts to aggregate and elute DNA from dried blood samples were also successful, and provided initial validation of the proposed method of sample preparation. DNA was extracted from blood samples dried on cotton fabric, denim, and foam swabs. The concentration of beads and elution volume were optimized to provide the highest signal during fragment separation. Each sample showed full aggregation of beads, and STR profiles were generated from each sample type, regardless of starting sample concentration. There remained some variation in the average peak height across different samples, and a correlation

between the difference in %DA and average peak height was not immediately apparent. Further studies are needed to improve consistency and determine the cause of variation.

3.5 References

1. Butler, J. M., Genetics and genomics of core short tandem repeat loci used in human identity testing. *Journal of Forensic Sciences* **2006**, 51, 253-265.
2. Funes-Huacca, M. E.; Opel, K.; Thompson, R.; McCord, B. R., A comparison of the effects of PCR inhibition in quantitative PCR and forensic STR analysis. *Electrophoresis* **2011**, 32, 1084-1089.
3. Reedy, C. R.; Hagan, K. A.; Strachan, B. C.; Higginson, J. J.; Bienvenue, J. M.; Greenspoon, S. A.; Ferrance, J. P.; Landers, J. P., Dual-domain microchip-based process for volume reduction solid phase extraction of nucleic acids from dilute, large volume biological samples. *Analytical Chemistry* **2010**, 82, 5669-5678.
4. Reedy, C. R.; Price, C. W.; Sniegowski, J.; Ferrance, J. P.; Begley, M.; Landers, J. P., Solid phase extraction of DNA from biological samples in a post-based, high surface area poly(methyl methacrylate) (PMMA) microdevice. *Lab on a Chip* **2011**, 11, 1603-1611.
5. Reedy, C. R.; Bienvenue, J. M.; Coletta, L.; Strachan, B. C.; Bhatri, N.; Greenspoon, S.; Landers, J. P., Volume reduction solid phase extraction of DNA from dilute, large-volume biological samples. *Forensic Science International-Genetics* **2010**, 4, 206-212.
6. Moss, D.; Harbison, S. A.; Saul, D. J., An easily automated, closed-tube forensic DNA extraction procedure using a thermostable proteinase. *International Journal of Legal Medicine* **2003**, 117, 340-349.

7. Nielsen, K.; Mogensen, H. S.; Hedman, J.; Niederstatter, H.; Parson, W.; Morling, N., Comparison of five DNA quantification methods. *Forensic Science International-Genetics* **2008**, 2, 226-230.

8. Georgiou, C. D.; Papapostolou, I., Assay for the quantification of intact/fragmented genomic DNA. *Analytical Biochemistry* **2006**, 358, 247-256.

9. Singer, V. L.; Jones, L. J.; Yue, S. T.; Haugland, R. P., Characterization of PicoGreen reagent and development of a fluorescence-based solution assay for double-stranded DNA quantitation. *Analytical Biochemistry* **1997**, 249, 228-238.

10. Heid, C. A.; Stevens, J.; Livak, K. J.; Williams, P. M., Real time quantitative PCR. *Genome Research* **1996**, 6, 986-994.

11. Hedman, J.; Ansell, R.; Nordgaard, A., A ranking index for quality assessment of forensic DNA profiles forensic DNA profiles. *BMC research notes* **2010**, 3, 290.

12. van Oorschot, R. A.; Ballantyne, K. N.; Mitchell, R. J., Forensic trace DNA: a review. *Investigative genetics* **2010**, 1, 14.

Development of Print-Cut-Laminate Devices and a Multicolor Detection System for Genetic Analysis

4.1 Introduction

Human identification in the field of forensic science is most commonly performed using DNA analysis in the form of short tandem repeats (STRs). STRs are short sequences of DNA, typically 2-6 base pairs in length, that are repeated many times in sequence at various locations within the genome. The role of these intronic repeats is not yet known, and they have been thought to be part of 'junk DNA'. The length of each of these repeats (alleles) at a given location (locus) can vary greatly between individuals, providing an effective mode for human identification. The national DNA database (Combined DNA Index System; CODIS) compares 13 different locations of repeats (loci) and the probability of two unrelated individuals having the same alleles across the 13 loci is 1×10^{-13}.[1]

Genomic sequences that contain the STRs are obtained for analysis through amplification of regions of interest in the genome, generating billions of copies of each locus through the polymerase chain reaction (PCR). Sequences containing STRs at multiple loci are amplified simultaneously, and different primers are labeled with different fluorescent dyes to facilitate analysis during separation of the alleles. STR PCR amplification is readily available through commercial kits, with each probing a varying number of loci for different applications. Currently, the most common method for separating STR fragments is multicolor capillary electrophoresis (CE). With this method, STRs are separated based on size in a capillary filled with a sieving polymer. CE provides single-base resolution in 30 minutes in a typical 30 cm separation length, and systems utilizing multiple capillaries in parallel have been developed. While multiple capillary systems are available with impressive throughput (this is the technology that sequenced the human genome), the size, speed, and cost remain as

hurdles to obtaining truly rapid, portable, and inexpensive DNA systems for human identification.

Microfluidics provides opportunities for reduced reagent cost, increased throughput, and the potential for portable, automated analysis. Separations on microfluidic devices have been demonstrated as far back as 1990[2] and strides have been made in throughput by using as many as 96 channels[3], or separating up to 4 loci in under 1 minute.[4] Progress has been made in using microfluidics to streamline the process of STR analysis through modular and integrated devices. The Landers lab and several companies have shown the development of devices and instruments that integrate multiple sample processing steps, including DNA extraction, amplification, and separation.[5] The integration of multiple steps onto a single device allows for decreased sample processing labor and time, reduced reagent and sample use, and a minimized footprint, with a goal towards portability.

As is often the case in microfluidics, the extent to which the microfluidic system can be down-sized is limited by the hardware. As more processes are integrated onto microfluidic devices, hardware such as pneumatic pumps, power supplies, vacuum pumps, etc., used for fluid flow, valving, and power, can limit the miniaturization of the overall footprint and increase the complexity of automation. One potential solution to some of these issues that has become increasingly popular in microfluidics is the use of centrifugation. Rotation allows centrifugal force to drive fluid flow without the need for pneumatic pumps, with the volumetric linear flow rate defined by the channel architecture, surface properties, distance from the center of rotation and spin speed. In addition, centrifugal systems offer the opportunity to exploit passive valving on such devices, circumventing the need for pneumatic or vacuum pumps, simplifying automation and reducing size while maintaining fluidic

control. Rotationally-driven 'lab-on-a-chip' devices from the Cho, Zengerle, Ducree, and Madou research groups, have shown the potential for integrated sample processing with limited hardware.[6-9]

In addition to reducing complexity of a microfluidic system through hardware minimization, a majority of 'lab-on-a-disc' devices are fabricated out of inexpensive polymeric materials such poly(methyl methacrylate) (PMMA), cyclic olefin copolymer (COC), and polycarbonate (PC). In addition to being cost-effective, these materials are amenable to rapid prototyping compared to traditional lithography techniques, via milling, laser ablation, and other processes. In 2003, a laser printing approach to device fabrication was presented by do Lago et al.[10] In this method, toner ink was selectively deposited on thin sheets of polyester (Pe), which were then bonded via lamination, and the areas void of toner became the microfluidic channels. This presented a rapid, inexpensive fabrication technique for microfluidic devices, however, channel dimensions were limited in depth by the number of toner layers applied (~6 μm/toner layer). The Landers group further expanded on this idea and created 3-, 5-, and 7-layer devices by laser ablating through toner-covered Pe layers to create fluidic architecture limited now by the combined number of ablated Pe layers and the layers of toner. Similar to do Lago et al., devices were bonded using lamination where the toner acted as an adhesive between layers. This method, referred to as the print-cut-laminate (PCL) method[11], is ideal for rapid prototyping and fabrication due to simplicity and minimal cost of reagents and materials, and has shown great promise for use in rotationally-driven microfluidics.

The combination of PCL, rotationally-driven microdevices (RDMs), and STR analysis shows potential for the successful development of rapid, cost-effective, portable, fully-

integrated human identification systems for point-of-contact use. In order for such a system to be impactful for point-of-contact use, a series of requirements would need to be met, dictated by local and national agencies. Cost-effectiveness and portability are key components and PCL provides a method for fabrication of RDMs with fluidic architecture that could integrate all necessary processes on to one 'lab-on-a-chip' device with inexpensive materials while minimizing the need for bulky equipment. The first DNA separations on non-PCL, Pe-toner (PeT) devices demonstrated that separation of DNA fragments was possible on PCL materials[12], however, with a reported resolution of only 56 base pairs, separation conditions would need to be dramatically improved to a minimum of 2-bp resolution in order to accurately separate all alleles in a given profile. Point-of-contact analysis also hinges on DNA extraction and PCR being completed in times closer to 30 minutes compared to >2 hours for conventional methods. Finally, hardware in the form of a detection system and motors for rotation need to be designed and optimized for optimal portability.

The goals for the work presented in this chapter are to optimize DNA separations and conditions when using PCL-RDMs for STR analysis and develop a portable multicolor detection system. Multiple materials compatible with RDMs and the PCL method were explored and improvements in fabrication of these devices were implemented. Effectiveness of centrifugal polymer loading and separation efficiency were studied on various different designs with different surface pretreatment and bubble removal protocols. A multicolor detection system was built around three dyes associated with a custom-made STR-PCR kit. Filter selection and accurate wavelength detection was confirmed using stock dyes representing the fluorophores used to label the DNA fragments. The sensitivity of the detection system was compared to the conventional capillary instrumentation using signal-to-

noise ratio as the metric. Finally, the full integration of optical alignment and clamping electrodes with centrifugal loading of polymer and reagents into a separation device was demonstrated. Data from STR separations with 2 bp resolution on the integrated system are shown.

4.2 Materials and Methods:

4.2.1 Chip Fabrication

Devices were made from a combination of cyclic olefin copolymer (COC), and toner-coated polyester (PeT), or COC and pressure-sensitive adhesive (PSA). Sheets of Pe (Film Source, Trans-NS) were coated twice on each side with toner (HP C-4127X) using a laser printer (HP Laserjet 400). CAD software was used to create the several different designs tested. A CO_2 laser system was use to ablate the PeT layer according to the CAD design. Holes were cut in the top COC layer (Zeon Chemicals, Louisville, KY) to allow for access to the created channels in the PeT layer. After laser ablation the PeT layer is placed between the two COC layers, aligned, and placed through a heated roll laminator at 200 °C (Model 305, Mega Dry film laminator). COC-PSA-COC devices were fabricated similarly with the middle PSA layer (Adhesives Research, Glen Rock, PA) also ablated using the CO_2 laser

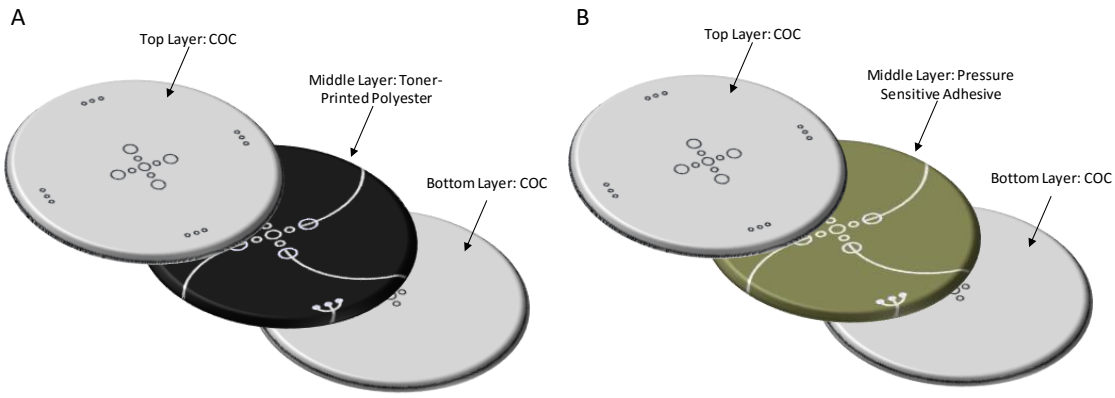

Figure 1: Schematic breakdown of the layers used to create a multi-layer microfluidic device. A) A COC-PeT-COC device B) A COC-PSA-COC device.

according to a CAD design. Heated bonding was not necessary and devices were sealed using finger pressure after alignment. Small reservoirs were 3D printed from poly(lactic acid) (PLA) and attached to the devices using 5-minute epoxy (Devcon, Danvers, MA, USA). Schematic illustrations of device layers are shown in **Figure 1**. Integrated devices were fabricated in the same manner out of Pe and PeT layers, with injection molded COC devices (ChipShop, Jena, Germany) attached to the bottom of the layers using PSA.

4.2.2 Detection Systems

For the single color electrophoresis system, a 488 nm solid-state laser was used as the excitation source. The incident beam was directed to a mirror and then up through a 525 nm short pass (SP) dichroic mirror and into the rear end of a 40X LD Acroplan, 0.6 NA objective (Zeiss, Thornwood, NY) where it was focused into the device channel. The emission beam was collected back through the objective and reflected off of the 525 nm SP dichroic mirror towards a photomultiplier tube (PMT) detector. A small pinhole (5 mm diameter) was used to filter out excess background light from the laser by only allowing the collimated emission beam to pass through to the PMT. Finally, before the PMT a 505 long pass (LP) filter was used to optically filter out any remaining 488 nm light. Data collection and electrophoresis conditions were controlled by custom-made LabVIEW programs.

The multicolor electrophoresis system utilized a 488 nm laser diode (ThorLabs) as the excitation source. The beam was collimated immediately using an aspheric lens attached to the housing of the laser diode before being reflected by a 505 nm LP dichroic mirror (Semrock) towards a front surface mirror and up into the rear of a 40X CF-N plan achromat, 0.7 NA objective (Nikon, Laboratory Optical Service, Inc., Abingdon, VA). The emission beam was collected back through the objective, off the front surface mirror and through the

505 nm LP dichroic mirror (Semrock). A 488 nm LP filter (Semrock) and a pinhole were used to filter unwanted light from the laser before the beam reached dichroic mirrors for beam splitting. The beam was split into three wavelength bands via a 580 nm LP dichroic mirror (Semrock) and a 535 nm SP dichroic mirror (Semrock). Prior to the beam reaching each detector, long pass or bandpass (BP) filters (Semrock) were used to detect specific bandwidths, and included a 568 nm LP, a 549/15 nm BP, and a 520/35 BP. After filtering, each beam was focused onto the respective PMT using plano convex lenses (ThorLabs). Data collection and electrophoresis conditions were controlled using LabVIEW programs that were build in-house.

4.2.3 Rotationally-driven Microdevice Electrophoresis System

Devices were mounted to a motor for centrifugal loading of polymer, buffer, and sample. An optical switch recorded the position of the device and allowed for automation of initial alignment of the device with the electrodes and heater. Electrodes in the form of pogo-pins were mounted to a piece poly(methyl methacrylate) (PMMA) (McMaster-Carr) while a resistive heater was mounted to a second piece of PMMA. Both pieces of PMMA were mounted to a custom built clamping motor that allowed the pieces to come together and clamp the device in place while the pogo pins made contact with the electrodes.

4.2.4 Chemicals and Reagents

Sieving polymer (hydrophobically modified poly(acrylamide), MicroLab Diagnostics, Inc.) was prepared between 4-5% (w/v) in 3X Tris-Borate-EDTA + 7M Urea (TBE, 49 mM Tris, 147 mM Borate, 1 mM EDTA; Sigma Aldrich). Ultrapure water was use to prepare all aqueous solutions. Stock solutions of fluorescein (FAM) (Sigma Aldrich), 6-carboxy-4',5'-dichloro-2'7'dimethoxyfluroescein, succinimidyl ester (JOE) (ThermoFisher),

and 5-carboxy-X-rhodamine, succinimidyl ester (ROX) (ThermoFisher), were used as reference dyes and diluted in 1X TBE.

4.2.5 Chip Preparation

COC-PeT-COC and COC-PSA-COC devices were pre-treated with 0.1 M NaOH for 10 minutes prior to loading polymer. The NaOH was removed and polymer was loaded onto the devices via centrifugation for 180 seconds at 1600 rpm. The devices were heated at 50 °C for 10 minutes and then spun for 60 seconds at 1600 rpm to remove any bubbles. Integrated devices were loaded with polymer in a series of steps. First, polymer was loaded into the main polymer chamber connected to the buffer waste outlet and spun at 1600 rpm for 25 min. Polymer was then loaded into the chamber connected to the sample waste before spinning at 2000 rpm for 2 minutes. The chamber connected to the buffer reservoir was filled with polymer and spun at 2000 rpm for 2 minutes before sample was added to the chamber connected to the sample reservoir. The sample was spun into the device at 2000 rpm for 10 seconds. Bubbles were removed from the sample reservoir by spinning at 2000 rpm for 10 seconds when necessary.

4.2.6 Sample Preparation

Samples were prepared using the heat-snap cool method in order to maintain single stranded fragments. Sample (5 μL) and size standard (5 μL) were mixed with hi-di formamide (10 μL), used as a chemical denaturant. The mixed sample was heated at 95 °C for 2 minutes and then immediately placed in ice for a minimum of 2 minutes. Sample was then loaded onto the integrated device as described above.

4.2.7 Separation Conditions

The CTC and CAC devices were placed on a heated stage (47 °C) so the laser was focused into the channel 4 cm from the cross-T intersection. Voltages were applied by a custom built high voltage power supply controlled by an in-house LabVIEW program. Platinum electrodes were placed in each of the wells and injection voltages of -100V and +100V were applied to the S and SW reservoirs, respectively, for 90 seconds. After injection, -200V was applied to the buffer reservoir, +800V was applied to the buffer waste reservoir, and both the sample and the sample electrodes were grounded. This provided a pull-back mechanism to limit plug size and sample leakage.

Integrated microdevices were aligned using an optical switch and encoded motor to place the detection point 4 cm from the cross-T design. Voltages were applied to the device using a new custom built high voltage power supply that was controlled using a microcontroller. Injection conditions were as described above, while separation conditions were as follows: B Ground, BW +1200V, S and SW +200V.

4.3 Results and Discussion:

4.3.1 Print-Cut-Laminate Prototyping

With a common goal of our group being the development of inexpensive microfluidic devices for real-world use, we reported a rapid prototyping method, Print, Cut, and Laminate (PCL) fabrication. As stated above, the original PCL method utilized polyester as both the printed toner layers and the top and bottom capping layers. These materials are inexpensive and have been shown to work for many different applications. For the application of laser-induced fluorescence, however, these materials were not feasible due to their optical properties. As shown in **Figure 2A**, Pe exhibits autofluorescent properties when the material

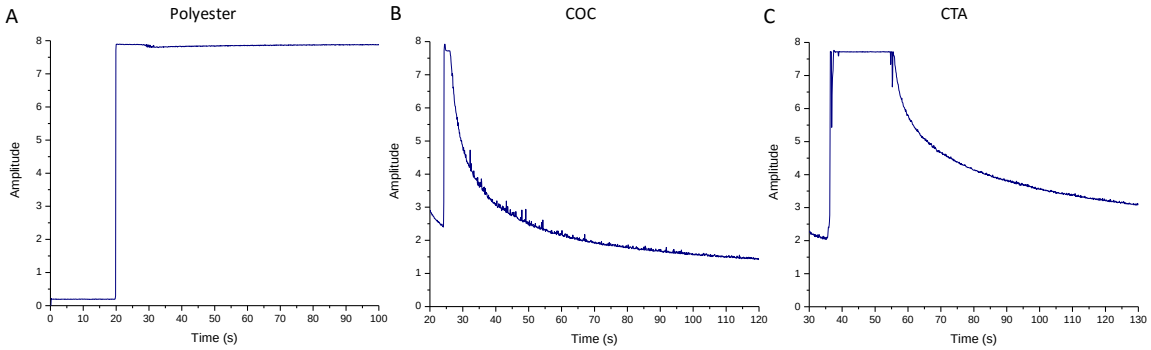

Figure 2: Autofluorescent properties of transparency materials A) Signal from a sheet of polyester B) Signal from a sheet of COC C) Signal from a sheet of CTA.

is excited by a 488 nm laser and results in a maximum output at the detector. Due to the autofluorescence, multiple materials including sheets of cyclic olefin copolymer (COC) and cellulose triacetate (CTA) were tested as suitable alternatives for Pe. When excited by a 488 nm laser, both the COC and CTA exhibited autofluorescent properties, however, photobleaching was observed and both materials saw the autofluorescent signal decrease over time (**Fig. 2B&C**). After analyzing the signal output, it was determined that the COC signal recovered the fastest and showed the lowest background signal after recovery. Therefore, COC was ultimately chosen for future device fabrication as the top and bottom layers. The decision to use COC was supported by previous reports using injection molded COC for DNA separations, citing optical clarity as one of the advantages.[13] Due to the coverage of toner on the middle layers, the middle Pe layers did not present a problem with autofluorescence and were not replaced.

4.3.2 Device Bonding

After selecting COC as an alternative, the ability to bond the COC layers to the Pe toner (PeT) layers in the PCL method was explored. Following the same procedure as Pe-layer bonding, a PeT layer was placed between two sheets of COC, and the entire device heated via a laminator at ~200 °C to melt the toner and adhere the layers together. It was

discovered that, under these conditions, toner was ineffective at bonding together the three layers of the device, and all three layers came apart under slight pressure. An indicator of poor bonding of the layers was the lack of toner transfer from the Pe layer to either COC layer, as shown in **Figure 3A**, implying the toner was not acting like an adhesive. A similar result was observed after applying a super hydrophilic coating to the COC layers in an effort to increase the hydrophilicity of the layer as a whole. Similar to COC sheets alone, there was no transfer of toner to the COC layers, and the layers were easily separated (**Fig. 3B**).

To improve the bonding of the COC layers, plasma oxidation prior to bonding was explored for both the coated and the uncoated sheets. It has previously been shown that the surface of COC can be significantly modified upon exposure to plasma oxidation, reducing the contact angle to <5° after 10 minutes of exposure.[14] The PeT and COC layers were exposed to plasma oxidation for 10 min, immediately followed by bonding at ~200 °C. The uncoated COC sheets showed a dramatic improvement in bonding, as indicated by the significant transfer of toner from the Pe layer to the COC layers (**Fig. 3C**). The devices were no longer able to separate under minimal pressure. The super hydrophilic-coated COC layers

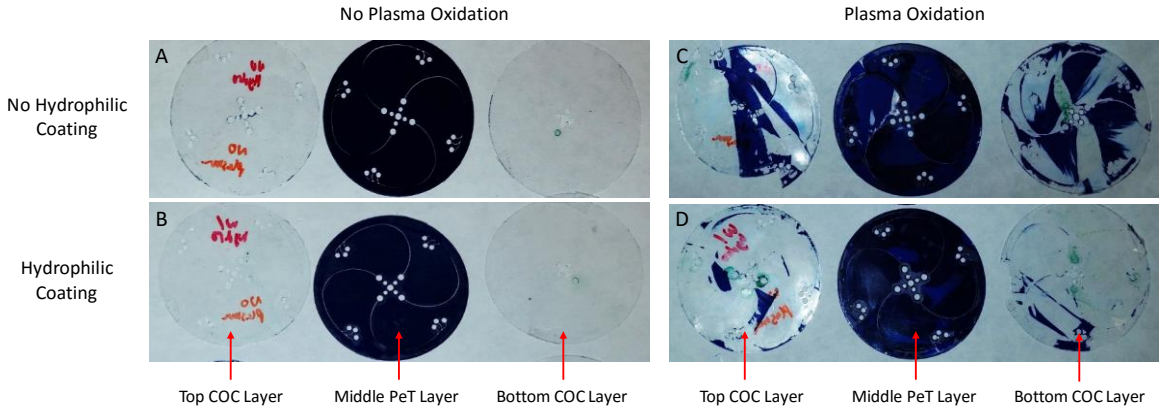

Figure 3: Impact of Plasma Oxidation on Bonding. A) No plasma oxidation, no hydrophilic coating B) No plasma oxidation, with hydrophilic coating C) Plasma oxidation for 7 minutes, no hydrophilic coating D) Plasma oxidation for 7 minutes, with hydrophilic coating.

also showed signs of improved bonding after plasma oxidation, however, the improvement was less than the uncoated layers (**Fig. 3D**).

Alternatively, the poor bonding of toner to the COC layers actually allowed for an improvement in the early stages of the PCL process. One potential drawback of using the PCL method for complex or fine architecture is the obstruction or alteration of channels and features due to melted toner. During the lamination process, the toner is heated and compressed, and this pressure can result in toner being pressed into the channels where Pe and toner had been ablated away. This can cause varying channel widths and can lead to blocked channels, rendering a device useless. After observing a lack of bonding of toner to COC layers, and the ability for the device layers to be pulled apart, it was noticed that excess toner that had been pressed into the channel architecture was able to easily be removed. Following removal of excess toner, the resulting devices showed much cleaner channels with no toner obstructions.

Another alternative method to toner bonding for these devices was also developed using pressure sensitive adhesive (PSA). Pressure-sensitive adhesives typically consist of a polyester film coated in various types of bonding agents that can be tailored for numerous applications in areas such as healthcare, electronics, and industry. In place of PeT layers, the desired microfluidic designs were laser cut into a layer of PSA before adding the two COC layers. Bonding required no heat, and layers were pressed together using finger pressure. The adhesive layer was clear but did not produce any negative effects when exposed to a 488 nm laser.

4.3.3 Centrifugal Microfluidic Architecture Design

After optimizing the bonding procedure for the newly developed COC-PeT-COC (CTC) and COC-PSA-COC (CAC) devices, various different microfluidic architectures were explored. With a goal being a rotationally-driven microdevice, the overall footprint and the impact of centrifugal loading reagents was taken into account when designing the microfluidic architecture. With a goal towards portability, attempts were made to limit the size of the microfluidic device to roughly the size of a CD (~6 cm radius), however, the need for a separation channel length of 10 cm was predicted based on previous reports of successful microfluidic DNA separations.[13] Therefore, the features with the greatest focus included separation length, channel shape, and cross-T design. Channel depth and channel width were limited by the thickness of the PeT layer and the width of the laser cutting pulse, respectively.

As a baseline test for a rotationally-driven design, a CTC device with a 4 cm standard cross-T separation channel was fabricated. A hydrophobically-modified polyacrylamide polymer (4% w/v), that had previously been used for successful separation of DNA[13, 15], was dyed blue, and loaded into a single reservoir (buffer waste) on the surface of the CTC device (Fig. 4A). After loading, the device was spun at 800 rpm for 2 minutes. After 2 minutes, the dyed polymer had filled the separation channel and was observed in the reservoir furthest from buffer waste reservoir (buffer) (**Fig. 4A**). As seen in **Fig. 4B**, the polymer did

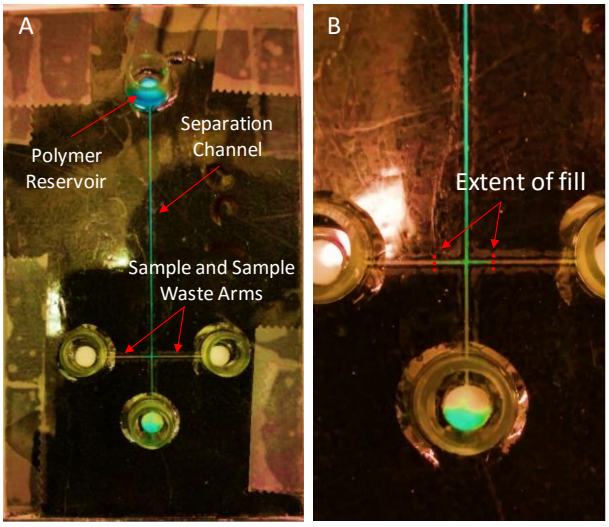

Figure 4: Centrifugal loading of polymer. A) Polymer (blue) was centrifugally loaded into a CTC device with a traditional cross-T design B) Polymer was not able to fill the side channels of the cross-T design, while filling the separation channel. Note: Saturation of images altered for improved visibility of blue polymer.

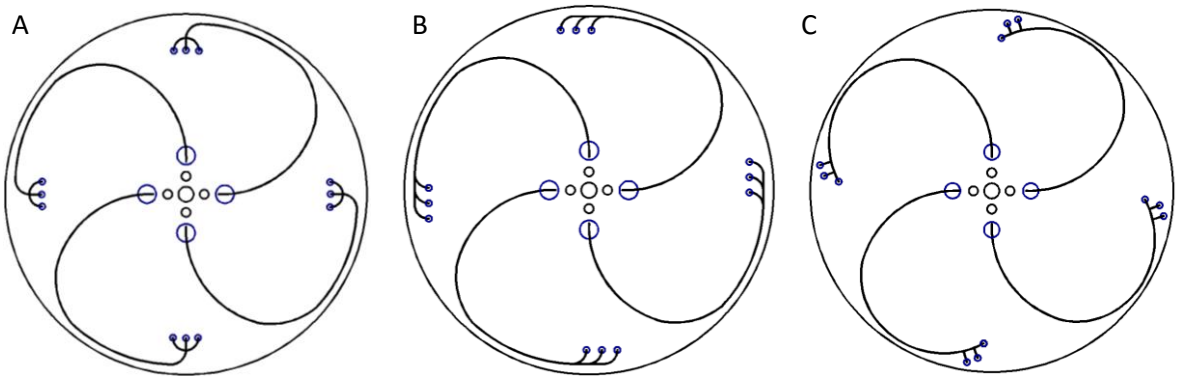

Figure 5: A series of microfluidic designs created to improve the filling of the cross-T channels A) Traditional cross-T design with a 10 cm long curved separation design B) Curved separation channel with 'comb'-like cross-T design C) A 10 cm curved separation channel with cross-T reservoirs facing away from the center of the device.

not fill the other two arms of the cross-T (sample and sample waste). This result was not unexpected, as the centrifugal force drives the polymer directly out from the center of rotation (near the buffer waste reservoir), and with the buffer reservoir at the end of the separation channel open to air, there is minimal force driving the polymer down the sample and sample waste arms.

A series of design changes were made to increase the channel length within the confines of a 12 cm-diameter device and allow for centrifugal loading of the cross-T. In order to make the separation channel as long as desired on a device with a radius of 6 cm, the separation channel was gradually curved away from the center of rotation, with the cross-T at the furthest point, similar to a design by Bedingham et al.[16] Multiple cross-T designs were explored to determine one most likely to fill with centrifugal loading and they are shown in **Figure 5**. Cross-T designs with reservoirs facing the center of rotation showed complete filling of all channels via centrifugation (**Fig. 6A&B**). Comparatively, when one or more of the cross-T channels were facing away from the center of rotation, only one of the channels filled due to a lack of resistance forcing the polymer to the remaining channels (**Fig. 6C**).

In addition to the 10-cm cross-T designs, two separate 4-6 cm separation designs were also created to test the feasibility of a shorter separation length and reduced footprint. The

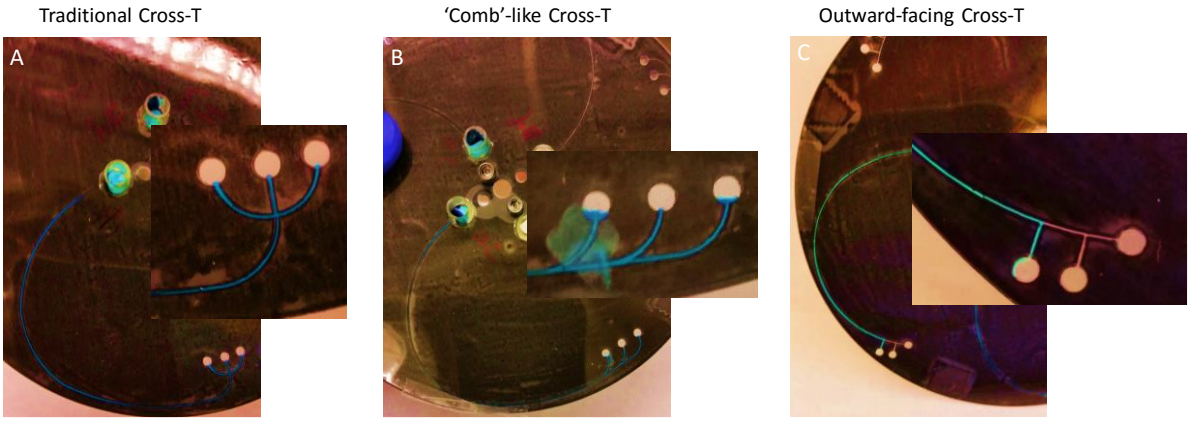

Figure 6: Effectiveness of Cross-T Filling A) Polymer (blue) effectively filled the separation channel and all cross-T channels B) 'Comb'-like cross-T design was also fully filled via centrifugal loading of polymer C) Cross-T reservoirs facing away from the center of the device were not successfully filled. Note: Saturation of images altered to improve visibility of blue polymer.

first design was a 4.3 cm straight separation channel with a unique 'anchor-like' cross-T design (**Fig. 7A**). The idea behind this design was that the radial force would drive the polymer to the base of the 'anchor' cross-T and the polymer would spread evenly through all channels of the cross-T. The second design was very similar to the 10 cm design described above, except the separation remained straight for 3.75 cm before curving 2.0 cm up into a more traditional cross-T (**Fig. 7B**).

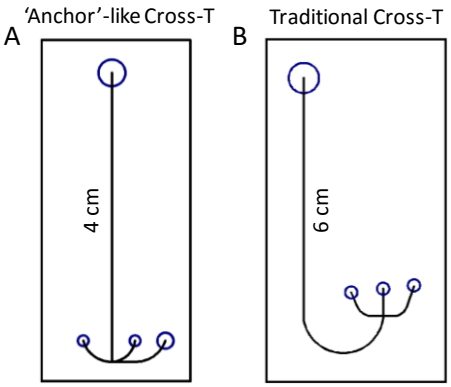

Figure 7: Reduced Footprint Designs A) Smaller 4 cm separation device with 'Anchor'-like cross-T design B) A slightly longer 4.5 cm separation device with a traditional cross-T design.

4.3.4 PCL Devices for STR Separations

With an immediate goal towards reduced footprint and rapid separations, the 4-6 cm devices were immediately tested for STR product. Preliminary PCL-STR separations were carried out on a single color laser-induced fluorescence (LIF) detection system that was built in house. A schematic of the system is shown in **Figure 8**. The single color detection in this system is of note due to the multi-color nature of STR polymerase chain reaction (PCR) which labels specific fragments with specific fluorophores. Despite the single color system, several different parameters such as sieving matrix, separation

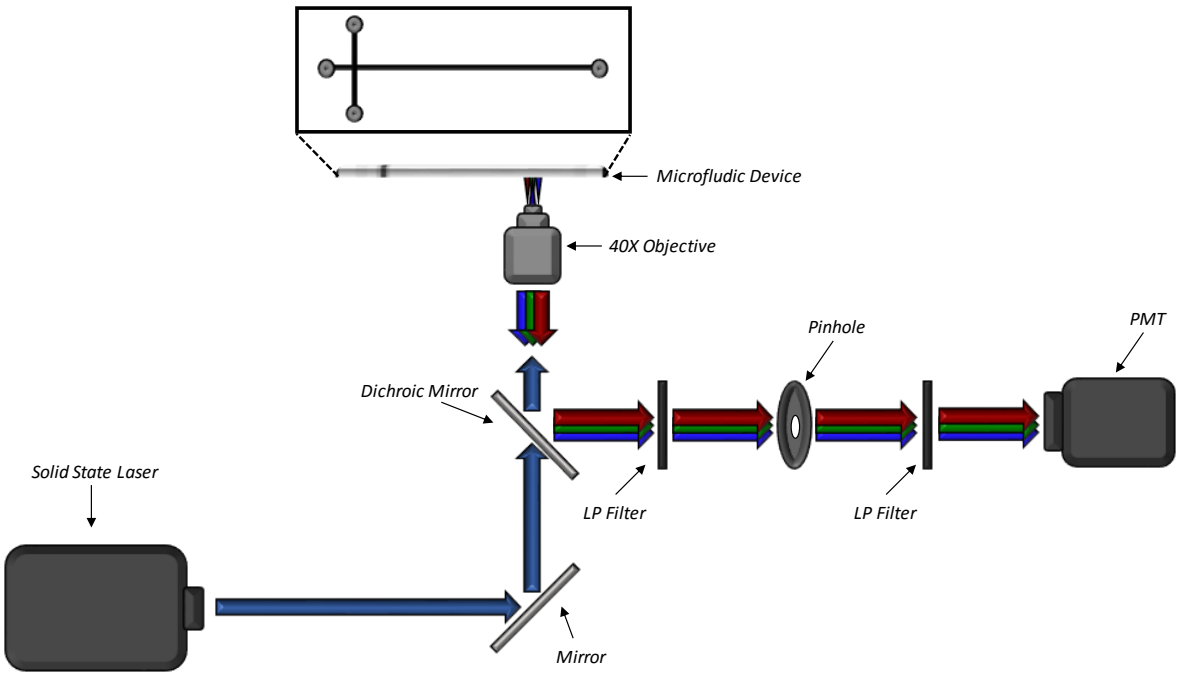

Figure 8: Single-Color Detection System. Laser is reflected up through a dichroic mirror and objective to the microfluidic channel. Emitted light is collected by the objective and then reflected off of the dichroic mirror towards the PMT detector. Background light is reduced through the use of a pinhole and a series of filters prior to the PMT.

temperature, channel coating, and injection and separation conditions could be optimized for the PCL devices.

The same hydrophobically-modified polymer described above continued to be studied as the sieving matrix while a custom made 6-plex STR kit (two color, three loci per color) was used for DNA amplification. Initial STR separations on a native 4-cm CTC device were unsuccessful at resolving each of the loci, as well as peaks within a given locus. **Figure 9** shows an example electropherogram showing the poor separation of the 12 expected peaks (2 peaks per locus, 6 loci total) with peak broadening and loss of signal. The poor separation and peak

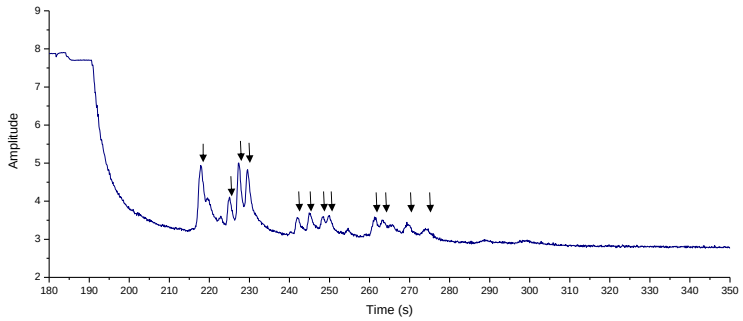

Figure 9: Example of early separations of STR product using a CTC device on the single color detection system. Several peaks are present, however, resolution is poor with signal decreasing and peaks broadening by the end of the separation.

broadening could be attributed to many different factors in the separation, including bubble formation, DNA interaction with toner walls, and joule heating.

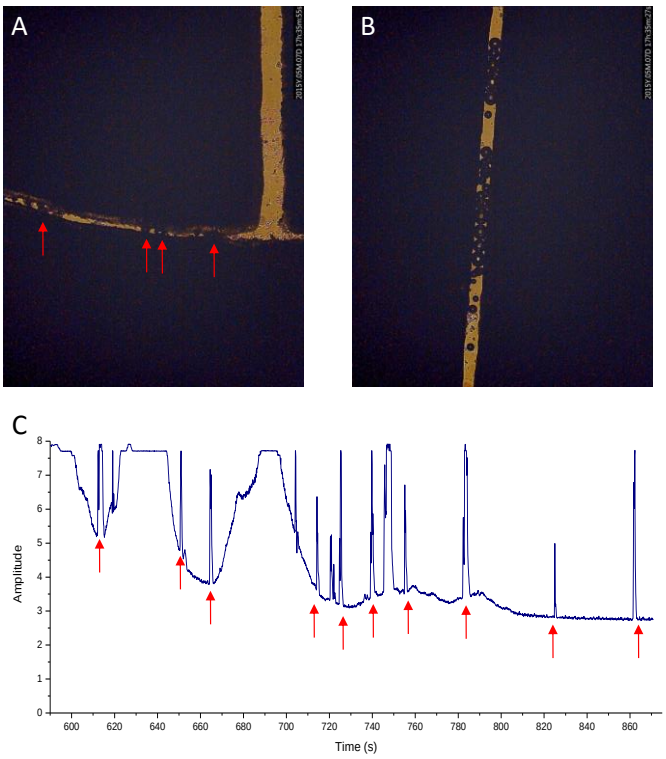

Figure 10: Impact of Bubbles on Separation A) Bubbles observed blocking an arm of the cross-T (red arrows) B) Numerous bubbles observed in the separation channel C) Large spikes in signal observed when bubbles passed the detection zone in the channel

4.3.4.1 Bubble Issues

Bubble formation likely played a major role in peak broadness by creating obstacles inside the channel and impacting the separation current. At temperatures above 40 °C, bubbles were observed obstructing the channel (**Fig. 10A**) and were often observed as large spikes in the signal when passing the laser (**Fig. 10B**). The bubble formation was likely linked to the porosity of the toner that can provide nucleation sites for air to expand as the device heats up. In order overcome this problem, a specific bubble removal protocol was established. Polymer was loaded as described above and the device was heated at 40 °C for 10 minutes where bubbles formed readily in the separation channel. Following heating, more polymer was added and the device was spun at 1600 rpm for 2 minutes. After completing this protocol, bubble formation was minimized and few bubbles were observed in the channel at temperatures as high as 60 °C. While the number of random spikes in the signal decreased dramatically by this removal procedure, there was not an immediate improvement in the resolution of the separations.

4.3.4.2 NaOH Pre-Treatment

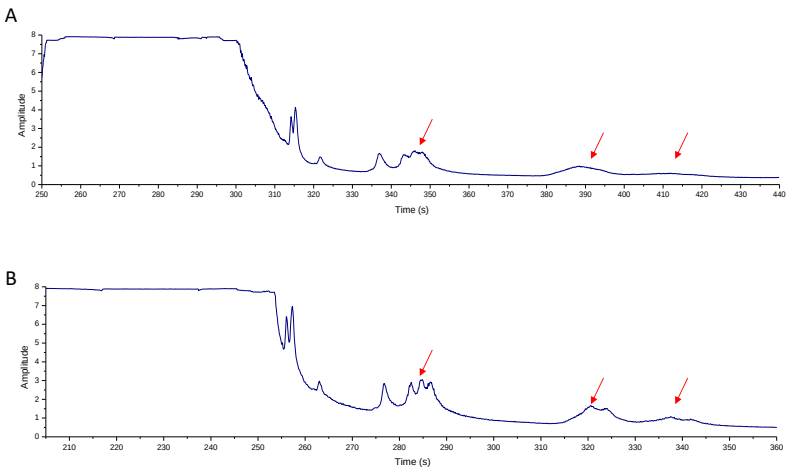

Figure 11: Effect of NaOH treatment on Separation A) Separation prior to NaOH treatment shows poor resolution across all peaks. B) Slight improvement in resolution observed when incubating device with NaOH for 10 minutes. Red arrows indicate areas of improved resolution.

Another potential cause of poor separations and resolution between peaks can be attributed to the composition of the channel walls. Duarte et al. reported limited resolution of DNA fragments for separations performed on similar materials due to interaction of the DNA with the toner that made up the walls of the channel.[12] While we cut through the Pe/toner layer in these devices to reduce the percentage of surface area that is toner, the portion of the channel walls consisting of toner might have been contributing to broadness. To try and overcome the issue of surface interaction with the toner, several different surface passivation methods were tested. First, the device was filled with 0.1 M NaOH for 10 minutes, was vacuumed out, and then refilled with 4% polymer, as previously described for COC materials.[13] **Figure 11** shows a separation on a CTC device before and after NaOH treatment, where resolution was originally very poor and saw a slight improvement after NaOH was used. The NaOH treatment occasionally showed significant improvement in peak resolution, as indicated in **Figure 12A**. Despite single color detection, almost all peaks were reasonably resolved, and when compared to the conventional capillary separation, each peak could qualitatively be identified (**Fig. 12B**). Overall, however, separations under these conditions, remained inconsistent.

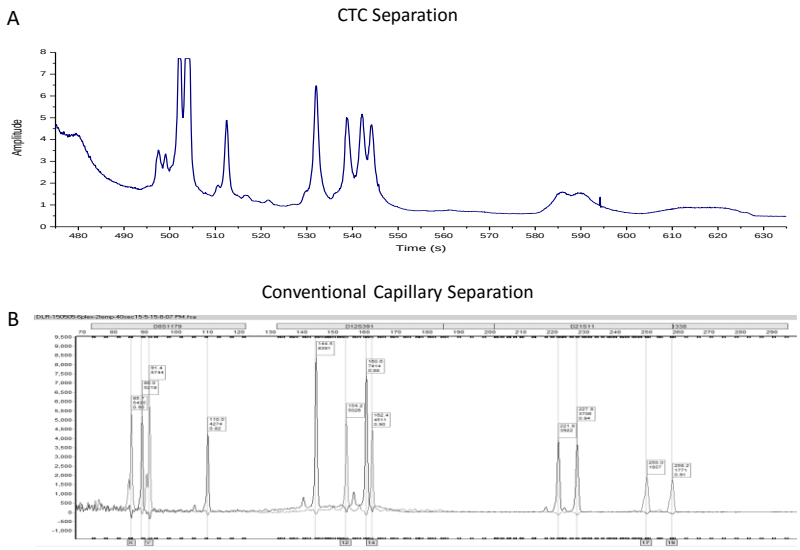

Figure 12: Significant improvement from NaOH A) NaOH treatment occasionally showed significant improvement in separation however peak broadening still observed at later loci B) Separation on conventional capillary system for peak comparison.

4.3.4.3 PEO Pre-Treatment

Another set of coating experiments involved the use of poly(ethylene oxide) (PEO). PEO has been shown to prevent adsorption of proteins on various surfaces[17], and was used here in an attempt to minimize nonspecific adsorption of DNA to the surface of our devices during the separation. Similar to NaOH, the PEO was used as a pre-coating technique prior to the addition of the polymer used for separation. A 1% solution of PEO was incubated in the device for 1 hour before being removed and replaced with the separation polymer. Separations of DNA ladder and the 6-plex PCR product on a CTC device using only PEO as a surface treatment did not yield improved results, as shown in **Figure 13 A&B**, respectively. **Figure 14** shows separations of the same DNA ladder (**A**) and 6-plex sample (**B**) after a 1-hour incubation of 1%

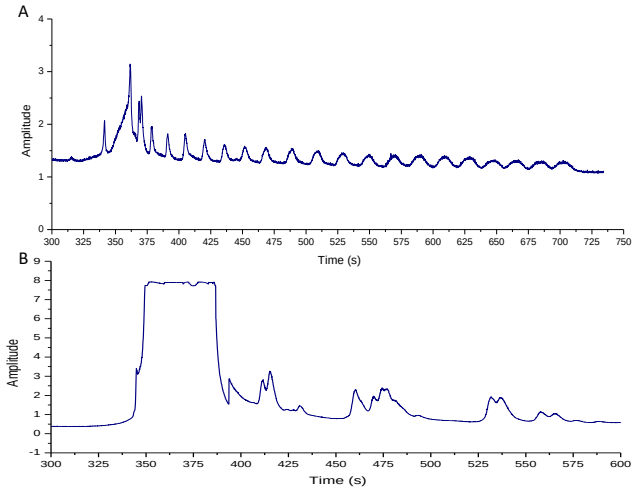

Figure 13: Impact of PEO treatment A) Separations after a 1 hr PEO treatment showed poor resolution of a DNA ladder separation with peaks gradually broadening with time. B) Resolution showed no significant improvement of a 6-plex separation compared to NaOH treatment.

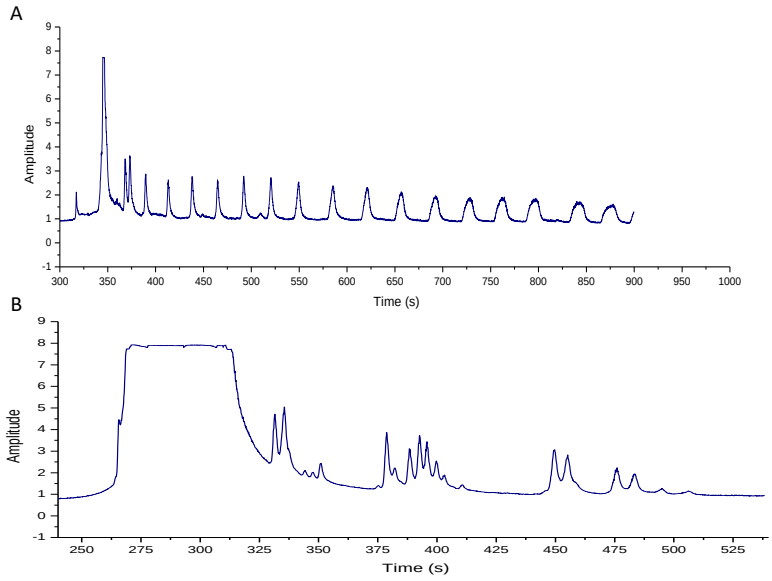

Figure 14: Combination of NaOH and PEO treatment A) Separation of a DNA ladder after 10 min NaOH and 1 hr PEO treatments showed significantly improved resolution and less peak broadening B) Significant improvement of a 6-plex separation was also observed after combined treatment.

PEO, followed by a 10-minute incubation of 0.1 M NaOH. As seen, each of the peaks in the ladder are much more resolved from one another, and each peak in the 6 plex sample is distinctly identified. While these conditions improved many of the separations, the results continued to lack consistency and still did not meet the 2-base pair requirement.

4.3.4.4 Joule Heating and Injection Plug Size

Two final explanations for the cause of poor separations included joule heating and injection plug size. Joule heating is the heat caused by passing current through a resistor, in this case the channel, and has negative effects during separations due to the temperature gradient that is created by the heating. Xuan et al. describe, quantitatively, the impact that this gradient can have on peak broadening, but in short, the gradient can cause variations in diffusion, viscosity, and conductivity, all contributing to peak broadness.[18] In capillary and microfluidic separations, one of the biggest ways to limit Joule heating is through minimizing the size of the capillary or separation channel in order to facilitate the dispersion of the heat generated by the current in the channel. Many separation instruments and devices operate at capillary diameters around 50 μm, however, in the case of our PCL devices, channel

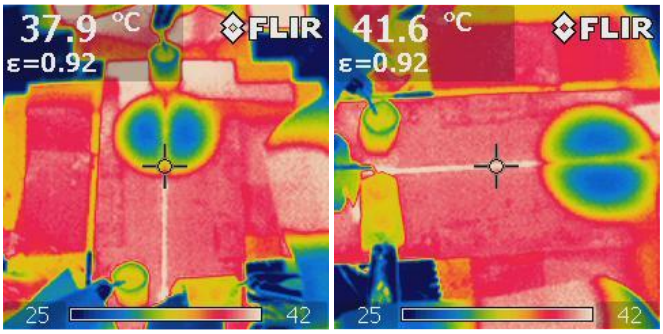

Figure 15: Infra-red imaging of Joule heating. A series of infra-red images of a 4 cm device during applied voltage. Joule heating indicated by the elevated temperature in the channel (white regions).

dimensions are limited both by the width of the laser use to ablate the channel features, and the thickness of the layer that is being cut through. In the case of the laser, the width of the beam is 100 μm and, therefore, results in channels no less than 100 μm. The PeT layer itself is 100 μm thick and each layer of toner (2 layers printed per side of Pe) is ~6 μm thick, making for a total channel depth of 124 μm. According to Xuan et al., in the case of a capillary under a given applied field strength, even an increase of just 10 μm in capillary radius (50 μm to 60 μm) can result in an increase in capillary wall temperature by 40 degrees.[18] Therefore, at dimensions of 100 μm x 124 μm, we can reasonably predict that we are experiencing significant Joule heating and may not be adequately dispersing the heat generated. Infrared (IR) imaging of our devices during separation corroborate this prediction (**Fig. 15**). The channel is shown to be at a significantly elevated temperature (white color) when current is running through the device. Finally, a brief study on the size of the injection plug showed that the CTC 'anchor-like' design may have been the cause of a very large sample plug that can lead to an undesirably large amount of sample entering the separation channel. **Figure 16A** shows the size of the sample plug generated by the CTC device compared to the sample plug generated by a traditional cross-T design (**Fig. 16B**). Large sample plugs have been shown to have a negative effect on the resolution in a given separation.[19] There is likely not sufficient time to fully separate the large plug of sample seen in **Figure 16A** in the 4 cm effective separation length of the CTC devices before reaching the detector.

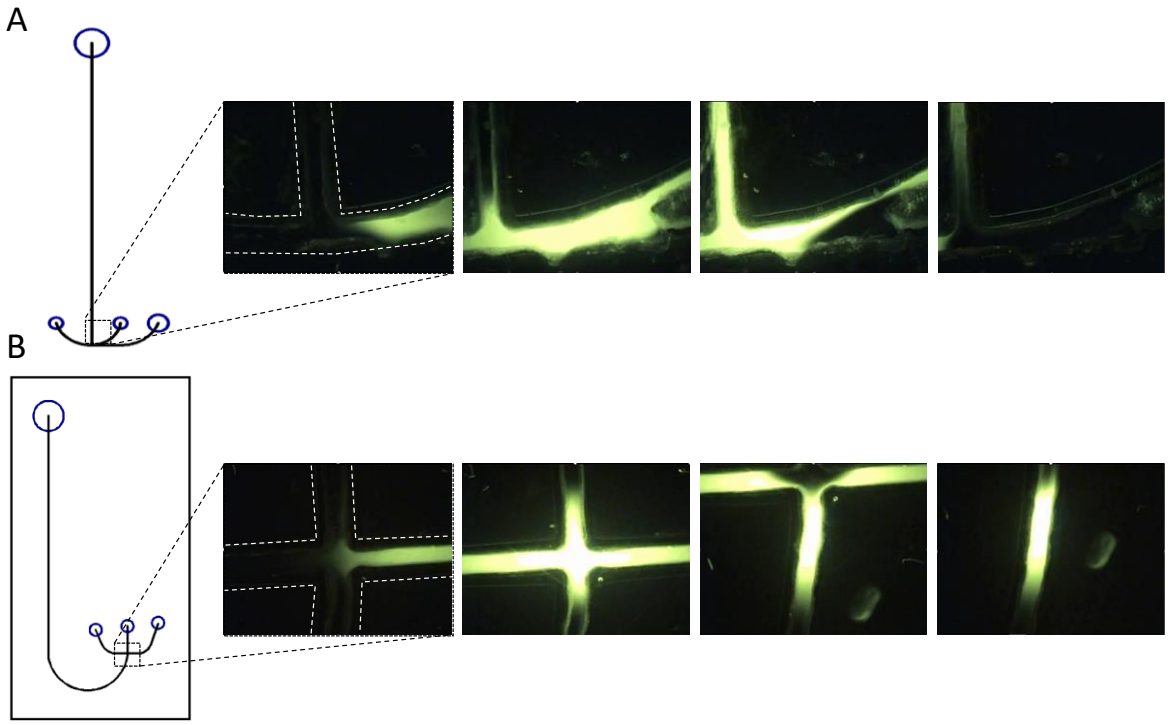

Figure 16: Sample plug size. A) A series of images showing the injection of fluorescein in the 'anchor'-like cross-T. B) Images of a fluorescein injection across the traditional cross-T on a 4 cm device.

4.3.4.5 CAC Devices

Ultimately, due to the many factors described above that have been shown to have negative effects on the separation and resolution of DNA fragments on the CTC devices, it seemed unlikely that these materials and devices would allow us to achieve 2 bp resolution. In addition to the CTC devices, many of these studies were performed on the CAC materials, however, these materials did not provide a significant improvement over CTC devices.

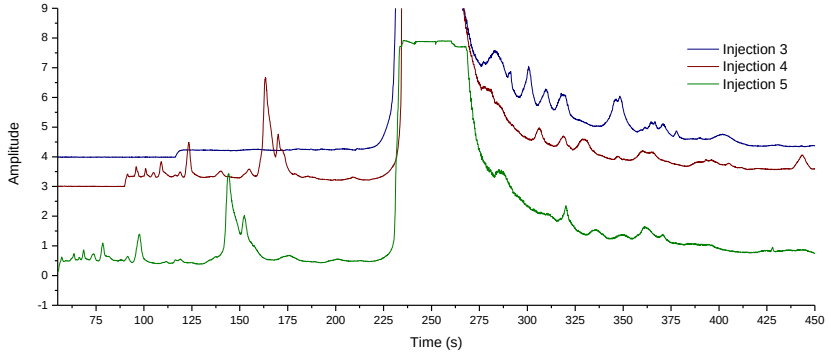

Figure 17: Three consecutive injections on a CAC device. Change to CAC materials did not provide an improvement in separation efficiency and resolution.

Figure 17 demonstrates three consecutive injections and separations of 6-plex PCR product on a CAC device, and

shows separation quality deteriorating with each injection. With each subsequent injection, the peak heights decrease and the resolution between peaks worsens. By the third injection, a series of peaks have disappeared entirely from the profile.

4.3.4.6 CTC and CAC Resolution

When analyzing the most promising data collected on both CTC and CAC materials, the maximum resolution achieved was 7.85 and 11.60 bp, respectively (**Fig. 18**). While the

A

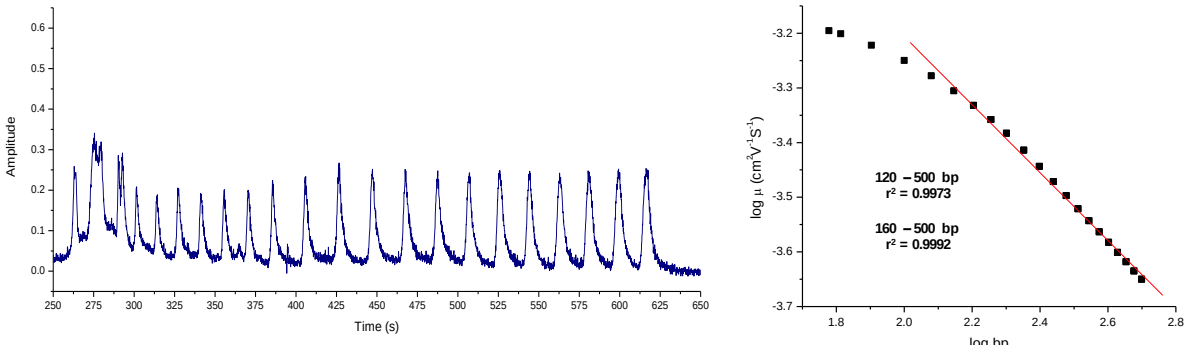

DNA Size (select bp)	Resolution (R_s)	Base Pair Resolution (R_{bp})	Separation Efficiency (N)
100	3.48	5.86	63083
200	3.60	6.68	78084
300	4.00	5.80	82648
400	2.84	8.77	88346
500	2.05	12.15	73357
Average (60-500 bp)	**3.13**	**7.85**	**79689**

B

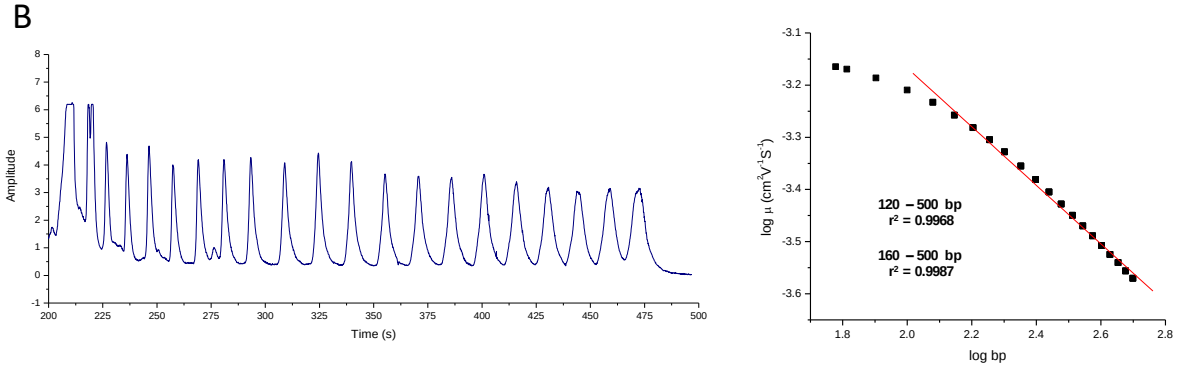

DNA Size (select bp)	Resolution (R_s)	Base Pair Resolution (R_{bp})	Separation Efficiency (N)
100	2.86	6.98	61052
200	2.95	9.01	73717
300	2.79	9.57	67569
400	1.75	15.20	42471
500	1.05	25.41	25793
Average (60-500 bp)	**2.35**	**11.6**	**55254**

Figure 18: Maximum Resolution A) Separation of DNA ladder on a CTC device with resolution calculated to be 7.85 bp B) Separation of the same DNA ladder on a CAC device and resolution calculated to be 11.60 bp.

calculated resolution for these do not meet the goal of 2 bp for forensically-relevant samples, it is noteworthy that, respectively, they represent a ~7- and ~5-fold improvement over previously reported DNA separations on similar substrates.[12] In addition, there are many applications that do not require such stringent resolution standards, such as basic PCR product and amplicon sizing, and such applications will be explored in the future.

4.3.5 COC Devices and Multicolor Detection System

In lieu of the inadequate separations and resolution achieved on the CTC and CAC devices, the use of these materials for the desired 2 bp resolution was abandoned and separations were optimized and carried out on devices made entirely out of injection-molded COC materials. The preliminary experiments and optimizations were carried out by other members in the Landers lab. Equally important in the progress towards a fully-automated, portable, forensically-relevant, rotationally-driven separation system, was the development of a multicolor detection system for full STR analysis.

4.3.5.1 First-Generation Multicolor Detection System

As mentioned above, the detection mode of choice for the development of this integrated system is laser-induced fluorescence (LIF), and the use of a single-color detection system was described in **Figure 8**. In order to fully detect and analyze STR fragments, a multicolor detection system with the capability of detecting three separate wavelengths needed to be developed. A custom made STR PCR kit was developed by Promega and contained multiple labeled primers with the fluorescent tags FAM and JOE. In addition to the primers for STR amplification, a series of size standards, typically introduced with the sample prior to separation, contain the fluorescent label ROX. The emission spectra, generated by

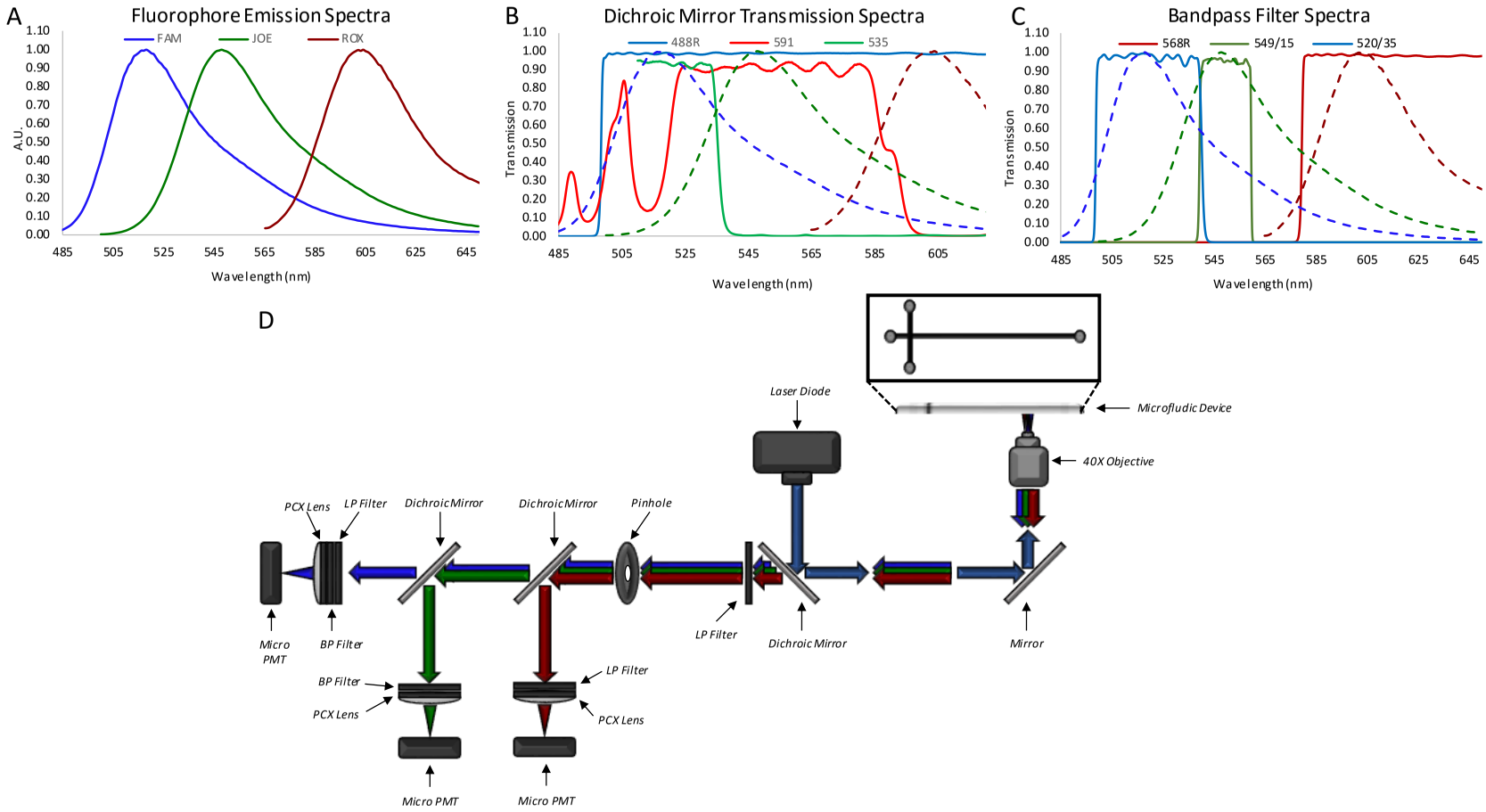

Figure 19: Multicolor filter selection A) Emission spectra for FAM, JOE, and ROX dyes used for STR PCR B) Transmission spectra for the selection of the dichroic mirrors C) Transmission spectra for the bandpass filters set before each detector D) A laser diode is reflected by a dichroic mirror and up into an objective and into the microfluidic channel. Emitted light is collected by the objective and then passes through the dichroic mirror towards the PMT detector. The beam is split into three wavelength bandwidths by two dichroic mirrors. Background light is reduced through the use of a pinhole and a series of bandpass filters prior to each PMT.

Chroma Technology Corporation and replotted, for all three of these fluorophores are presented in **Figure 19A**. A series of dichroic mirrors and filters were explored to selectively detect the specific wavelength ranges described. When deciding on the set of filters and mirrors to be used, the order in which each color will be detected was carefully considered. All three dyes can be excited at a single wavelength, in this case a 488 nm laser diode, however, the absorption wavelengths for each dye are very different. Therefore, because the ROX dye has an absorption wavelength of 575 nm, it would be expected that when excited by 488 nm, the intensity of emission would be lower compared to the absorption wavelengths of FAM (494 nm) and JOE (520 nm). Taking this into account, it was decided that, in order to minimize the chance for loss of signal, the ROX dye would be detected first, followed by JOE, and then FAM. To detect the ROX signal (602 nm emission) first, a short pass dichroic mirror was used to split the beam at 591 nm, reflecting all wavelengths above 591 nm toward the detector. The remaining wavelengths passed through the mirror and a second short pass dichroic mirror was used to split the beam again at 535 nm, reflecting all wavelengths above 535 nm. This was used to reflect the JOE signal (548 nm emission) toward the second detector. Finally, the remaining wavelengths below 535 nm passed through the second mirror and were collected by the third detector. Just before the last detector, a 488 nm long pass filter was selected to help limit the amount of background detected from the laser diode. **Figure 19B** shows the transmission spectra for each of the described mirrors, generated by Semrock Inc. and replotted, and how they compare to the wavelengths of the emission spectra for each of the dyes.

In addition to the dichroic mirrors that were used to split the emission beam, a series of bandpass and long pass filters were selected to further narrow down the wavelengths

collected at the detectors and limit detection of undesired wavelengths. For the ROX dye, a 568 nm long pass filter was selected to help limit the detection of lower wavelengths at the ROX detector, while a 549 nm bandpass filter with a bandwidth of 15 nm was selected for the JOE detector and a 520 nm bandpass filter with a bandwidth of 35 nm was selected for the FAM detector. **Figure 19C** describes the transmission spectra, generated by Semrock Inc. and replotted, for each of the filters in comparison with the emission spectra for each of the dyes. A schematic breakdown of the beam path with all of the mirrors and filters described is shown in **Figure 19D**.

4.3.5.2 Detector Comparison and Selection

At the end of each beam path was either an avalanche photodiode (APD) or a micro photomultiplier tube (μPMT) for signal detection. While APDs are known to have high quantum efficiency over a large range of wavelengths, they are limited in their ability to amplify the signal (gain) and can maintain a high dark current. Alternatively, μPMTs do not have a high quantum efficiency but can significantly amplify the signal through voltage gain while maintaining a low dark current. Given the low signal expected from STR fragments, amplification of the collected signal would play a large role, further improved by a low background current from the detector itself. A comparison of the sensitivity between both detectors is shown in **Figure 20** using spectral response curves from Hamamatsu.

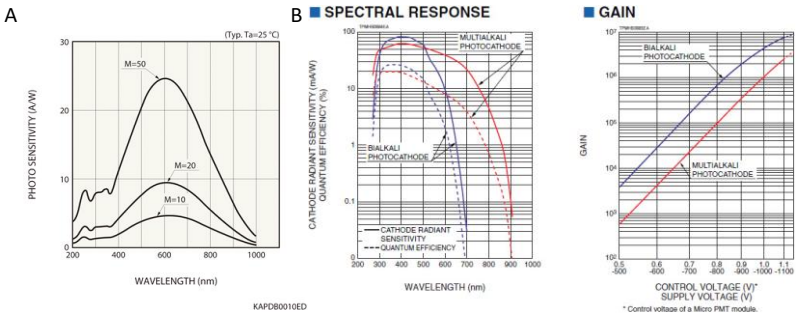

Figure 20: Detector Comparison. A) A plot of the photosensitivity of the APDs across all wavelengths. B) The spectral response and gain plots for the PMTs

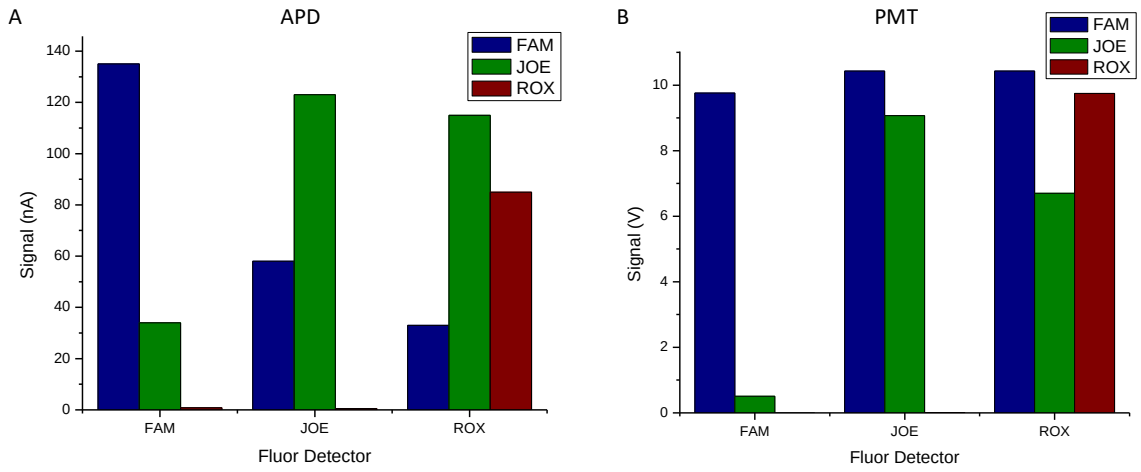

Figure 21: Wavelength Breakdown. A) A histogram describing the amount of signal detected from each dye at a given APD. B) A histogram describing the amount of signal detected from each dye at a given PMT.

In order to confirm experimentally the theoretical breakdown of emission wavelengths to all three detectors, solutions of each individual dye were placed in a microfluidic channel, and the signal from that dye was measured at each detector location. A series of APD detectors were studied first and **Figure 21A** shows the amount of signal from a given fluorophore that was detected at each of the three detectors. At the detector dedicated to collecting the FAM signal based on filtering, the highest detected signal came from FAM dye, while a small amount of JOE dye was also detected. At the JOE detector, a small amount of FAM was detected, however a majority of the signal came from JOE dye. Finally, the ROX detector measured signal from all three dyes and unexpectedly saw the highest signal from JOE dye rather than the desired ROX. In general, the detection of dyes at non-designated detectors was not unexpected due to the broad spectrum of wavelengths each of the dyes emit, and typically the overlapping signals can be deconvoluted in data processing. It was unclear, however, why the ROX detector did not match theoretical predictions. The same series of experiments were completed with three μPMTs and the results were similar, as expected (**Fig. 21B**). In one exception, however, the FAM dye was detected very strongly at all three

detectors. The reason for this came simply from use of FAM dye at a concentration that was too high for the more sensitive μPMTs compared to the APDs. Overall, the spectral breakdown at each detector closely matched theoretical predictions and confirmed the correct filter selections for the dyes of interest.

4.3.5.3 Preliminary Multicolor STR Separations

After confirming the filter set for the optics system, preliminary STR separations further corroborated the individual dye studies. **Figure 22** shows the raw data from the first multicolor separation of 6-plex STRs with size standards included. This is the first separation of its kind using a custom built, three-color detection system with a custom made 6-plex STR PCR kit. The raw data shows that the ROX-labeled DNA ladder was only observed at the ROX detector, the JOE-labeled peaks were only visible at the JOE and ROX detectors, and the signals from the FAM-labeled peaks were observed at all three detectors. Interestingly, as suggested by the dye studies, the signal from the FAM-labeled peaks was actually higher at the JOE detector than the FAM detector. Upon closer examination of the filter and mirror selections, it was noted that the dichroic mirror used to reflect the ROX wavelengths, and

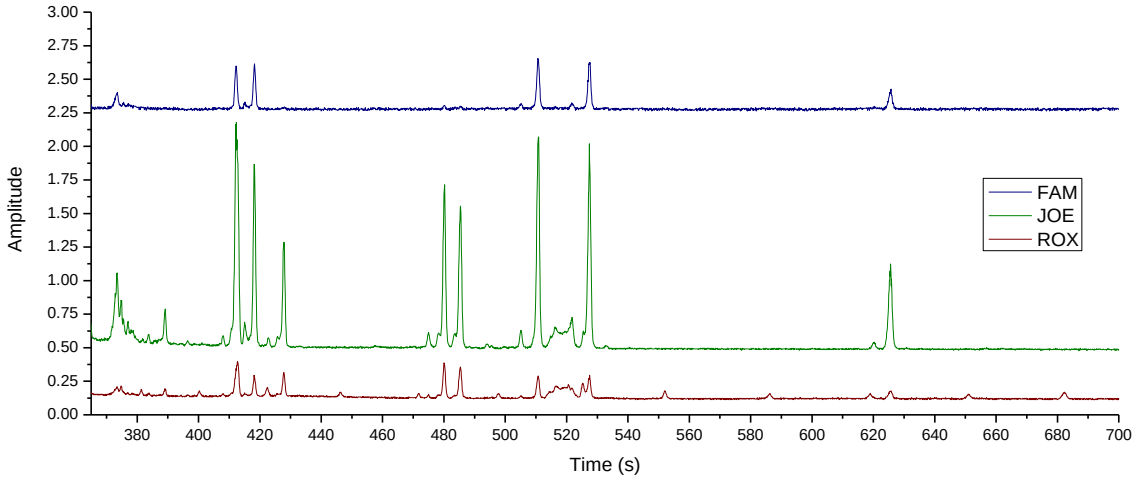

Figure 22: Preliminary separation of 6-plex product with the newly built multicolor system. Peaks in the FAM channel show strongest signal at the JOE detector.

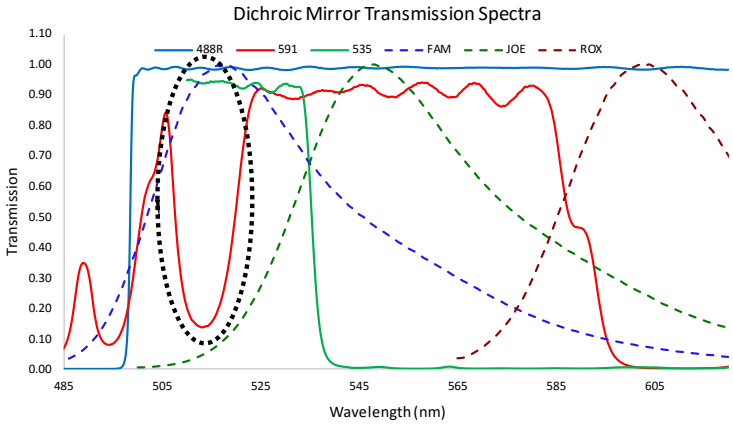

Figure 23: Analysis of dichroic mirror transmission shows significant bandwidth in the FAM channel reflected towards the ROX detector. May account for reduced FAM signal.

transmit the JOE and FAM wavelengths, actually shows a large decrease in transmission around 514 nm, near the peak emission wavelength of the FAM dye (**Fig. 23**). This would suggest that a large amount of the FAM signal is being reflected towards the ROX detector. The reason we do not see a large increase in the FAM signal at the ROX detector, however, is due to the bandpass filter directly in front of the detector. Therefore, a majority of the FAM signal is being lost and not detected at all.

4.3.5.4 Second Generation Multicolor Detection System

To overcome this issue, a new dichroic mirror needed to be selected. The availability of short pass mirrors near 590 nm, however, was limited and a different approach was required. As an alternative to short pass mirrors, a long pass mirror was selected around 580 nm that would reflect all wavelengths below 580 nm and transmit all wavelengths above 580 nm. This would reflect the FAM and JOE signals while allowing the ROX signals to pass through the mirror to the ROX detector. **Figure 24B** shows the transmission spectrum for the new mirror, while all other filters and mirrors remained the same. In order to maintain the order of signal detection with the change in mirror from short pass to long pass, a change in the building of the detection system as a whole was required. A schematic showing the new orientation of filters and mirrors is shown in **Figure 24D** and a picture of the system with the

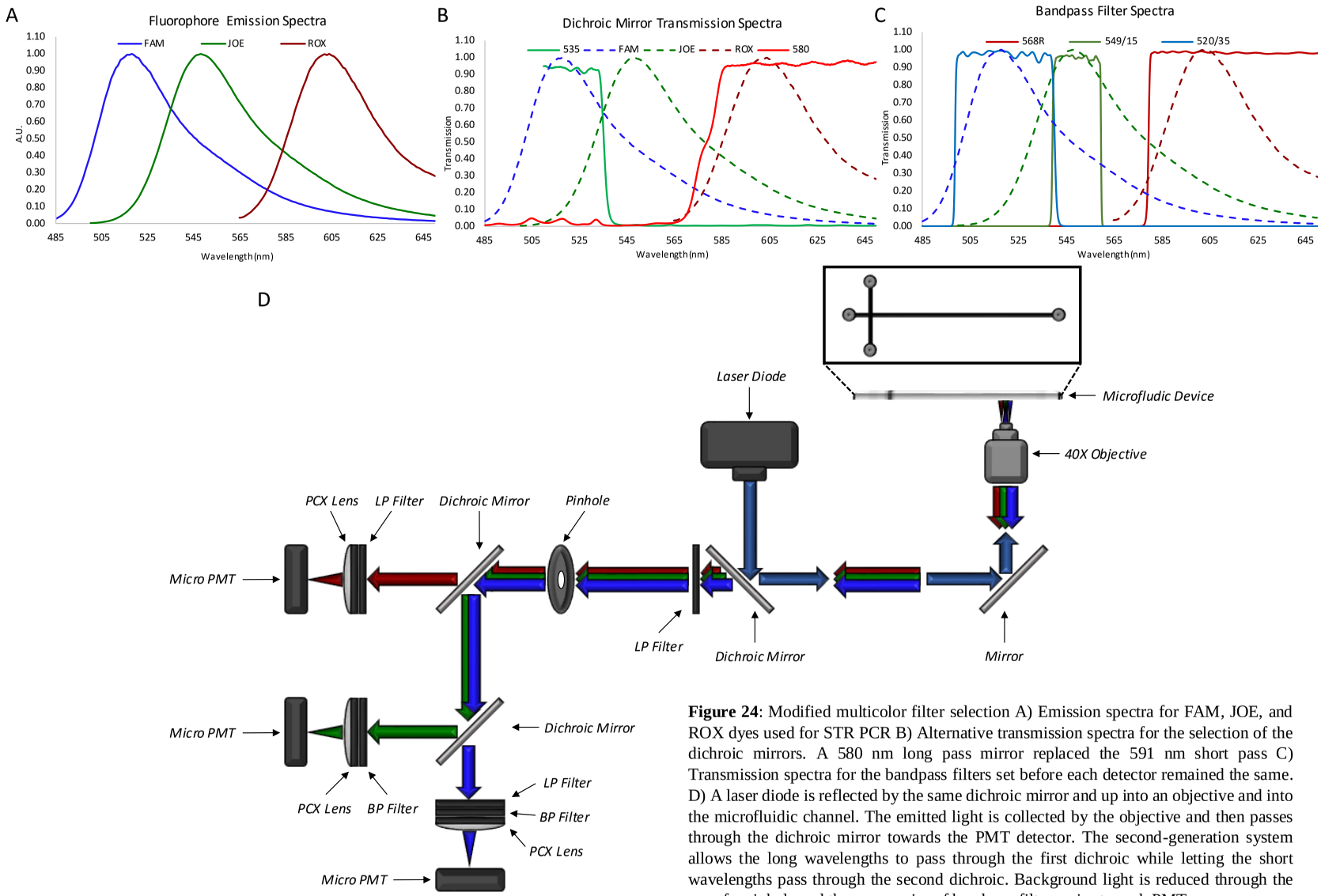

Figure 24: Modified multicolor filter selection A) Emission spectra for FAM, JOE, and ROX dyes used for STR PCR B) Alternative transmission spectra for the selection of the dichroic mirrors. A 580 nm long pass mirror replaced the 591 nm short pass C) Transmission spectra for the bandpass filters set before each detector remained the same. D) A laser diode is reflected by the same dichroic mirror and up into an objective and into the microfluidic channel. The emitted light is collected by the objective and then passes through the dichroic mirror towards the PMT detector. The second-generation system allows the long wavelengths to pass through the first dichroic while letting the short wavelengths pass through the second dichroic. Background light is reduced through the use of a pinhole and the same series of bandpass filters prior to each PMT.

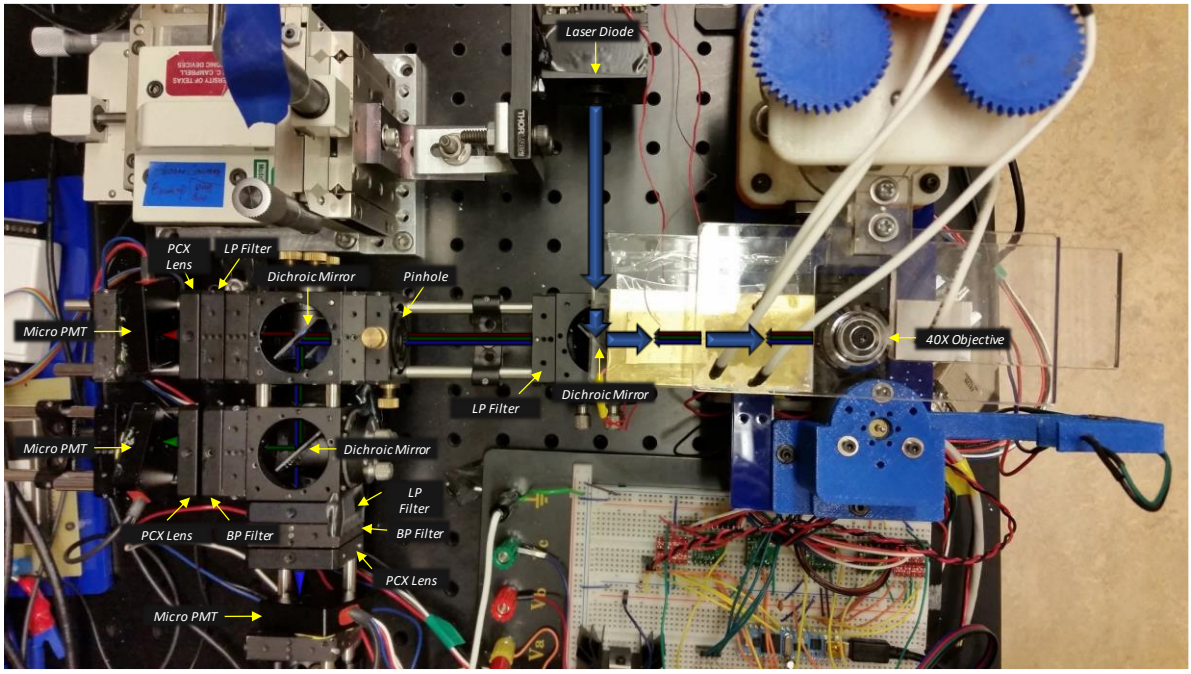

Figure 25: A picture of the second-generation system with beam paths represented.

same layout is shown in **Figure 25**. After switching the mirror and system orientation, the overall FAM signal increased, and while not significantly greater, the signal at the FAM detector became comparable to the signal at the JOE detector (**Fig. 26**). After improving the signal, the sensitivity of the system was studied and compared to the conventional capillary-based separation method.

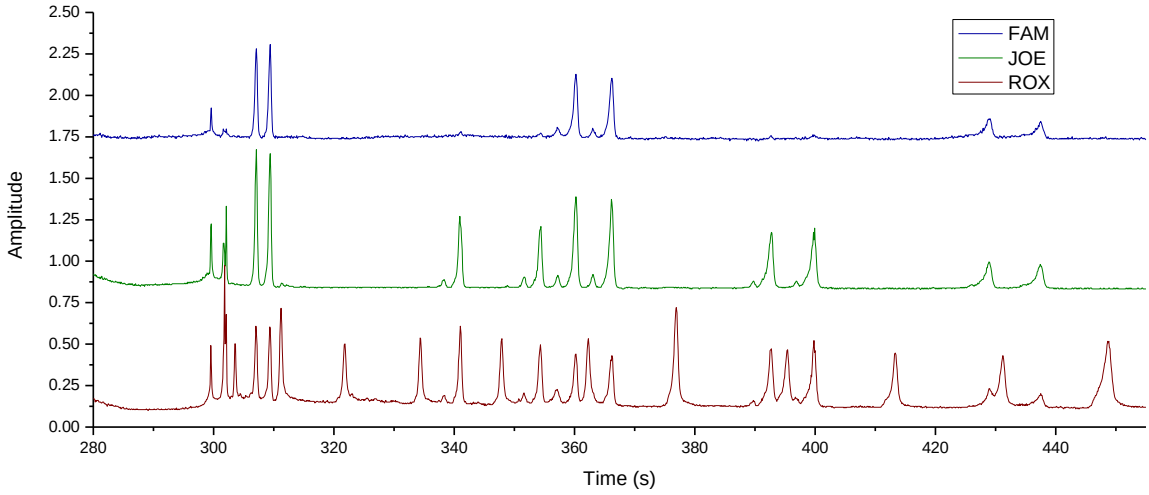

Figure 26: A 6-plex separation after mirror replacement shows FAM signal more comparable to JOE signal.

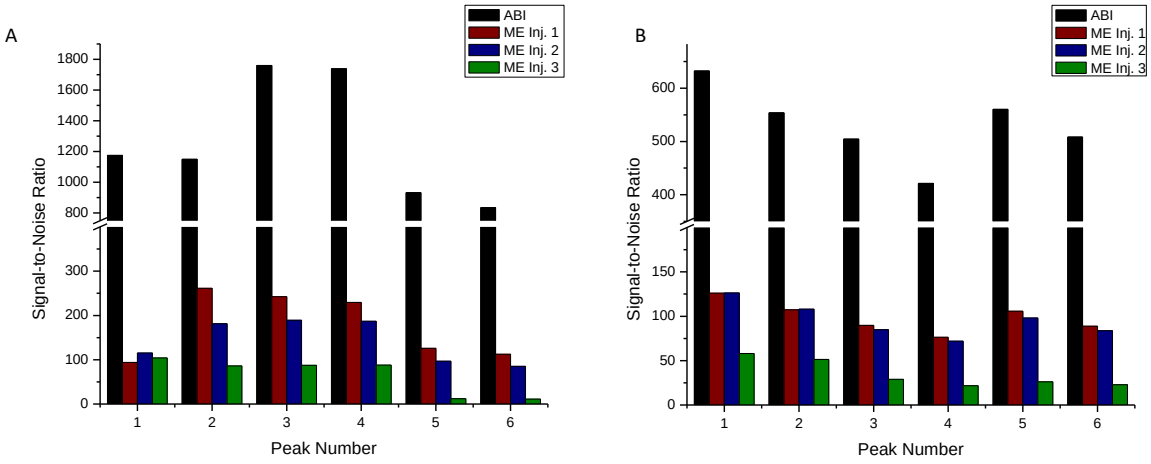

Figure 27: Signal-to-Noise Comparison A) S/N ratio comparison between the conventional ABI and the integrated ME system across the blue peaks B) S/N ratio comparison between the ABI and the ME system across the green peaks. All values were greater than 10:1 until injection 3.

4.3.5.5 Signal-to-Noise Comparisons

The signal-to-noise (S/N) ratio was used as the marker for comparison and is defined as a comparison of the level of desired signal to the level of background noise. In analytical chemistry, the limit of quantitation is typically described by a S/N of 10, and therefore was the metric used for our system. To measure and compare the S/N between conventional capillary electrophoresis and our system, a 6-plex sample was divided and run separately on both instruments. **Figure 27** shows the S/N ratios of each peak in the sample on both instruments. The conventional system shows significantly higher S/N ratios than the multicolor system, reaching as high as 1760:1 and no lower than 400:1. Comparatively, the first injection of the sample on the multicolor system showed S/N ratios between 75:1 and 250:1 across both the blue and the green channels. In addition, it was noted that as the sample is injected multiple times on the same device, the S/N ratio decreases. Despite S/N ratios between 10% and 20% of the conventional instrument (**Fig. 28**), none of the peaks in the sample approached the limit of quantitation (S/N = 10:1) until after the third injection, demonstrating the robustness of the system and the ability to complete replicate analyses.

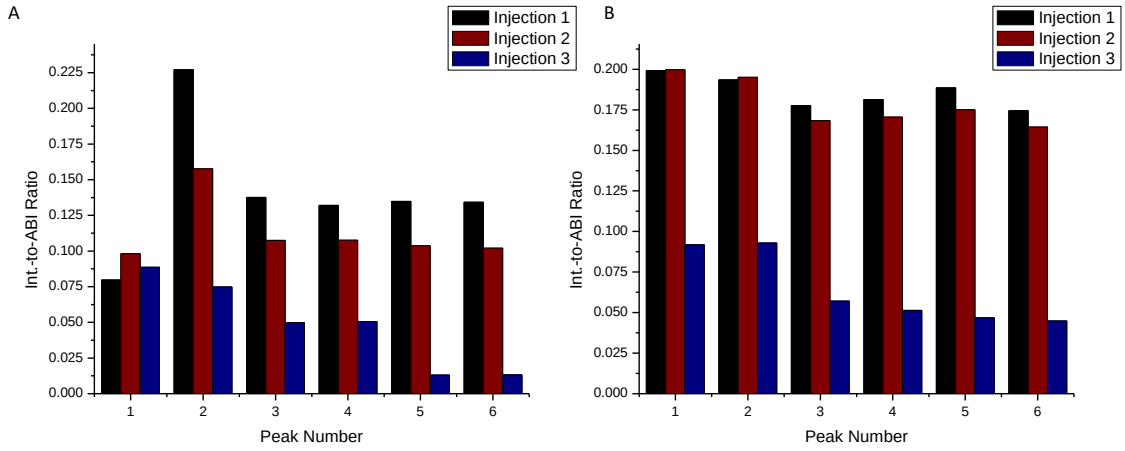

Figure 28: Ratio of Signal-to-Noise A) The ratio of S/N between the integrated ME system across the blue peaks and the conventional ABI. B) The ratio of S/N between the ME system across the green peaks and the ABI. S/N ratio of the ME system was, on average, 10-20% that of the ABI.

4.3.6 Integrated Separations

4.3.6.1 Two-base Resolution

The first fully integrated, multicolor separations, were completed after confirming sensitivity and color selections, and the building of other mechanical components in the system. As previously described, for our device to be relevant in the forensic community, our goal was to achieve 2 base-pair resolution on a fully integrated, rotationally-driven microdevice. The conditions for such a separation were optimized by other members of the

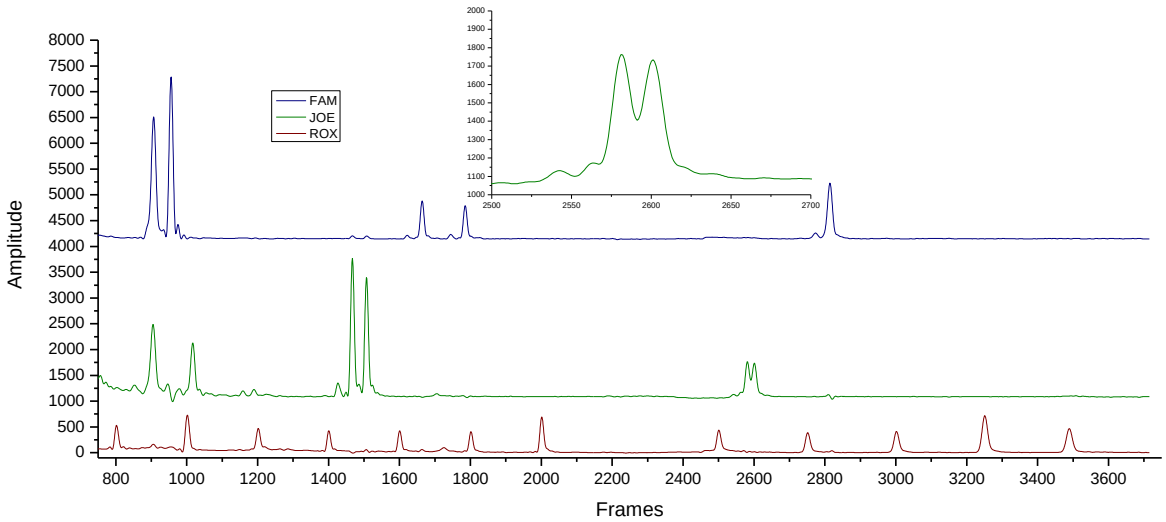

Figure 29: A separation on the fully integrated, multicolor system. Two-base pair resolution observed in the D21S11 locus (inset), with a trough/peak ratio of 0.481.

Landers laboratory on the single-color system during the building and optimization of the multicolor system described here. A 6-plex sample with a 2-bp region in the D21S11 locus was separated on an integrated device and is shown in **Figure 29**. The profile shows strong peak height from all peaks with high S/N. A simple metric that can be used to determine how well two peaks are resolved from one another is called the trough-to-peak (T/P) ratio. This value is determined by taking the lowest point in the curve between the two peaks of interest and dividing that by the average height of the two peaks. The threshold for two peaks to be described as resolved was set to be 0.700. For the separation in **Figure 29 (inset)**, the T/P was calculated to be 0.481, well below the threshold.

4.3.6.2 Impact of Gated Injection

In an effort to increase the signal of the separation, the size of the sample plug can be increased through gating. The introduction of more sample, however, can have a negative effect on the resolution between peaks, as described earlier. The impact of gating on the 2-bp resolution was tested by comparing the T/P ratio across three injections at both no gate and a two-second gate injection modes. When no gate is applied to the injection, the T/P ratio was calculated to range from 0.665 during injection 1 to 0.720 during injection 3 (**Fig. 30A**). After applying a two second gate, the first injection yielded a T/P of 0.675, while injection 3 showed a T/P of 0.799 (**Fig. 30A**). The two second gate showed only a slight loss in resolution on the first injection, while showing a slight increase in overall signal for those peaks (**Fig. 30B**), and was therefore implemented for future separations. Similar to the loss in S/N by the third injection, the T/P ratios above 0.700 for both modes on injection 3 further illustrate that the number of injections per sample is limited.

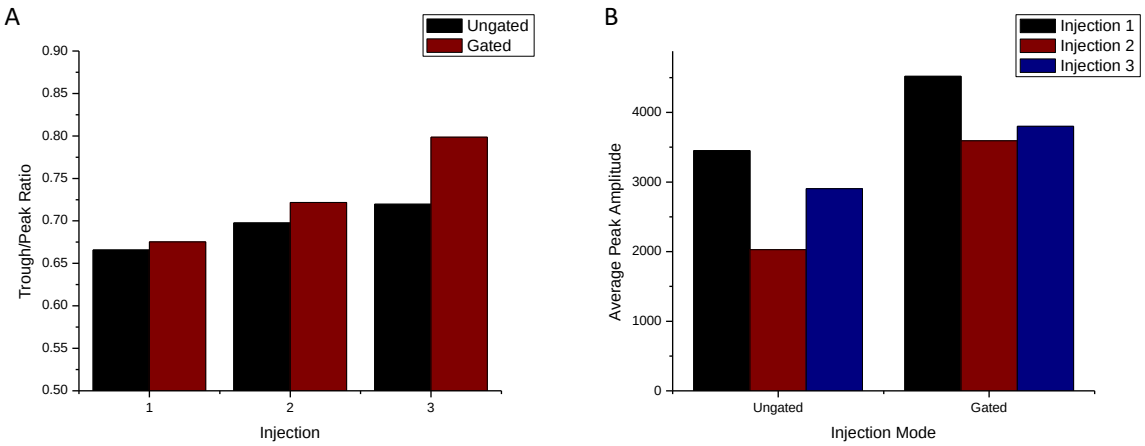

Figure 30: Gated vs. Ungated Injection: A) A histogram showing the impact of gated vs. ungated injections across three consecutive injections. Dashed line represents threshold in T/P that indicates that two peaks are resolved when below 0.7. B) The average peak amplitude across three injections for both modes of injection.

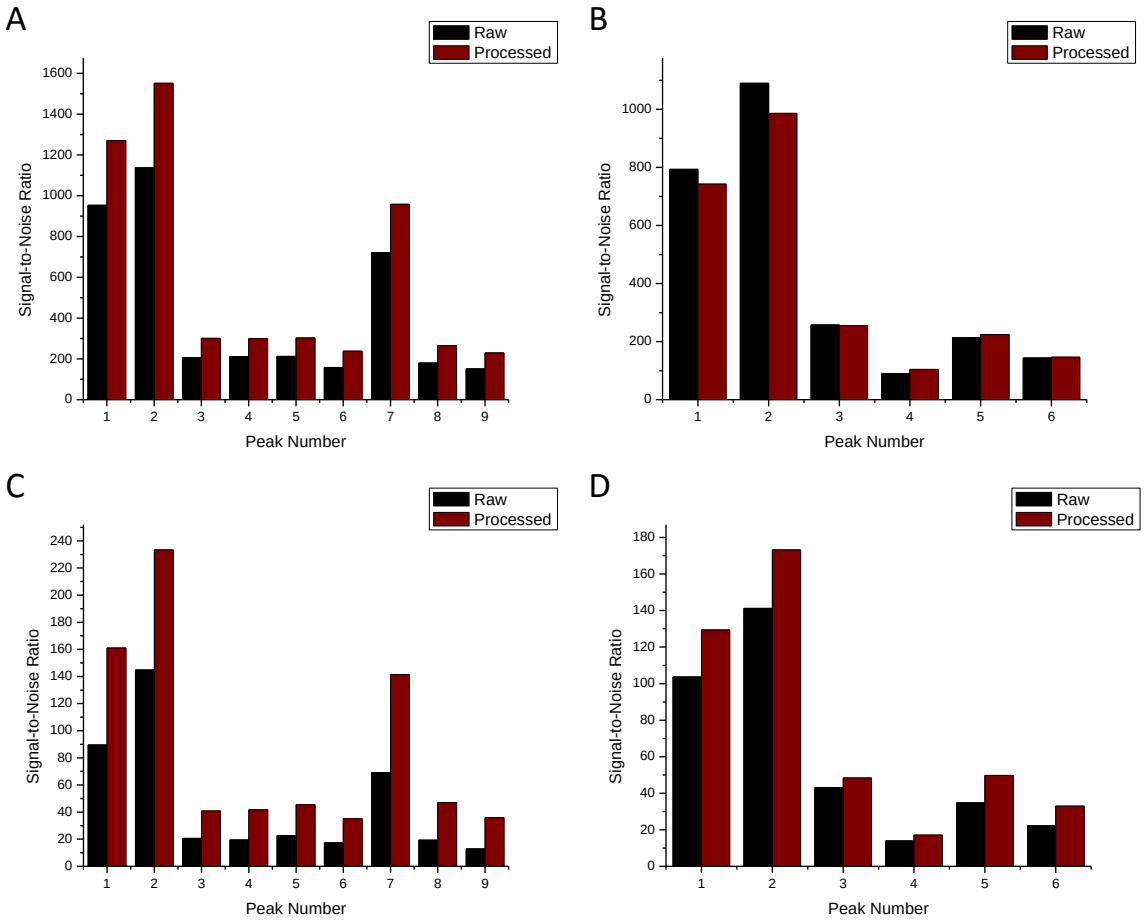

Figure 31: Signal Processing Comparison A) Signal-to-Noise ratios for each peak in the blue channel on the ABI system before and after data processing. B) Comparison of the green channel on the AB. C) Signal-to-noise ratios for the same peaks in the blue channel on the ME system before and after data processing. D) Comparison of the green peaks on the ME system.

4.3.6.3 Raw vs. Processed Data

Finally, once the parameters were optimized on the integrated devices to achieve 2-bp resolution with strong signal, proper data processing and allele calling was established. First, a comparison between raw and processed data was completed to determine the impact of baseline subtraction and deconvolution on the S/N ratios (**Fig. 31**). In most cases, the processed data provided higher S/N ratios compared to the raw data, confirming that there are no negative effects from baseline subtraction and deconvolution.

4.3.6.4 Allele Calling

Further, data processing in the form of allele calling needed to be established for this system. In order to correctly call alleles for random samples, the location of all possible alleles needed to be determined. This process is typically completed by obtaining an allelic ladder that contains all of the possible locations of the alleles for the loci of interest. A commercial allelic ladder was not available for the unique 6-plex STR kit developed for this project.

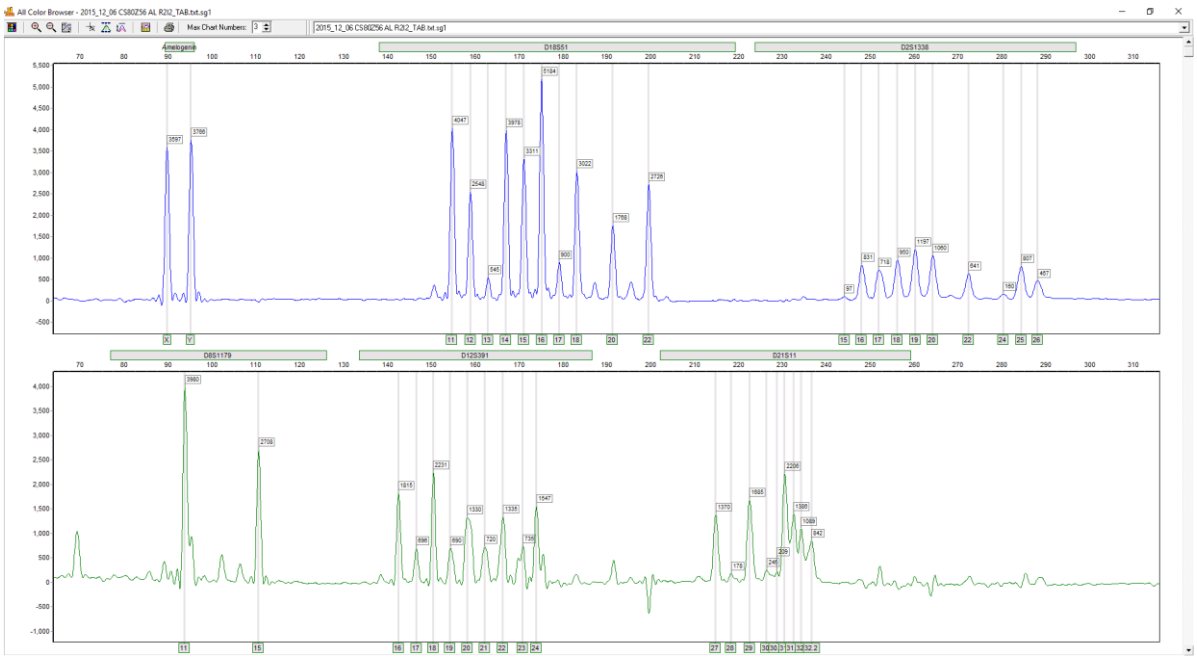

Figure 32: Custom-made Allelic Ladder. An allelic ladder created in-house was separated on the integrated multicolor system and showed required resolution. Peaks in D21S11 locus were sufficiently resolved.

Therefore, a custom made allelic ladder was created by pooling the DNA from several individual donors until as many alleles were represented as possible. Once collected, this sample was successfully separated on a 4-cm device, with the D21S11 region of specific note due to several alleles only 2-bp apart, and was used to identify the appropriate locations of all of the alleles for 6-plex STR separations (**Fig. 32**).

4.3.6.5 First-Generation Integrated System

Briefly, **Figure 33** shows a photograph the final system built as the first iteration of a fully integrated system, and used for the multicolor separations described above. Components of the system uniquely engineered and integrated but not described here include a portable high voltage power supply, a motor system, an optical switch, a unique clamping mechanism, heated stage, and pogo-pin electrodes. These components were engineered and optimized by one member of the Landers lab and a one member of Swami lab. The portable high voltage power supply was designed to achieve up to 2000V while running on four 4V rechargeable

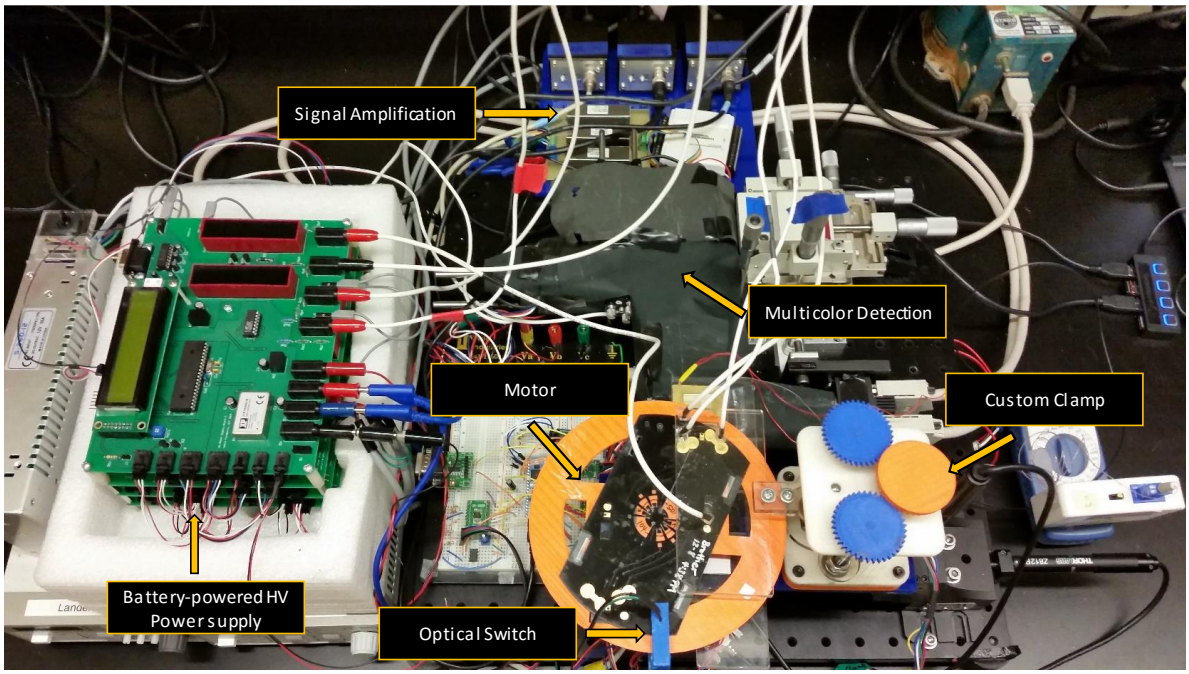

Figure 33: An image of the final integrated multicolor system that includes: portable power supply, motor and optical switch, custom clamping mechanism, multicolor detection, and signal amplification.

batteries. The motor system and optical switch were employed to spin-load the polymer and reagents into the device and then align the device with the electrodes and the laser. The clamping mechanism utilized both left- and right-hand screws to open and close two paddles. A resistive heater was attached to the bottom paddle to heat the separation device to 45 °C during separations. The high voltage power supply was attached to the device through the use of pogo-pins that were installed on the top paddle of the clamp.

4.4 Conclusions

This chapter described progress towards an inexpensive, fully-automated, rotationally-driven microdevice system for the separation and detection of STR fragments for forensic applications. A series of materials were tested for use in the PCL development process, with devices fabricated out of COC-PeT-COC and COC-PSA-COC demonstrating the greatest success. With a goal towards 2-base-pair resolution of STR fragments, conditions were optimized on these materials, with a focus on bubbles, surface coating, and joule heating. Bubbles were limited via pre-heating of the device prior to centrifugation, and surface coatings such as NaOH and PEO showed promise for improving the resolution of 6-plex STR separations. Joule heating was determined to likely be a major cause for peak broadness stemming from large channel dimensions that were limited by the width of the laser during ablation. Further, large sample plug size as a byproduct of large channel dimensions was also hypothesized to have a negative effect on the separations. Ultimately, resolutions of CTC and CAC devices were limited to ~7 and ~11 bp, respectively, and provide an opportunity for use in several other DNA separation applications.

In addition to materials testing and optimization, a multicolor separation and detection system was built and optimized for the separation of STR fragments on an integrated RDM.

Filter and mirror selection for beam splitting was based on the three colors associated with the custom 6-plex kit. Correct breakdown of signal at each of three detectors was confirmed through measurement of individual dyes and the detection system provided S/N ratios well above 10:1 for all peaks in STR separations. The effect of sample plug size and post-run data analysis showed there was little to no loss in resolution from gating the sample or data processing. A fully integrated system for rotation, clamping, and heating was built around the multicolor detection system and 2 bp resolution was achieved using an integrated RDM.

4.5 References

1. Butler, J. M., Genetics and genomics of core short tandem repeat loci used in human identity testing. *Journal of Forensic Sciences* **2006**, 51, 253-265.
2. Manz, A.; Graber, N.; Widmer, H. M., Miniaturized Total Chemical-Analysis Systems - A novel concept for chemical sensing. *Sensors and Actuators B-Chemical* **1990**, 1, 244-248.
3. Paegel, B. M.; Emrich, C. A.; Wedemayer, G. J.; Scherer, J. R.; Mathies, R. A., High throughput DNA sequencing with a microfabricated 96-lane capillary array electrophoresis bioprocessor. *Proceedings of the National Academy of Sciences of the United States of America* **2002**, 99, 574-579.
4. Schmalzing, D.; Koutny, L.; Adourian, A.; Belgrader, P.; Matsudaira, P.; Ehrlich, D., DNA typing in thirty seconds with a microfabricated device. *Proceedings of the National Academy of Sciences of the United States of America* **1997**, 94, 10273-10278.
5. Easley, C. J.; Karlinsey, J. M.; Bienvenue, J. M.; Legendre, L. A.; Roper, M. G.; Feldman, S. H.; Hughes, M. A.; Hewlett, E. L.; Merkel, T. J.; Ferrance, J. P.;

Landers, J. P., A fully integrated microfluidic genetic analysis system with sample-in-answer-out capability. *Proceedings of the National Academy of Sciences of the United States of America* **2006**, 103, 19272-19277.

6. Haeberle, S.; Brenner, T.; Zengerle, R.; Ducree, J., Centrifugal extraction of plasma from whole blood on a rotating disk. *Lab on a Chip* **2006**, 6, 776-781.
7. Gorkin, R.; Park, J.; Siegrist, J.; Amasia, M.; Lee, B. S.; Park, J. M.; Kim, J.; Kim, H.; Madou, M.; Cho, Y. K., Centrifugal microfluidics for biomedical applications. *Lab on a Chip* **2010**, 10, 1758-1773.
8. Madou, M.; Zoval, J.; Jia, G. Y.; Kido, H.; Kim, J.; Kim, N. Lab on a CD. In *Annual Review of Biomedical Engineering*; Annual Reviews: Palo Alto, 2006; Vol. 8, pp 601-628.
9. Haeberle, S.; Zengerle, R., Microfluidic platforms for lab-on-a-chip applications. *Lab on a Chip* **2007**, 7, 1094-1110.
10. do Lago, C. L.; da Silva, H. D. T.; Neves, C. A.; Brito-Neto, J. G. A.; da Silva, J. A. F., A dry process for production of microfluidic devices based on the lamination of laser-printed polyester films. *Analytical Chemistry* **2003**, 75, 3853-3858.
11. Thompson, B. L.; Ouyang, Y. W.; Duarte, G. R. M.; Carrilho, E.; Krauss, S. T.; Landers, J. P., Inexpensive, rapid prototyping of microfluidic devices using overhead transparencies and a laser print, cut and laminate fabrication method. *Nature Protocols* **2015**, 10, 875-886.
12. Duarte, G. R. M.; Coltro, W. K. T.; Borba, J. C.; Price, C. W.; Landers, J. P.; Carrilho, E., Disposable polyester-toner electrophoresis microchips for DNA analysis. *Analyst* **2012**, 137, 2692-2698.

13. Le Roux, D.; Root, B. E.; Reedy, C. R.; Hickey, J. A.; Scott, O. N.; Bienvenue, J. M.; Landers, J. P.; Chassagne, L.; de Mazancourt, P., DNA analysis using an integrated microchip for multiplex PCR amplification and electrophoresis for reference samples. *Analytical Chemistry* **2014**, 86, 8192-8199.

14. Bhattacharyya, A.; Klapperich, C. M., Mechanical and chemical analysis of plasma and ultraviolet-ozone surface treatments for thermal bonding of polymeric microfluidic devices. *Lab on a Chip* **2007**, 7, 876-882.

15. Le Roux, D.; Root, B. E.; Hickey, J. A.; Scott, O. N.; Tsuei, A.; Li, J. Y.; Saul, D. J.; Chassagne, L.; Landers, J. P.; de Mazancourt, P., An integrated sample-in-answer-out microfluidic chip for rapid human identification by STR analysis. *Lab on a Chip* **2014**, 14, 4415-4425.

16. Bedingham, W.; Rajagopal, R.; Seshadri, K. Providing an electrophoresis channel containing an electrophoresis sieving polymer, comprises rotating a sample processing device comprising electrophoresis channels and electrophoresis medium chamber about a rotation axis. US6532997-B1; JP2005514619-W, US6532997-B1 18 Mar 2003 G01N-027/00 200351 Pages: 15 English JP2005514619-W 19 May 2005 G01N-027/447 200538 Pages: 21 Japanese.

17. Claesson, P., Poly(ethylene oxide) suface-coatings - Relations between intermolecular forces, layer structure and protein repellency. *Colloids and Surfaces a-Physicochemical and Engineering Aspects* **1993**, 77, 109-118.

18. Xuan, X. C.; Li, D. Q., Joule heating effects on peak broadening in capillary zone electrophoresis. *Journal of Micromechanics and Microengineering* **2004**, 14, 1171-1180.

19. Woolley, A. T.; Mathies, R. A., Ultra-high-apeed DNA fragment separations using microfabricated capllary array electrophoresis chips. *Proceedings of the National Academy of Sciences of the United States of America* **1994**, 91, 11348-11352.

Development of a Novel Microfluidic Device for the Separation of Circulating Tumor Cells from Whole Blood via Acoustophoresis

5.1 Introduction

Research has shown that metastatic tumors, not primary tumors, are the cause of most cancer related deaths, and that early detection of tumors, both primary and metastatic, can significantly increase survival rates.[1, 2] Circulating tumor cells (CTCs) are abnormal cells, metastasized from cancers into the blood stream, and they provide an opportunity for the early detection, study, and characterization of such cancers. The isolation and detection of these cells is an area that continues to see rapid growth and increased interest in the clinical field. CTCs show the potential to be used as tumor biomarkers for early diagnosis, post-treatment monitoring, and increasing understanding of tumor biology and the spreading of tumors. Furthermore, they may provide insight into the biology of metastasis, as well as tumor resistance to current cancer therapies.[3-5] Research has been limited in these areas, however, due to the rarity of CTCs in circulation. The number of tumor cells in a given sample has been estimated to be as low as one cell per billion normal blood cells.[3, 4, 6] Due to such rarity, significant effort has been put towards developing and finding accurate, sensitive techniques that can not only identify the cells of interest but also isolate them for further study.

Current techniques for isolating CTCs from blood range from FDA-approved immunomagnetic isolation to density gradient centrifugation to microfluidic isolation by size, and can include combinations of two or more such techniques.[3, 4] Immunological methods for isolation rely on the expression of specific cell surface antigens, such as epithelial cell adhesion molecule (EpCAM), and their interaction with specific antibodies. Size-based filtration techniques utilized the fact that CTCs are typically larger than erythrocytes and

leukocytes in a blood sample[7] and use both filters and microfiltering devices with different sized pores and microstructures to capture the larger CTCs while removing the smaller erythrocytes and leukocytes.[1, 7, 8]

Techniques other than the FDA-approved immunomagnetic isolation technique have yet to find broad clinical use, as they often suffer from low sensitivity, low-throughput capabilities, low purity of captured cells, unintended lysing of cells, issues of viability post-capture, and reliance on antigens not expressed in all CTCs.[3, 4] Immunological studies have shown that not all CTCs express the desired cell surface antigens (as high as 65% do not express)[1] due to heterogeneity between CTCs, and therefore, non-expressing CTCs will not be captured via immunochemistry-based methods.[1,3] Methods with higher cell capture efficiencies can be limited by low throughput (≥1 hr/ml or multiple post-washing steps), or in the process of counting, are unable to retrieve the captured cells for further study.[4, 7]

In order to overcome issues of selectivity or poor viability that can arise from label- and antibody/antigen methods, and provide an improvement over size-based filtering methods, the technique of acoustophoresis can be utilized. [9, 10] Similar to the filtering methods described above, acoustophoresis takes advantage of the fact that CTCs are typically larger than erythrocytes and leukocytes, but uses ultrasonic waves to separate CTCs from other cells in blood.

The use of acoustic cell manipulation in a microfluidic device relies on generation of ultrasonic standing waves via the actuation of a lead-titanate-zirconate ceramic piezoelectric transducer (PZT) that results in the creation of a pressure field distribution in the microchannels. When the pressure distribution reaches a sound-reflective cavity, resonance

is reached between the incoming and reflected acoustic waves resulting in a standing wave. At the center of the standing wave is a node that indicates an area of zero pressure variation, which is where particles are directed and trapped. Regions outside of this pressure node experience alternating high and low pressure (oscillating roughly 2 million times each second), which ultimately forces cells into the relatively stable pressure node (see force equation below). Furthermore, modulating the voltage applied to the PZT affects the amplitude of the pressure in the standing wave, and this allows for additional tuning of the radial acoustic force. Generally in microfluidic acoustophoresis, and in this paper, channel dimensions are defined such that the standing wave is generated horizontally in a 375 μm wide channel (operating at 2 MHz)[11], with a nodal plane in the center of the channel that spans the entire length of the channel where the width is 375 μm.

The most important acoustic force acting on a particle in an ultrasonic standing wave is the primary radiation force[12], F_r, described by:

$$F_r = -\left(\frac{\pi p_0^2 V_p \beta_m}{2\lambda}\right) \cdot \Phi(\beta, \rho) \cdot \sin\left(\frac{4\pi \cdot x}{\lambda}\right) \quad (1)$$

V_p is the volume of the particle, p_0 is the applied pressure amplitude, β_m is the compressibility of the medium, λ is the wavelength of the acoustic standing wave, x is the distance from a pressure node, and Φ is the compressibility factor, represented by:

$$\Phi = \frac{5\rho_p - 2\rho_m}{2\rho_p + \rho_m} - \frac{\beta_p}{\beta_m} \quad (2)$$

where ρ_p and ρ_m are the density of the particle and medium respectively, and β_p and β_m correspond to their compressibilities.

In order for a particle in solution to be moved via an ultrasonic wave, F_r must exceed the force due to the viscous drag of the fluid medium. In a typical microfluidic system, the flow is dominated by viscous drag and therefore considered laminar, and for a given rigid spherical particle with radius *a*, the viscous drag can be represented by Stoke's law:

$$F_v = 6\pi\eta a v \tag{3}$$

where *v* represents the velocity of the particle, and η the viscosity of the medium. By calculating the viscous drag for a given particle, the magnitude of the primary radiation force can be estimated.

In Equation (1), when all other parameters are kept constant, the radiation force is proportional to the volume of the particle $V_{p,}$ indicating that larger particles will experience a greater F_r than smaller particles. As the radiation force each particle experiences increases by a^3, the viscous drag force only increases by *a*, and therefore, the increase in radiation force outweighs the increase in viscous drag for the larger particle and it will move to the center of the channel before the smaller particle. For particles of the same or similar size, differences in density and compressibility result in different F_r values and ultimately net force that aid in their separation from one another in an ultrasonic standing wave.

The effects of acoustic forces on the focusing of particles has been studied extensively, and Augustsson *et al.* have shown the potential for separation of cancer cells from diluted, lysed whole blood in a microfluidic channel via acoustophoresis.[10, 13] Whole blood samples were lysed, and spiked with three different prostate cancer cell lines which were separated from leukocytes in a silicon/glass microchannel using acoustophoretic forces. While separation efficiencies between 85% and 90% were achieved, Augustsson and coworkers

subjected blood samples to a lysis step prior to processing that significantly changes the properties of the sample (viscosity, density, etc.) and could potentially lyse CTCs along with the erythrocytes.[13] Furthermore, the silicon-based devices are expensive to fabricate relative to glass devices. Therefore, the development of a microfluidic device in glass that has the capability to efficiently separate and isolate CTCs from a non-lysed whole blood sample using acoustophoresis would be a significant development of this technology.

The goal of the work in this chapter is to develop a microfluidic device that allows for the separation and isolation of CTCs from an unlysed whole blood sample using acoustophoresis. This device would provide an initial purification step for cells of interest and allow for further study, including culturing, counting, and interrogating collected CTCs. The design and theoretical modeling of various microfluidic designs, the study of fluid flow in the design, and the removal of RBCs via the device is presented. In addition, acoustic focusing was optimized using 20 μm fluorescently-labeled polystyrene beads in both buffer and 1:1 diluted whole blood as a CTC mimic. Further, prostate adenocarcinoma (PC3) cells were used to better represent the cells of interest that would be found in patient samples, and flow cytometry was used to count the collected cells and determine capture efficiency and purity.

5.2 Materials and Methods

5.2.1 Microdevice Fabrication

Microfluidic channel designs were created in COMSOL Multiphysics (Version 4.0, COMSOL Inc., Burlington, MA) and were converted to AutoCAD LT 2004 (AutoDesk Inc., San Rafael, CA) files for photomask creation and laser ablation. Photomasks were ordered

for glass etching from Fine Line Imagaing (Colorado Springs, CO) while laser ablation fabrication was completed for poly(methyl methacrylate) (PMMA) devices on an in-house commercial CO_2 laser (VersaLASER, Universal Laser Systems Inc., AZ). PMMA devices were fabricated by laser ablation on a 1.5 mm thick sheet of PMMA (McMaster-Carr, Atlanta, GA) to a depth of 400 μm and reservoir holes were cut through a second piece of the same thickness. The two pieces were thermally bonded at 170 °C as previously described.[14] Glass devices were fabricated in borosilicate glass (Schott Inc., Louisville, KY) using conventional photolithography and chemical etching followed by drilling and thermal bonding.[15]

5.2.2 Instrumentation

A sinusoidal wave was generated by an Agilent 33220A Arbitrary waveform generator with a maximum amplitude of 10.0 V at 2.329 MHz and the signal was amplified 5-fold via an amplifier. After being amplified, the signal was split and used to actuate a piezoelectric transducer (PZT) (Ferroperm, Denmark) as well as provide an input to a Tenma 72-3060 oscilloscope to monitor the actuation signal in real time. Experimental videos were captured with a Hitachi CCD color camera (Hitachi Ltd, Tokyo, Japan) on an Olympus IMT-2 fluorescent microscope. Sample and buffer were infused and withdrawn using either four Aladdin-1000 (World Precision Instruments, Sarasota, FL) or neMESYS (CETONI GmbH, Germany) syringe pumps with 1 mL (sample) and 5 mL (buffer, waste collection) glass syringes (Hamilton Co., Reno, NV) that were networked and controlled using Syringe Pump Pro software (version 1.51, TBITC Pty Ltd). Flow cytometry analysis was completed using a Gallios

5.2.3 Reagents

Prostate adenocarcinoma cell lines were purchased from ATCC (Manassas, VA) and cultured at 5.0% CO_2 and 37 °C, in media composed of RMPI without phenol red plus 10% FBS/% PenStrep/1% L-glutamine/1% HEPES/1% sodium pyruvate (Gibco, Thermo Fisher). Blood samples were de-identified and supplied by the UVA Medical Laboratory. All samples were analyzed within 24 hours of collection.

5.3 Results and Discussion

5.3.1 2D modeling for design and flow determination

Microfluidic device designs were optimized to achieve desired flow effects by computer modeling in the COMSOL Multiphysics® software suite. Finite element modeling in COMSOL was used for basic fluid dynamics modeling of microdevice designs that could be adapted experimentally. Adapting from a previously created microfluidic design[13], a device with a trifurcated sample inlet, a long straight separation channel, various sets of angled waste channels, and finally a trifurcated outlet, was developed (**Fig. 1**). COMSOL was used to determine the optimal number of angled waste channels, as well as channel dimensions and flow rates, which should allow effective removal of the majority of

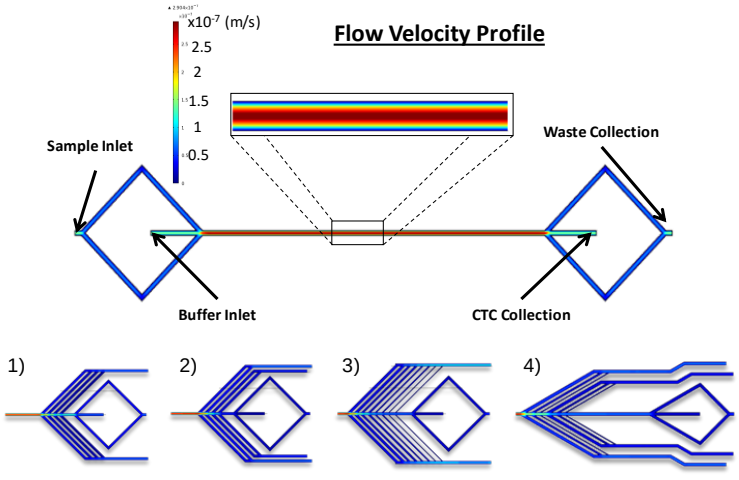

Figure 1: COMSOL Multiphysics® Modeling. A) Basic acousto-filtering design, as previously described[12], generated in COMSOL. Color gradient indicates magnitude of flow velocity in channel. B) Angled waste channel array designs. A small sample size of conceptual designs generated via COMSOL. Each design looks to maximize the filtering capacity of the chip while maintaining high flow velocities in the proper directions (1-4).

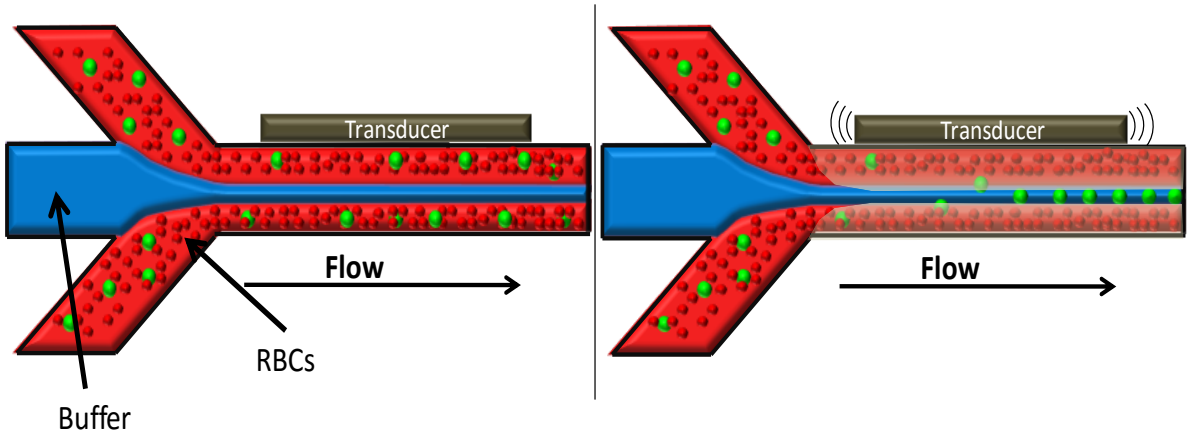

Figure 2: Schematic illustrating the preliminary acoustophoresis of beads in whole blood when the transducer is off (A) and then actuated (B).

sample while allowing for the collection of the desired product. In this case, devices were designed for the removal of RBCs and WBCs down angled waste channels while collecting CTCs at the central outlet of the separation channel.

The trifurcation at the inlet allows for the splitting of sample flow in the separation channel by flowing from either side of the trifurcation while clean buffer flows down the center. Due to laminar flow in the microfluidic channel, this creates three layers of fluid consisting of two sample layers along the walls of the channels, and a clean buffer layer in the middle. This is advantageous for acoustophoresis to allow for the movement of CTCs from the sample layers into the clean buffer layer where they can be collected (**Fig. 2**)

Prior to using acoustophoresis, the microfluidics of the design needed to be established and optimized in order to create a device that had the ability to efficiently process unlysed whole blood. Individual 2D models, each representing different sets of parameters (flow rates, channel dimensions, number of angled waste channels), illustrated the effect that each parameter had on several different operational parameters such as the velocity of the fluid flow and the direction of flow at any given point in the design (**Fig. 3**). Interpretation of these results led to an optimized design shown in **Figure 4**. Key features of the design include the

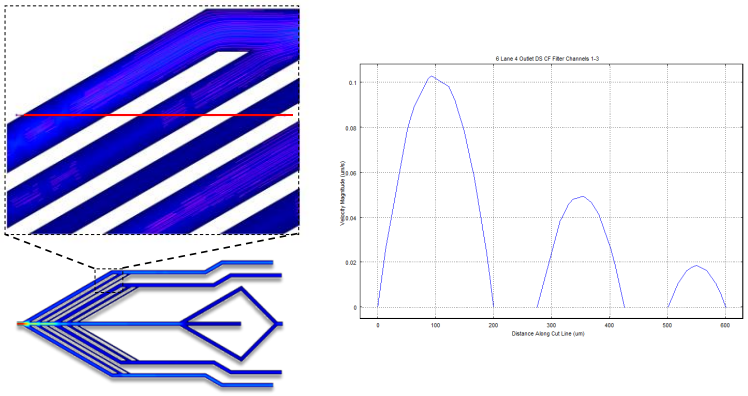

Figure 3: Quantitative information can be gathered from a cut line taken across any area of the design. A 1-D plot of the Magnitude of Flow Velocity vs. Distance Along Cut Line is generated. Information can also be gathered regarded flow patterns and stream lines as well as flow direction and many other parameters.

angled waste channels, the increase in the waste collection channel width after the addition of each angled waste channel, the differences in channel width at the product trifurcation, and the length of the chip as a whole. The angled waste channels allow for the removal of as many undesirable particles as possible before reaching the collection channel. The stark contrast in the dimensions of the product trifurcation is necessary for the resistance to be equal down all three channels. This is due to the fact that the outlets are open to atmospheric pressure while the waste collection channels are pulled by a syringe to improve the efficiency of removing all unfocused particles.

Figure 4 also illustrates the effect of flow rates on the direction of flow in the design and it was determined that the chosen flow rates and the output to input ratios are vital to the success of the design. **Figure 4A** is shown with input flow rates of 15 µl/min and 25 µl/min for the sample and buffer inlets respectively, and output withdrawal flow rates of 15 µl/min at each waste outlet, a ratio of output to input flow rates of 75%. It can be seen that fluid flows through each channel in the direction expected, indicated by the color scale. In comparison, when the ratio of output to input flow rates is reduced to 50% (**Figure 4B**), the direction of the flow in the second set of waste channels is reversed, indicating fluid returning to the separation channel. At ratios much greater than 75%, the flow velocity in the main channel is seen decreasing, indicating that too much fluid is being drawn down the waste channels,

resulting in the possibility of pulling desired product from the center channel. Ultimately, it was determined that a design with two sets of angled waste channels, shown in Figure 1, and an output to input flow rate ratio around 75%, would provide the best design for chip fabrication and experimentation.

5.3.2 Flow Studies with Dye and Blood

PMMA devices were used to validate the device design and parameters seen in COMSOL modeling before fabricating them in glass used for acoustic compatibility. Even though the acoustic properties of PMMA are unsuitable for acoustophoresis, devices were fabricated in this material instead of glass due to the length of the glass etching process, as

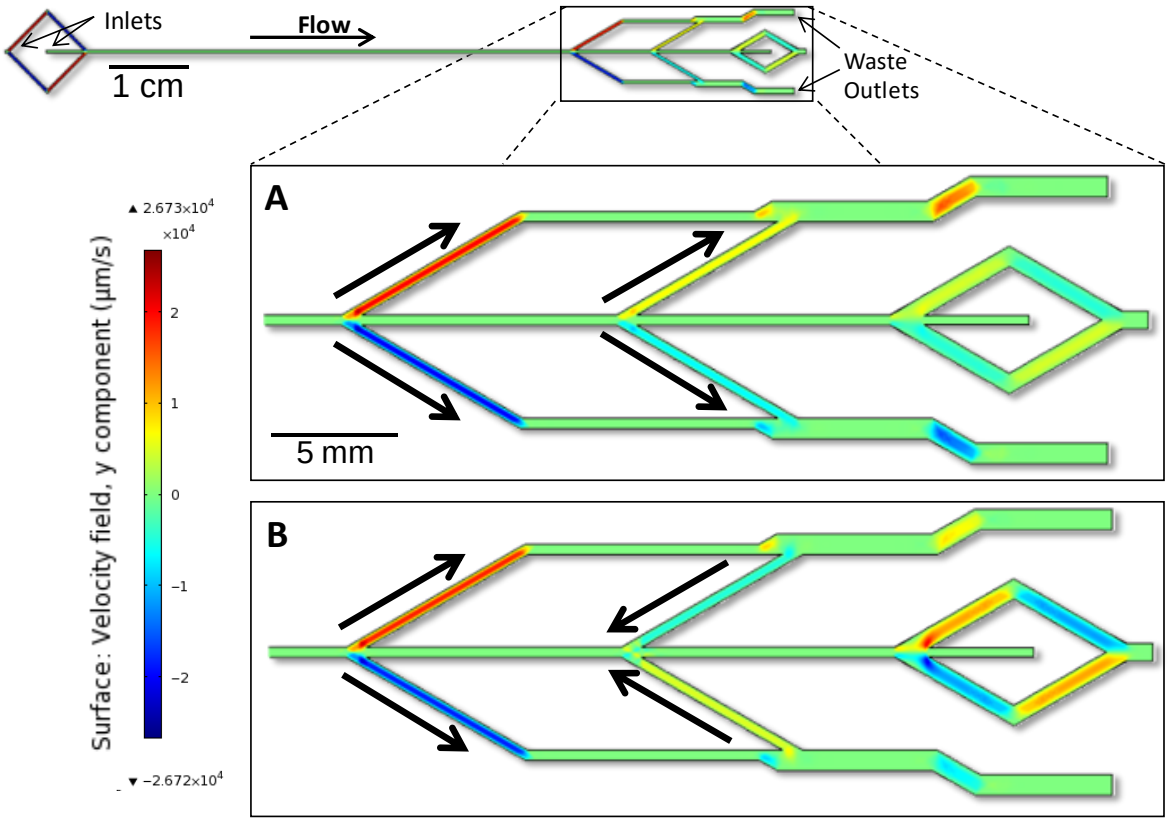

Figure 4: Images rendered from COMSOL Multiphysics of the optimized Acousto-Filtering Design. The color scale represents the y-component of the flow, or direction of the flow. Flow in the positive y-direction indicated by yellow/orange/red, and the negative y-direction indicated by shades of blue. A. Output-to-input ratio set at 75% shows flow in uniform direction down each angled waste channel. B. Output-to-input ratio set at 50% shows flow reversed in the second set of angled waste channels. This indicates that fluid would return to the separation channel and would not be removed under these conditions.

well as the cost and hazards associated with glass fabrication techniques, including the use of hydrofluoric acid (HF). The experiments were used to visualize and confirm that the laminar flow, hydrodynamic focusing, and flow direction were comparable to the theoretical modeling. Blue and yellow food color dyes were used to represent the sample and buffer, respectively. As seen in **Figure 5A**, at the inlet trifurcation, laminar flow and hydrodynamic focusing are clearly visible. As the three layers progress down the separation channel, the colors remain separated from one another with minimal mixing. Once the flow reaches the waste channels the fluid changes to a green color indicating slight diffusive mixing between the sample and buffer in the sample layer. The now green color is seen moving down the first set of waste channels with very little passing to the second set of waste channels **(Figure 5B**). Finally, the color of the fluid beyond the waste channels is seen as solely yellow as it passes into the outlet trifurcation. This was a simple, qualitative indication that the majority of the blue dye was removed via the waste channels and an initial validation of the fluid dynamics indicated in the COMSOL modeling.

To further validate the observed flow patterns and theoretical modeling, and more closely relate it to the properties of blood, mixtures of glycerol in water were

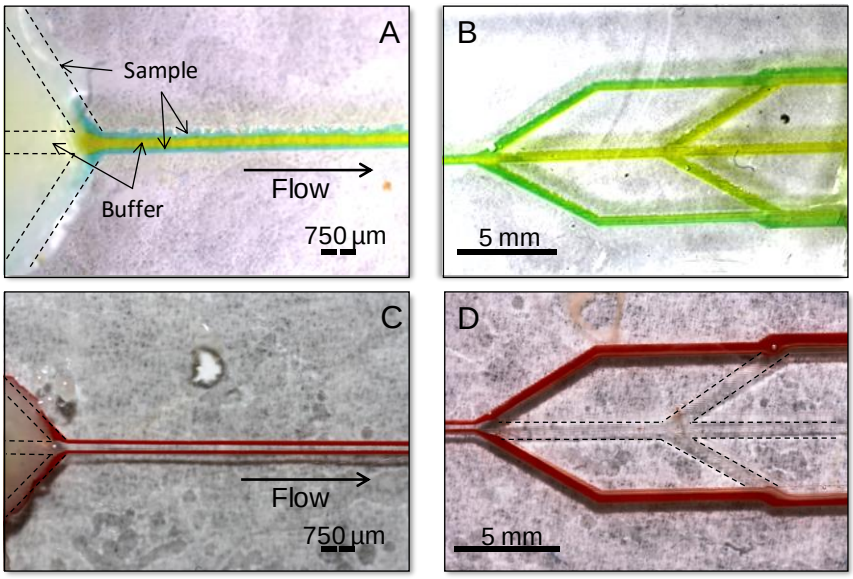

Figure 5: Flow studies in PMMA – A. Trifurcation at which "sample" (blue) and "buffer" (yellow) meet entering the separation channel. B. Filtering region of chip. Blue dye seen flowing down filter channels. Minimal blue dye seen in separation/isolation channel. C. Efficient filtering of whole blood seen at a sample flow rate of 15 µL/min. buffer flow rate: 25 µL/min. D. Filtering seen at a sample flow rate of 60 µL/min and a buffer flow rate of 100 µL/min. No traces of RBCs seen in separation/isolation channel.

used to mimic the viscosity of blood (~4.4 centiPoise (cP)).[16] Laminar flow and hydrodynamic focusing were seen as the viscosities between the sample and the buffer became comparable. When analyzing the flow patterns, the higher viscosity solutions mirrored the same results as the dyes in water, with little to no sample seen beyond the waste channels.

As a final assessment of the design, undiluted whole blood was used as the sample with a 30% glycerol to water mixture used as the clean buffer to closely match viscosities.[16] The flow patterns matched what had been seen previously with the dyes and glycerol mixtures. The majority of the RBCs were seen flowing down the first set of waste channels, and what sample remained in the separation channel was then removed down the second set of waste channels (**Figure 5C&D**). Minimal sample was seen past the last set of waste channels except in cases of pulsing from the syringe pumps that disrupted the hydrodynamic focusing.

This final experiment indicated that the design should be highly efficient at removing RBCs and undesired sample, however, the PMMA devices were fabricated with a greater volume capacity than would be possible in fabricating glass. Laser ablation allowed for the creation of any size channel depth desired, in this case 400 μm was selected, and in turn allowed for processing of greater volumes of whole blood at high flow rates. For a 2 MHz transducer, a single node standing wave is generated in a reflecting channel with a width of 375 μm. A channel depth of just greater than 375 μm was initially selected in order to represent a large square-like cavity that would not allow for the generation of a standing wave in the vertical direction should acoustics be applied. With glass fabrication, feature depth is limited by isotropic etching. Since the lateral etch rate is equal to the vertical etch rate with isotropic etching, the maximum depth that could be achieved in a glass-etched device was approximately 120 μm for a channel width of 375 μm.

5.3.3 Whole Blood Acoustophoresis

Glass microdevices were fabricated for acoustophoresis experiments due to the favorable acoustic resonance properties of glass, such as having high acoustic impedance that allows for ultrasonic waves to easily permeate the device. The effectiveness of the acoustic properties in this design was initially verified via the acoustic focusing of 20 μm fluorescently labeled polymer beads in water. The beads are a suitable mimic for CTCs due to their comparable size. Successful focusing was achieved using a 2 MHz PZT transducer with an applied voltage of 13.5 V, resulting in particles migrating to the collection channel. While the transducer remained off, beads were observed along the walls of the separation channel and then seen exiting at the first set of waste channels.

Before analyzing blood samples, beads in 30% glycerol-in-water solutions (~ 4.0 cP)[16] were tested to monitor the effect of viscosity on acoustic focusing. The greater the viscosity, the greater the voltage required to overcome viscous drag and achieve focusing and focusing was only achieved at an applied voltage above 26.0 V compared to 13.5 V in water. However, at such high voltages the temperature of the PZT transducer, and its effect on the solutions in the microchannels, become significant factors to consider. Heat generated from the PZT can cause bubbles inside the solution effecting hydrodynamic flow, and temperatures much higher than 37 ºC could potentially harm the cells in a sample. Ultimately, the less viscous, biologically relevant buffer, phosphate buffered saline (PBS) would be used as the clean buffer stream, and with the potential to reduce blood viscosity via dilution, the experiments indicated that a whole blood sample could be processed via acoustophoresis on this device.

5.3.3.1 Preliminary 2 MHz Bead Separations

Human whole blood samples were diluted one to one in 10x PBS buffer before flowing through the glass device to achieve a lower working viscosity and increase efficiency of RBC removal. Fluorescent beads (20 μm) were used to mimic CTCs in the blood and were collected and counted. Initial attempts to focus, isolate, and capture the fluorescent beads were only partially successful on the glass device. At the initial parameters, beads were focused to the center as expected but poor purity of capture was seen due RBCs also being focused. The result was a large portion of the cellular content bypassing the first set of angled waste channels, proceeding to the second set of angled waste channels, overloading those channels, and ultimately collecting with the focused beads in the bead collection channel (**Figure 6**).

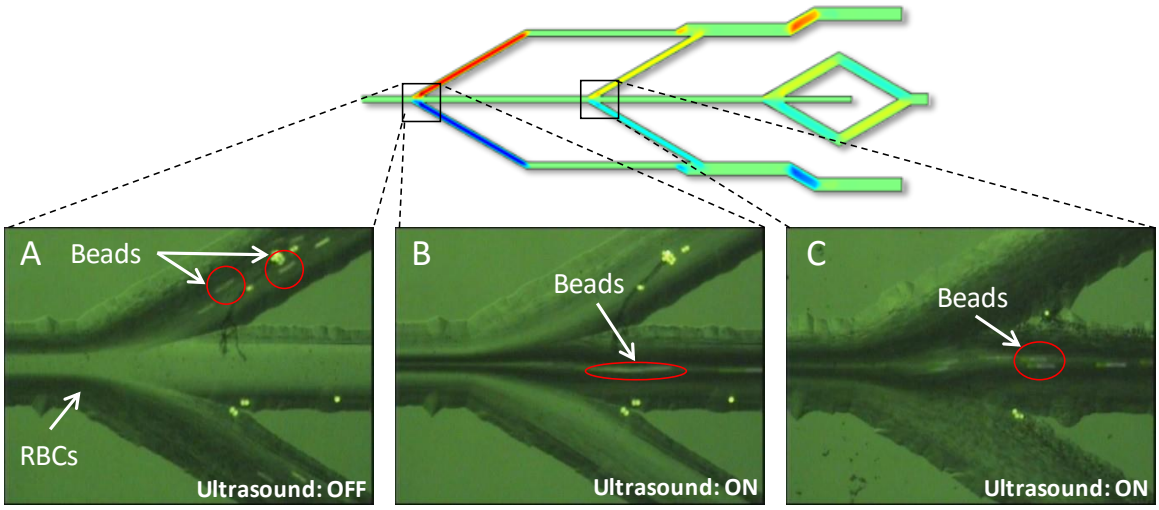

Figure 6: Still frames from video of acoustic focusing of beads in 1:1 diluted whole blood. A. No transducer actuation: Whole blood sample flowing down first set of angled waste channels with beads. B. Transducer actuated: Both the whole blood sample and the beads are seen focused to the center of the separation channel with only slight separation. Almost no RBCs are seen removed at the first angled waste channel. C. Snapshot of second set of waste channels where the sample has overloaded the channel capacity and RBCs are seen passing the waste channels and flowing towards the bead collection channel.

5.3.3.2 Impact of Applied Voltage

As the voltage was reduced to decrease the force being applied to the system, the movement of RBCs towards the center of the channel was much less prominent. When 7.0 V were applied, the majority of the cells were removed via the first set of angled waste channels as previously expected (**Figure 7A**). While the reduction of voltage had a positive effect on the RBCs by reducing the focusing, it had a negative effect on the particles of interest. The reduced acoustic force resulted in the beads moving much more freely within the channel instead of a tight stream seen at higher applied voltages. Ultimately this led to a higher number of beads being removed via the angled waste channels rather than collected **(Figure 7C**).

5.3.3.3 Optimization of Flow Rates

The flow rate of the clean buffer was increased in order to limit the passive and acoustic movement of the RBCs and other smaller, undesirable particles, towards the center of the separation channel. The flow rate was gradually increased from 15 μL/min to 100 μL/min where 100 μl/min had the most favorable effect. The movement of sample towards the center was drastically reduced while the fluorescent beads were still able to be focused. Finally, as the overall flow rate increased for all solutions, the applied voltage was also increased to 22.0 V in order to balance forces and induce tighter focusing (**Figure 8**).

After optimizing the flow rates and acoustic parameters, the efficiency of particle capture and the purity of collected sample were investigated. The efficiency of capture, defined as the number of beads collected divided by the total number of beads added, was 61.7% ± 23.3% (n=3). The average efficiency of capture goes up to 68.4% ± 21.6% (n=3) with the inclusion of beads that passed through the outer channels of the trifurcated outlet but

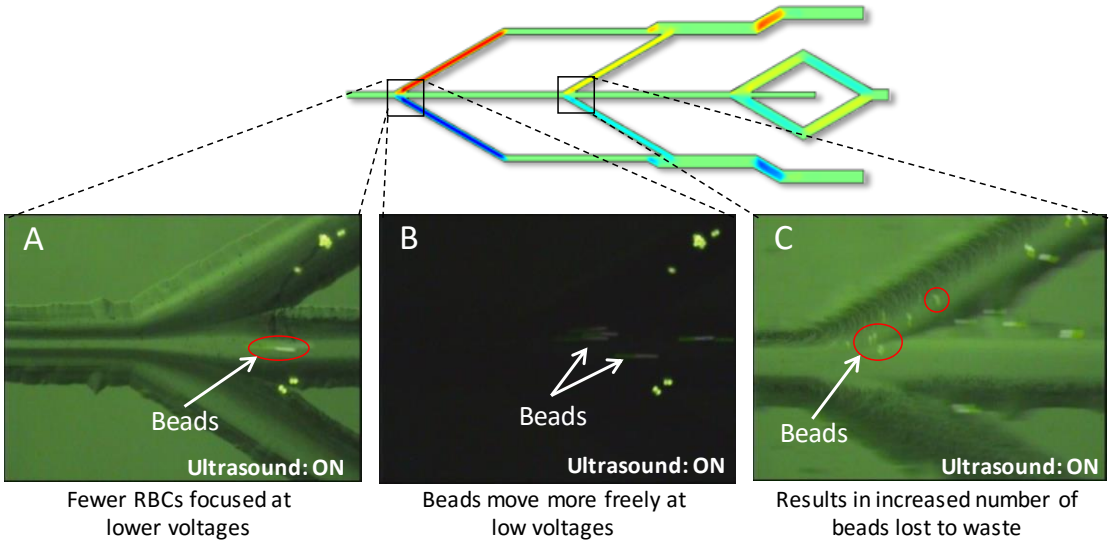

Figure 7. Still frames showing effect of decreasing applied voltage. Voltage was decreased from 13.5 V to 7.0 V. A. The amount of sample focused to the center with the beads is reduced and more RBCs are seen being removed down the first angled waste channel. B. Due to the reduction in voltage, the tightness of focusing of beads is reduced and are seen moving around in channel more. C. The increased movement of beads in channel increases the probability for the beads to exit the separation channel down the second set of angled side channels.

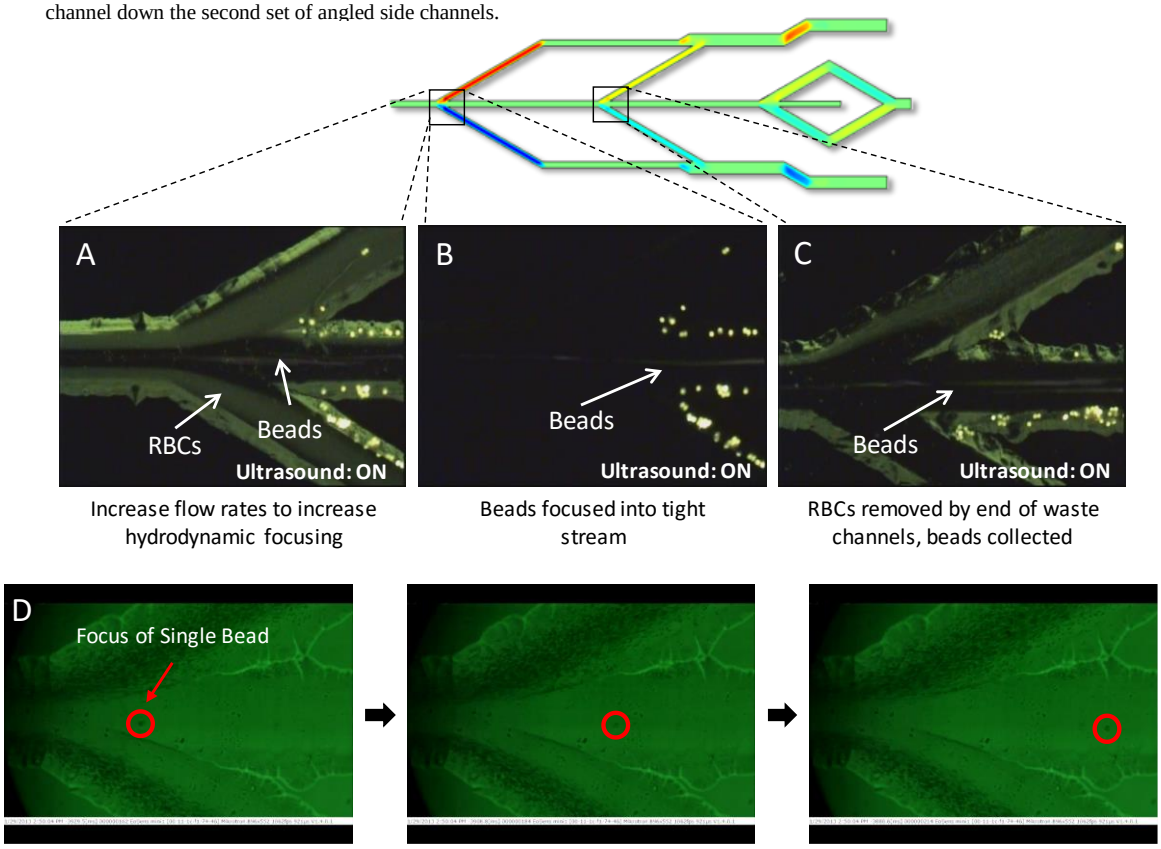

Figure 8. Still frames showing effect of increasing flow rates and applied voltage. A. Increase in hydrodynamic focusing leads to a majority of sample being removed at the first set of angled waste channels. Applied voltage increase required but results in a tight stream of focused beads. B. Indication that the stream seen is the focused beads. C. At the second set of waste channels the beads remain in a focused stream flowing towards the bead collection reservoir while any remaining RBCs are removed. D. High-resolution still frames from a high-speed camera showing the focusing of a single bead in the presence of blood cells.

were not collected in the bead collection reservoir. With the goal of the device to not only collect CTCs but also remove as many RBCs and other cells as possible, it is important to consider the purity of the collected sample. The purity in this case is defined as the number of beads collected compared to all other particles/cells collected. The average purity of the collected samples was calculated to be 2.47% ± 1.46% (n=3). Despite the low percentage, the average purity of sample before processing was only 0.00189% ± 0.00106% (n=3), and therefore an average of a 1638-fold ± 1043 (n=3) increase in purity is observed. These initial values of both efficiency and purity are lower than many literature values but demonstrate the early possibilities of such a device for the separation and isolation of CTCs from whole blood.[17, 18]

5.3.3.4 PC3 Cells vs 20 µm Beads

While 20 µm polystyrene beads were good mimics for CTCs during initial optimization, they differ significantly in density and compressibility compared to epithelial cells, and therefore respond differently in an acoustic field. To better optimize the acoustic parameters for patient samples, a prostate adenocarcinoma cell line (PC3) was cultured and

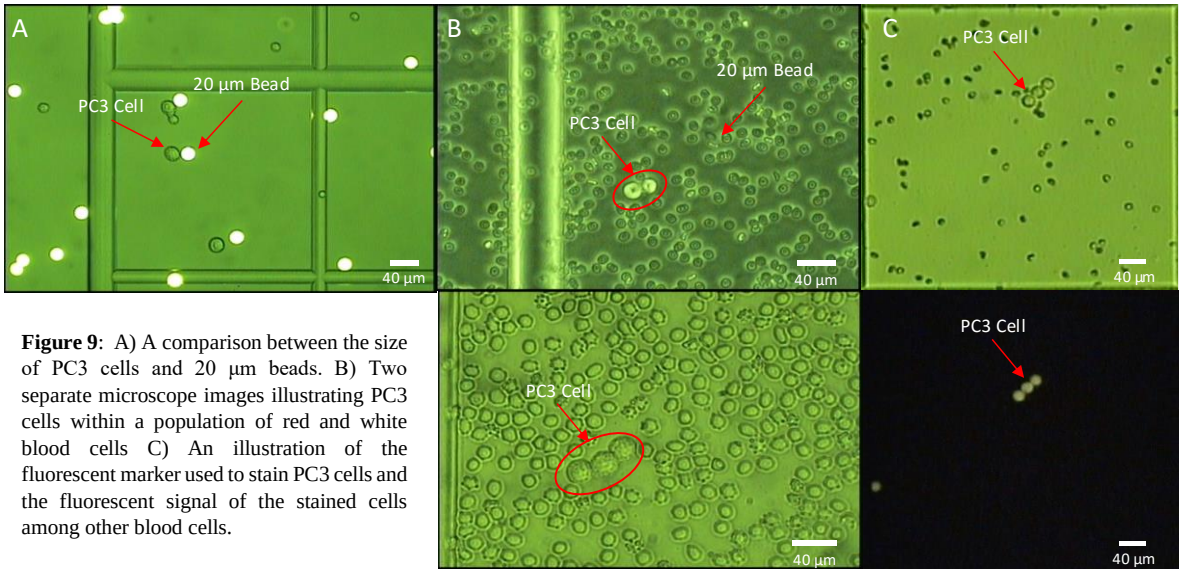

Figure 9: A) A comparison between the size of PC3 cells and 20 µm beads. B) Two separate microscope images illustrating PC3 cells within a population of red and white blood cells C) An illustration of the fluorescent marker used to stain PC3 cells and the fluorescent signal of the stained cells among other blood cells.

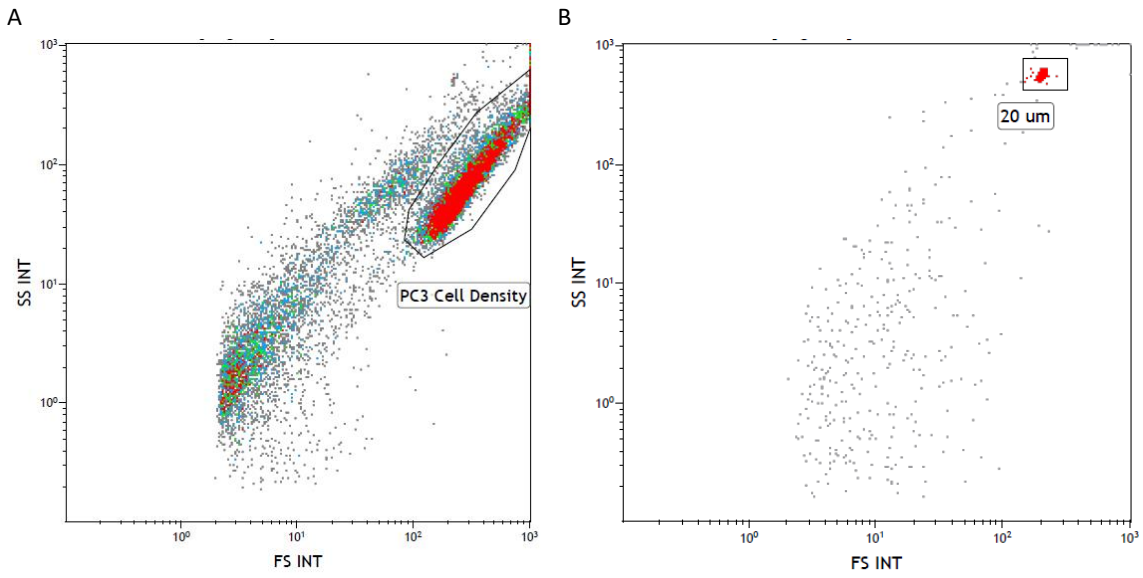

Figure 10. A) A dot plot showing the population of PC3 cells when plotted using forward and side scatter. B) A dot plot of a population of 20 µm polystyrene beads using the same forward and side scatter parameters.

spiked into a 1:10 diluted whole blood sample. As shown in **Figure 9A**, the PC3 cells are similar in size (~20 µm) to the fluorescent beads. Once again, these cells are larger than a majority of blood cells, and the size difference can be seen in **Figure 9B**. To visualize these cells during analysis, and prepare them for flow cytometry analysis, they were stained using a fluorescein-based cytoplasm stain (**Fig. 9C**). The labeled cells, along with the 20 µm beads used previously, were first characterized using a flow cytometer where forward scatter (FS, qualitative indicator of size) and side scatter (SS, indicator of granularity) were used to identify each population individually. The PC3 cells show a large bandwidth in size and granularity (**Fig. 10A**), while the polystyrene beads show a tight population, as expected (**Fig. 10B**).

5.3.4 Flow Cytometry Optimization

In addition to the PC3 cells and 20 µm beads, the varying populations of white blood cells were also characterized using flow cytometry. As stated previously, some populations

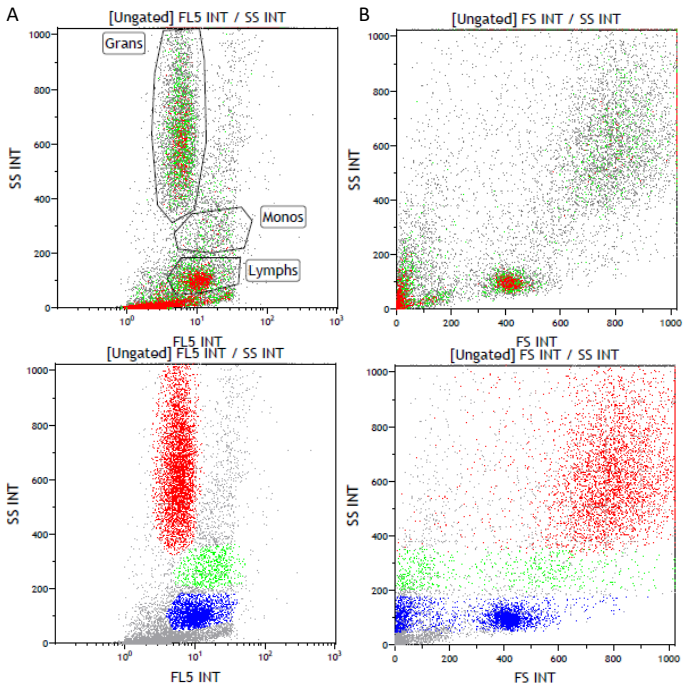

Figure 11. A) A blood sample was stained with anti-CD45 antibodies and processed on a flow cytometer. Varying populations of white blood cells were identified and gated using fluorescence and side scatter B) The same sample plotted using forward and side scatter. Colors represent the respective gates across both plots.

of WBCs are likely to overlap in size with the PC3 cells, and therefore, other differences between the cells must be utilized for differentiation. The blood sample was stained with anti-CD45 antibody and the resulting population breakdown after flow cytometry is shown in **Figure 11A**. The three main populations identified using the anti-CD45 emission were granulocytes, monocytes, and lymphocytes. The same data was also plotted using FS and SS (**Fig. 11B**).

As described above the PC3 cells were labeled with a fluorescein-based cytoplasm dye. This dye had a similar emission to the anti-CD45 antibodies, allowing both populations to be detected on the same channel of the flow cytometer. The labeled PC3 cells and a whole blood sample were each individually characterized again on the same channel and gates were established that would provide a cellular count of each population (**Fig. 12 A&B**). A sample with a 1:1 ratio of WBCs to PC3 cells was prepared and analyzed on the flow cytometer. **Figure 12C** shows the distinct populations of WBCs and PC3 cells and confirmed that each population could be identified on the same detection channel. To determine the limit of detection of the flow cytometer for PC3 cells, the number of PC3 cells was gradually decreased after the initial 1:1 ratio of WBCs to PC3 cells. **Figure 13** shows the expected

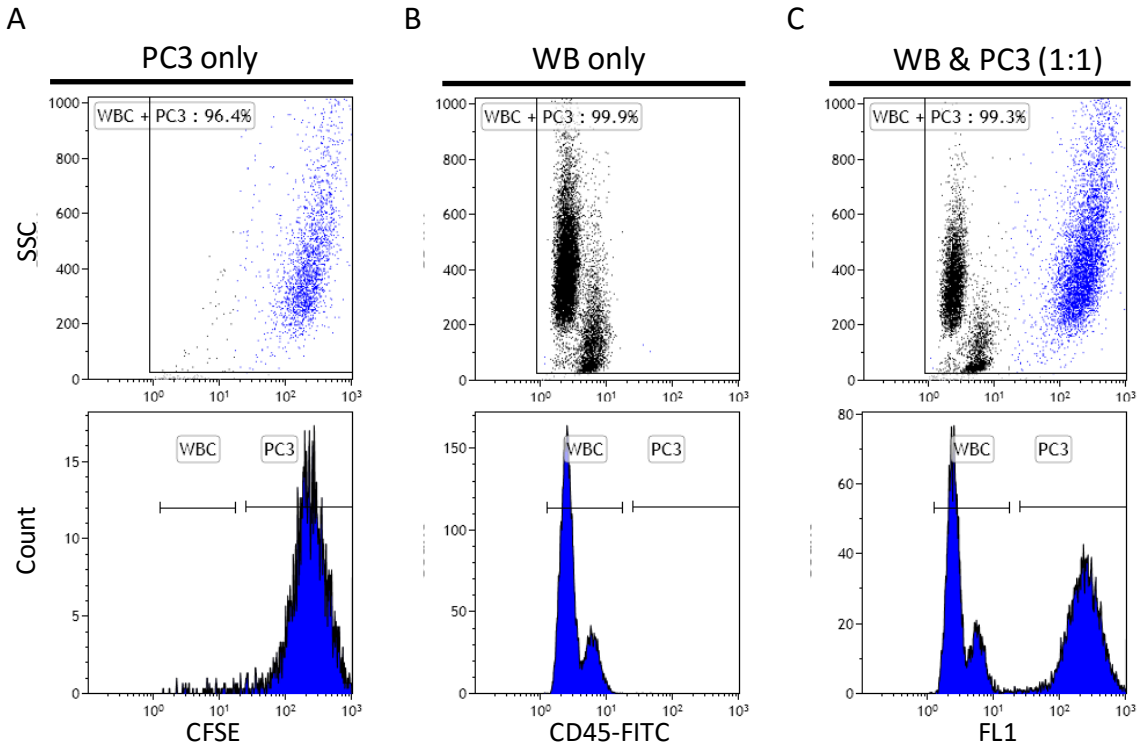

Figure 12: A) A dot plot and histogram representing a population of PC3 cells identified using fluorescence and side scatter. Gates for counting were set based on the histogram output. B) Similar plots were generated for anti-CD45 labeled white blood cells and used to create a gate for counting. C) A dot plot and histogram of a sample containing a 1:1 ratio of WBCs to PC3 cells.

frequency and actual number of events at each indicated ratio. The actual values showed strong correlation to the expected values at each ratio and based on this data, the limit of detection was determined to be 1 PC3 cell/μL. Below this concentration, it became difficult to differentiate between debris/artifacts and cellular events.

After fully characterizing each population of cells that might be expected in collected samples, PC3 cells were spiked into a 1:10 diluted, anti-CD45 labeled, blood sample and acoustophoretically processed, as described above. Starting with the parameters optimized by bead analysis, a large number of PC3 cells were observed focusing to the center of the separation channel, however, as expected, the increase in compressibility and the decrease in density of the cells caused them to focus differently than the beads. The frequency and voltage applied to the transducer were tuned to optimize the focusing of the PC3 cells while

minimizing collection of unwanted blood cells. The high-resolution, high-speed camera still-frames in **Figure 14** show the focusing, and collection, of a single PC3 cell from surrounding blood cells. Compared to the bead images shown in **Figure 8**, the PC3 cell was not as distinctly removed from the blood cells when the cell reached the first trifurcation. Alternatively, the cell is observed much closer to the blood cells and the channel wall before being separated by the microfluidic architecture.

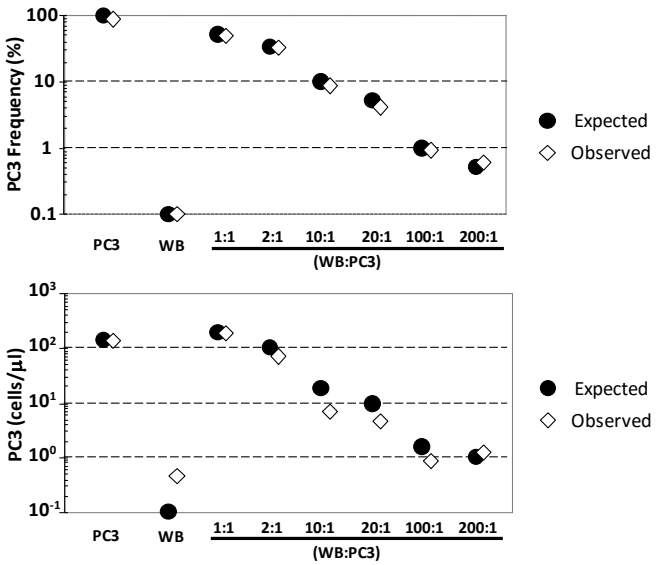

Figure 13. The expected and observed values for frequency (A) and number of events (B) at each indicated ratio of WBCs to PC3 cells. The observed values showed strong correlation to the expected values at each ratio. The limit of detection was determined to be 1 PC3 cell/µL.

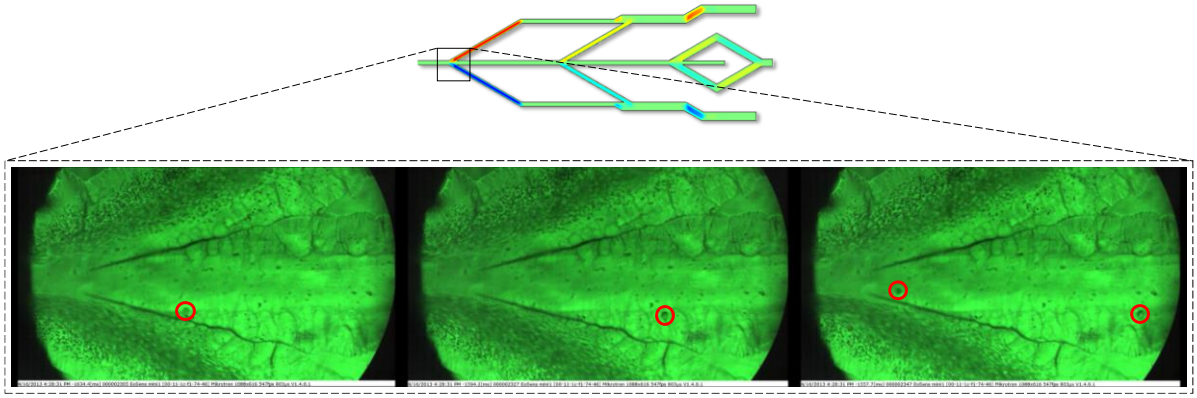

Figure 14. High-resolution still frames from a high-speed camera showing the focusing of a single PC3 cell in the presence of blood cells.

5.3.5 Analysis of PC3-Cell Spiked Whole Blood Samples

After processing the sample, the fraction of acoustically-collected cells was analyzed on the flow cytometer to count the number of PC3 cells collected and determine the efficiency of PC3 capture. The population of PC3 cells-only remained constant from previous studies and no changes to population gates were necessary (**Fig. 15A**). Analysis of the collected cell

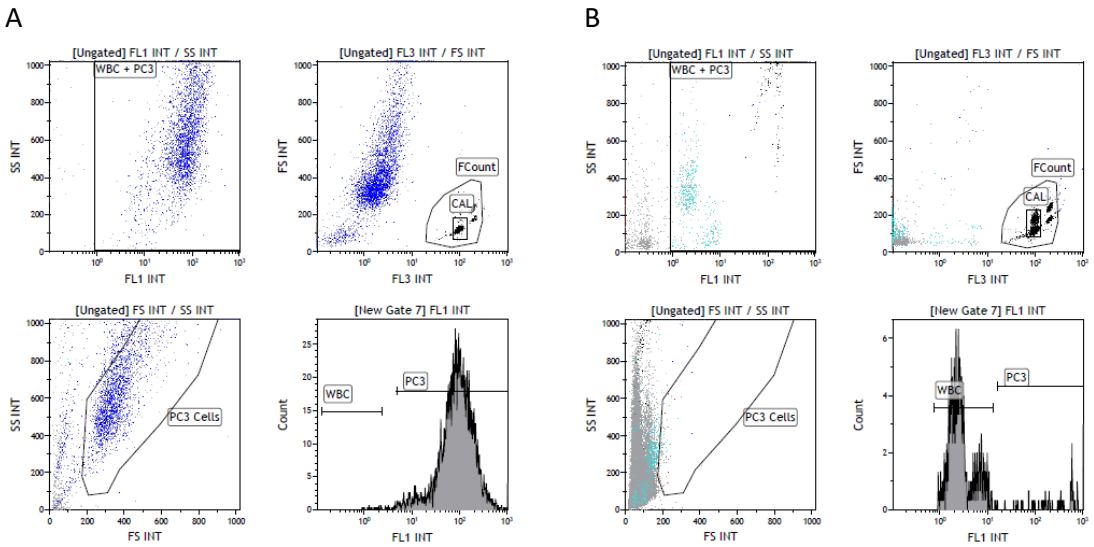

Figure 15. A) Flow cytometry data of a PC3 sample analyzed independently prior to addition to a blood sample. B) Data from flow cytometry analysis of a acoustophoretically-processed sample.

sample is shown in **Figure 15B**. The population of PC3 cells collected was scarce compared to the other blood cells collected and overall, the total capture efficiency for the PC3 cells was determined to be only 32%. The same experiments were completed on four more PC3-spiked samples and one bead-spiked sample. The percentage of capture for each cell/particle type was calculated and is shown in **Figure 16**. Subsequent PC3-spiked samples showed an average capture efficiency of 39%, with a high of 49.6%, while 20 µm beads were captured at an efficiency of 82% (n = 1). Despite the low capture efficiency, the method did provide significant purification by removing 98.5% of the starting amount of red blood cells and 99.1% of white blood cells (**Fig. 16**). Ultimately, this

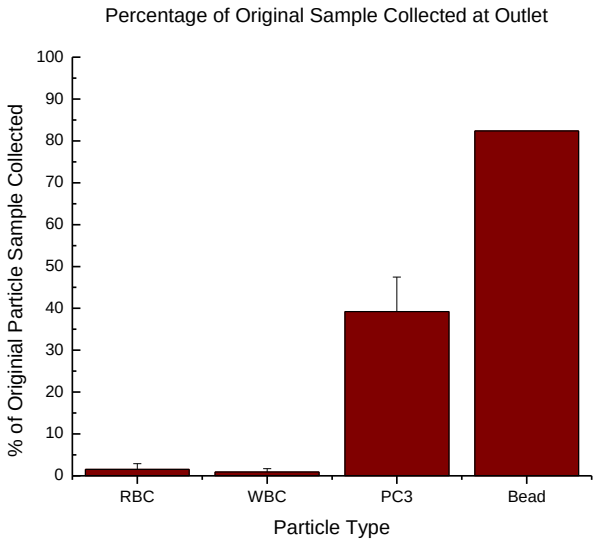

Figure 16. A histogram representing the percent of original sample particles collected at the outlet of the acoustophoresis device. Only 1.5% and 0.9% of RBCs and WBCs from the original sample were collected, respectively. PC3 cells were collected at an efficiency of 39% and beads were collected at 82%.

provides an indication that a greater acoustic force is likely required to better focus the PC3 cells, however, as a consequence, due to the similarities in density and compressibility between the PC3 cells and the blood cells, this would also focus more blood cells to the center and decrease the purity.

5.3.6 Two-Transducer 'Pre-Focusing'

In order to improve capture efficiency while maintaining high purity levels, additional methods of sample manipulation were explored. Laurell et al. (ref) described a method that

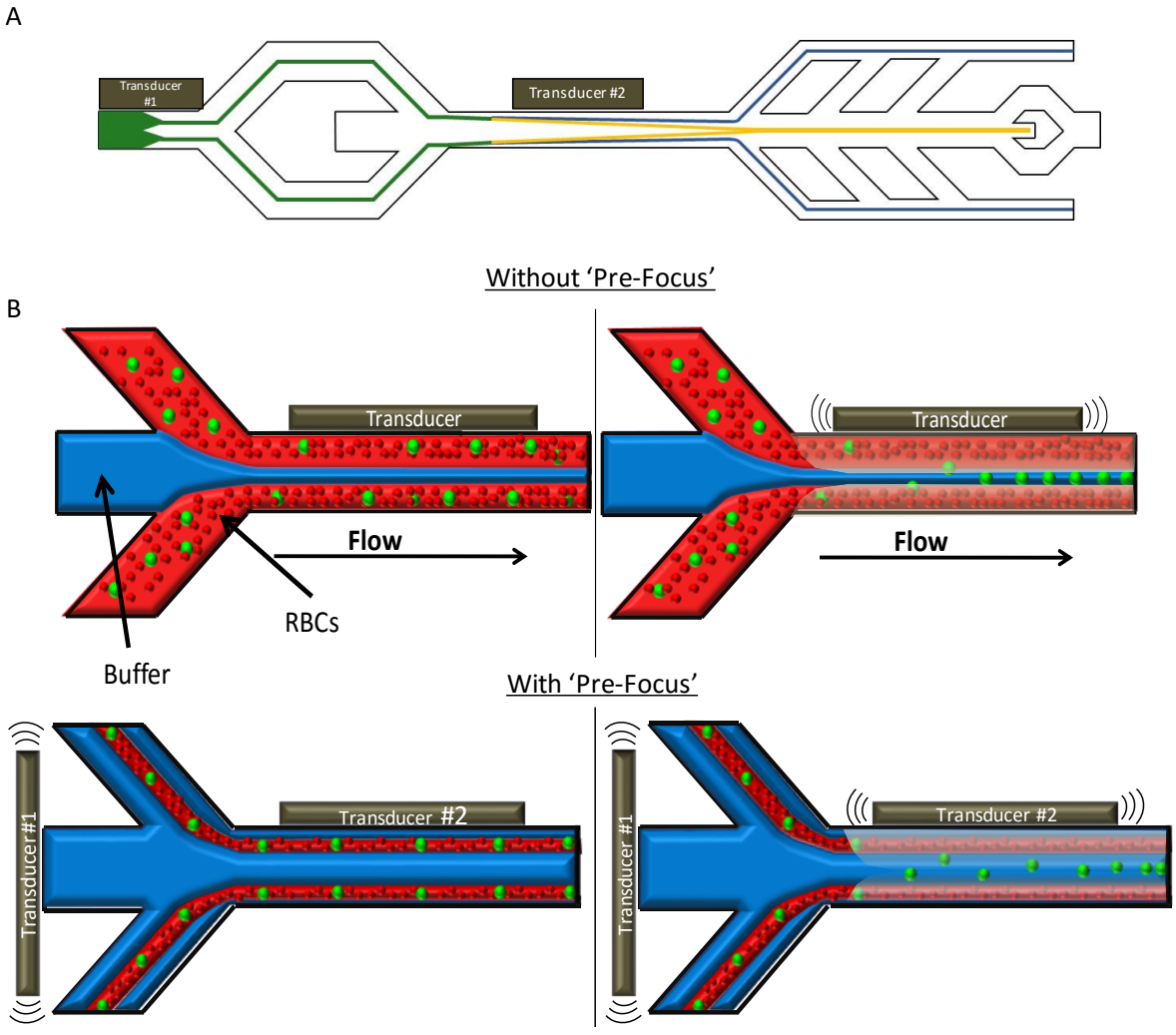

Figure 17. A) A schematic representation of the impact the pre-focusing step was predicted to have on the sample and the separation. B) A schematic comparing the predicted flow pattern of the sample before and after the application of a second transducer for pre-focusing. The first transducer focuses the entire sample into a single stream before reaching the separation channel.

took advantage of two transducers at different frequencies to 'pre-focus' a sample before acoustically separating particles. The acoustic 'pre-focus' forces the entirety of a sample into a single node and makes for a tighter sample stream entering the separation channel. By bringing the entire sample into a single node, the impact of variable flow velocity in the channel is reduced. The resolution of acoustic separation is improved because the separation of two particles would rely solely on the difference in acoustic mobility between the particles. A schematic representation of the two-transducer system and the impact on flow is presented in **Figure 17A**. Further, a schematic representation comparing the input sample flow before and after the addition of a 'pre-focusing' step is shown in **Figure 17B**.

5.3.6.1 5 MHz 'Pre-Focus' Transducer

To apply such a technique, a fundamental design change was needed. The pre-focus step would rely on the use of a frequency that differed from the acoustic separation frequency. Adapting from the previously published work, a 5 MHz transducer was selected to provide the pre-focusing. The channel width for the sample inlet channels was fabricated to 300 μm wide to generate two waves at 5 MHz (3λ/2) (**Fig. 18**). The separation channel remained 375 μm wide to generate a single node for particle separation at 2 MHz (λ/2). In addition to the change in channel width, a third set of angled filter channels was added to the design to provide increased filtering capability should more blood cells not be removed at the first set of filter channels under increased acoustic force.

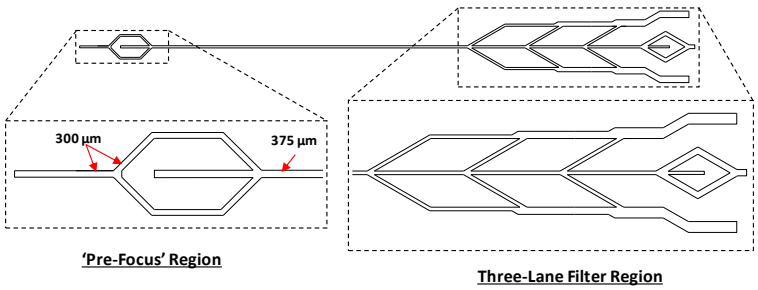

Figure 18. A diagram describing the modified fluidic design to allow for focusing of two separate waves on the device. The channels in the pre-focusing region are 300 μm for a 5 MHz wave, while the separation channel remains 375 μm for the 2 MHz wave. In addition, a third set of filter channels was added to facilitate filtering.

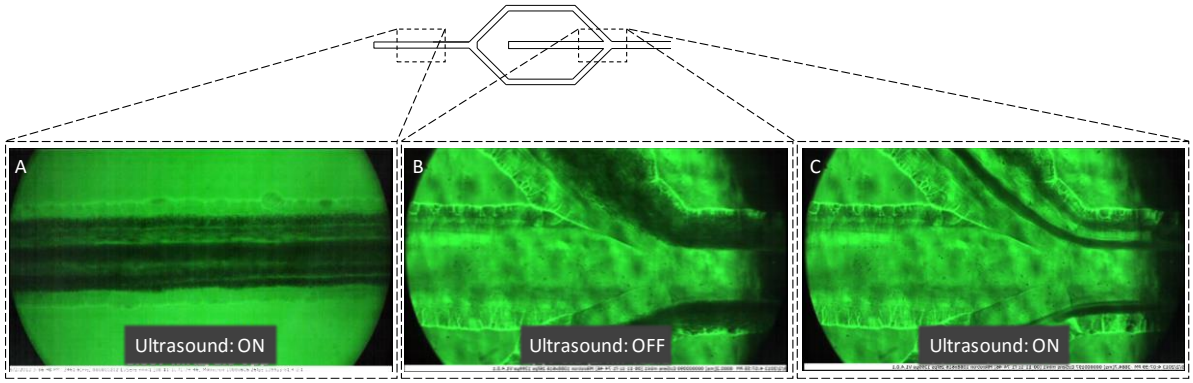

Figure 19. A) A screenshot image of the focusing of sample using the 5 MHz transducer. A single node is observed in the center with sample seen on either side against the walls. B) A screenshot of the sample entering the separation channel before the 5 MHz transducer is applied. C) The same region after the 5 MHz transducer has been applied, where two streams of sample are observed in each channel.

Attempts to pre-focus a whole blood sample using the new design and second transducer at 5 MHz were unsuccessful. As shown in **Figure 19A**, when applying ultrasound to the system, a majority of the sample was focusing into a single node in the center of the channel with the remainder of the sample observed along the walls. A comparison with the ultrasound both off and on is shown in **Figure 19B&C**. Two individual streams in each sample channel were observed rather than one focused stream in each channel. In an effort to diagnose the focusing problem, the acoustic field in the system was modeled using COMSOL (**Fig. 20**). The low-pressure nodes are represented by the blue regions, while the high-pressure

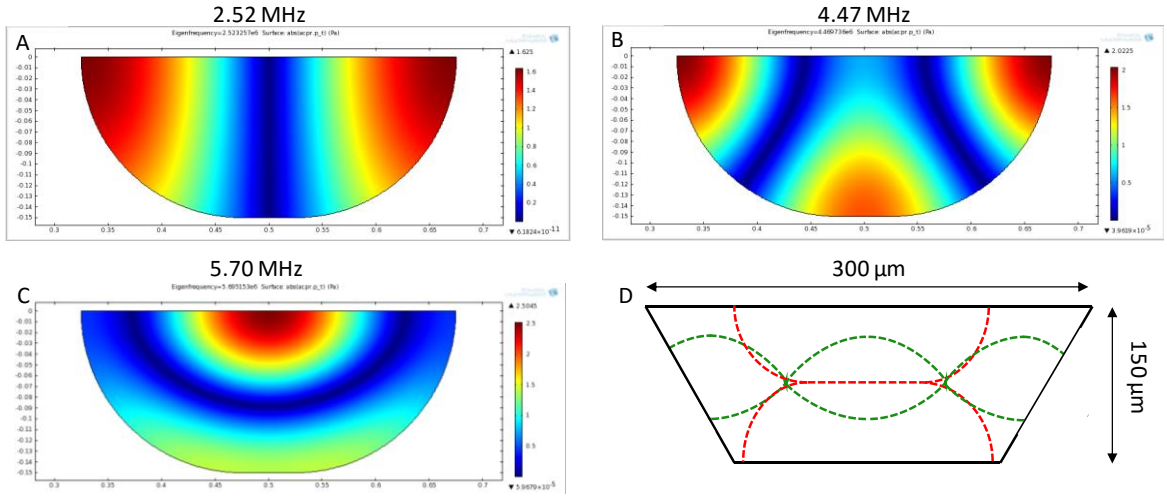

Figure 20. COMSOL modeling of the acoustic pressure within a channel at a frequency of 2.52 MHz (A), 4.47 MHz (B), and 5.70 MHz (C). D) A schematic representation of the waves predicted to be present in a channel that is 300 µm wide and 150 µm deep.

regions are represented in red. As the frequency approached 5 MHz from 2 MHz, two low-pressure nodes are modeled, as expected (**Fig. 20B**). Beyond 5 MHz, the model showed potentially two low-pressure nodes connected through the center of the channel (**Fig. 20C**). It was determined that the focusing observed on the actual device likely represented a combination of the two theoretical results. A 300 μm-wide channel was fabricated because it provided 3λ/2 resonance of a 5 MHz wave, generating two low pressure nodes. Due to isotropic etching, however, this also resulted in a 150 μm-deep channel, which would provide λ/2 resonance and a single node in the vertical direction. It was hypothesized that both waves were influencing the particles in the channel, leading to a single visible node, rather than two distinct nodes.

5.3.6.2 3 MHz 'Pre-Focus' Transducer

The effect of a vertical node was countered by changing the pre-focusing frequency from 5 MHz to 3 MHz. To achieve 3λ/2 resonance at 3 MHz, the channel needed to be 500 μm wide (**Fig. 21A**). The depth of the channel remained 150 μm deep after isotropic etching, outside of the λ/2 resonance for 3 MHz. **Figure 21B** shows the impact of the 3 MHz ultrasound in the pre-focusing region of the device. When the ultrasound remains off, the sample completely fills the channels. When the

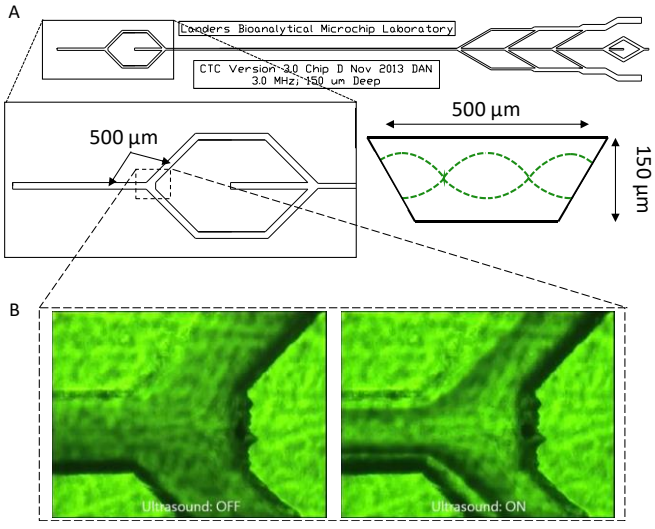

Figure 21. A) An image of the design change made to accommodate a 3 MHz transducer and a schematic of the wave generated in a 500 μm-wide channel. Due to the resonance of 3 MHz, no vertical node is observed at 150 μm deep. B) Screenshot images of the sample channel before and after the application of the 3 MHz transducer. The sample was successfully focused into two streams.

ultrasound is turned on, the sample is focused into two focused streams, as intended.

5.3.6.3 Impact of Each Transducer on Focusing

With the pre-focusing performing as expected with 3 MHz, spiked blood samples were analyzed under several different conditions to better understand the impact of the two-transducer system. **Figure 22** presents a series of screen shots illustrating the effect of each transducer and variations on the applied voltage. Starting from the far left and moving clockwise, the 3 MHz ultrasound forces the sample into a tight stream as it enters the separation channel **(A)**. At the first trifurcation, when the 3 MHz transducer is turned on, the stream becomes visibly more focused **(B,C)** and the blood cells are removed down the first set of filter channels. Prior to the application of the 2 MHz transducer, the 20 μm beads can also be seen removed down the filter channels **(C)**. When the 2 MHz transducer is turned on, there is a small shift in the blood cells, but the largest impact is on the focusing of the beads to the center of the separation channel **(D)**. If the 3 MHz transducer is turned off while the 2 MHz is left on, the blood cells can be seen moving closer to the center of the separation channel **(E)**. The impact of an applied voltage change when both transducers are on can be seen in **(F)** and **(G)**, where dropping the voltage from 25 V_{pp} to 14.5 V_{pp} showed the de-focusing of the blood cells from the separation channel into the first set of filter channels. Under these conditions, almost no undesirable blood cells are observed at the second and third trifurcations, while the beads remain focused **(H, I)**.

5.3.6.4 Two-Transducer Acoustophoretically-Processed Sample

Following the optimization of the two-transducer system, a PC3-spiked sample was processed using the pre-focus method and the collected cell fraction was analyzed using flow

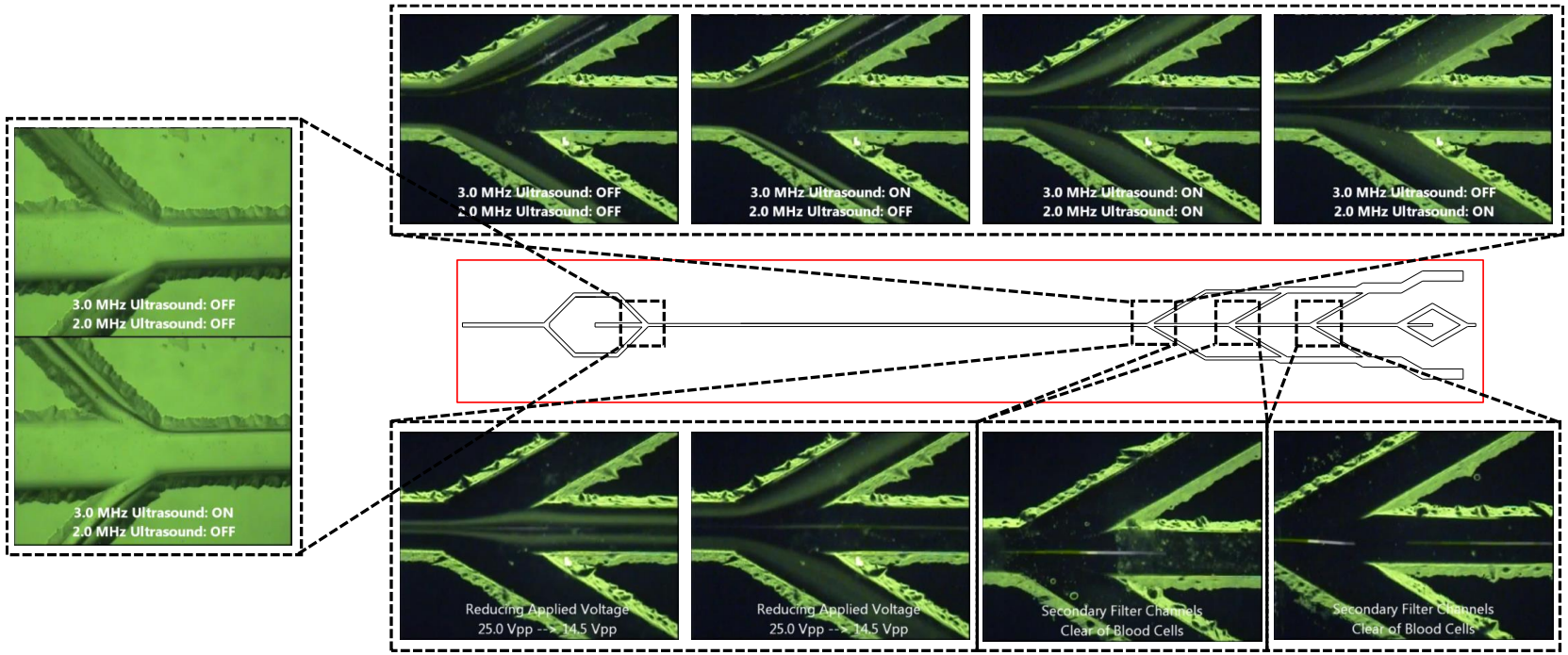

Figure 22. A series of images illustrating the impact of each transducer and the applied voltage on the sample and separation. A) The 3 MHz ultrasound forces the sample into a tight stream as it enters the separation channel. B) At the first trifurcation, the 3 MHz transducer is turned on, the stream becomes visibly more focused (B,C) as the blood cells are removed down the first set of filter channels. The 20 μm beads can be seen removed down the filter channels when the 2 MHz transducer is off (C). When the 2 MHz transducer is turned on, there is a small shift in the blood cells and focusing of the beads to the center of the separation channel (D). If the 3 MHz transducer is turned off while the 2 MHz is left on, the blood cells can be seen moving closer to the center of the separation channel (E). The impact of an applied voltage change when both transducers are on can be seen in (F) and (G), where dropping the voltage from 25 V_{pp} to 14.5 V_{pp} showed the de-focusing of the blood cells from the separation channel into the first set of filter channels. Under these conditions, almost no undesirable blood cells are observed at the second and third trifurcations, while the beads remain focused (H, I).

cytometry. **Figure 23A** shows the population of a PC3-only sample, and **Figure 23B** shows the population of PC3 cells in the presence of blood cells before acoustic processing. According to flow cytometry the concentration of cells in the raw sample was determined to be 19.68 PC3 cells/µL, however, based on the concentration of the cells analyzed from the PC3-only sample, the expected concentration in the blood sample was 302 cells/µL. This discrepancy likely stemmed from the overwhelming number of blood cells in the raw sample masking the fluorescent signal of the PC3 cells. This effect was also likely observed in the

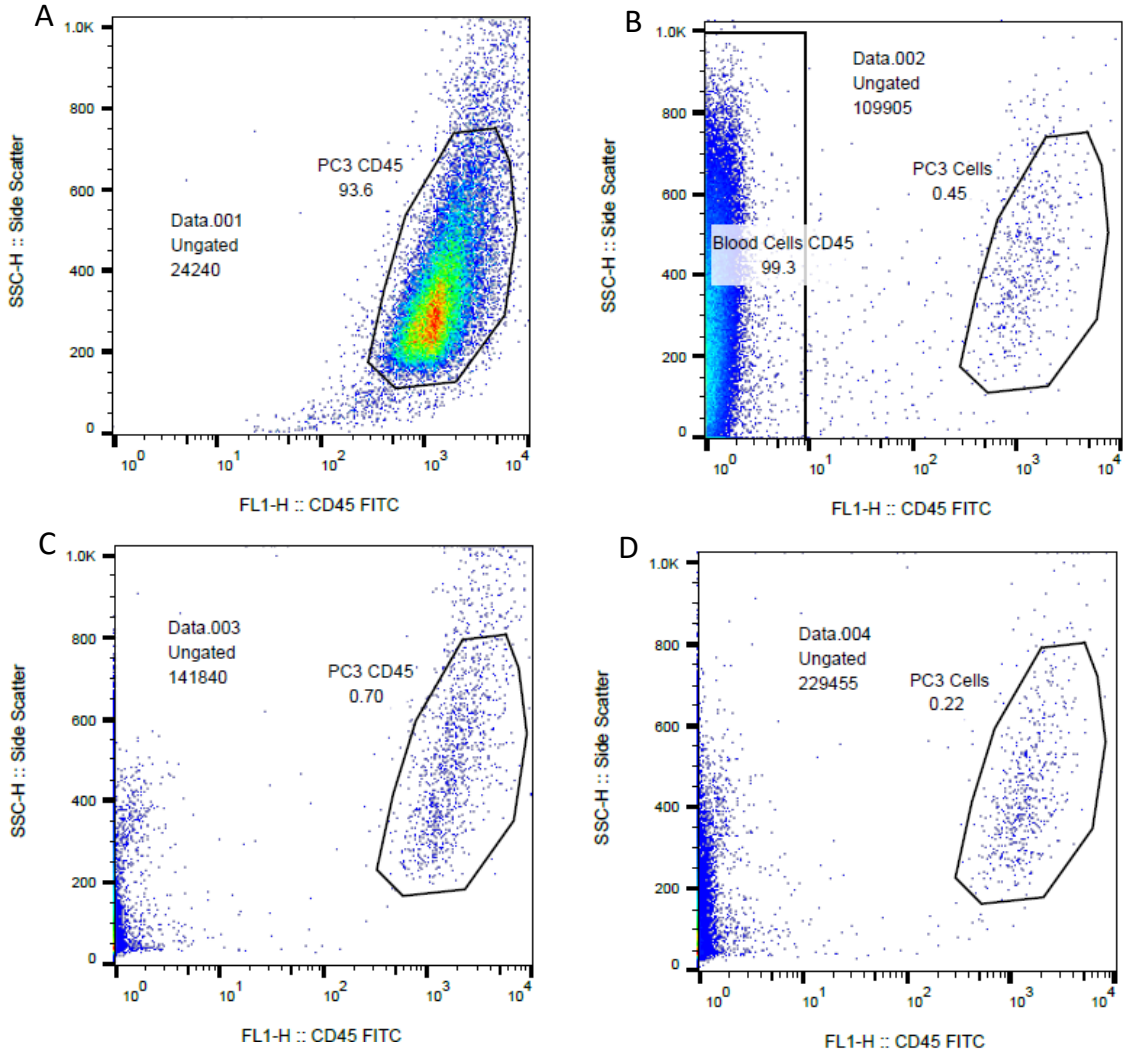

Figure 23. A) A dot plot representing the population of PC3 cells before addition to blood sample. B) A representation of the amount of PC3 cells in the presence of blood cells prior to acoustophoretic processing. C) The first of two fractions of collected PC3 cells after acoustophoretic processing. D) The second of two fractions of collected PC3 cells after processing.

analysis of the collected fractions. Flow cytometry reported the collection of ~5.02 x 10^4 cells against an expected number of 3.63 x 10^5 cells (when using flow cytometer raw sample numbers), for a capture efficiency of only 13.8%. As seen in the dot plots (**Fig. 23C&D**), there was also a high population of untagged blood cells that may have limited the detection of labeled PC3 cells. Future experiments should include a dilution of both the raw sample and the collected fractions prior to flow cytometry analysis in order to eliminate the possibility of masking and provide more accurate cell counts. Ultimately, the source of the low capture efficiency numbers needs be determined, however, the two-transducer method showed great promise for improving the separation of PC3 cells from blood cells, while maintaining a high purity.

5.4 Conclusions

Progress towards the development of a microfluidic system for the separation of circulating tumor cells from whole blood using acoustophoresis was described in this chapter. A series of fluidic designs for handling the complexity of whole blood samples, as well as the sheer number of cells present, were modeled and compared. After selecting a design, the fluidic modeling was corroborated using dyes and whole blood. Acoustic parameters were optimized using 20 μm beads as a CTC mimic. Parameters such as flow rate, frequency, and applied voltage were varied until the 20 μm beads were successfully focused and collected, while red and white blood cells were removed by the filter channels.

Prostate adenocarcinoma (PC3) cells provided samples that would more closely represent the cells of interest in a tumor patient sample. These cells were shown to be similar in size to the 20 μm beads used for optimization, and were characterized using flow cytometry

for comparison to blood cell populations. Acoustophoretic separation of PC3 cells from whole blood was successful with an average capture efficiency of ~40%. Separation and collection of beads showed an efficiency of ~80%. In addition to these efficiencies, the device was very efficient at removing red and white blood cells. An average of 98.5% and 99.1% of original red and white blood cells were removed from the system, respectively. This demonstrated the effectiveness of the device to provide an initial purification of the cells of interest.

Attempts were made to increase the capture efficiency through the use of a two-transducer system. The second transducer at 3 MHz was used to add a pre-focusing step, whereby, the sample was focused entirely into two distinct nodes prior to entering the separation channel. The focusing step brought all of the particles in a sample to roughly the same velocity and eliminated the variable of flow velocity. This allowed the particles to be separated strictly by their acoustic mobility, and was used to provide improved separations at 2 MHz.

5.5 References

1. Mohamed, H.; Murray, M.; Turner, J. N.; Caggana, M., Isolation of tumor cells using size and deformation. *Journal of Chromatography A* **2009**, 1216, 8289-8295.
2. Lu, W. L.; Jansen, L.; Post, W. J.; Bonnema, J.; Van de Velde, J. C.; De Bock, G. H., Impact on survival of early detection of isolated breast recurrences after the primary treatment for breast cancer: a meta-analysis. *Breast Cancer Research and Treatment* **2009**, 114, 403-412.

3. Lianidou, E. S.; Markou, A., Circulating tumor cells in breast cancer: Detection systems, molecular characterization, and future challenges. *Clinical Chemistry* **2011**, 57, 1242-1255.

4. Yu, M.; Stott, S.; Toner, M.; Maheswaran, S.; Haber, D. A., Circulating tumor cells: approaches to isolation and characterization. *Journal of Cell Biology* **2011**, 192, 373-382.

5. Marrinucci, D.; Bethel, K.; Bruce, R. H.; Curry, D. N.; Hsieh, B.; Humphrey, M.; Krivacic, R. T.; Kroener, J.; Kroener, L.; Ladanyi, A.; Lazarus, N. H.; Nieva, J.; Kuhn, P., Case study of the morphologic variation of circulating tumor cells. *Human Pathology* **2007**, 38, 514-519.

6. De Giorgi, V.; Pinzani, P.; Salvianti, F.; Panelos, J.; Paglierani, M.; Janowska, A.; Grazzini, M.; Wechsler, J.; Orlando, C.; Santucci, M.; Lotti, T.; Pazzagli, M.; Massi, D., Application of a filtration- and isolation-by-size technique for the detection of circulating tumor cells in cutaneous melanoma. *Journal of Investigative Dermatology* **2010**, 130, 2440-2447.

7. Vona, G.; Sabile, A.; Louha, M.; Sitruk, V.; Romana, S.; Schutze, K.; Capron, F.; Franco, D.; Pazzagli, M.; Vekemans, M.; Lacour, B.; Brechot, C.; Paterlini-Brechot, P., Isolation by size of epithelial tumor cells - A new method for the immunomorphological and molecular characterization of circulating tumor cells. *American Journal of Pathology* **2000**, 156, 57-63.

8. Desitter, I.; Guerrouahen, B. S.; Benali-Furet, N.; Wechsler, J.; Janne, P. A.; Kuang, Y. A.; Yanagita, M.; Wang, L. L.; Berkowitz, J. A.; Distel, R. J.; Cayre, Y. E., A new

device for rapid isolation by size and characterization of rare circulating tumor cells. *Anticancer Research* **2011**, 31, 427-441.

9. Nilsson, A.; Petersson, F.; Jonsson, H.; Laurell, T., Acoustic control of suspended particles in micro fluidic chips. *Lab on a Chip* **2004**, 4, 131-135.
10. Petersson, F.; Aberg, L.; Sward-Nilsson, A. M.; Laurell, T., Free flow acoustophoresis: Microfluidic-based mode of particle and cell separation. *Analytical Chemistry* **2007**, 79, 5117-5123.
11. Evander, M.; Lenshof, A.; Laurell, T.; Nilsson, J., Acoustophoresis in wet-etched glass chips. *Analytical Chemistry* **2008**, 80, 5178-5185.
12. K Yosioka, Y. K., Acoustic radiation pressure on a compressible sphere. *Acustica* **1955**, 5167, p. 5167-173.
13. Augustsson, P.; Magnusson, C.; Grenvall, C.; Lilja, H.; Laurell, T., In *14th International Conference on Miniatruized Systems for Chemsitry and LIfe Sciences*; Groningen, The Netherlands, 2010, pp 1592-1594.
14. Sun, Y.; Kwok, Y. C.; Nguyen, N. T., Low-pressure, high-temperature thermal bonding of polymeric microfluidic devices and their applications for electrophoretic separation. *Journal of Micromechanics and Microengineering* **2006**, 16, 1681-1688.
15. Hibara, A.; Tokeshi, M.; Uchiyama, K.; Hisamoto, H.; Kitamori, T., Integrated multilayer flow system on a microchip. *Analytical Sciences* **2001**, 17, 89-93.
16. Yousif, M. Y.; Holdsworth, D. W.; Poepping, T. L., A blood-mimicking fluid for particle image velocimetry with silicone vascular models. *Experiments in Fluids* **2011**, 50, 769-774.

17. Nagrath, S.; Sequist, L. V.; Maheswaran, S.; Bell, D. W.; Irimia, D.; Ulkus, L.; Smith, M. R.; Kwak, E. L.; Digumarthy, S.; Muzikansky, A.; Ryan, P.; Balis, U. J.; Tompkins, R. G.; Haber, D. A.; Toner, M., Isolation of rare circulating tumour cells in cancer patients by microchip technology. *Nature* **2007**, 450, 1235-U10.

18. Stott, S. L.; Hsu, C. H.; Tsukrov, D. I.; Yu, M.; Miyamoto, D. T.; Waltman, B. A.; Rothenberg, S. M.; Shah, A. M.; Smas, M. E.; Korir, G. K.; Floyd, F. P.; Gilman, A. J.; Lord, J. B.; Winokur, D.; Springer, S.; Irimia, D.; Nagrath, S.; Sequist, L. V.; Lee, R. J.; Isselbacher, K. J.; Maheswaran, S.; Haber, D. A.; Toner, M., Isolation of circulating tumor cells using a microvortex-generating herringbone-chip. *Proceedings of the National Academy of Sciences of the United States of America* **2010**, 107, 18392-18397.

Conclusions and Future Directions

6.1 Overarching Conclusions

This dissertation has focused on the development and use of several different modes of separation on the microfluidic scale for DNA quantification, cell counting, human identification, and tumor cell isolation. **Chapter 2** described the development and optimization of a system that combined a rotating magnetic field with irrotational vorticity for multiplexing capabilities of a bead-based DNA quantification method. The DFA method not only allowed for multiplexing, it also resulted in a ~4-fold increase in sensitivity with an LOD of 0.250 pg/μL over the 1 pg/μL of the fluorospectrometer. In addition, the capabilities of the DFA system for both rapid WBC count screening, and accurate, multiplexed WBC counts were presented. The ability for the DFA system to analyze 13 samples in 2 minutes and 20 seconds with a total analysis time of 9.5 minutes (including incubation and dilution), represents as high as a 60-fold decrease in total assay time per sample compared to previously described methods. The accuracy of the system was made apparent by the correct call of 18 different patient samples as either being normal, or suffering from leukopenia or leukocytosis.

The multiplexed DFA method was applied to sample preparation in **Chapter 3**. In an effort to eliminate the time-consuming step of DNA quantification prior to amplification and subsequent analysis, the DFA assay eliminated the need for quantification of DNA in a forensically-relevant sample, while providing a simplified combination of both solid- and liquid-phase extraction. STR PCR was successful on samples of human genomic DNA and dried blood, and when a buccal swab was eluted immediately, the eluent could be frozen for long-term storage, and aggregation of beads in the presence of the DNA after extraction was

unaffected. STR profiles were successfully generated from DNA collected from the assay, without the need for quantification.

In **Chapter 4**, progress towards an inexpensive, fully-automated, rotationally-driven microdevice system for the separation and detection of STR fragments for forensic applications was described. A series of materials were tested for use in the PCL development process, with devices fabricated out of COC-PeT-COC and COC-PSA-COC demonstrating the greatest success. With a goal towards 2-base-pair resolution of STR fragments, conditions were optimized on these materials, with a focus on bubbles, surface coating, and joule heating. Ultimately, the resolutions of CTC and CAC devices were found to be ~7 and ~11 bp, respectively. In addition to materials testing and optimization, a multicolor separation and detection system was built and optimized for the separation of STR fragments on an integrated RDM. The detection system provided S/N ratios well above 10:1 for all peaks, demonstrating acceptable sensitivity. A fully integrated system for rotation, clamping, and heating was built around the multicolor detection system and, using an injection-molded microdevice, 2 bp resolution was achieved.

Finally, progress towards the development of a microfluidic system for the separation of circulating tumor cells from whole blood using acoustophoresis was described in **Chapter 5**. An optimized microfluidic design was developed to handle the complexity of whole blood samples, and multiple transducers were used to improve the separation of PC3 cells from red and white blood cells. Capture efficiencies of PC3 cells was found to be ~40%, around 80% of polystyrene beads were captured, and an average of 98.5% and 99.1% of original red and white blood cells were removed from the system, respectively, demonstrating effective purification of beads and cells of interest.

6.2 Future Directions

Many of the experiments and separation modes presented in this dissertation demonstrated proof-of-principle concepts for isolating and quantifying cells and DNA in various ways on a microfluidic scale. More work is required, however, to fully realize the potential shown for these assays. The DFA assay was effective for the counting of white blood cells in a patient sample, and therefore, may hold promise as a method for cell counting in other applications. Bacterial cell counting is an example where the efficacy of antibiotics on cell growth can be monitored. Furthermore, the DFA system showed promise as a rapid screening technique, however, integration of image capture and analysis, along with system automation, would be necessary in order to apply this assay in a clinical setting.

The use of the DFA system as a quantification-free, sample preparation method for STR analysis also demonstrated the potential of the system. While proof-of-principle STR profiles were generated from DNA collected with the assay, further study is required to improve the amplification and the profiles generated, while demonstrating success on different substrates. In addition, DFA was shown to have an LOD at the sub-single cell level, and therefore, may be suitable for trace or rare DNA analysis. Once again, automation and integration would allow for this system to be used in the field at the point of collection.

Finally, while the acoustphoresis method was shown to be decently effective at separating tumor cell lines from blood cells in **Chapter 5**, there are many improvements that would need to be made in order to see this method applied to patient samples. First, capture efficiencies need to be improved through further optimization of flow rates and applied voltages. After capture efficiencies are improved, secondary analysis steps would likely be

required. Because acoustophoresis is a size-based technique, and some white blood cells are similar in size to epithelial tumor cells, another form of separation could be coupled to the initial acoustophoresis enrichment step. One possible solution is an anti-CD45 negative selection step that would capture any white blood cells expressing CD45 antigen, while the epithelial tumor cells would pass through. In-line detection of collected cells would also simplify the analysis process of CTCs. Current methods using PCR or microscopy are time consuming, laborious, require highly-trained personnel, and require the cell to be lysed or fixed, preventing downstream processing such as cell culture. One alternative option, is the use of Raman spectroscopy to characterize cells in a non-destructive manner. This method was developed by Stevens et al.[1-5], and would provide an opportunity to identify and enumerate cells directly in line with upstream acoustophoretic processing.

6.3 Summation

The use of microfluidic devices offers many advantages over conventional benchtop instrumentation and the coupling of microfluidics with various modes of separation has shown great potential to be used as fast, portable, and accurate analysis systems for clinical and forensic applications. The separation modes described here were shown to be effective, and in many cases, improvements over conventional instrumentation. With continuing study, these methods can be further improved and applied to an increasing number of applications, including venturing outside the fields of clinical and forensic chemistry.

6.4 References

1. Gentleman, E.; Swain, R. J.; Evans, N. D.; Boonrungsiman, S.; Jell, G.; Ball, M. D.; Shean, T. A. V.; Oyen, M. L.; Porter, A.; Stevens, M. M., Comparative materials differences revealed in engineered bone as a function of cell-specific differentiation. *Nature Materials* **2009**, 8, 763-770.

2. Notingher, L.; Jell, G.; Notingher, P. L.; Bisson, I.; Tsigkou, O.; Polak, J. M.; Stevens, M. M.; Hench, L. L., Multivariate analysis of Raman spectra for in vitro non-invasive studies of living cells. *Journal of Molecular Structure* **2005**, 744, 179-185.

3. Swain, R. J.; Stevens, M. M., Raman microspectroscopy for non-invasive biochemical analysis of single cells. *Biochemical Society Transactions* **2007**, 35, 544-549.

4. Owen, C. A.; Notingher, I.; Jell, G.; Selvakumaran, J.; Stevens, M. M.; Hench, L. L., Raman spectroscopy as a tool for preliminary drug testing on human cells. *Journal of Pharmacy and Pharmacology* **2004**, 56, S51-S52.

5. Swain, R. J.; Kemp, S. J.; Goldstraw, P.; Tetley, T. D.; Stevens, M. M., Spectral monitoring of surfactant clearance during alveolar epithelial type II cell differentiation. *Biophysical Journal* **2008**, 95, 5978-5987.